University of Sussex

Yb^+ ion trapping and optimum planar trap geometries for scalable quantum technology

Altaf Hussain Nizamani

Submitted for the degree of Doctor of Philosophy

University of Sussex, Brighton, United Kingdom.

February 2011

Declaration

I hereby declare that this thesis has not been and will not be submitted in whole or in part to another University for the award of any other degree.

Signature:

Altaf H. Nizamani

UNIVERSITY OF SUSSEX

Altaf H. Nizamani, Doctor of Philosophy

Yb^+ ion trapping and optimum planar trap geometries for scalable quantum technology

Abstract

Trapped ions in linear Paul traps are largely isolated from interaction with the environment. This property of trapped ions make them a primary choice for quantum technology. Over the last decade, trapped atomic ions in linear radio frequency Paul traps have shown to be an important tool to implement quantum algorithms. The scalability of linear ion traps is required to handle large numbers of qubits, in order to implement useful quantum computation. Advance micro-fabrication technology allows the realisation of scalable ion traps. Further developments of micro-trap designs, for the purpose of scalable quantum technology, requires inter-disciplinary investigations of ion traps. Micro-scale ion trap designs typically require a versatile experimental setup. The first part of this thesis describes such an experimental setup including a chip bracket that can host macroscopic ion traps as well as advanced symmetric and asymmetric ion trap chips with up to 90 control electrodes. The system provides versatile optical access for both type of traps and the vacuum chamber is designed in a way so the ion traps can be replaced within a short amount of time. To test the working of the setup, a macroscopic ion trap with an ion-electrode distance of 310±10 μm is used to trap ytterbium ions (Yb^+). The trap is characterised by measuring the heating rate, $\langle \dot{n} \rangle$, and spectral noise density $S_{\mathrm{E}}(\omega)$. A photoionisation technique is used to ionise the different isotopes of Yb in our trap. Isotope selective photoionisation requires exact measurements of ${}^1S_0 \leftrightarrow {}^1P_1$ transition for the different Yb isotopes. A technique to measure these resonant frequencies is described. This technique works by observing and aligning fluorescence spots and by using this technique, the ${}^1S_0 \leftrightarrow {}^1P_1$ transition frequencies for stable isotopes of Yb were measured with an accuracy of 60 MHz. These new measured transition frequencies for stable Yb isotopes differ from previously published work by 660 MHz. Furthermore, this technique can also be used to obtain the transition frequencies at different laser-atomic beam angles, typical for non-perpendicular laser-atomic beam angles.

The second part of this thesis discusses the optimisation of surface trap geometries as they are being used to implement scalable ion trap designs which consist of a large number of trapping zones. The trap depth in surface traps is low compared to symmetric traps of similar dimensions. How to optimise the trap geometry to achieve maximum trap depth for a given ion height above the trap electrodes, is discussed. Fast and adiabatic ion shuttling operations in one dimension as well as ion separation and recombination processes are important for many quantum information implementations. The maximum speed of separation of trapped ions for adiabatic shuttling operations depends on the secular frequencies, the trapped ion experiences in the process. It will be shown how such ion trap structures have to be designed for fast ion separation process and linear shuttling. Numerical results of adiabatic shuttling operations for trapped ions in such trap structures are also presented.

Acknowledgements

I would like to express my heartiest gratitude to my supervisor, Winfried Hensinger for giving me the opportunity to work on this exciting research and for the experience of building a new research lab. He was always there to help me when ever I needed it; his enthusiasm about Physics never ceases to amaze me.

My deepest thanks must go to my colleagues, James McLoughlin for helping me to understand the laser setup, Robin Sterling who shared with me his knowledge of laser locking and building the ion traps, James Siverns and Marcus Hughes, who provided me useful knowledge of the resonator and imaging setup. They all made significant contribution to the project described in this thesis. Thanks must also go to Nik Davies, Bjoern Stein, Bjoern Lekitsch and Seb Weidt for the same. We all worked together during the building of the lab and shared the "hardest" and most "jubilant" moments during the fulfillment of the project.

A big thank you goes to all the members of Wolfgang Lange's lab whose help and advice was always on hand, and also to Barry Garraway for the same.

I must thank the University of Sindh, Jamshoro, Pakistan, for most of the financial support for my studies, without that this work would never have come into existence.

Many thanks go to my colleagues from the University of Sindh, Zeeshan Patoli, Yasir Malkani, Lachman Dhomeja, Faraz Bughio, Irfan Rind and Ayaz Keerio with whom I enjoyed my stay in the UK. Special thanks must go to Fatima Soomro for her support and encouragement, and for the many useful discussions. I am also thankful to Akhtar Rind for his much appreciated support and friendship.

On a personal note, I owe my deepest gratitude to my parents, teachers, relatives and friends who have always been extremely supportive and had far more confidence in me than I have had in myself. They all have contributed towards the stage that I have now proudly reached. I would also like to thank my grandparents, who understood the impor-

tance of education even when they had none and impart this belief into their children and grandchildren. Alas my father would have alive today to see this auspicious moment, I want to express my deepest gratitude to him for everything he did for me.

And, of course, I want to thank Aapa, Amma, my wife Zohra and my children Zareen and Irtaza, who suffered a lot due to my absence in the past years. Specially Zohra, without her support from the home front, I would not have been able to do any of this. She is my strength and support and I thank her with all my heart.

Thesis Contributions

Some parts of this thesis are not completely my work but were carried out or aided by other members of the group. This work is included for the completeness of the thesis. Here I wish to acknowledge and outline the contributions provided by each group member.

Chapter 3: Ultra High Vacuum System

Most of the vacuum system and custom parts were designed by myself with significant contributions from undergraduate project student Nik Davies. Most of the custom parts were built in the university workshop. The system was assembled by myself with assistance from James McLoughlin and Philippa Young. The atomic-oven testing was performed by myself and James McLoughlin. The cleaning, degassing and pumping down procedures were performed by myself.

Chapter 4: Experimental Setup

The external cavity diode lasers were constructed by James McLoughlin.
The frequency reference Rb locked 780-nm laser setup was built and implemented by Robin Sterling.
The laser locking scheme was implemented by James Siverns and myself.
The magnetic coils were constructed by myself.
The imaging system was designed and constructed by James Siverns with assistance of Marcus Hughes.
The data acquisition programs for the imaging system were written and implemented by myself and James McLoughlin.
The resonator was designed and built by James Siverns.

Chapter 5: Yb^+ Trap Experiment

The macroscopic trap was designed by Robin Sterling and the construction of the trap was jointly carried out by Robin Sterling, James McLoughlin, Marcus Hughes, James Siverns and myself.
The trap experiment and several frequency measurements were carried out by myself, James McLoughlin, James Siverns, Robin Sterling and Marcus Hughes.
In order to characterise the ion trap a heating measurement experiment was performed by all members of the group. The theoretical model was reproduced by Bjoern Lekitsch and James McLoughlin. The computer control and data acquisition scheme for the experiment was implemented by myself and James McLoughlin.
The plot in figure 5.13 was produced by Marcus Hughes.

Chapter 6: Yb Spectroscopy

In order to measure the 399-nm transition line frequencies for Yb isotopes, the florescence spot method was developed by myself and the experiments were carried out by myself and James McLoughlin.

Chapter 7: Surface Traps

Most of the work in this chapter was carried out by myself. The microfabricated SOI trap is designed by Robin Sterling. The trap modelling and simulations were performed by Robin Sterling and myself.

Publications and conference contributions

Journal publications

The work presented in the following paper is based on chapter 3, 4 and 5. The experiment was performed by all the group members and James McLoughlin had the primary responsibility for writing the paper.

Versatile ytterbium ion trap experiment for operation of scalable ion-trap chips with motional heating and transition-frequency measurements,
James J. McLoughlin, Altaf H. Nizamani, James D. Siverns, Robin C. Sterling, Marcus D. Hughes, Bjoern Lekitsch, Björn Stein, Seb Weidt, and Winfried K. Hensinger,
Phys. Rev. A 83, 013406 (2011).

The work presented in the following paper is based on chapter 6. The experiment was performed by myself and James McLoughlin and I had the primary responsibility for writing the paper.

Doppler-free Yb Spectroscopy with Fluorescence Spot Technique,
Altaf H. Nizamani, James J. McLoughlin and Winfried K. Hensinger,
Phys. Rev. A 82, 043408 (2010).

The work presented in the following paper is based on chapter 7, 8 and 9. The trap modelling and simulations were performed by myself and I had the primary responsibility for writing the paper.

Optimum electrode configurations for fast ion separation in microfabricated surface ion traps,

Altaf H. Nizamani and Winfried K. Hensinger,
arXiv:1007.3542v1 [quant-ph] (2010).

Conference contributions

Scalable quantum technology with trapped ytterbium ions,
Altaf Nizamani.
Talk at 1st European Conference on Trapped Ions (ECTI 2010), 19-24 September 2010, at Redworth Hall, County Durham, UK.

Optimum surface trap geometries for fast ion separation and the development of junctions within ion trap arrays,
A. H. Nizamani, B. Stein and W. K. Hensinger.
Poster at 1st European Conference on Trapped Ions (ECTI 2010), 19-24 September 2010, at Redworth Hall, County Durham, UK.

Trapped ytterbium ions for scalable quantum technology,
J.J. McLoughlin, A.H. Nizamani, J.D. Siverns, R.C. Sterling, M.D. Hughes, B. Lekitsch, B. Stein, S. Weidt and W. K. Hensinger.
Poster at 1st European Conference on Trapped Ions (ECTI 2010), 19-24 September 2010, at Redworth Hall, County Durham, UK.

Microfabricated ion traps for quantum information and simulation,
R. C. Sterling, P. Srinivasan, H. Rattanasonti, D. Brown, A. H. Nizamani, K. Schwab, M. Kraft and W. K. Hensinger.
Poster at 1st European Conference on Trapped Ions (ECTI 2010), 19-24 September 2010, at Redworth Hall, County Durham, UK.

Design and setup of an ytterbium ion trap experiment towards scalable ion quantum information processing,
Altaf H. Nizamani, James J. McLoughlin, James D. Siverns, Robin C. Sterling, Marcus Hughes and Winfried K. Hensinger.
Poster at ICOLS 2009 - 19th International Conference on Laser Spectroscopy, 08-14 June

2009, Kussharo, Hokkaido, Japan.

Towards laser cooling and trapping of $^{171}Yb^{+}$ ions: The vacuum system, arbitrary electrode modelling and design of a chip carrier mounted linear Paul trap,

Altaf H. Nizamani, Robin C. Sterling, James J. McLoughlin, James D. Siverns, Nicholas Davies, Tim Short and Winfried K. Hensinger.

Poster at QuAMP 2007, 10-13 September, 2007, at University College London, London, UK.

Towards laser cooling and trapping of $^{171}Yb^{+}$ Ions: lasers and their stabilisation, transitions, cooling cycles and radio frequency applications for Paul traps,

J. D. Siverns, J. J. McLoughlin, R. C. Sterling, B. S. Pruess, J. N. M. Grove-Smith, D. N. Scrivener, A. H. Nizamani and W. K. Hensinger.

Poster at QuAMP 2007, 10-13 September, 2007, at University College London, London, UK.

Contents

Abstract **iv**

Acknowledgements **v**

Thesis Contributions **vii**

Publications and conference contributions **ix**

List of Tables **xvi**

List of Figures **xxi**

1 Introduction **1**

2 Theoretical background **5**

2.1 Paul Traps 5

2.2 Principal axes 11

2.3 Linear trap geometry 13

2.4 Doppler cooling 17

2.5 Yb^+ ions 19

3 Ultra High Vacuum system **22**

3.1 Vacuum chamber 25

3.1.1 Chip bracket 25

3.1.2 Chamber 26

3.1.3 Viewports 30

3.1.4 Atomic source ovens 31

3.2 Assembly of the vacuum system 35

3.2.1 Cleaning and pre-baking 38

3.2.2 Pumps and gauges 40

3.2.3 Assembly . . . 44
3.3 Pumping down procedures . . . 48
3.3.1 Degassing . . . 48
3.3.2 Leak test . . . 50
3.3.3 Final baking . . . 51

4 Experimental setup **54**
4.1 Introduction . . . 54
4.2 Lasers . . . 55
4.2.1 Photo-ionisation laser (399-nm) . . . 56
4.2.2 Doppler cooling laser (369-nm) . . . 56
4.2.3 Re-pump laser (935-nm) . . . 56
4.2.4 Re-pump laser (638-nm) . . . 57
4.3 Laser locking scheme . . . 57
4.3.1 Reference laser (780-nm) . . . 58
4.3.2 Transfer cavity lock . . . 59
4.3.3 Data acquisition and feedback control program . . . 59
4.3.4 Wavemeter lock . . . 65
4.4 Dark states destabilisation . . . 65
4.5 Imaging system . . . 68
4.5.1 Data acquisition . . . 69
4.6 The resonator . . . 73

5 Yb^+ Trap Experiment **77**
5.1 Introduction . . . 77
5.2 Blade trap . . . 78
5.3 Trap experiment . . . 80
5.3.1 Ion loading . . . 80
5.3.2 Ion trap operations . . . 83
5.3.3 Wavelengths measurements . . . 84
5.3.4 Error analysis . . . 86
5.4 Heating measurements . . . 86

6 Yb Spectroscopy **94**
6.1 Introduction . . . 94
6.2 Yb 399-nm line Spectroscopy . . . 96

6.2.1 Experimental Setup . . . 96
6.2.2 Fluorescence spot technique . . . 99
6.2.3 Error analysis . . . 104
6.3 Saturation absorption spectroscopy . . . 105
6.4 Doppler Shifted frequency measurements . . . 107

7 Surface Traps **111**
7.1 Introduction . . . 111
7.2 Trap potential . . . 112
7.3 Optimisation of trap depth . . . 117
7.4 Optimum voltages . . . 120
7.5 Control electrode design . . . 122
7.6 SOI trap chip . . . 123
7.6.1 Fabrication . . . 125
7.7 Modelling and simulation . . . 126

8 Ion Separation **130**
8.1 Introduction . . . 130
8.2 Design considerations . . . 131
8.3 Ion separation: theory . . . 131
8.4 Optimisation of ion separation process . . . 134

9 Ion Shuttling **145**
9.1 Introduction . . . 145
9.2 Ion dynamics . . . 146
9.3 Shuttling in one-dimension . . . 152
9.3.1 Outer segmented electrode geometry . . . 153
9.3.2 Centre segmented electrode geometry . . . 156
9.3.3 Discussion on results . . . 158
9.4 Ion separation in one dimension . . . 159
9.4.1 Ion separation in outer segmented static electrode geometry . . . 160
9.4.2 Ion separation in centre segmented static electrode geometry . . . 163

10 Conclusion **166**

A Chip bracket pin receptacles map **168**

B Re-entrant viewport drawing **170**

C LabVIEW program for laser locking scheme **172**

D LabVIEW program for EMCCD camera **184**

E FPGA LabVIEW program for PMT **190**

F FPGA LabVIEW program for the heating measurement experiment **194**

Bibliography **202**

List of Tables

3.1 Mean free path at different ranges of pressure and required vacuum pumps. 24

5.1 The $^1S_0 \leftrightarrow {}^1P_1$ transition wavelengths 83
5.2 RF and static voltage on the trap electrodes. 84
5.3 The cooling $^2S_{1/2} \leftrightarrow {}^2P_{1/2}$ and 85

6.1 Relative abundance of Ytterbium isotopes 95
6.2 The frequency shifts for the various isotopes of Yb from 103
6.3 The absolute frequencies for $^1S_0 \leftrightarrow {}^1P_1$ transition line 103

9.1 Applied voltages on the electrodes 160
9.2 Applied voltages on the trap electrodes for centre segmented 163

List of Figures

1.1 An artistic illustration of a highly segmented trap geometry 2

2.1 (a) Linear rf Paul trap. (b) Ring rf Paul trap for point confinement. 6
2.2 (a) Mathieu stability diagram in a and q space for quadrupole ion 8
2.3 The motion of a charged particle in an rf Paul trap. 9
2.4 (a) The principal axes are same as the trap axes when there 11
2.5 (a) The principal axes are same as the trap axes when 13
2.6 (a) Two layer linear rf trap geometry implemented with 15
2.7 (a) Three layer linear rf trap geometry implemented with 16
2.8 (a) Planer or surface rf trap geometry implemented with 18
2.9 Two photon ionisation scheme for Yb using its 19
2.10 Energy level diagram for Yb^+ ion having zero nuclear spin 20
2.11 Energy level diagram for $^{171}Yb^+$ ion 21

3.1 90 pin receptacles inserted on the chip bracket plate. 26
3.2 (a) Front view of custom made chip bracket and mounting position 27
3.3 Vacuum chamber assembly connected with custom made T-piece. 27
3.4 Top cut-view of the chamber to show the laser access 28
3.5 Chip bracket is mounted inside the hemisphere using groove grabbers. . . . 29
3.6 Transmission curves for the viewports used in 31
3.7 Re-entrant custom 4.5" CF flange viewport for 32
3.8 Atomic oven testing system. (a) The position of an atomic oven 34
3.9 Partial pressure curves for (with gain factor of ≈1000) 36
3.10 Partial pressure curves (with gain factor of ≈1000) 37
3.11 CF tightening pattern for ConFlat flanges with 38
3.12 AR-coated viewport cleaned in methanol compared with 39
3.13 Internal structure of a sputter ion pump. 41

3.14 Pumping speed of an ion pump as a function of pressure and voltage. . . . 42
3.15 Pressure measurement devices: (a) Extorr RGA (200M) filament 43
3.16 Dimensions of the UHV system: (a) Front view 45
3.17 (a) Picture of the inner section of the chamber taken from the 47
3.18 (a) SolidWork design of the UHV system and 49
3.19 The roughing vacuum system consists of a 60L turbomolecular 50
3.20 Baking oven and the UHV system. 51
3.21 Bake-out process of 16 days. The pressure in the system on 53

4.1 (a) The saturation absorption spectroscopy signal obtained by scanning . . 60
4.2 The distance between the two reference laser (780-nm) peaks 61
4.3 The block diagram of the real-time laser locking program 62
4.4 The block diagram shows working scheme of the RTOS and the 62
4.5 Front panel of the real-time laser locking program. 63
4.6 Laser locking-scheme and alignment into the trap. 64
4.7 (a) Zeeman degenerate states in $^2S_{1/2} \leftrightarrow ^2P_{1/2}$ of $^{171}Yb^+$ 66
4.8 Three magnetic coils are suspended around the chamber to 67
4.9 Imaging system consists of a triplet (object lens) and 68
4.10 The block diagram shows the data flow from FPGA to Host PC. 69
4.11 User interface for the LabVIEW program which controls 70
4.12 User interface for the LabVIEW program which counts the 72
4.13 The schematic of a helical resonator. 74
4.14 Picture shows the resonator built in our lab. 76

5.1 Trap electrode sizes and the numbering for voltage application. 79
5.2 Trap electrodes. 79
5.3 (a) Design of the PEEK base. (b) Design of the metal cage. 81
5.4 Blade trap assembly. 82
5.5 Pseudopotential created by the trap electrodes at the centre of the trap. . . 82
5.6 (a) Three Yb^+ ion crystal, (b) multi-isotope Yb^+ ion 85
5.7 The cooling laser is turned off and on again using AOM for 87
5.8 User interface for the labVIEW programs written in labVIEW FPGA . . . 88
5.9 Overlap of the probability density of the Doppler shift, $P_D(\Delta_D)$ 89
5.10 Averaged fluorescence curve obtained from 500 re-cooling cycles 90
5.11 Change in ion energy in terms of motional quanta, Δn 91

5.12 Heating rate $\dot{n}$ at three different secular frequencies 92
5.13 Electric field noise density, $S_E(\omega_z)$ versus ion-electrode 93

6.1 Two colour photoionisation scheme for neutral Yb. 95
6.2 Schematic diagram (a) shows the counter propagating laser beams 98
6.3 Illustration of the fluorescence spots movement according to laser detuning 100
6.4 Illustration of the resolution of the spectroscopy method. 100
6.5 Yb isotope shifts for the 399-nm $^1S_0 \leftrightarrow^1 P_1$ transition line. 102
6.6 Absorption saturation spectroscopy arrangement. 105
6.7 $^1S_0 \leftrightarrow^1 P_1$ transition peaks for different isotopes 106
6.8 (a)Illustration of the counter propagating laser beam pairs making an . . . 107
6.9 Pictures show the atomic oven and fluorescence spots 108
6.10 Doppler frequency shift in $^1S_0 \leftrightarrow^1 P_1$ transition 109

7.1 The *five-wire* planar trap designs (a) with outer and 113
7.2 The position of an electrode defined in $x - z$ plane 114
7.3 Illustration of pseudopotential field over the surface trap 115
7.4 3D plots of the pseudopotential field over the surface trap 116
7.5 Plot of the pseudopotential field over the surface trap 117
7.6 The rotation of the principal axis by breaking the symmetry of 118
7.7 In order to keep the static potential electrodes' position symmetric 119
7.8 For a given ion height, trap depth geometric factor κ 120
7.9 Potential curvature $\partial^2\phi/\partial z^2$ in the 122
7.10 (a) Unmodified junction region and (b) Modified junction region 124
7.11 (a) Horizontal displacement of the rf-nodal path from the central 128
7.12 The barrier potential of the unmodified (solid line) and modified 129
7.13 Variation of the radial secular frequencies (ω_x and ω_y) 129

8.1 Plots of the potential when $\alpha > 0$, zero and $\alpha < 0$ 132
8.2 In design (a) outer electrodes are segmented in (b) the inner 135
8.3 At least three control electrodes are required to provide 136
8.4 Arbitrary applied voltages on the *control* and *wedge* 137
8.5 Creation of a double well is illustrated. (a) Both ions are 138
8.6 α is plotted against electrode widths (W=C=E) in the units of 139
8.7 β is plotted against the ratio of wedge electrode 141
8.8 β is plotted against electrode widths (W=C=E) in the 142

8.9 (a) α and (b) β are plotted vs rf-electrode 143

9.1 Plot of the position of the potential minimum versus time 149
9.2 Two zone trap array implemented with outer segmented 154
9.3 Voltage variation in time to move the ion from the trapping 155
9.4 The distance shuttled by the ion when the static voltage 155
9.5 The gain in the average motional quanta $\langle n \rangle$ by the ion in 156
9.6 Two zone trap array implemented with centre segmented 157
9.7 Voltage variation in time to move the ion from the 158
9.8 The gain in the average motional quanta $\langle n \rangle$ by the ion 159
9.9 External segmented electrode surface trap geometry 160
9.10 Applied voltages variation in time on the *control* and 161
9.11 Variation of the z-secular frequency during the ion-separation 161
9.12 The gain in the average motional quanta $\langle n \rangle$ by the ion 162
9.13 Centre segmented electrode trap geometry for separation 163
9.14 The gain in the average motional quanta $\langle n \rangle$ by the ion in 165

A.1 Pin receptacles mapping with 50×2 D-type electrical 169

B.1 SolidWork drawing of the custom view port. 171

C.1 Schematic diagram of laser locking project. 173
C.2 Front panel of LabVIEW program for laser locking scheme. 175
C.3 Wavemeter lock section. 176
C.4 Scanning cavity lock section. 179
C.5 Wavemeter lock code. 181
C.6 Scanning cavity lock code. The code reads the data 182
C.7 Error signal output code. The code generates 183

D.1 Front panels of the EMCCD camera program. 187
D.2 The LabVIEW code which access the data 189

E.1 FPGA project 191
E.2 Front panel of the PMT LabVIEW program. 191
E.3 Program code of the PMT LabVIEW program. 193

F.1 FPGA project 195
F.2 The different time scales of the heating measurement experiment 196

F.3 Front panels of the *Target* and the *Host* programs 197
F.4 The code of the *Target* program for the heating measurement experiment . 200
F.5 The code of the *Host* program for the heating measurement experiment . . 201

Chapter 1

Introduction

The idea of quantum computing was initially proposed by Richard Feynman [1]. David Deutsch using the idea of a quantum Turing machine, showed certain algorithm for which quantum computer can be faster than a classical computer. When Peter Shor [2] and others in mid 90's suggested an algorithm that would exponentially speed up factorisation of large numbers as well as solving the problem of code breaking using a quantum computer, the scientific community realised the great potential of quantum computation. Apart from the code breaking, communication can also be made more secure using quantum information technologies which use physical quantum properties of the information carriers. In contrast with classical computation systems which use 'binary bits' known as '0' or '1', quantum information and computation resources use 'quantum bit', well known as '*qubit*', which can also exist in a superposition state of '$|0\rangle$' and '$|1\rangle$'. Many of the Qubit operation are well demonstrated using atomic ions. Due to their long trapping times as well as coherence properties, trapped ions are natural choice for quantum information processing.

In past decade many key aspects of quantum computation have been demonstrated in various experiments [3–15]. To perform a large scale quantum computation, it would be useful if qubits can be stored in separate trapping regions, *storage zones*, and only be brought together in a single trap, *interaction zone*, when quantum operations are required [5, 15–17]. The ability of the control and storage of a large qubit system requires several independent trap regions, connected by junctions. These regions can be interconnected using junctions. This scheme is illustrated in an artistic approach in figure 1.1.

These trap arrays can be implemented by using highly segmented trap geometries. The use of microfabrication techniques is promising to integrate a large number of trap segments

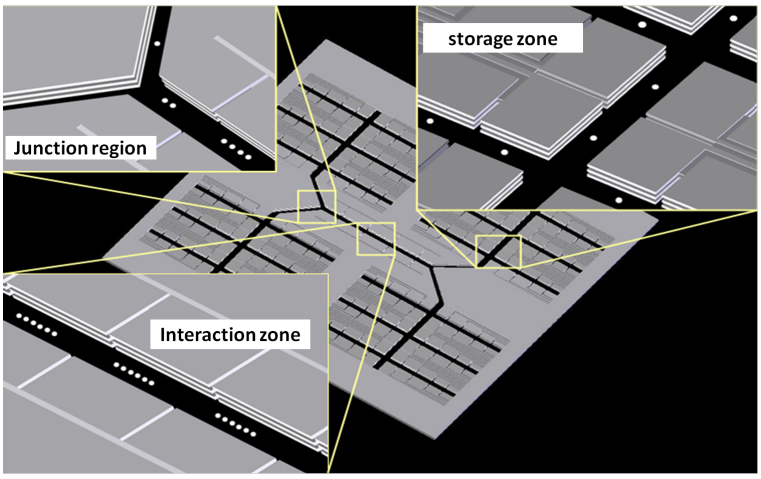

Figure 1.1: An artistic illustration of a highly segmented trap geometry with interaction and ion storage zones.

where a large set of qubit systems can independently be controlled. Several trap geometries are already demonstrated using microfabrication techniques. [12, 18–25].

Recently, planar electrode trap geometries have been used to implement scalable ion trap designs which consist of a large number of trapping zones. One type of traps is classified as asymmetric or surface trap and is characterised by a weaker trap depth and simpler fabrication methods [12, 23–29]. The trap depth in planar trap geometries can be maximised by decreasing the ion-electrode distance. Decreasing the ion height also increases the heating rate, which leads to decoherence during quantum gate operations [30–33]. Although, recently it is shown that by using a cryogenic environment, the heating rate can be decreased by six orders of magnitude [32, 34], still surface trap geometries can be optimised to achieve higher trap depths at larger ion-electrode distance.

Furthermore, research in practical development of scalable traps characterised by low heating rates and decoherence is required for the realisation of scalable quantum computation. Adiabatic ion shuttling operations within multi-segmented scalable microtraps will play an important role.

This thesis can be divided in three parts. The first part (chapter 3, 4 and 5) covers a new experimental setup for a Yb ion trap operation of a symmetric ion trap as well as microfabricated asymmetric trap. Demonstrating successful isotope selective ionisation and trapping of Yb^+ ions including $^{171}Yb^+$, whose hyperfine levels can be used for qubit operations. In order to test more complicated trap geometries and ion trap arrays, chapter 3 will describe a vacuum system which can handle ion trap geometries having up to

90 control electrodes and provide laser access for both symmetric and asymmetric trap design. Atomic ovens inside the the vacuum system provide natural abundance Yb as well as enriched ^{171}Yb vapours for both trap geometries.

Chapter 4 describes an overview of the experimental setup for an Yb ion trap experiment including laser setup for ionisation and Doppler cooling of Yb ions and imaging setup to image and detect the fluorescence of the trapped ions. Furthermore in this chapter, a computer controlled locking scheme of the laser frequencies is described which works in real time operating system. In order to destabilise the dark states of the trapped ions, an arrangement of magnetic coils is also discussed.

Chapter 5 describes the operation and characterisation of a two-layer symmetric ion trap in which different isotopes of Yb were successfully ionised and trapped. Furthermore, heating rate measurements procedures are also discussed.

A photoionisation technique is used in our ion trap experiment to ionise Yb isotopes which works by exciting the $^1S_0 \leftrightarrow {}^1P_0$ transition in Yb atoms. Unfortunately in published literature, wavelengths for this $^1S_0 \leftrightarrow {}^1P_0$ transition for Yb ions are not given accurately. To resolve discrepancies in the given wavelengths, a simple method was devised in our lab which works by detecting the florescence from the Yb atoms. The second part of the thesis (chapter 6) describes this experimental arrangement and provides a set of new wavelengths for S-P transition in Yb isotopes which differs from recently published work. In real ion trap experimental arrangement, it is not necessary that the the ionisation laser is perpendicular to the atomic beam. To solve this problem, the devised technique can also be used to measure appropriate Doppler shifts at different angles between the lasers and the atomic beams.

The third part of the thesis is based on the optimisation of surface trap geometries for high trap depth at the given ion height and for the separation and shuttling of the ions in the multi-segmented trap regions. In this part of the thesis, chapter 7 describes the optimisation of the trap depth in surface trap geometries by choosing an appropriate size of rf electrodes and their separation in ion traps. In this chapter a Y-junction ion trap is also discussed which consists of 44 control electrodes and three ion trap arrays joining at

a junction. In order to implement a large scale quantum computer, it is suggested to trap ions in different regions of an ion trap array, where ions can be trapped and then separated and shuttled to different storage and memory regions. During the separation process of the two trapped ions, the secular frequency of an ion trap varies a lot and reaches at a minimum when a *wedge* potential is introduced to produce a *double well* in a single potential well. This fast reduction in the secular frequency slow downs the separation process. In order to provide fast ion separation process in surface trap geometries, a detailed discussion is given in chapter 8 where the surface trap geometries are optimised to provide high secular frequencies during the separation process. Finally chapter 9 describes in detail the dynamics of the ion during the linear shuttling and ion separation process.

Chapter 2

Theoretical background

Ion traps are classified into, Paul Traps and Penning traps. Paul traps use an electric quadrupole field oscillating at radio frequency, while Penning traps use magnetic field to confine the ions. Ion traps used in this thesis are based on the Paul traps developed by Noble laureate Wolfgang Paul [35] in 1950s. The Paul trap was originally developed for use in particle accelerators and mass spectrometry, but they have been used for many experiments including frequency standards [36–39], atomic clocks [40–43], quantum electrodynamics and quantum information and computing [3, 7, 14, 44–46] due to their ability to trap single to millions of atomic ions in good isolation from the outside world. Paul shared the 1989 Nobel Prize for his work in developing the trap and its applications.

2.1 Paul Traps

Several books and reviews give an extensive mathematical treatment of the motion of an ion in a Paul trap [5, 35, 47–49]. Following the description given by [48, 49], the principle behind a Paul trap, to confine an ion in a quadratic electric potential, is of the form [48]

$$\phi(\vec{r}) = -\frac{\phi_o}{2r_o^2}(\alpha x^2 + \beta y^2 + \gamma z^2) \tag{2.1}$$

where ϕ_o is an applied electric potential, r_o is a length depending on the electrode geometry, and α, β and γ are coefficients chosen to satisfy the Poisson equation. The electric field $\vec{E}$ produced by such a potential can be calculated as [48]

$$\vec{E} = -\vec{\nabla}\phi(\vec{r}) = -\frac{\phi_o}{r_o^2}(\alpha x\hat{x} + \beta y\hat{y} + \gamma z\hat{z}) \tag{2.2}$$

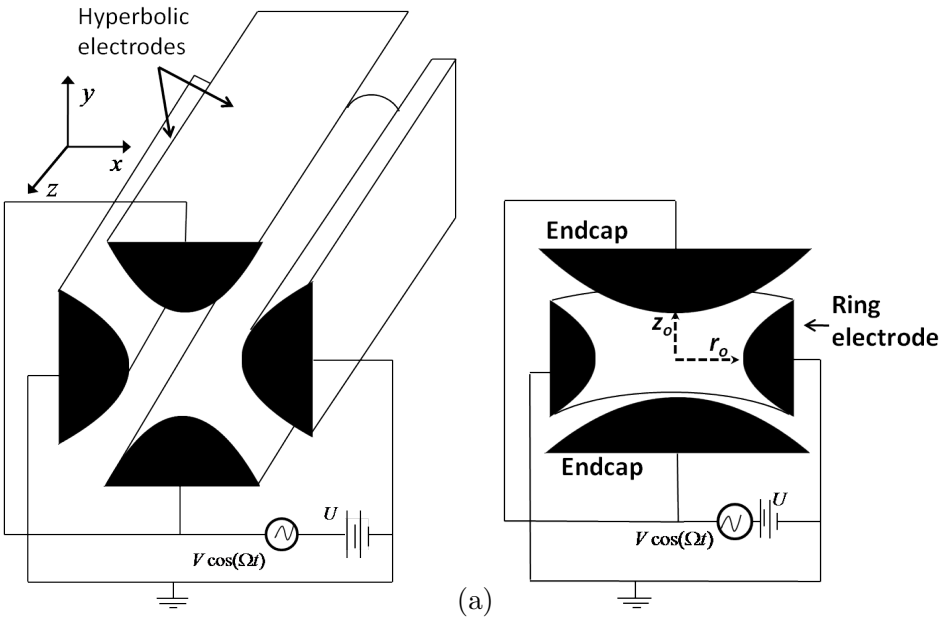

Figure 2.1: (a) Linear rf Paul trap. (b) Ring rf Paul trap for point confinement.

if α, β and γ are positive in x, y and z-directions respectively, then a positive ϕ_o is considered a restoring force in that particular direction and has to satisfy the Poisson equation which requires that [48]

$$\nabla^2\phi(\vec{r}) = \frac{\phi_o}{r_o^2}(\alpha + \beta + \gamma) = 0 \tag{2.3}$$

This condition can be satisfied if [48]

$$\alpha + \beta + \gamma = 0. \tag{2.4}$$

Therefore, to create a potential which is simultaneously harmonic in all directions is not possible. This is well known Earnshaw's theorem, which states that a charged particle can not be trapped with static fields alone. Two possible following solutions can satisfy the constraint given in equation 2.4 [48]

1. $\alpha = -\beta$, $\gamma = 0$ (linear confinement)
2. $\alpha = \beta$ =-2γ (point confinement)

1. Linear confinement

In the case of the linear confinement, $\alpha = -\beta$ and $\gamma = 0$, the potential takes a form of $\frac{\phi_o}{2r_o^2}(\alpha x^2 - \beta y^2)$. Such potential can be achieved with a configuration of the four electrodes having hyperbolic cross-section [48], as shown in figure 2.1(a). The static voltage U and

peak rf voltage V with a drive frequency Ω can be applied to the electrodes to produce the confinement potential $\phi_o = (U - V\cos\Omega t)$ in the centre of the trap, where the cosine dependence of the rf voltage will periodically change the sign of the second term. The potential in equation 2.1 can be written for a linear confinement as [48]

$$\phi(x, y, t) = \big(U - V\cos(\Omega t)\big)\left(\frac{x^2 - y^2}{2r_o^2}\right) \tag{2.5}$$

where, r_o is the shortest distance between the trap centre and the electrodes. If Ω is chosen correctly, the ion can be trapped in both x and y directions. The equation of motion for a particle of charge e and mass m in the trap can then be written as [48]

$$\ddot{x} = -\left(\frac{e}{m}\right)\frac{\partial\phi(x, y, t)}{\partial x} = -\frac{e}{mr_o^2}(U - V\cos(\Omega t))\; x \tag{2.6}$$

$$\ddot{y} = -\left(\frac{e}{m}\right)\frac{\partial\phi(x, y, t)}{\partial y} = \frac{e}{mr_o^2}(U - V\cos(\Omega t))\; y \tag{2.7}$$

$$\ddot{z} = 0 \tag{2.8}$$

These differential equations are generally re-written in the form of the Mathieu' equations by substituting $2\zeta = \Omega t$ and using the chain rule for $\frac{d}{dt} = \frac{d}{d\zeta}\frac{d\zeta}{dt} = \frac{\Omega}{2}\frac{d}{d\zeta}$ [48]

$$\begin{aligned} \frac{d^2x}{d\zeta^2} + (a - 2q\cos(2\zeta))x = 0 \\ \frac{d^2y}{d\zeta^2} - (a - 2q\cos(2\zeta))y = 0 \end{aligned} \tag{2.9}$$

where

$$a = \frac{4eU}{mr_o^2\Omega^2}, \qquad q = \frac{2eV}{mr_o^2\Omega^2}, \qquad \zeta = \frac{\Omega t}{2} \tag{2.10}$$

The solution of Mathieu equations (2.9 and 2.9) are widely studied and their numerical solutions are known [48]. The Mathieu equation has stable or unstable solutions depending on the parameters a and q. In a quadrupole ion trap, an ion is either trapped within the device (ion trap) or is ejected from the device (mass spectrometer) and the dynamics are dependent on the stability (and instability) of the trajectory of the ion within the potential [50]. The stability zones corresponding to stable solutions of the Mathieu equation in the x and y-directions are labelled and shaded in figure 2.2(a). If the ion trajectories are stable in the x and y-directions simultaneously then the ion can be trapped in the trap. Such stability region is nearest to the origin as shown in figure 2.2(b) where the overlapping stability region for both x and y is highlighted.

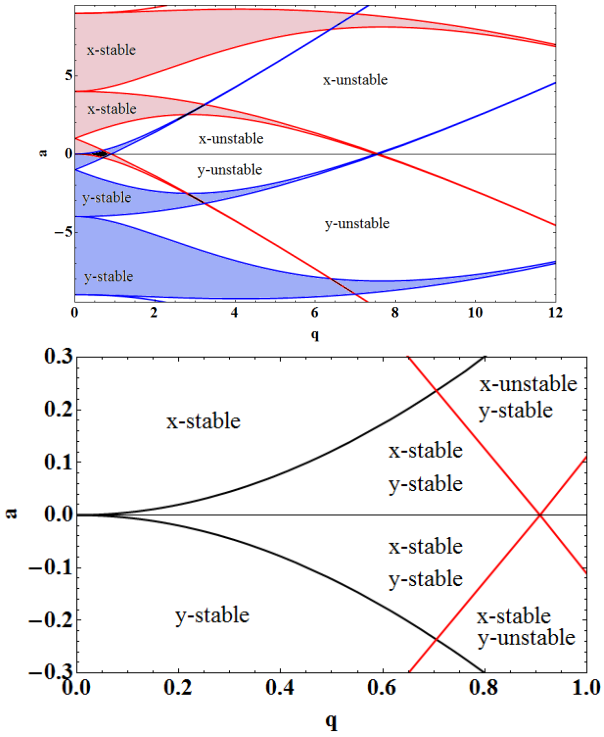

Figure 2.2: (a) Mathieu stability diagram in a and q space for quadrupole ion trap in both the x and y -directions. (b) Simultaneous overlapping stability region for x and y-direction.

Solution for the Mathieu equation for x (or y) can be simplified by assuming that, at the drive rf frequency Ω, the motion in x is the sum of 'low-frequency' term, X, known as 'secular frequency' and a 'high frequency' term, ε, known as 'micromotion' [48]

$$x = X + \varepsilon \tag{2.11}$$

The secular frequency term has much larger amplitude than the micromotion, $|X| \gg |\varepsilon|$, therefore, and considering the case where $U \ll V$, hence $a \ll q$, equation 2.9 for the micromotion term ε becomes [48]

$$\frac{d^2\varepsilon}{d\zeta^2} = 2q\cos(2\zeta)X \tag{2.12}$$

by integrating the above equation and treating X as an integration constant, because it varies slowly relative to ε, the above equation yields [48]

$$\varepsilon = -\frac{q}{2}\cos(2\zeta)X \tag{2.13}$$

This gives the functional form for the micromotion term ε. As the secular motion occurs

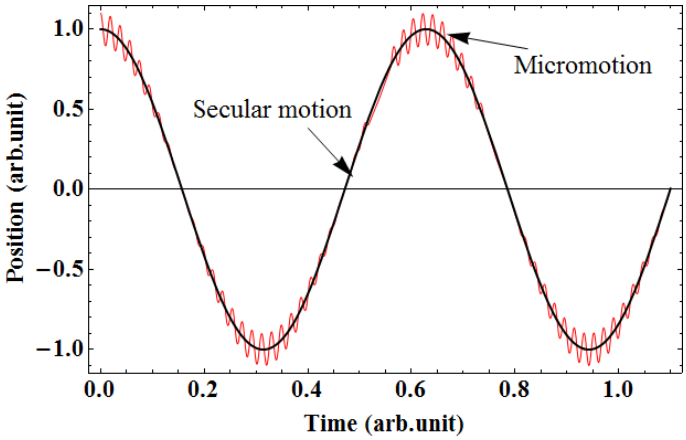

Figure 2.3: The motion of a charged particle in an rf Paul trap. The slower, larger amplitude oscillation is the secular motion, resulting from the time-averaged force of the inhomogeneous electric field. The micromotion occurs at the drive frequency Ω and is superimposed on the secular motion with amplitude proportional to the secular motion.

on a larger time scale than the micromotion, the amplitude of $|\varepsilon|$ is proportional to the instantaneous amplitude of the secular motion $|X|$. This is illustrated in figure 2.3.

In order to analyse the slower and larger amplitude secular motion in the x direction ($u = x$), the equation 2.9 takes form of [48]

$$\frac{d^2x}{d\zeta^2} = -ax + 2q\cos(2\zeta)\, x \tag{2.14}$$

and by substituting 2.11 in the equation 2.14 and by using equation 2.13 for ε follows for the secular motion X, [48]

$$\begin{aligned}\frac{d^2X}{d\zeta^2} &= -a(X+\varepsilon) + 2q\cos(2\zeta)(X+\varepsilon) \\ &= -aX + a\varepsilon + 2q\cos(2\zeta)X + 2q\cos(2\zeta)\varepsilon \\ &= -aX + \frac{aq}{2}\cos(2\zeta)X + 2q\cos(2\zeta)X - q^2\cos^2(2\zeta)X \end{aligned} \tag{2.15}$$

By taking the average of the above equation over one period of the rf, cosine terms average to zero and $\cos^2(2\zeta)$ averages to $1/2$, and considering that there is no static potential ($a = 0$) results in [48]

$$\frac{d^2X}{d\zeta^2} = -\frac{q^2}{2}X \tag{2.16}$$

or, by replacing the $\frac{d^2}{d\zeta^2} = \frac{4}{\Omega^2}\frac{d^2X}{dt^2}$, equation 2.16 takes a form of [48]

$$\frac{d^2X}{dt^2} = -\frac{q^2\Omega^2}{8}X \tag{2.17}$$

which is the equation of motion of a harmonic oscillator with frequency ω [48]

$$\omega_x = \frac{q\Omega}{2\sqrt{2}} = \frac{eV}{\sqrt{2}m\Omega r_o^2} \tag{2.18}$$

In the same way solution for y in equation 2.9 also yields [48]

$$\omega_y = \frac{q\Omega}{2\sqrt{2}} = \frac{eV}{\sqrt{2}m\Omega r_o^2} \tag{2.19}$$

From the above equations it can be seen that there is a harmonic potential in both x and y directions. The depth of this potential, Ξ_o, can be calculated by integrating the restoring force, [48]

$$m\frac{d^2X}{dt^2} = -\frac{1}{8}mq^2\Omega^2X \tag{2.20}$$

from the trap centre to the edge of an electrode or distance r_o, and by substitution for q from equation (2.10) yields [48]

$$\Xi_o = \frac{e^2V^2}{4m\Omega^2r_0^2} \tag{2.21}$$

Ξ_o is known as the *pseudo-potential* and contains no time dependence term, enabling trap configurations to be analysed by electrostatics alone.

2. Point confinement

In this case the potential can take a form of [48]

$$\phi(r,z,t) = (U - V\cos(\Omega t))(\frac{r^2 - 2z^2}{2r_o^2}) \tag{2.22}$$

where $r^2 = x^2 + y^2$. This potential can be generated by a ring shaped electrode with hyperbolic cross-section and two hyperbolic (endcap) electrodes, as illustraded in figure 2.1(b). The equation of motion for a charged particle in the point trap can be written as [48]

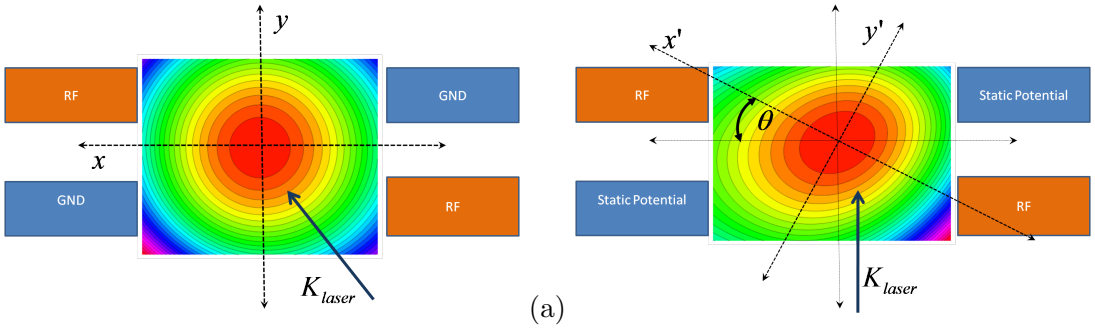

Figure 2.4: (a) The principal axes are same as the trap axes when there is no static potential applied on static electrodes. (b) When small amount of voltage is applied on static electrodes, the principle axes are rotated by an angle θ.

$$\ddot{r} = -\left(\frac{e}{m}\right)\frac{\partial\phi(r,z,t)}{\partial r} = -\frac{e}{mr_o^2}(U - V\cos(\Omega t))\, r \tag{2.23}$$

$$\ddot{z} = -\left(\frac{2e}{m}\right)\frac{\partial\phi(r,z,t)}{\partial z} = \frac{e}{mr_o^2}(U - V\cos(\Omega t))\, z \tag{2.24}$$

Both equations (2.29,2.30) have the same form of equation 2.6 and 2.7, with the same parameters a, q and ζ for the r, while a and q have the twice the value for z. This results in different secular frequencies in r and z coordinates [48].

$$\omega_r = \frac{eV}{\sqrt{2}m\Omega r_o^2} \qquad \omega_z = \frac{\sqrt{2}eV}{m\Omega r_o^2} \tag{2.25}$$

The above results are for an ideal hyperbolic electrode quadrupole trap. Due to poor laser access, these type of traps are impractical for quantum computation. However, by using a set of circular or rectangular shaped electrodes which provide favourable laser access, the trapping potential can be created at the centre of the trap.

2.2 Principal axes

The principal axes of an ion trap can be described as the axes in which an ion's motion can be referred to in terms of one displacement variable alone. This means that the ion's motion along one of the principal axes of a trap is independent of its motion along the other two. Therefore, the principal axes of trap provide a natural coordinate system for the electrode structure. The equations of motion along the principal axes are given by [51]

$$\ddot{x} = \omega_x^2 x \qquad \ddot{y} = \omega_y^2 y \tag{2.26}$$

The principal axes of a linear ion trap are determined by the static potential and are of concern when laser cooling of the trapped ion is required with the lasers propagating only in one direction. Sufficient cooling is achieved if the $\vec{k}$-vectors of the lasers have components along each of the ion's principal axes. In practice, this can be achieved by rotating the principal axes. In a symmetric trap geometry shown in figure 2.4, where static voltage electrodes lie diagonally in the opposite plane, the ions' principal axes are the same as the trap axes if equal magnitude of V_{rf} is applied to each rf electrode without the application of any static voltage. Therefore, in order to cool the ion, the cooling lasers have to enter the trap at an angle to the electrodes and could lead to scattering off the electrodes as shown in figure 2.4(a). This issue can be handled by adding a small amount of static voltages to diagonally opposite electrodes which give rise to an xy cross-term in the static potential and rotate the principal axes, thus enabling the lasers to enter perpendicular to the electrodes and reduce the unwanted effects of scattering, as shown in figure 2.4(b). In planar trap geometries, the rotation of principle axes can be achieved by using rf electrodes of different widths [52] as shown in figure 2.5. If the principal axes are rotated, then equation 2.26 will take the form of [51]

$$\ddot{x}' = \omega^2 x + Ay \qquad \ddot{y}' = \omega^2 y + Bx \tag{2.27}$$

where x and y are cross-terms and A and B are the constants. To find the new principal axes, one can rotate the coordinate system using, [51]

$$x = x'\cos\theta + y'\sin\theta$$

$$y = -x'\sin\theta + y'\cos\theta \tag{2.28}$$

until the cross-terms in equation 2.27 vanishes and the rotated principal axes can take a form of [51]

$$\ddot{x}' = \omega^2 x' \qquad \ddot{y}' = \omega^2 y' \tag{2.29}$$

In fact, the rotation of the principal axes is a linear transform of the electric field inside the trap. Using trap simulations, it is possible to calculate the angle of rotation of the principal axes. This can be achieved by finding the Hessian matrix of the electric field in

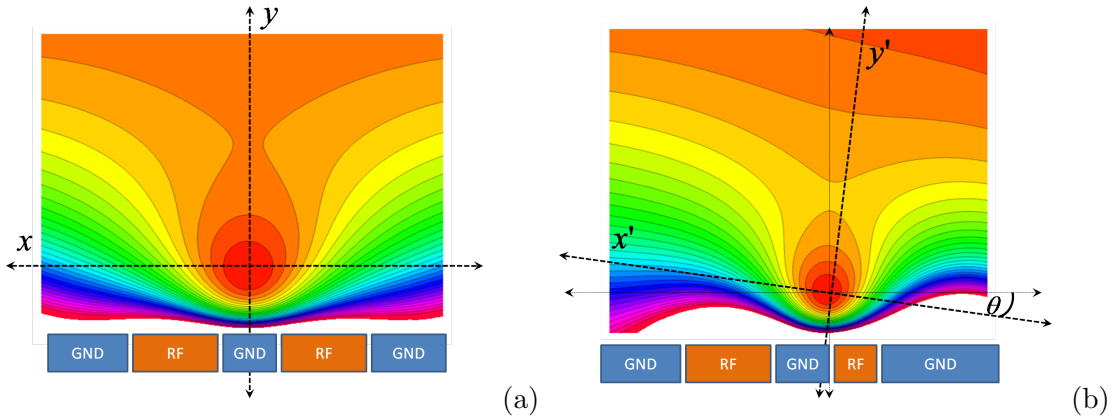

Figure 2.5: (a) The principal axes are same as the trap axes when both rf electrodes are of equal widths. (b) The principal axes are rotated by an angle θ when rf electrodes are of different widths.

the central region of the trap. When the principal axes do not lie along the axes of the trap, then there are cross terms in the equations describing the electric field. The electric field can be described by a new set of axes where the cross terms vanish by rotating the coordinate system by an angle θ. This can be calculated using the trap simulations. The Hessian matrix of the simulated potential for a trap in two-dimensions is

$$H(\phi(x_o, y_o)) = \begin{bmatrix} \frac{\partial^2\phi}{\partial x^2}(x_o, y_o) & \frac{\partial^2\phi}{\partial x \partial y}(x_o, y_o) \\ \frac{\partial^2\phi}{\partial y \partial x}(x_o, y_o) & \frac{\partial^2\phi}{\partial y^2}(x_o, y_o) \end{bmatrix} \tag{2.30}$$

Here x_o and y_o are the points where the Hessian matrix is evaluated, which is the centre of the trap. The principal axes of the system lie along the eigenvectors of the Hessian matrix of equation 2.30. The secular frequencies ω_p along the principal axes then can be determined by fitting the pseudopotential along these axes to a parabola (other polynomial terms may be included in the fit, but the quadratic term should dominate) and using the quadratic coefficient of the fit, A_{qp}.

$$\omega_p = \sqrt{\frac{2eA_{qp}}{m}}, \tag{2.31}$$

where m is the mass of an ion and e is the charge of the ion.

2.3 Linear trap geometry

These are the traps in which the ponderomotive potential traps only in two dimensions in such a way that the rf node is a line, and static voltages provide confinement along this

line in the 3rd dimension. One of the main benefits of this type of trap is that multiple ions can be trapped along the rf node line if the secular frequency along the static axis (rf nodal line) is lower than the ponderomotive secular frequency. In order to confine ions along the RF node, linear traps require static fields. Therefore these static fields are anti-trapping along the radial direction and partially cancel the ponderomotive potential as Gauss' law states that those electric field lines that converge at the trap centre must be radially anti-trapping. Therefore, static potentials should be applied carefully so that axial trap should be strong but not at the cost of radial trap.

There are two major types of linear trap geometries;

- Symmetric traps
- Asymmetric traps

Symmetric traps

In this kind of trap geometries, electrodes symmetrically surround the ion. A symmetric trap geometry can be implemented with either two rf wires/electrodes symmetrically surrounding the centre of the trap in opposite direction along with segmented static wires/electrodes on either sides in a *two-layer design*, as seen in figure 2.6, or a *three-layer design* in which the rf electrodes are surrounded by the dc electrodes as seen in figure 2.7. These trap geometries are considered more difficult to fabricate.

Asymmetric traps

In contrast to the symmetric traps, trapping region for the ions lies above the trap electrodes, hence commonly known as surface trap or planar trap. The trap geometry can be implemented with two rf-electrodes separated by a ground electrode and segmented static potential electrodes on either side of the rf electrodes can be used to provide confinement in axial direction. Planar and their equivalent wire geometry are shown as seen in figure 2.8. A cross section view in figure 2.8 shows the location of rf-node above the surface, therefore the lasers are to be brought across the surface. It offers the possibility of easy fabrication as compared to symmetric trap electrodes in which lasers are brought through a hole in the substrate. Due to the lack of one symmetry, in surface traps, the trap depth is weaker as compared to symmetric traps given the same voltage and distance from the ion to the electrode [29]. For surface traps, one design consideration must be fulfilled so

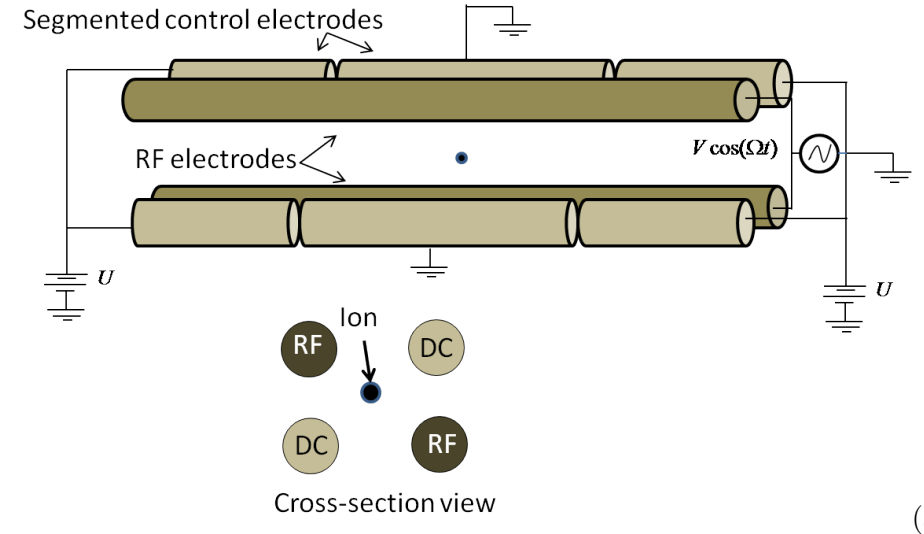

(a)

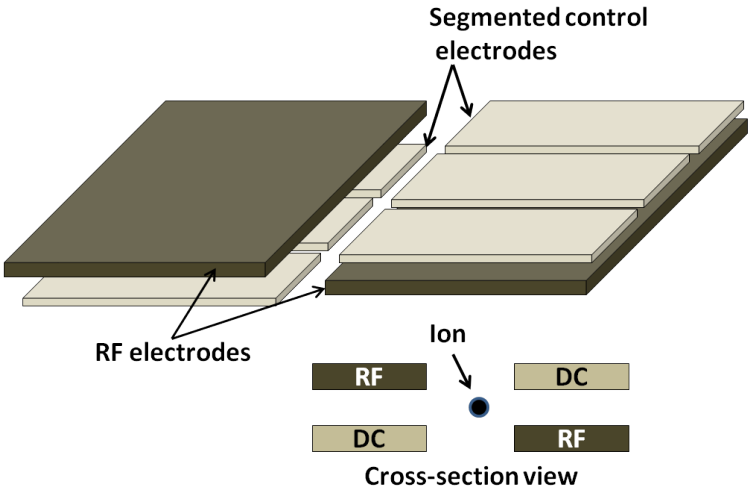

(b)

Figure 2.6: (a) Two layer linear rf trap geometry implemented with (a) wire electrodes and (b) rectangular electrodes.

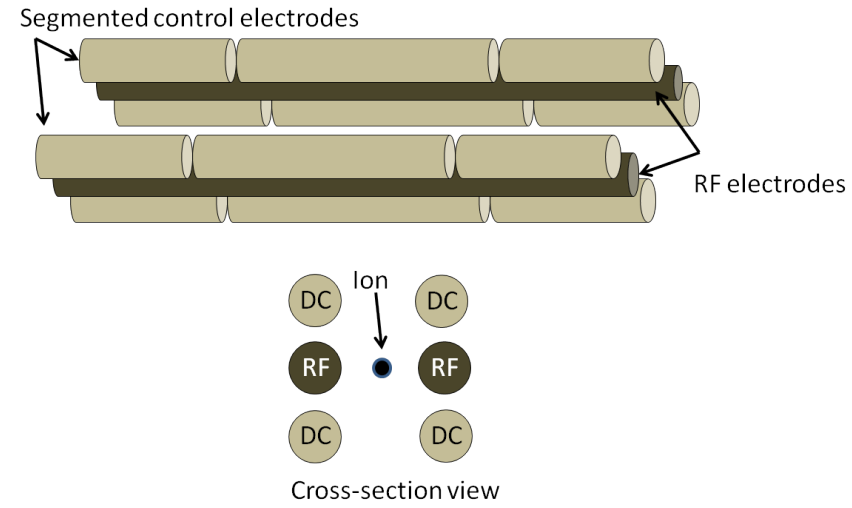

(a)

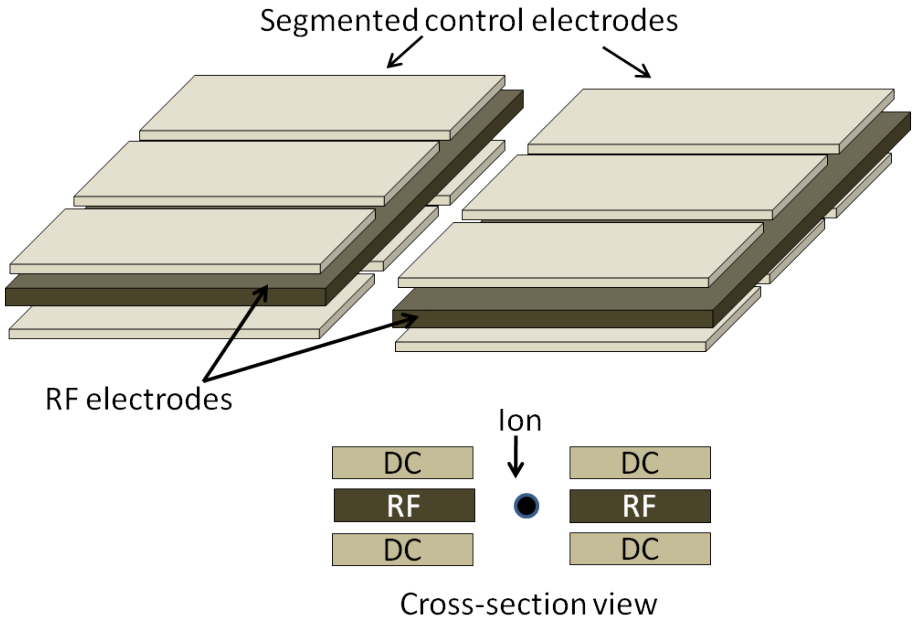

(b)

Figure 2.7: (a) Three layer linear rf trap geometry implemented with (a) wire electrodes and(b) rectangular electrodes.

that the principal axes must be rotated in a way that one axis is not perpendicular to the surface of the trap. Otherwise the ion cannot be cooled if one of its principal axes is perpendicular to the surface. This can be achieved by breaking the symmetry of rf electrodes so that both electrodes have different widths, further details on this geometry are discussed in chapter 7.

2.4 Doppler cooling

Doppler cooling is the simplest and most widely used method of laser cooling, in which the laser frequency is detuned to red (low frequency side) from the resonance frequency. In the reference frame of the atom which is moving towards the laser, the photons are on resonance and the atoms absorb photons more frequently. During such an atom-laser interaction, the atom feels a recoil force when momentum is transferred from the photon while scattering it. The momentum kick that the atom receives from each scattered photon is quite small. However, by exciting a strong atomic transition, it is possible to scatter more than a million photons per second, depending the natural line width of the transition, which produces an overall acceleration of more than $10^4 \cdot g$ [48]. A detailed mathematical description of laser cooling is given by Metcalf [53] and Ghosh [48]. For a two level atom, the scattering rate γ_p (the rate at which the atom absorbs and then re-emits a photon) can be written as [53]

$$\gamma_p = \frac{s_o \gamma/2}{1 + s_0 + (2\delta/\gamma)^2} \tag{2.32}$$

where γ is the linewidth, δ is the laser detuning from the resonance and s_o is the saturation parameter $s_0 = I/I_s$ with laser intensity I and characteristic saturation intensity I_s of the particular transition at wavelength λ and lifetime $\tau = 1/\gamma$ [53]

$$I_s = \frac{\pi h c}{3\tau\lambda^3} \tag{2.33}$$

The cooling is achieved by making the photon scattering rate velocity-dependent using the Doppler effect. In this case, the scattering rate is dependent on the atom's velocity and is [53]

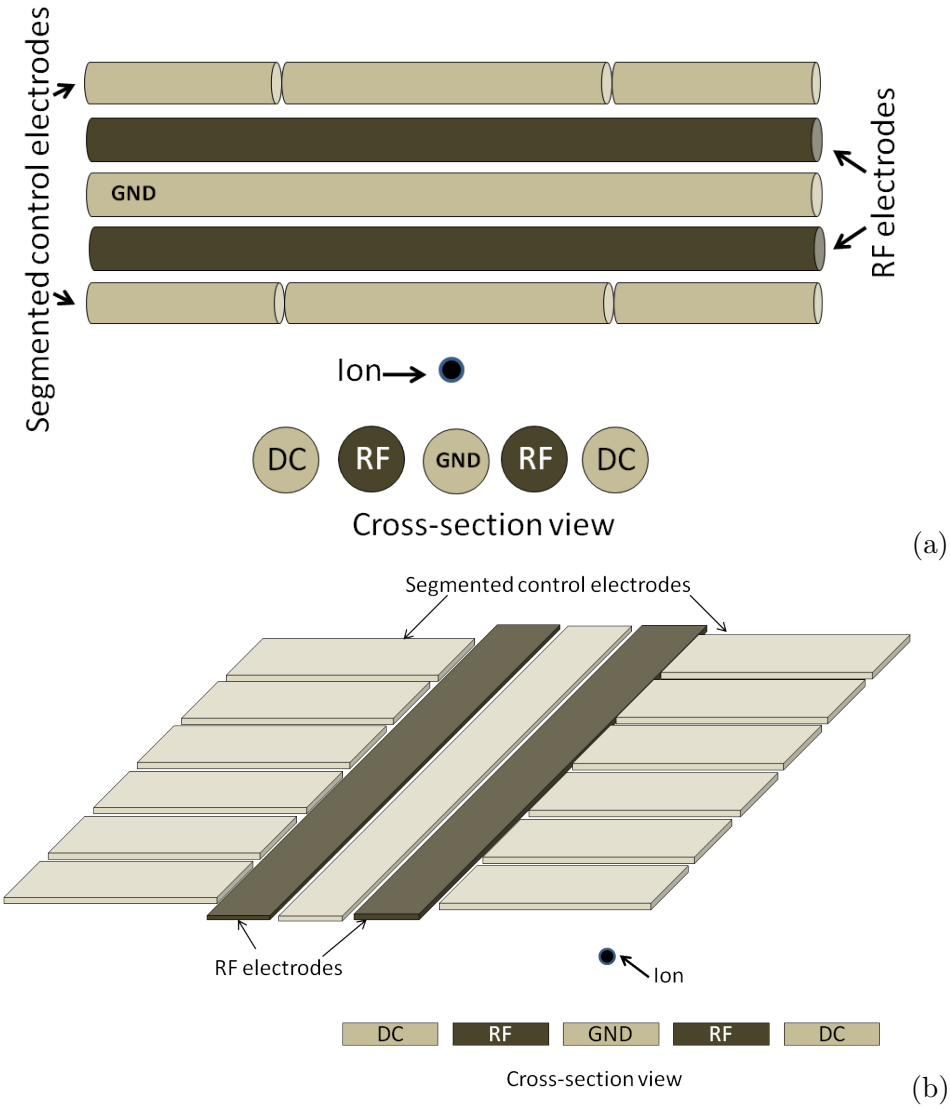

Figure 2.8: (a) Planer or surface rf trap geometry implemented with (a) wire electrodes and(b) rectangular electrodes.

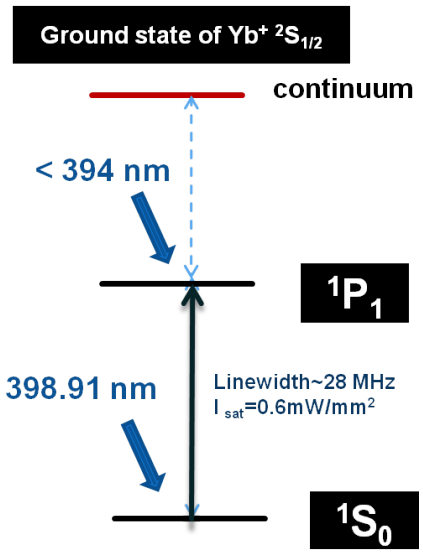

Figure 2.9: Two photon ionisation scheme for Yb using its $^1S_0 \leftrightarrow ^1P_1$ transition.

$$\gamma_p = \frac{s_o\gamma/2}{1 + s_0 + (2(\delta - v_D)/\gamma)^2} \tag{2.34}$$

where v_D is the shift in the scatter rate for an atom that is moving with velocity $\vec{v}$ due to the Doppler effect and equals $-\vec{k}.\vec{v}$, where the negative sign represents the velocity being opposite to the laser wave vector $\vec{k} = 2\pi/\lambda$.

On average the atom will gain a momentum of $\hbar\vec{k}$, and its velocity will change by the recoil velocity of $v_r = \hbar k/m$ due to each photon and the atom will experience an average force due to photon scattering [53]

$$F = \frac{\text{momentum transfer}}{\text{time}} = \hbar k\gamma_p = \frac{\hbar k s_o\gamma/2}{1 + s_0 + (2(\delta - v_D)/\gamma)^2} \tag{2.35}$$

The direction of this damping force is along the wavevector $\vec{k}$, therefore, the atoms which are only moving towards the laser feel a strong opposing force and the atoms moving away from the laser feel very low force. In order to cool the atom in all three directions, three laser beams are required. However, only one beam is required if the laser wavevector has a component in all three direction of the principal axes.

2.5 Yb^+ ions

The neutral Yb atom can be photo-ionised, first by exciting its ground state $^1S_0 \leftrightarrow ^1P_1$ transition with a photon at 398.91 nm and then any photon at wavelength less than 394

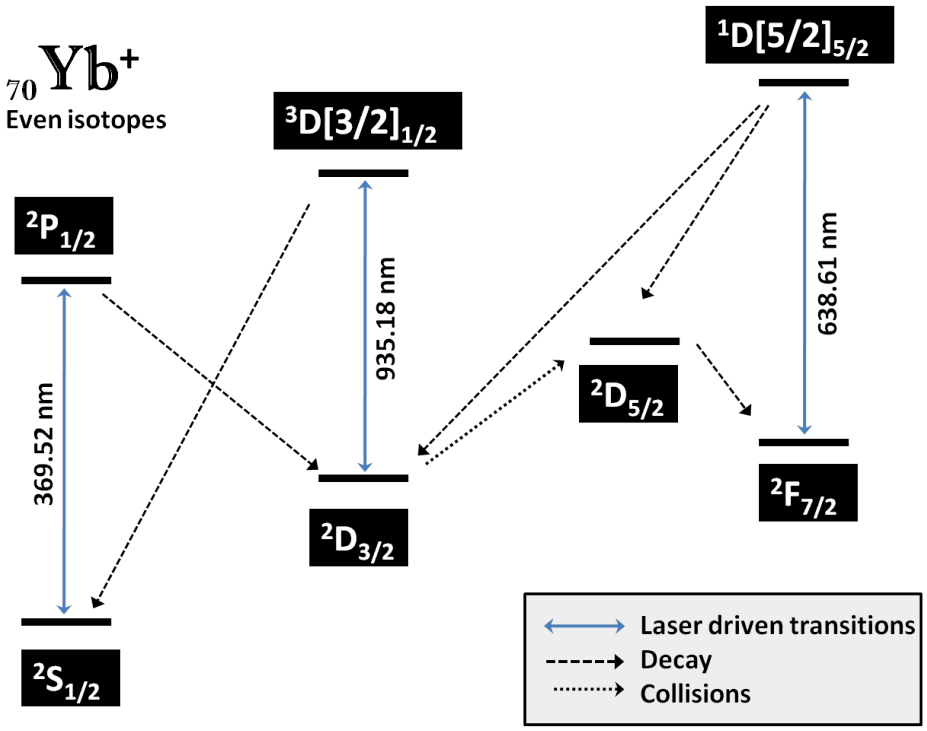

Figure 2.10: Energy level diagram for Yb^+ ion having zero nuclear spin (even number isotopes).

nm can ionise the atom [54]. Isotope selective ionisation is achieved using this technique [55–57]. The two-photon ionisation scheme is illustrated in figure 2.9. Two singly-ionised ytterbium isotopes, $^{174}Yb^+$ and $^{171}Yb^+$, are used in the ion trap experiments in our lab. Both the ions have the same energy level structure (except for hyperfine levels) and one can utilise the same laser systems. The simpler of the two is the even isotope $^{174}Yb^+$ as it has no hyperfine structure as shown in figure 2.10. In order to laser cool the ion, a laser on the 369 nm transition is required to excite the $^2S_{1/2}$ state to the $^2P_{1/2}$ state of the ion. The ion falls from $^2P_{1/2}$ state to the $^2D_{3/2}$ state, with a branching ratio of 1:150 [58]. This means that the chance of this transition is very likely to occur every 1 ms. Hence, a laser at 935 nm is needed to re-pump this transition to keep the ion's state in the cooling cycle. If the ion undergoes a collision with residual atoms inside the vacuum chamber, it can be transferred to the $^2F_{7/2}$ state via $^2D_{5/2}$ state, resulting in its loss from the cooling process. The chance of this transition to occur varies from several minutes to hours, depending on the pressure in the chamber. To re-pump the ion from this state and bring it back to the cooling cycle via its D-states, a laser at 638 nm can be used.

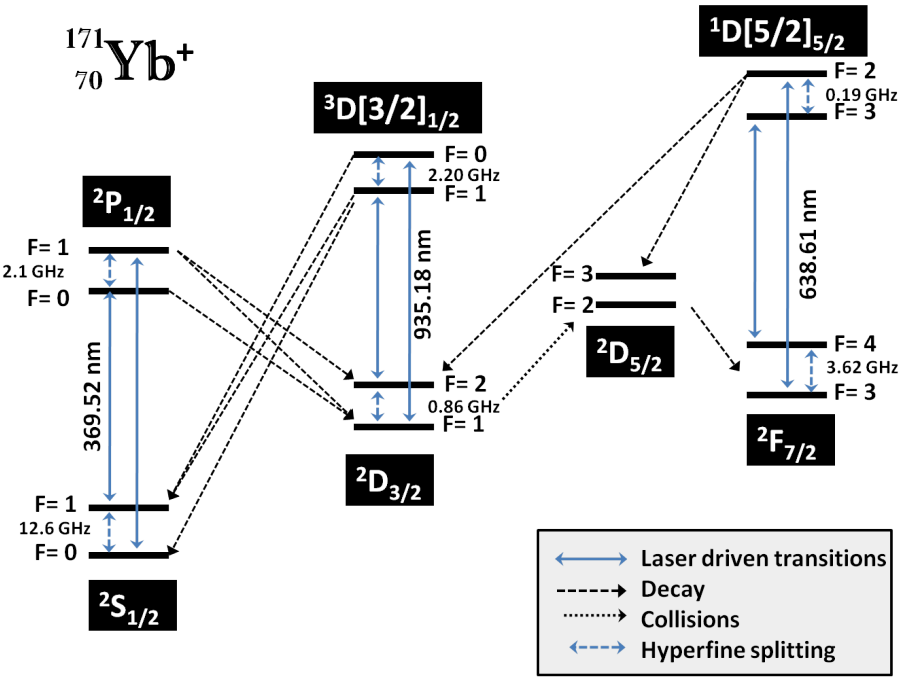

Figure 2.11: Energy level diagram for $^{171}Yb^{+}$ ion with hyperfine structure.

$^{171}Yb^{+}$

However, the aim of our trap experiments, is to perform quantum computation with trapped ions. For this purpose $^{171}Yb^{+}$ is used due to its half-integer nuclear spin which produces a hyperfine structure as shown in figure 2.11. The hyperfine levels of the ground state level in $^{171}Yb^{+}$, $^{2}S_{1/2}(F = 0)$ and $^{2}S_{1/2}(F = 1)$ can be used as *qubit* states $\mid 0\rangle$ and $\mid 1\rangle$ respectively. The cooling scheme of $^{171}Yb^{+}$ is more complicated than $^{174}Yb^{+}$ due to its hyperfine structure. As the $^{2}P_{1/2}(F = 0)$ to $^{2}S_{1/2}(F = 0)$ decay is strictly forbidden, the $^{2}S_{1/2}(F = 1) \leftrightarrow {}^{2}P_{1/2}(F = 0)$ transition is chosen for Doppler cooling which requires 14.7 GHz side bands on the 369-nm laser. In order to maintain a closed cooling cycle, side bands of 3.08 GHz are required on the 935-nm laser to drive the $^{2}D_{3/2}(F=1) \leftrightarrow {}^{2}D[3/2]_{1/2}(F=0)$ as the $^{2}P_{1/2}$ state can decay to $^{2}D_{3/2}$. From the D-states, the ion can fall to the $^{2}F_{7/2}$, therefore, it is necessary to return the ion into the cooling cycle by exciting the hyperfine transitions of $^{2}F_{7/2} \leftrightarrow {}^{2}D[5/2]_{5/2}$ which are separated by 3.81 GHz. These hyperfine transitions also requires 3.81 GHz sidebands on 638-nm laser. In order to excite the Yb transition and its hyperfine levels, the required laser setup is discussed in chapter 4.

Chapter 3

Ultra High Vacuum system

The term "vacuum" is defined as a region of space in which pressure is significantly less than the atmospheric pressure. Many units of pressure measurement are in use but the traditional unit of pressure is torr which is approximately equal to 1 mm of mercury (1 mm Hg). In the S.I unit system, the unit of pressure is the pascal or Newton/meter (N/m). One torr is equal to ≈ 133.32 pascal. The perfect or absolute vacuum, which implies a space that is entirely devoid of matter, is impractical. Hence, a vacuum region can be categorised by different physical phenomena like pressure, mean free path, average inter molecular distance, molecular density etc.

In order to isolate the trapped ions from surrounding background atoms in ion trap experiments to prevent background collisions destroying the quantum state of the *qubit* or knock the ion out of the trapping region, a vacuum on the order of $\sim 10^{-12}$ torr is required. At this pressure, the mean free path reaches $> 10^4$ km. Hence the collision rate between the residual atoms and trapped ions inside the vacuum chamber drops significantly, and ions can remain trapped for a time of a few hours to a few days.

The Mean free path (*mfp*) can be defined as the average distance covered by a molecule or atom before colliding with another atom, and is given by

$$\lambda = \frac{kT}{\sqrt{2}\pi d_0^2 P} \tag{3.1}$$

where k and T are Boltzmann's constant and the temperature in Kelvin respectively, P is the pressure in units of N/m and d_o is the molecular diameter $\sim 10^{-10}$m.

A Large mean free path does not indicate that the atoms or molecules are separated by such a large distances but implies that the chance of collision between two molecules or atoms in a vacuum vessel is very low if the *mfp* is very large. The average molecular distance at very low pressure will still be in the range of few micrometres. The different levels of vacuum together with the required pumping mechanism and measurement devices are summarised in table 3.1

Table 3.1: Mean free path at different ranges of pressure and required vacuum pumps.

Pressure level	Pressure range (torr)	Mean Free Path (m)	Average distance between molecules (m)	Type of pump	Type of Gauge
Low vacuum	$1 - 10^{-3}$	$10^{-5} - 10^{-2}$	$10^{-8} - 10^{-7}$	Diffusion Pump	Thermocouple gauge
High vacuum	$10^{-3} - 10^{-6}$	$10^{-2} - 10^{1}$	$10^{-7} - 10^{-6}$	Turbo-molecular Pump	Cold cathode ionisation gauge
Very high vacuum	$10^{-6} - 10^{-9}$	$10^{1} - 10^{4}$	$10^{-6} - 10^{-5}$	Ion Pump	Standard ionisation gauge
Ultra high vacuum	$10^{-9} - 10^{-12}$	$10^{4} - 10^{7}$	$10^{-5} - 10^{-4}$	Ion Pump and Titanium Sublimation Pump(TSP)	Bayard-Alpert-type ionisation gauge (Limit 5×10^{-12} torr)

The requirements of a vacuum system for an ion trap experiment are that it should be able to produce and sustain a pressure of 10^{-12} torr and provide laser access for different types of ion trap geometries. Furthermore, in order to investigate various ion trap geometries to determine which is more feasible for scalable quantum computing, the vacuum chamber must be capable of accommodating different trap geometries. There are two types of Paul trap geometries, the symmetric traps and the asymmetric or surface traps. The basic difference between the trap geometries is the location of the electrodes with respect to the trapped ion requiring the laser access along different axes.

Outgassing

In vacuum terminology, slow release of trapped, absorbed or desorbed gases from the surfaces is called *outgassing*. The outgassing rate can be defined as the amount of gas leaving the surface in a vacuum per unit time. The outgassing process controls the ultimate pressure in high and Ultra High Vacuum systems (UHV) [59]. In a UHV system, outgassing depends on a number of factors, including, desorption, vaporisation of materials, gas diffusion from the bulk materials and gas permeation through the walls. All solid and liquid surfaces have the tendency to attract molecules in the surrounding atmosphere. Gas molecules landing on the surfaces can be adsorbed in certain conditions of temperature and pressure, and can be desorbed. The desorption of gases are the major source of outgassing in a well designed ultra high vacuum system and can be reduced by baking the vacuum parts at certain temperature for a period of at least two weeks. Vaporisation of materials can be quantified by their vapour pressure at a certain temperature. The materials used in UHV devices and components have small vapour pressures. Care must be taken in the selection of materials used for ion traps. Lists of low outgassing materials are widely available [60].

3.1 Vacuum chamber

3.1.1 Chip bracket

The vacuum chamber is designed in a way that the ion traps can be replaced within a short amount of time and do not require the change of hardware inside the chamber. To ensure this, a chip bracket shown in figure 3.1 and 3.2 made of two plates of PEEK,

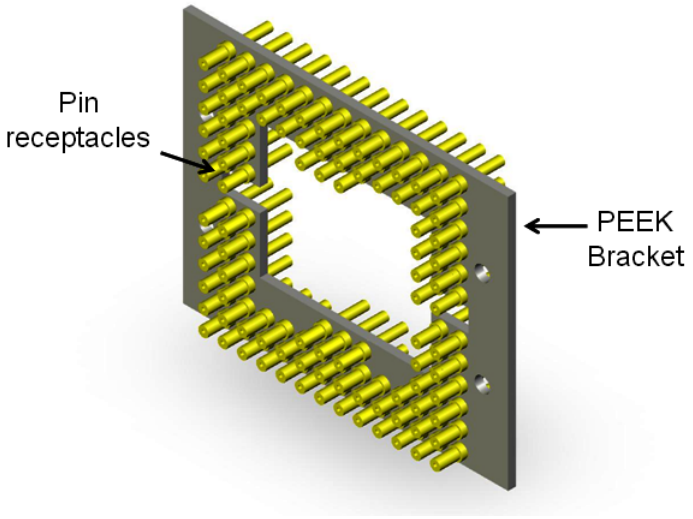

Figure 3.1: 90 pin receptacles inserted on the chip bracket plate.

sandwiching 100 pin receptacles, is custom made, on which an ion trap installed on a chip carrier can be mounted. PEEK is an electrical insulator which is highly resistant to thermal degradation with a negligible water absorption rate and very low outgassing rate, making it the prime candidate for the use as a chip mount in a UHV environment. In order to provide electrical connections to the chip carriers and ion traps, appropriate gold plated pin receptacles were found from Mill-Max. The standard pin receptacles have one disadvantage, the length on the wire clamp side is too short to successfully crimp the wires. Custom parts (part number: 0672-4-15-15-30-27-10-0) from the company were requested for increasing this length to 0.2". The arrangement of the pin receptacles on the PEEK plate is shown in figure 3.1.

In order to provide an Yb atomic beam to symmetric ion traps, two atomic ovens are attached on the steel plates which carry the chip bracket. A front and rear view of the chip bracket and the arrangement of atomic ovens are shown in figure 3.2.

3.1.2 Chamber

The vacuum chamber used in the lab consists of the Magdeburg hemisphere and the spherical octagon (Part Number: MCF450-MH10204/8-A and MCF450-S020008-C from Kimball Physics respectively). The hemisphere with a diameter of 4.5" CF flange has two large windows of 2.75" CF flange size and four small widows of 1.33" CF flange size. The octagon with diameter of 4.5" CF flange has eight 1.33" CF flange windows.

The chamber shown in figure 3.3 is assembled by combining both, the hemisphere, and

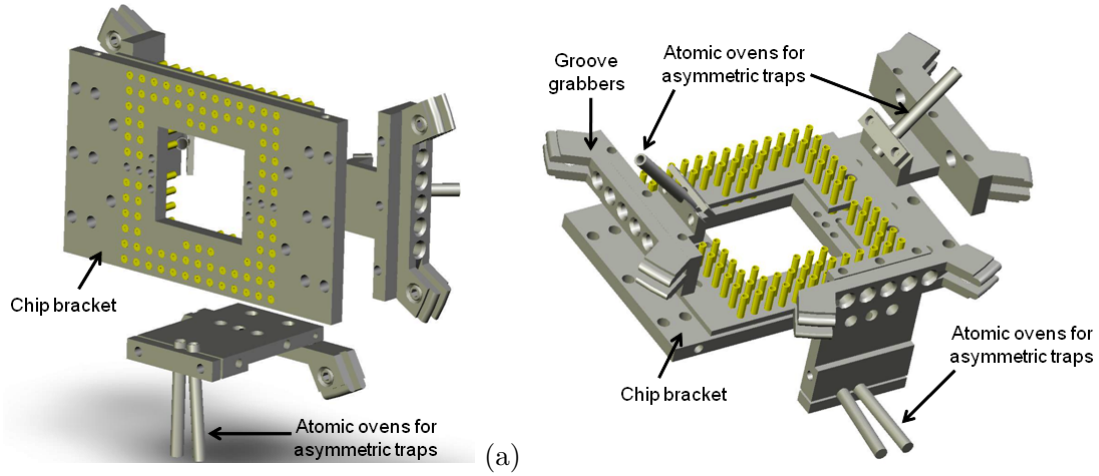

Figure 3.2: (a) Front view of custom made chip bracket and mounting position of symmetric ovens, (b) rear view of the bracket and mounting position of symmetric ovens.

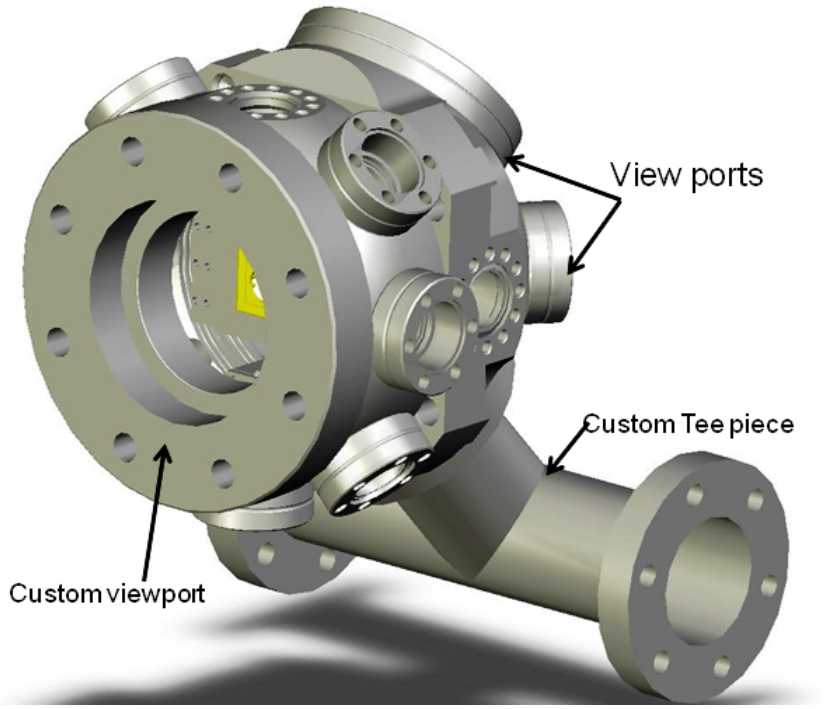

Figure 3.3: Vacuum chamber assembly connected with custom made T-piece.

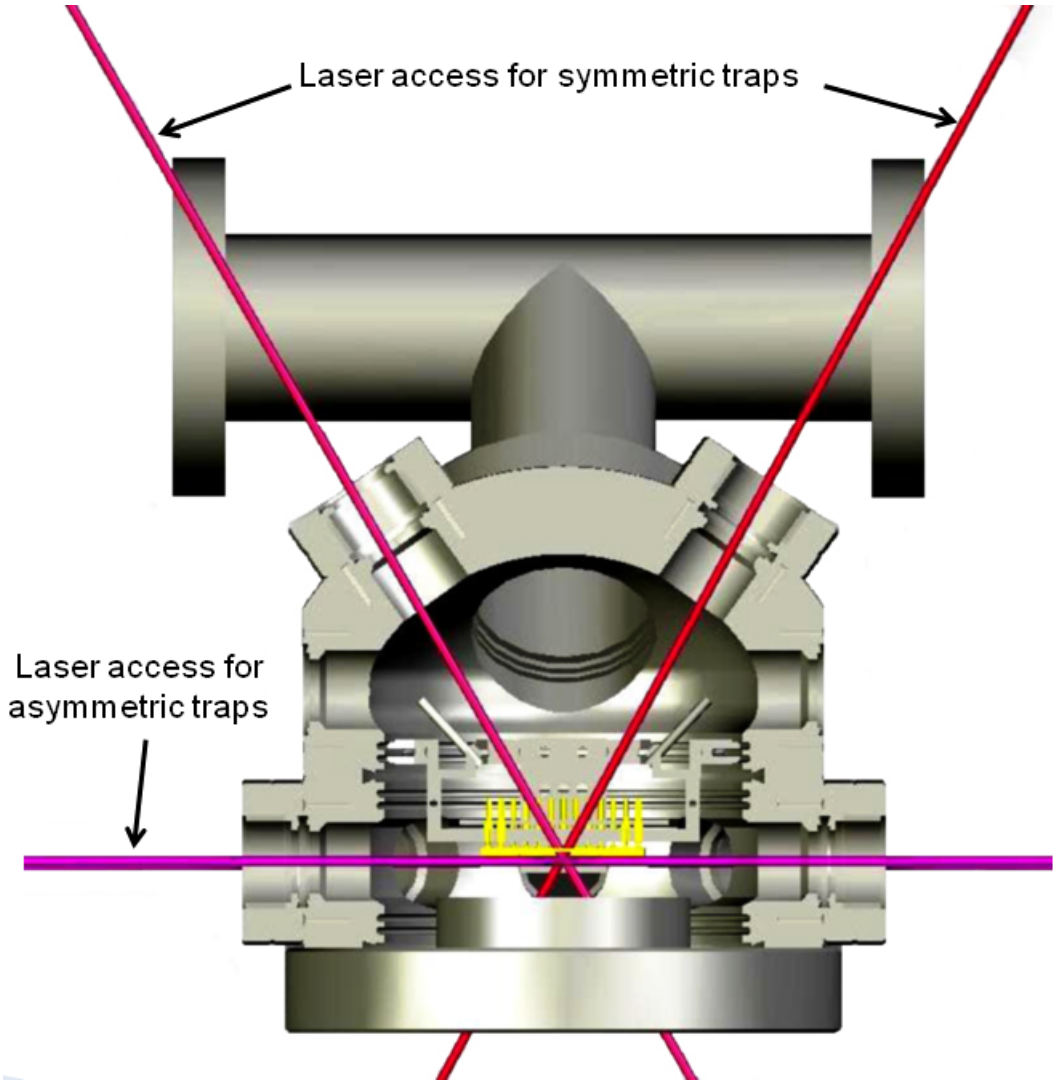

Figure 3.4: Top cut-view of the chamber to show the laser access for symmetric and asymmetric traps.

the octagon providing a UHV seal. The hemisphere is connected by one of its 2.75" CF flange to rest of the vacuum system using a custom made 2.75" CF flange T-piece. The T-piece was designed to keep the centre of the chamber at a height of 5.0" to make it compatible with the height of the optical mounts used in the lab. The T-piece was manufactured on request from K. J. Lesker as no available standard T-piece can be used to achieve this height. For the laser access to an asymmetric trap, six anti-reflection (AR) coated 1.33" CF flange viewports are mounted on the octagon. Two AR coated 1.33" CF flange viewports are also mounted on the hemisphere to ensure the proper laser access to a symmetric trap. The 4.5" CF flange AR coated custom made re-entrant viewport is mounted on the front of the chamber for imaging purpose. The laser access to both type of traps is illustrated in figure 3.4.

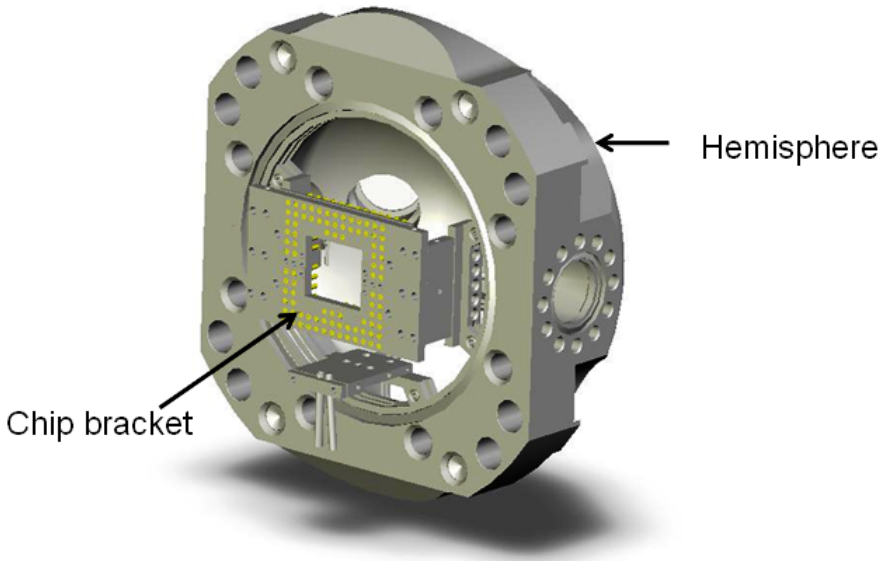

Figure 3.5: Chip bracket is mounted inside the hemisphere using groove grabbers.

The custom made chip bracket is fixed with screws on stainless steel plates and mounted on the hemisphere using groove grabbers (from Kimball Physics Part Number: MCF450-GG-CT02-A). Figure 3.5 shows the chip bracket assembly and mounting position inside the chamber. The chip carrier can easily be replaced by removing the front viewport and the spherical octagon.

Electrical connections and measurements

In order to supply the rf power to ion traps, helical resonators with high Q-factors are in common use. The Q-factor of a resonator is very sensitive to the load capacitance. For the resonator used in our experimental setup the Q-factor is 200 (discussed in sec: 4.6). To maintain the high Q-factor, it is necessary to keep the stray capacitance below 20 pF. The major cause of the capacitance on the chip bracket is from a number of factors, involving, the length of the rf wires, the electrical feedthrough and the separation between the pin receptacles on the chip bracket. The capacitance contribution from the electrical feedthrough can not be avoided but the length of the rf wires should be kept short as possible by mounting the electrical feedthrough to the nearest unused window of the chamber. Furthermore, the static potential receptacles surrounding the rf receptacles are removed to increase the pin to pin separation. By taking the above precautions, the final capacitance between the rf and ground electrodes at the power feedthrough was measured to 17 ± 2 pF. The rf and ground pin receptacles were initially connected to a power electric feedthrough (5 kV, 5 A per pin, Part Number: EFT 0521052 from K.J.Lesker) using a

pair of UHV compatible Kapton wires. But during the electrical tests at high vacuum described in section 3.3.1, it was observed that at very high rf voltages (well above 500 V), the Kapton wires shorted to the walls of the chamber. To avoid this problem it was decided to replace the Kapton wires with thick bare copper wires of 1 mm diameter insulated by white ceramic fish-spine beads (2.5 mm bore) (Part number:536-4090 from RS Components).

For the static voltage supply to the trap electrodes, Kapton insulated wires are used to connect pin receptacles with 2×50 pin D-type customised electrical feedthroughs (K.J.Lesker part number: IFDGG501056A). Materials with a higher outgassing rate in a UHV environment must be avoided within the chamber. Glue or soldering techniques cannot be used to attach the wires to the receptacles. Therefore the wires are simply crimped into place.

Due to the large number of electrodes, it is necessary to make a map showing the connection of each pin receptacle with the D-type feedthrough. This can be done by checking the electrical connection using a multimeter. For the current chip bracket used in the vacuum system, this map is shown in appendix A. Furthermore, the capacitance of the DC and rf pin receptacles should be measured with respect to ground and with respect to each other and recorded. This practice will be helpful in finding any disconnection or shorting of the wirings after the pumping down process. In our chip bracket the capacitance of the rf pins with respect to ground and DC pin receptacles is $\approx 17 \pm 2$pF. The capacitance of the DC pin receptacles to the ground is measured to be $\approx 115 \pm 5$ pF. The resistance of the pin receptacles to the feedthrough connector is measured to $0.2 \pm 0.1\ \Omega$.

3.1.3 Viewports

The laser wavelengths used in this research range from infra-red to ultra violet light (935 nm to 369 nm). Ordinary glass has poor transmission for this wide range of light spectrum. The viewports are therefore made of quartz fused silica UV-grade glass with 90% transmission (shown in figure 3.6) for the wavelengths used in our experiment. The view ports in our vacuum system are AR (anti-reflection) coated (from Laseroptik) for all the laser wavelengths used in our experiment to enhance the transmission ability to 97%. For laser access to asymmetric ion traps, six standard 1.33" CF flange viewports (from K. J. Lesker, Part Number: VPZL-133Q) are mounted on the octagon. Two 1.33" CF flange

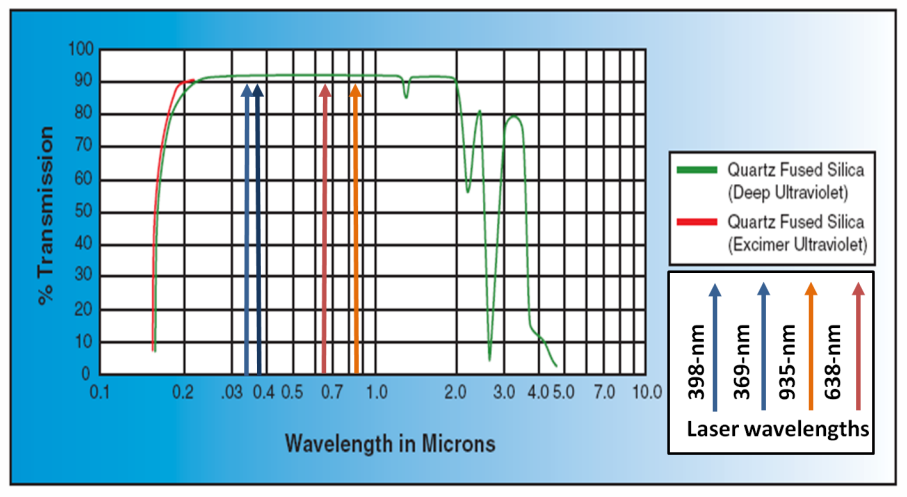

Figure 3.6: Transmission curves for the viewports used in our experiment (Figure from K.J.Lesker catalog).

and one 2.75" CF flange viewports (Part number: VPZL-275Q) are mounted on the hemisphere for laser access to symmetric ion traps. To provide diffraction limited imaging of the ions using an objective lens, it is required to put the trap as near to the imaging window as possible. For the imaging set up used in our experiment, the ion to imaging lens distance is set to be $\sim$ 23 mm. This requires the viewport glass to be very close to the trap surface. The front viewport also requires a sufficient opening to allow the lasers which pass through the viewports on the hemisphere, to exit the chamber. Mounting of a standard flat viewport on the front of the octagon does not satisfy all the constraints. Alternatively, it requires a re-entrant type of viewport, in which the glass is recessed away from the steel part. A customised 4.5" CF flange re-entrant viewport was designed and sent to K.J. Lesker and ISI vacuum parts companies for manufacturing . Due the the manufacturing limitations, the design was slightly changed by both companies and alternative designs were proposed. The KJ-Lesker's design shown in figure 3.7 was very close to our requirement and therefore decided to be used. The engineering drawing of the customised viewport is given in appendix B

3.1.4 Atomic source ovens

The purpose of atomic source ovens is to create a beam of neutral atoms in the surrounding area of the trap where the atoms will be ionised and trapped. The atomic ovens are fabricated from stainless steel hypodermic needle tubing with 0.0325" inner diameter and 0.042" outer diameter purchased from Small Parts (Part number: B000FMUSNM). The length of the oven tube is 20 mm. The metallic tubes are crimped on one end and spot

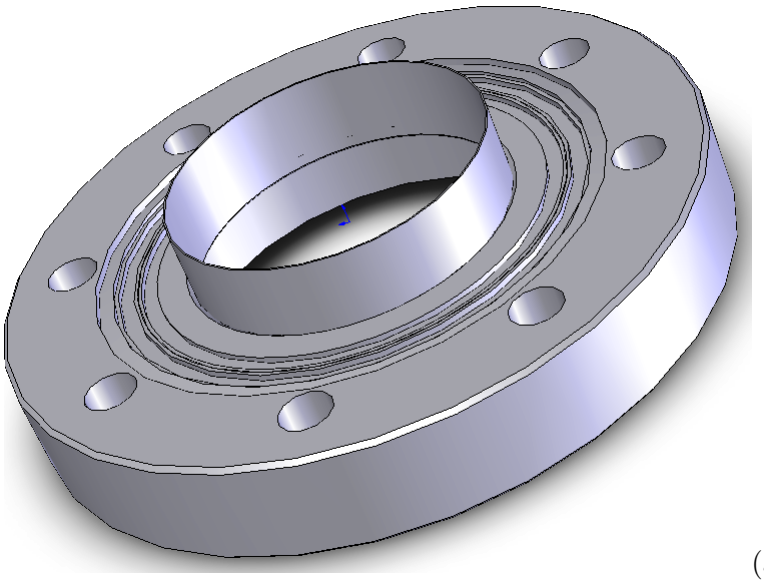

(a)

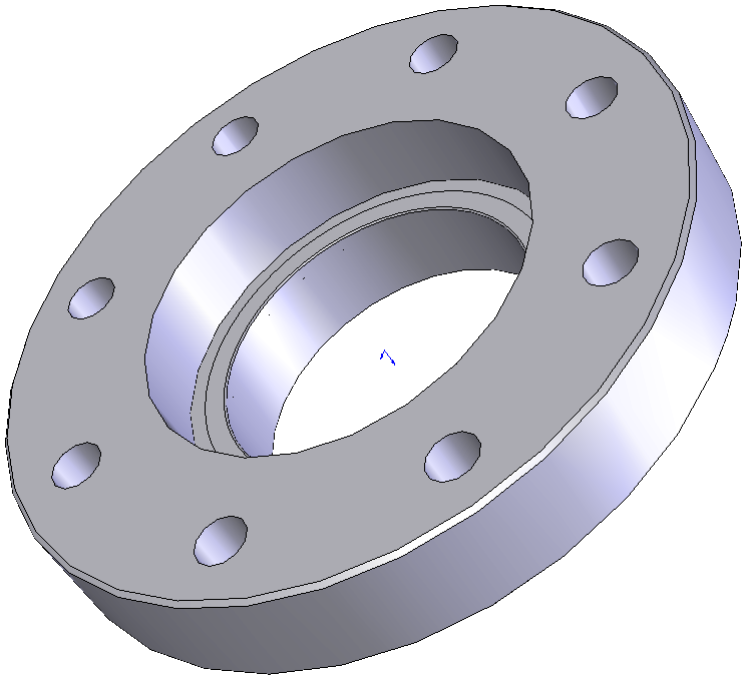

(b)

Figure 3.7: Re-entrant custom 4.5” CF flange viewport for imaging: (a) vacuum side and (b) air side.

welded using a constantan foil (Part number: 245-709-96 from Goodfellow Cambridge Limited) to avoid any leakage of vapours. For the electrical connections, Kapton wires are spot welded to the foil. A small piece of solid ytterbium (Yb) is kept inside the oven tube. The Yb can be heated up to 400^oC by operating the oven with a current of 5 to 6 amperes. The vapour pressure of the Yb at this temperature is enough to produce an atomic beam. There are four atomic ovens inside the vacuum chamber, of which two are for symmetric and two for asymmetric traps. One of the ovens for each trap contains a small wire piece (diameter 0.0035") of 90% enriched ^{171}Yb (Part Number: OA0036 from Oak Ridge National Laboratory) and others contain a small piece of natural Yb (part number: GO0196 from Goodfellow Cambridge Limited). Two ovens, one for the purpose of providing natural Yb and one providing enriched ^{171}Yb vapours are used for symmetric and asymmetric traps each.

By using custom made stainless steel bracket mounts, the ovens for symmetric traps are mounted on the metallic plates which hold the chip bracket in the chamber and pointed to its centre. The ovens are oriented towards the centre of the chip bracket and make an angle of $\approx 63^o$ to the corresponding laser axes for symmetric traps. While the other two ovens are facing the surface of the chip bracket and make a right angles with the laser axis for asymmetric traps. The ovens for asymmetric traps are mounted on a bracket held by groove grabbers attached to the octagon. The mounting position of the ovens is shown in figure 3.2. The oven brackets provide an electrical ground for the current running through the back of the ovens. The oven brackets also work as a heat sink for the ovens. A 1.33" CF flange 6-pin power electrical feedthrough (Part Number: EFT 0265062 from K.J. Lesker) was mounted on the hemisphere for an electrical supply to the ovens.

Oven testing

The ovens must be tested prior to placing them inside the chamber, for the purpose of determining the amount of current required to heat up the oven up to a certain level so that enough Yb vapour is produced. For this, ovens were placed inside a glass bell jar (Part Number: GMPS150F3RN from K.J.Lesker) mounted on a 2.75" CF flange cross piece. The front of the ovens were mounted on a bracket made of aluminum as shown in figure 3.8(a). The electrical contacts with the oven were made by using power electrical feedthrough (Part Number: EFT0265063 from K. J.Lesker). The bell jar was evacuated down to a pressure of 10^{-6} torr using a turbo molecular pump (Part Number: PM S03 525 from Pfeiffer). A residual gas analyser (RGA) from ExTorr (Part Number XT200M)

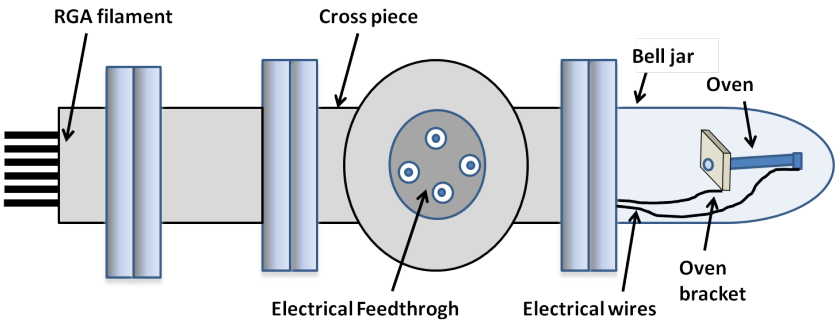

(a)

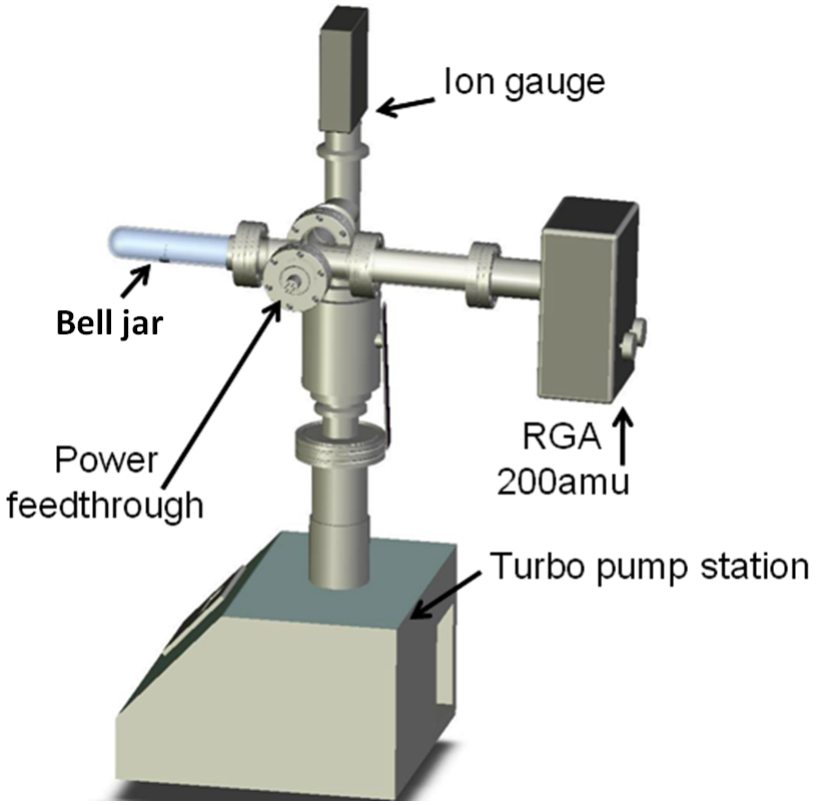

(b)

Figure 3.8: Atomic oven testing system. (a) The position of an atomic oven inside the bell jar. The bell jar and RGA are mounted on a cross-piece in a way that line of sight between the atomic beam generated by the oven and the RGA remains clear. (b) Oven testing system connected with the vacuum pump.

was attached to one end of the cross piece to detect the Yb vapour. The experimental arrangement is shown in figure 3.8(b). Due to the metallic nature of Yb, its vapour quickly condenses on the glass of the bell jar. It was observed that the line of sight must be kept clear between the oven and ExTorr RGA filaments to detect any Yb vapour. The RGA is poor at detecting vapours of heavy elements, therefore the electron multiplier option in the RGA software was enabled and set to 2000 V to amplify the signal. This setting of the RGA gave gain factor of 1000 for the partial pressures curves.

Initially the oven was pointing towards the glass of the bell jar. By running a current of 6 to 7 A through the oven for about 4 to 5 minutes, a shining black spot was observed on the glass of the bell jar but no partial pressure traces for Yb isotopes were detected by the RGA. The oven was then directed towards the RGA and the partial pressure curves were observed by selecting the *mass trend* option given in the RGA software. Most abundant isotopes (^{171}Yb, ^{172}Yb, ^{173}Yb and ^{174}Yb) were included in the mass trend list and partial pressure curves were recorded at different amounts of current. It can be seen that in figure 3.9 that after running a current of 5 to 7 amperes for at least 3 minutes, almost every oven showed increase in partial pressure curves (with a gain factor of approximately 1000). The test was performed for all ovens that were to be used in the chamber. The partial pressure curves with a gain factor of ≈1000 for natural Yb and enriched Yb filled ovens as a function of applied current are shown in figure 3.10. In order to work out the actual partial pressure for the Yb isotopes, first, the partial pressure curves for all the included masses were recorded without running current through the oven. The given curves show the noise of the RGA for a particular atomic mass and is subtracted from the value of the partial pressure given by the RGA when the oven is heated. The data from the partial pressure curves were then used to determine the required amount of current for the oven to produce sufficient Yb vapour.

3.2 Assembly of the vacuum system

Due to the fact that baking the vacuum assembly is essential to achieving a pressure of the order of 10^{-12} torr, it is necessary to use all metal ConFlat (CF) flanges in the system. Soft copper gaskets are used to ensure a vacuum seal in the CF flange system. CF flanges can be baked at 450^{o}C. CF flanges are sexless with knife edges and press the gasket to make a tight seal during mating. Care must be taken during the tightening of CF flanges because it requires the gaskets to be evenly pressed. The star pattern shown in figure 3.11

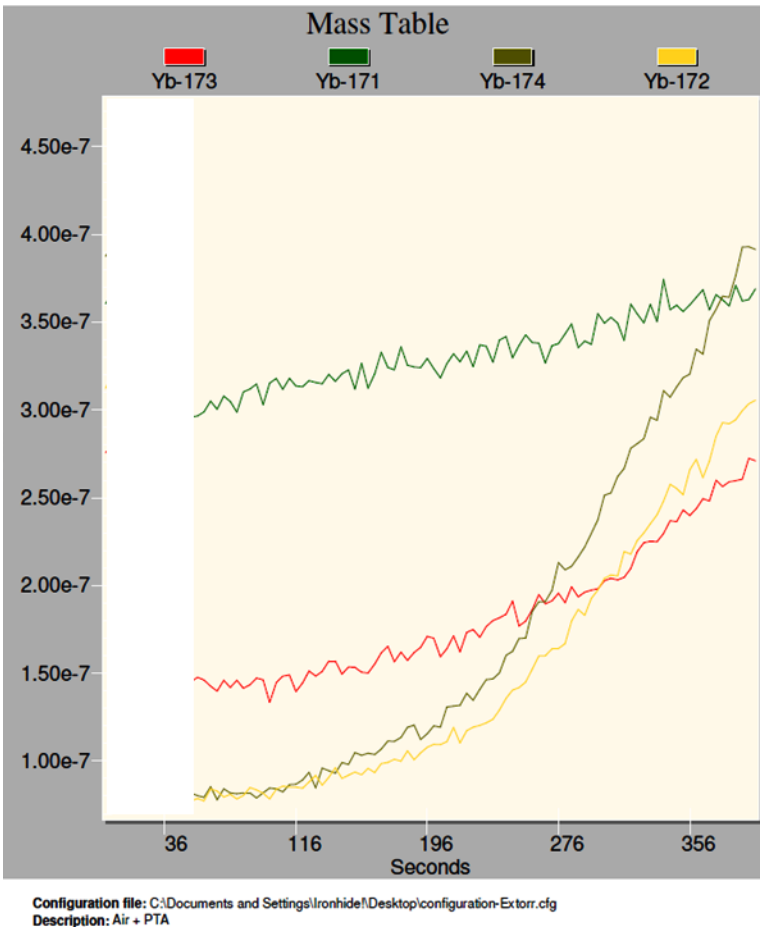

(a)

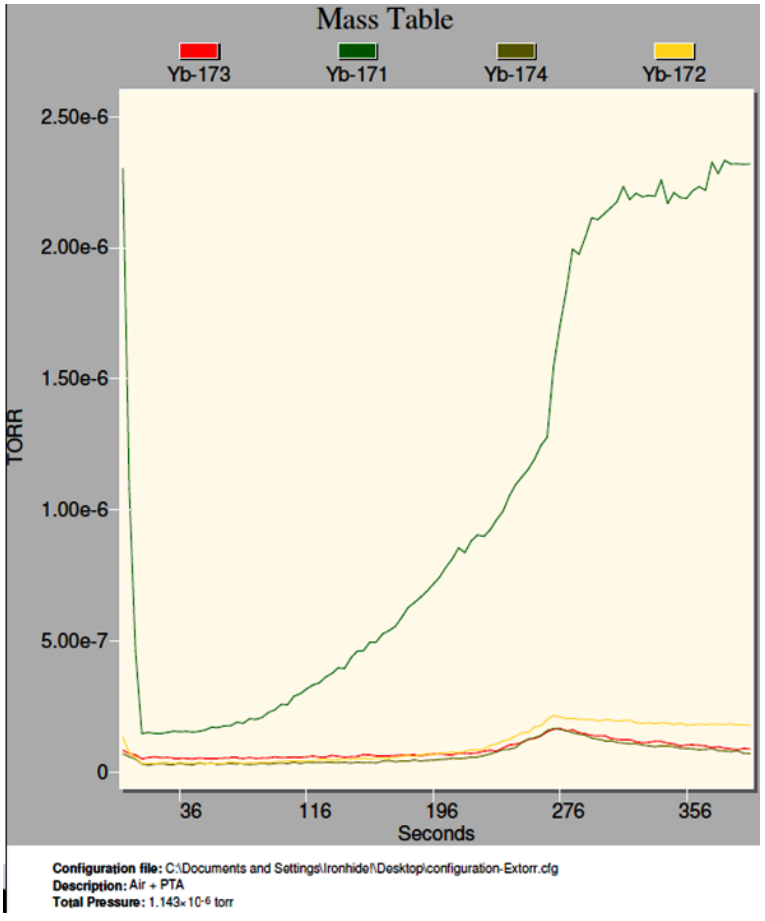

(b)

Figure 3.9: Partial pressure curves for (with gain factor of ≈1000) ^{171}Yb,^{172}Yb,^{173} and Yb^{174}Yb: (a) for natural Yb filled oven and in (b) ^{171}Yb enriched filled oven. Partial pressure (in units of *torr*) rises after running 5.5 A current for ≈3 minutes.

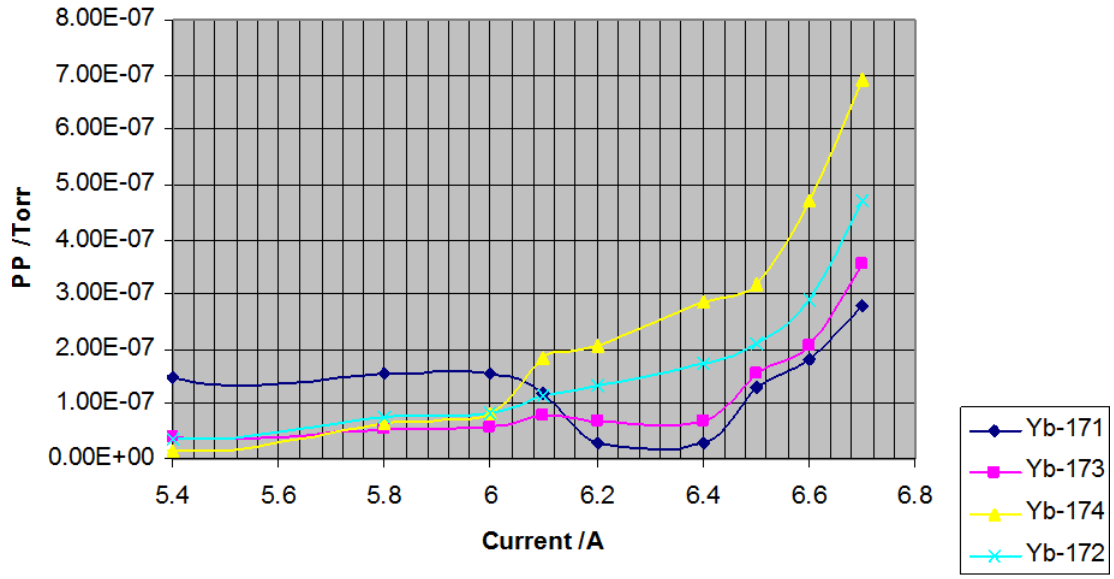

(a)

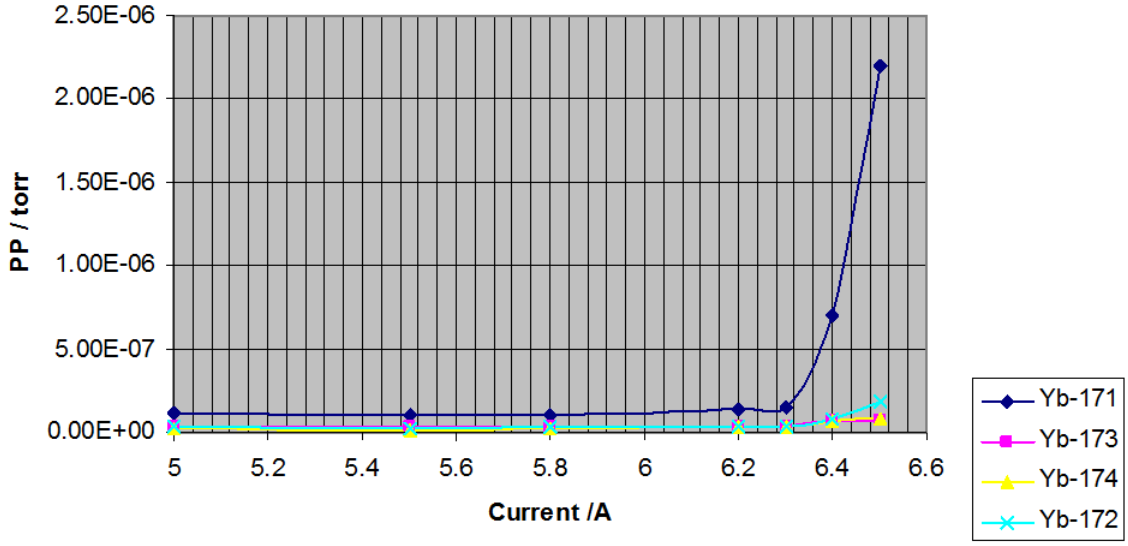

(b)

Figure 3.10: Partial pressure curves (with gain factor of ≈1000) for ^{171}Yb,^{172}Yb,^{173} and Yb^{174}Yb are plotted against applied current in (a) for natural Yb filled oven and in (b) ^{171}Yb enriched filled oven.

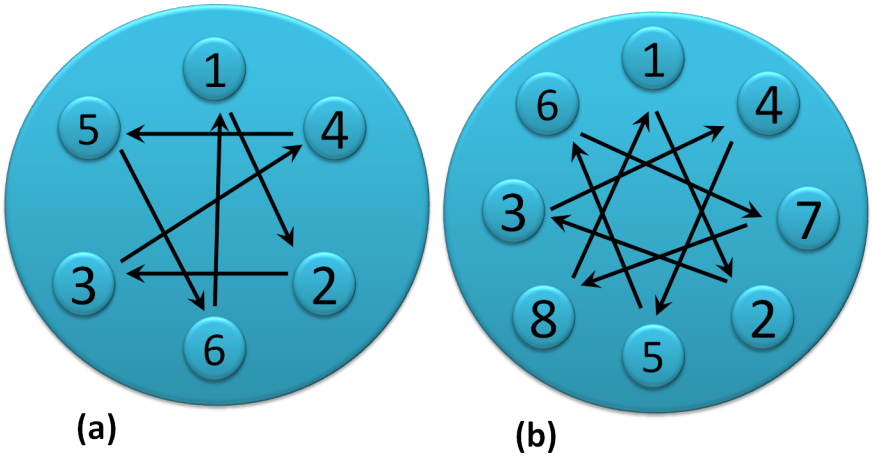

Figure 3.11: CF tightening pattern for ConFlat flanges with (a) six bolts (b) eight bolts.

must be followed to tighten the seals properly. The round head socket screws should be used on those flanges which sit on the optical table as hex-head screw corners may set off the flange and cause rocking of the system.

3.2.1 Cleaning and pre-baking

To avoid any risk of residual organic materials on the vacuum hardware, all the metal parts which are used in the UHV system including, the hemisphere, octagon, T-pieces, cross piece, nipples, blank flanges, conical reducers and chip bracket parts including PEEK plates, pin receptacles, fixing screws, oven brackets, must be cleaned extremely well even when their packaging says that they are clean and ready to use. This can be done in a number of ways. We cleaned all the hardware parts using HPLC (high-performance liquid chromatography) grade acetone (from Fisher Scientific) in an ultra sonic bath. For this purpose, the parts were submerged in acetone using a glass jar kept in a water filled tank of the ultrasonic cleaner. Care must be taken during cleaning in the ultrasonic bath, so not mix the water with acetone. Each part was cleaned for at least 10 minutes. After cleaning in the ultrasonic bath, each part was rinsed with HPLC grade methanol. Outgassing of absorbed water vapours in the steel parts can be a significant problem when trying to achieve UHV. Furthermore, pre-baking of these components establishes a chromium-oxide layer on the surface of the steel that reduces outgassing of hydrogen [61]. Therefore, after cleaning, all the metal parts were baked for a week at 200^{o}C until the colour of the steel became golden brown which is a sign of chromium-oxide. After baking all the parts, they were re-cleaned in the same way as described earlier. In order to keep all the parts clean until the system is assembled, after cleaning, all the metal parts were wrapped in an

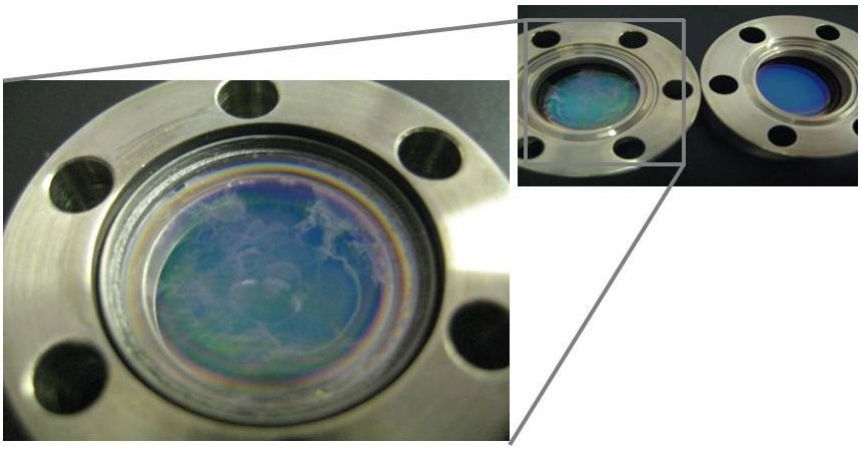

Figure 3.12: AR-coated viewport cleaned in methanol compared with un-cleaned AR coated viewport. White spots appeared on the glass of the viewport.

aluminum foil (shiny side towards the part) and kept inside an enclosed nitrogen flushed cabinet. It is not necessary to pre-bake electrical feedthroughs but they must be cleaned in the same way as the metal parts. In addition to cleaning, latex free vinyl gloves must be worn all times to keep body oils and other contamination off the vacuum parts. The vinyl gloves are soluble in acetone, therefore, care must be taken so as to not touch the vacuum side of the parts during cleaning, which may cause a residue of the glove material on the surface. Furthermore, it is important to follow the safety precautions in order to use the chemicals as they are highly flammable and toxic. Fumes from these chemicals are hazardous and can cause suffocation. The cleaning procedures must be carried out in a well ventilated area.

Viewport cleaning

Care must be taken in cleaning of the viewports as their seals can be damaged or the glass material or AR coating can be degraded in chemical solvents. Ultrasonic cleaning must not be used for viewports as intense waves of the ultrasonic cleaner can damage the seal between the glass and flange of the viewport. Vendors suggest to use HPLC grade or spectroscopy grade methanol to clean viewports but it was observed during the cleaning process that methanol had adverse effects on the glass material of the viewports. White spots appearing on the glass of a viewport, after cleaning it in methanol, are shown in figure 3.12. The cause of these spots was not further investigated. They might be caused by the dissolution of the AR coating or the seal of the viewport in the solvent. To avoid this problem, HPLC isopropanol (from Fisher Scientific) was used. All the viewports were

kept submerged in isopropanol for at least 20 minutes. Due to the reason that the material used in viewports is sensitive to temperature change and limited to 200^oC, the pre-baking process must be avoided for the viewports.

Ion traps

The ion traps are to be mounted inside the vacuum chamber, which result in a limited number of materials that can be used in an ion trap. Most of the inorganic metals and ceramics are UHV compatible. Some organic compounds like, Teflon, PEEK and Kapton can also be used. The ion trap is also to be cleaned using acetone in an ultrasonic bath prior to mounting inside the chamber.

3.2.2 Pumps and gauges

As with any vacuum system, the primary equipment for achieving a UHV environment are the vacuum pumps. No single vacuum pump would be able to cope with lowering the pressure within the chamber from atmosphere to that of 10^{-12} torr, so a series of pumps must be used. The pumping down strategy in our vacuum system is based on two stages. In the first stage, to pump down the pressure from atmospheric to the order of 10^{-7} torr, a diaphragm pump and turbo-molecular pump were used in combination. The turbo pump system has no oils and lubricants, and therefore is very clean and does not add any contamination to the system. This is very important when working on a UHV system, as back-streaming of oil vapours from conventional pumps would contaminate the system. As the roughing system has to pump the pressure of the vacuum chamber down to 10^{-7}torr, an economical ISO-Klein Flange (KF) flange system was used. In ISO-KF flanges, a vacuum seal is ensured by a viton O-ring rubber gasket and can be re-used multiple times. A 20 litre Varian StarCell (Part number: 9191145 from Varian) ion pump is also connected in the roughing system by an angle valve (part Number: SA0150MCCF from K.J. Lesker). The angle valve is connected to the turbo-molecular pump (Part Number: PM S03525 from Pfeiffer Vacuum) using an ISO-KF to CF flange adapter. The ion pump is used during the final baking of the vacuum system. The roughing vacuum assembly is shown in figure 3.19. A one metre long 2.75" CF flexible tube (part Number:MH-CF-C36 K.J. Lesker) is used to connect the roughing system with the UHV system. A bakeable UHV-all metal angle valve (Part Number: VZCR40R from K.J. Lesker) is used to isolate the roughing vacuum system from UHV system.

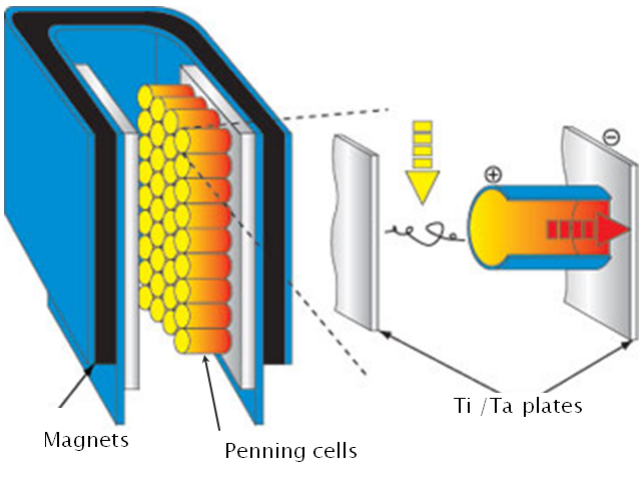

Figure 3.13: Internal structure of a sputter ion pump.(Picture taken from Varian catalog)

For the second stage which leads the pressure down from 10^{-7} torr to the order of 10^{-12}torr, a Varian 20 litre StarCell ion pump and Titanium Sublimation Pump (TSP) (Part Number: 9160050 from Varian) are attached to the vacuum system. The StarCell ion pump is connected with the pump controller (MidiVac Part number: 9295002 from Varian) using a bakeable cable (Part number: 9290705 from Varian). A high power current controller with an automatic on/off timer was used to supply a high current to TSP filaments. TSP pumps run for a short time ($\approx$ 1 to 2 minutes). There is no need for a bakeable cable for the TSP, as it only runs for a couple of days for short time intervals after the baking procedure or whenever the pressure in the system rises above the required base pressure.

A StarCell is a type of sputter ion pump. The primary pumping action of a sputter ion pump is produced by *gettering*, which refers to a chemical combination between the surface and the pumped gas. The design of a modern ion pump is based on a Penning cell [62] and is called sputter ion pumps, because the supply of a titanium film is produced by a process called sputtering. Pumping speed is achieved by the parallel connection of many individual penning cells. A basic sputter ion pump design consists of a parallel array of short stainless tubes serving as anodes, and two cathode plates made of titanium (Ti) or tantalum (Ta) spaced at a short distance from the open ends of the tubes. The magnetic field is oriented along the axis of the anode tubes (figure 3.13).

Electrons are emitted from the cathode due to the action of the electric field caused by the high voltage applied to the electrodes. Emitted electrons travel in helical trajectories due to the applied magnetic field and ionise the gas molecules inside the Penning cell. Ions impacting on the cathode surface sputter Titanium (Ti) or Tantalum (Ta) away from

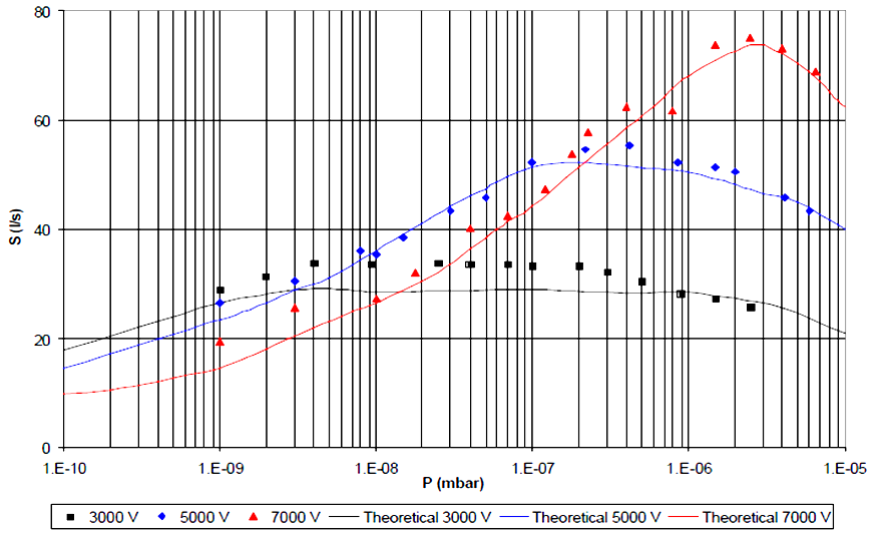

Figure 3.14: Pumping speed of an ion pump as a function of pressure and voltage. Pumping speed is maximum with the applied voltage of 7 kV when the pressure in a vacuum chamber is in the order of 10^{-6} mbar. Pumping speed of an ion pump is higher with the applied voltage of 3 kV when the pressure is in the range of 10^{-10} torr.(Plot taken from Varian Inc.)

the cathode, and form a getter film on the neighbouring surfaces and stable chemical compounds with the reactive or "getterable" gas particles (e.g. CO, CO_2, H_2, N_2, O_2). In addition to the sputtering process, the energy of the ionised gas particles allows them to penetrate deeply into the cathode material and remain buried inside it. This sorption process is particulary helpful to pump out noble gases which do not react chemically with the titanium layer formed by sputtering. The starCell pump offers greater pumping speed for the noble gases than any other kind of ion pump.

In general, the pumping speed of the ion pumps depends upon the applied voltage and varies with the pressure in the system [63]. Figure 3.14 shows the variation of the pump speed with pressure at different voltages. It can be seen that the pumping speed is maximum when the pressure is of the order of 10^{-6} mbar when the applied voltage is 7 kV. When the pressure is in the range of 10^{-10} mbar, the pumping speed is higher with the applied voltages of 3 to 5 kV. It is recommended to change the control voltage on the pump according to the pressure variation to achieve the maximum pumping speed.

In a TSP, Ti coated filaments are periodically heated up to temperatures of 1500°C with high currents of up to 50 A. The titanium evaporates and deposits a getter film directly onto the chamber wall in the vacuum system. Active gas molecules (no noble gases) react with the getter film. Standard TSP comes in the form of three disposable filaments and is to be mounted directly in the vacuum system making sure that the filaments clear the

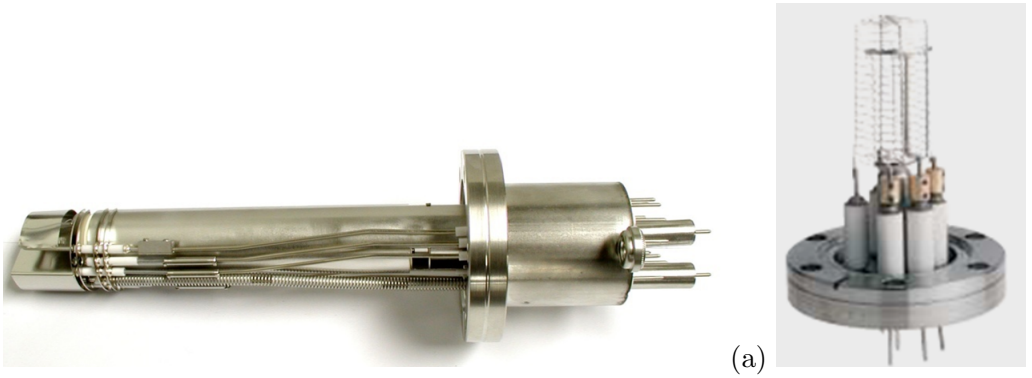

(a) (b)

Figure 3.15: Pressure measurement devices: (a) Extorr RGA (200M) filament (b) Varian nude B-A UHV-24p ion gauge.

chamber walls by at least 2 cm. Each filament has a life time of 12 hours at 50 A, and one filament can be used at a time. The run-time of the filament can be recorded by the pump controller. Only one of the TSP filament has to be run for about a minute or two at a time with the current settings of $\approx$ 47A. The cyclic run (which may be 2 to 3 times an hour) of the TSP filament can automatically be set on the controller. It was observed that pressure rises sharply while running the pump which is due to the evaporation of Ti. The pressure in the system will start to settle down once the TSP is turned off and after at least 30 to 40 minutes, depending on the running time of the TSP, the base pressure will be reached. After each running cycle, the final base pressure would be less than the pressure achieved in the previous cycle. The TSP mounting chamber becomes hot during running, therefore, the chamber should not to be touched. To monitor the vacuum pressure in the system, an Ion Gauge is required. There were several different options open for the ion gauge. One US based company, Extorr, manufactures RGAs which can be used to measure the UHV pressure down to 10^{-11} torr and the partial pressure of the residual gases up to 10^{-14} torr with its electron multiplier option. The accuracy in the measurement of the gauge is restricted by the "x-ray limit". Soft x-rays can be produced by the energetic electrons hitting the grid of the gauge, which in turn can produce photoelectrons from the collector of the gauge. The measurement electronics of the gauge can not distinguish between a positive ion or losing a photoelectron. This inability of a gauge sets the minimum pressure range of the gauge.

The x-ray limit of Extorr RGA is specified as 10^{-9} torr. Therefore any measurement of the pressure below this range can not be reliable. Further to this, it was also observed that the RGA cannot be used when the pressure in the system drops below 10^{-10} torr. Whenever it was operated in this pressure region, it always raised the pressure in the vacuum system. Even with these deficiencies, Extorr RGA (Part Number: XT200M from

ExTorr) was included in the system for the purpose of leak detection as it provides partial pressure measurements for a wide range of elements up to a mass number of 200 a.m.u. For the accurate measurement of total pressure, a Varian nude Bayard-Alpert UHV-24p ion gauge with a tungsten filament (Part Number: 9715015 from Varian) is included in the vacuum system. The pressure measurement sensitivity (or x-ray limit) of the UHV-24p ion gauge is around 5×10^{-12} torr. The ion gauge is controlled by a SenTor (Part Number: L91103010100 from varian) controller using a bakeable cable (Part Number: L64403010). Figure 3.15 shows the pictures of the RGA and the ion gauge.

3.2.3 Assembly

The assembly of all the vacuum parts should not block any optical access and must leave plenty of space for optical mounts. The design and larger diameter of pipes ensure high conductance of the gases from the system during evacuation process. The vacuum system has been designed in SolidWorks. The dimensions of the UHV system along with optics and laser orientation are shown in figure 3.16.

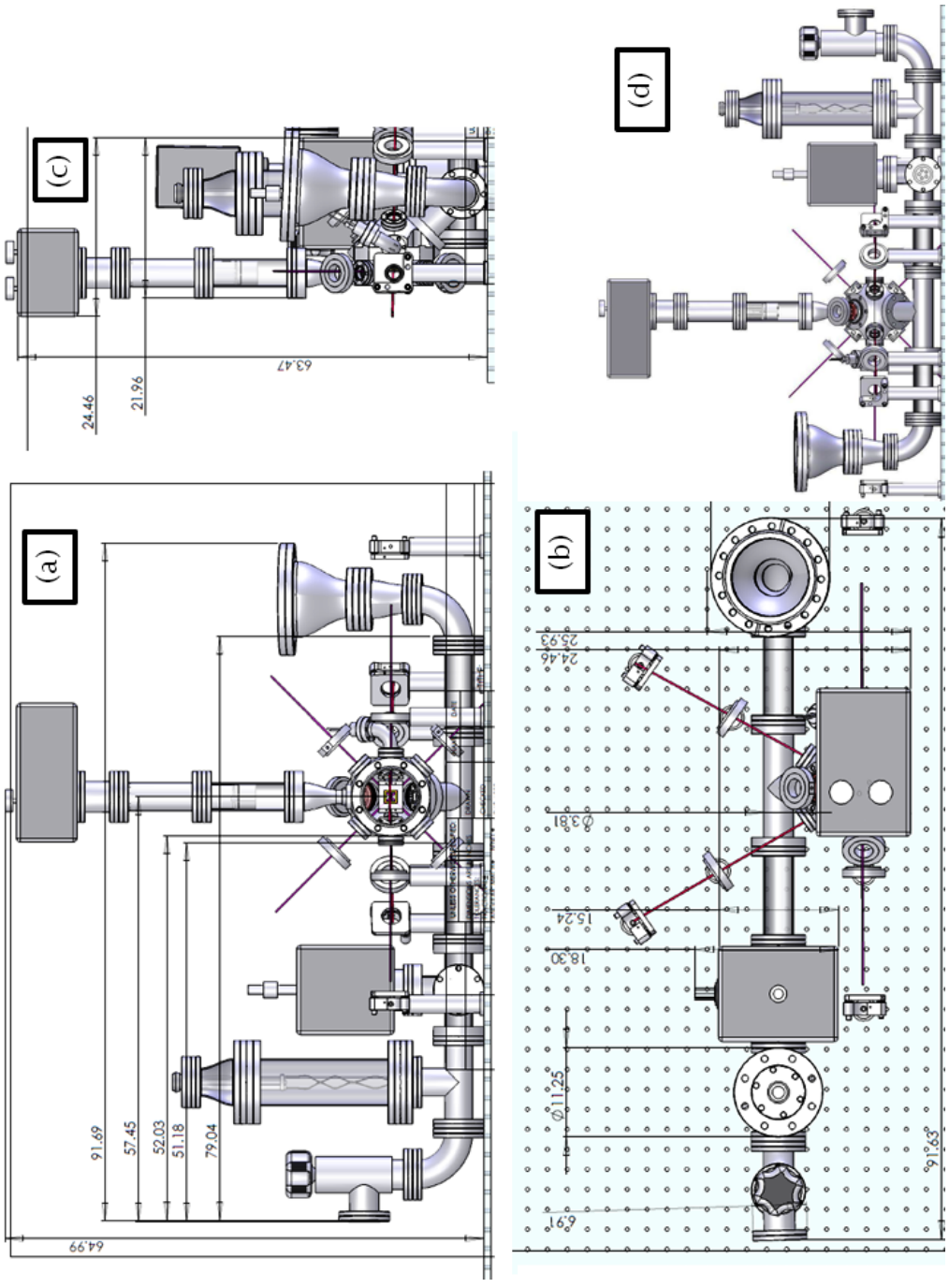

Figure 3.16: Dimensions of the UHV system: (a) Front view, (b) Top view, (c) Side view and (d) Back view.

Before the final assembly of the vacuum system takes place, the space where the system will be assembled, should be cleaned, and all parts must be kept wrapped in aluminum foil until they are used for assembly. Extreme precautions must be taken to ensure that no foreign particle enters the system. To implement this, a full disposable lab coat with hair net, face mask and powder free latex gloves must be worn at all times during the assembly process. The vacuum system should be assembled in a careful order. It is good practice to make a proper strategy for the assembly process to avoid any complications during the construction. The construction strategy for the current vacuum system in the lab was drawn as follows,

- Assemble the chip bracket outside the chamber and crimp D-type connector Kapton wires in to the pin receptacles,
- Mount the atomic ovens for the symmetric traps onto the chip bracket,
- Mount the atomic ovens for the asymmetric traps onto the octagon grab grooves using the groove grabbers,
- Pass the wires of all the ovens through the 1.33" CF flange window of the hemisphere and connect with the electrical feedthrough,
- Fix the symmetric ovens electrical feedthroughs to the hemisphere of the chamber,
- Pass the two 50 pin D-type connector wires through the 2.75" CF flange window of the hemisphere,
- Pass the ceramic fish beads insulated copper wires for the rf power supply through the 1.33" CF flange window of the hemisphere and connect it with the power feedthrough,
- Mount the chip bracket into the hemisphere grab grooves using the groove grabbers,
- Finish the assembly of the chamber by attaching the octagon and front re-entrant viewport with the hemisphere,
- Attach all the viewports to the chamber,
- Attach the chamber assembly to the custom T-piece after passing the 2 D-type connector wires through it,
- Mount the ion pump, ion gauge, TSP and RGA on the corresponding flanges.

Figure 3.17(a) shows the internal picture of the chamber looking into the rear side 2.75"CF

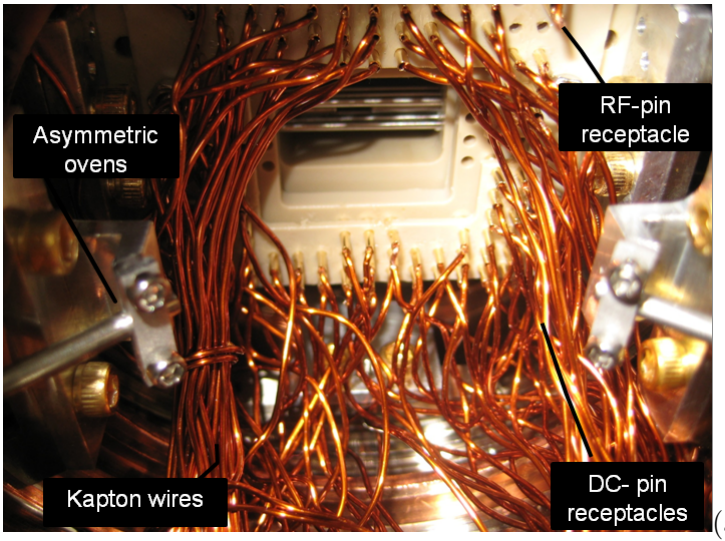

(a)

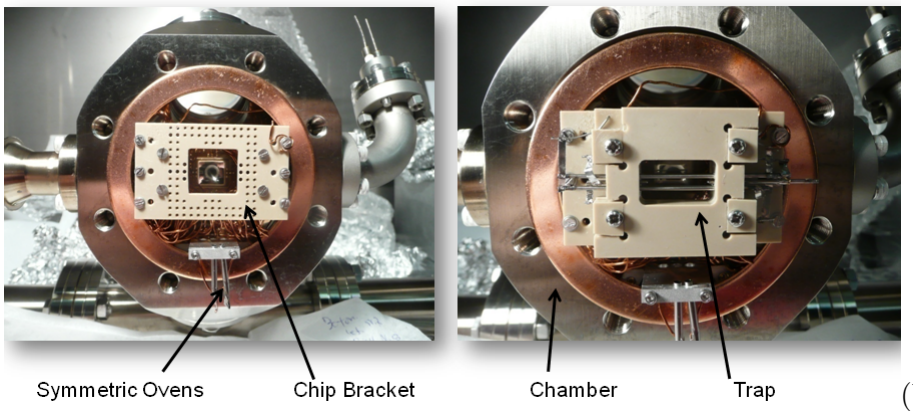

(b)

Figure 3.17: (a) Picture of the inner section of the chamber taken from the rear 2.75"CF viewport. Kapton wires are crimped in the receptacles inside of the chamber. (b) Front view of the chamber shows the chip bracket and mounted symmetric ion trap.

flange viewport and 3.17(b) shows the pictures of the chamber with and without the symmetric ion trap.

The solidWork design of the complete UHV system assembly is shown in the figure 3.18 and the picture of the assembled system is shown in figure 3.18.

3.3 Pumping down procedures

3.3.1 Degassing

After finishing the vacuum assembly and before the final baking procedure, it is necessary to perform the degassing procedure on some vacuum components which get hot in the chamber. The first step is to pump the vacuum system down to 10^{-6} mbar using a turbo molecular pump in the roughing vacuum system shown in figure 3.19.

The degassing procedure can be performed in the following order;

TSP filaments

TSP is used at a very high current when the pressure in the system has already reached the range of 10^{-10} torr. Therefore, it is very important to degas the TSP filaments properly. Each filament can be degassed by running a current of 35 A through each filament for at least one hour in turn. The current should be raised slowly in steps of 5 A per minute so that the pressure does not change abruptly in the vacuum system. Once the current has reached 35 A, it should be kept running through the filaments for an hour.

Atomic ovens

Each oven should be fired for at least 5 minutes, with the current not being higher than the threshold current for Yb vapours which was determined during the atomic oven tests.

Ion trap

This is also the right time for testing the rf power supply to the trap. Using the Helical resonator, (discussed in section: 4.6) apply 3 to 4 watts of rf power to the trap for a few minutes. The rise in pressure implies that the trap is getting hot and working properly.

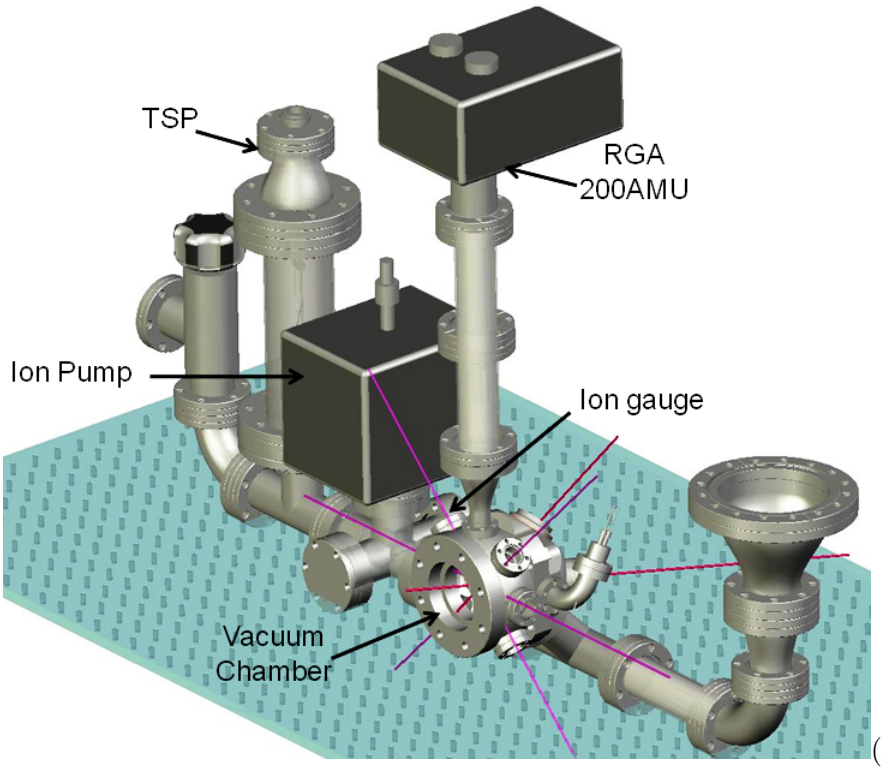

(a)

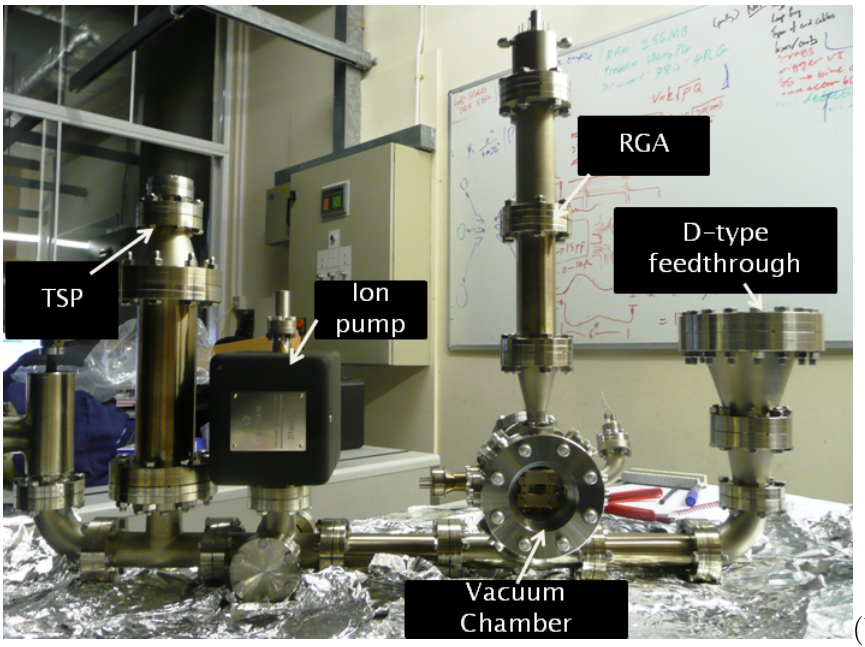

(b)

Figure 3.18: (a) SolidWork design of the UHV system and (b) Picture of the assembled UHV system.

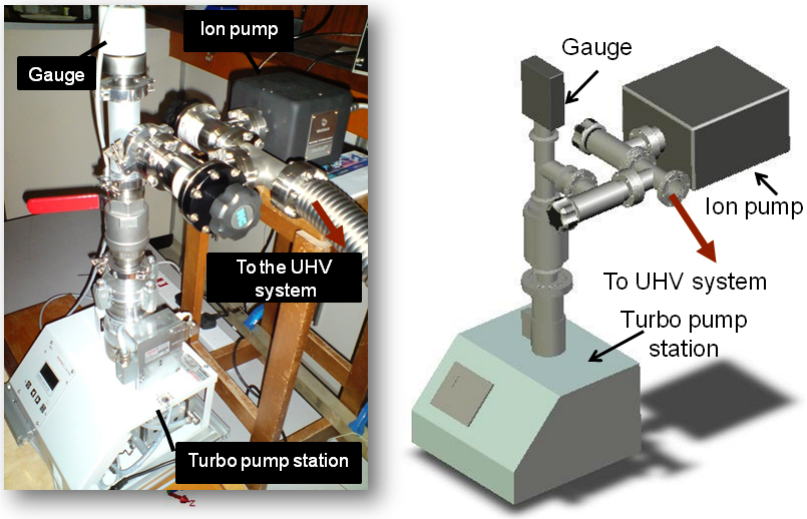

Figure 3.19: The roughing vacuum system consists of a 60L turbomolecular and 20L StarCell ion pump.

Measure the capacitance and resistance of the trap before and after applying the rf power. If a short develops during the degassing or final bake-out, this will help to diagnose it.

RGA

The RGA can be degassed using the option given in the control software. This will run a current of 10 A through the RGA filament for 15 minutes.

Ion gauge

Using the degas option given on the gauge controller, the ion gauge can be degassed properly.

3.3.2 Leak test

At this point, it is worth while checking for any possible leaks in the system. To perform a leak test, Helium (He) gas can be used. Set the RGA to mass trend mode, select He as an element and turn on the electron multiplier options because at normal setting, detection signal may be too small to be detected. Spray He over every flange and simultaneously look for any rise in the mass trend plot on the computer screen display. Any sign of the mass trend rise represents a leak in the system. Therefore tighten the flange where the leak is suspected with full torque until the mass trend sets at its base value.

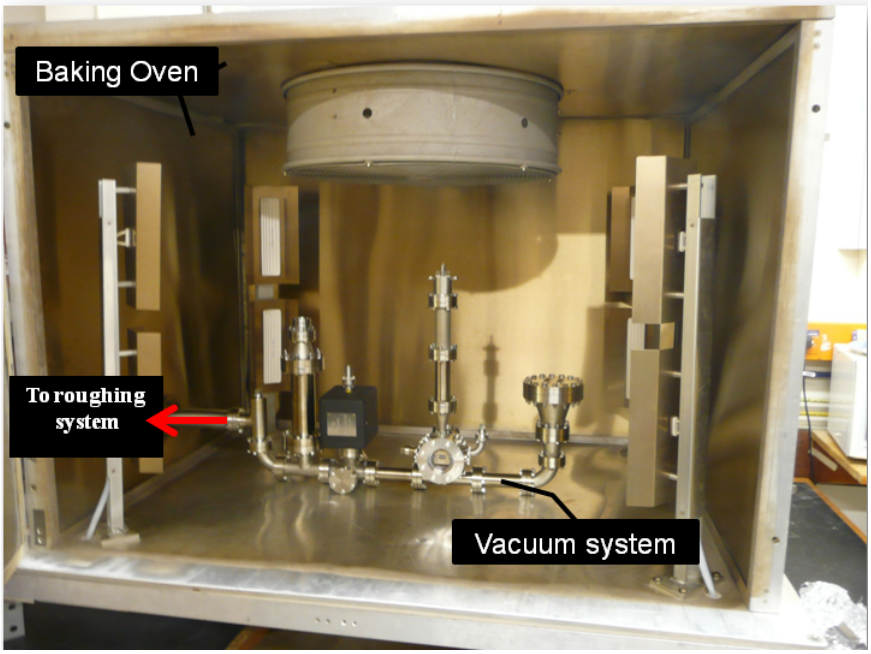

Figure 3.20: Baking oven and the UHV system.

3.3.3 Final baking

After performing all the required tests and degassing procedures, the system is ready for final pumping down to the order of 10^{-12} torr. For the final bake-out of the vacuum system, an oven was built in the lab. The internal dimension of the oven are 1m×1m×1.4m, sufficient enough to accommodate the vacuum system. Eight heating filaments are installed in the oven to keep the oven at a temperature well above 200^{o}C. A fan is also mounted inside the oven to avoid any temperature gradients. The walls of the oven are 4 cm thick and insulated with rockwool. The temperature of the oven is maintained by a PID control circuit. Figure 3.20 shows the oven and the vacuum system ready for final bake-out. The maximum temperature to bake at is determined by the viewports. The ramp in the temperature is also limited by the viewports. The viewports used in our system can be baked at 200^{o}C and rated for 5^{o}C temperature change per minute. In practice, the ramp up time is limited by the pressure and 10 to 15^{o}C per hour is quite safe if the vacuum parts are already pre-baked at 300^{o}C.

Baking procedure is:

1. Connect the roughing system to the vacuum system through the exhaust port given in the oven by using a flexible 36” long tube.

2. Cover all exposed viewports and feedthroughs with aluminum foil (shiny side toward the viewports).

3. Connect the ion gauge and 20L StarCell ion pump to the respective controllers using bakeable cables through the oven exhaust port.

4. If the vacuum system is at atmospheric pressure, open the all-metal angle valve before starting the turbo pump. If the vacuum system is already pumped down to 10^{-6} torr, leave the system valve closed and first open the valve to the turbo pump and start the turbo pump. When the pressure on the roughing system side reaches 10^{-6} then slowly open the valve to the UHV system.

5. Slowly ramp up the oven temperature. Keep the ramp speed slow enough (12 to 15^{o}C per hour), so that the pressure does not rise above the 10^{-5} torr range. Keep a record of the bake-out including the following information: Date, time, actual oven temperature, oven set point, turbo gauge pressure, ion gauge pressure, ion pump voltage and current and any other notes on the bake-out.

6. When the temperature has reached 200^{o}C and the pressure does not change significantly any more, start the external ion pump with the voltage set to 3 kV and gradually raise the voltage to 7 kV after 10 to 15 minutes.

7. Start the ion gauge and close the turbo valve and after a few minutes stop the turbo pump.

8. When the pressure does not change over the course of a day (usually a few days into the bake), it is time to start the internal ion pump with the voltage set to 3 kV and raise to 7 kV after 10 to 15 minutes.

9. Hand tighten the vacuum system valve, do not close it to full torque as the valve is hot and can be damaged when tightened hot.

10. After a couple of days, once the pressure does not fall any further, slowly ramp down the temperature (12 to 15^{o}C per hour).

11. When the temperature of the oven reaches room temperature, open the doors of the oven and tighten the internal valve with appropriate torque (given in the valve manual). Make a log book entry for the torque used to close the valve. In future always higher torque would be used to close the valve properly.

12. Close the valve to the external ion pump and disconnect the flexible tube from the

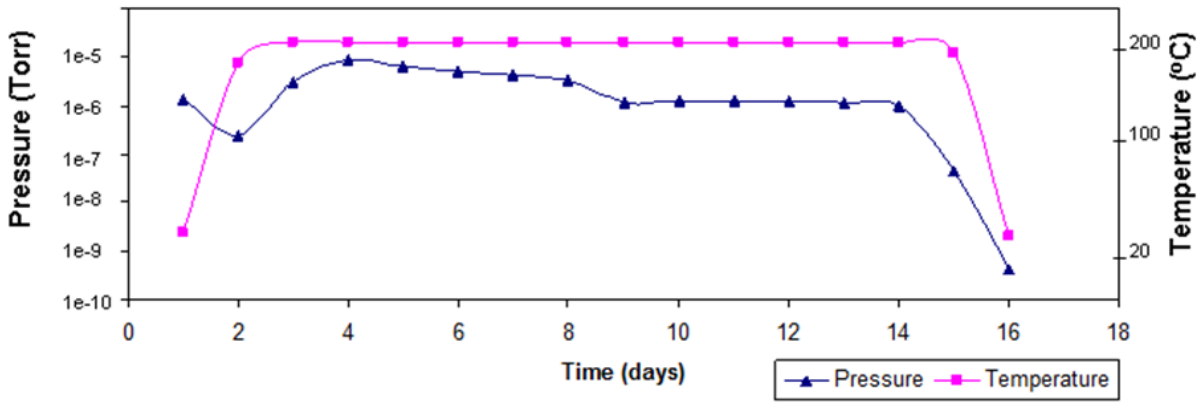

Figure 3.21: Bake-out process of 16 days. The pressure in the system on the 16^{th} day was in the range of 10^{-10} torr.

vacuum system.

13. At this stage, pressure in the vacuum system should be in the range of 10^{-10} torr.

14. Turn off the pump and gauge controllers and unplug all the cables, and immediately shift the vacuum system to the optical table.

15. Reconnect the pump and ion gauge to the controllers.

16. Connect the TSP to the controller and fire the filament for 60 seconds once every two hours on a regular basis (see notes on TSP in section 3.2.2).

17. Pressure spikes can be observed while running the TSP, therefore, care must be taken so that the pressure does not rise above 10^{-9} torr. If the pressure goes above this limit, the pump may need to be turned off.

18. The pressure slowly decreases after each run of the TSP, and ends up with a factor of 2 or so below the starting pressure.

19. Turn off the TSP when the pressure drops down to 10^{-11} torr.

20. Switch the ion pump to the 5 kV setting.

Figure 3.21 shows the record of the 16 days bake-out process. The baking process ended with a base pressure on the order of 10^{-10} torr. After the bake-out procedure and by running the TSP for a couple of days, a pressure below 10^{-11} torr is achieved in the vacuum system. The pressure in the vacuum system was measured near the chamber. Elsewhere in the system the pressure might be slightly different due to a non uniform distribution in the vacuum system.

Chapter 4

Experimental setup

4.1 Introduction

In our experiment an Yb atom is efficiently photo-ionised and trapped in a linear rf Paul trap. The trapped ion is then Doppler cooled successfully. We also performed a heating measurement for our ion trap. This chapter covers the basic layout and equipment used for the ion trap experiment described in this thesis. Neutral Yb atoms from an atomic oven are photoionised via a two-step resonant process by excitation of the atom on the $^1S_0 \rightarrow ^1P_1$ transition with 399-nm light followed by 369-nm light photons to cross the continuum level. The ionised atom is trapped in a linear Paul trap where it is Doppler cooled by exciting its $^2S_{1/2} \leftrightarrow ^2P_{1/2}$ dipole transition with 369-nm light. In order to bring the ion back to the cooling cycle as it frequently decays from its $^2P_{1/2}$ level to $^2D_{3/2}$ level or undergoes infrequent decay to $^2F_{7/2}$ from its D-levels, a light at 935-nm and 638-nm resonant to these transition are required (as discussed in chapter 2). Details of the laser setups and their computer controlled locking-scheme are discussed in this chapter. The trapped and laser cooled ion needs to be imaged and its fluorescence to be detected for performing experiments. For this to be implemented an imaging setup is constructed including a camera and photo-multiplier tube. In order to supply rf power to the trap a helical resonator is built in the lab. The design and construction of the resonator is also discussed at the end of this chapter.

4.2 Lasers

In order to ionise Yb and excite its internal energy states in an ion trap experiment, 399-nm, 935-nm and 638-nm coherent light sources are home built as an external cavity diode laser (ECDL) setup, while the Doppler cooling laser (369-nm) is a frequency doubling system which is purchased from Toptica. In the ECDL laser setup, the cavity is formed between the laser diode's rear facet and the diffraction grating. The use of an external diffraction grating effectively increases the length of the cavity of the laser diode. Furthermore, this set up allows us to obtain the selected frequencies by reflecting the light of a specific frequency using the diffraction grating back to the laser diode.

The frequency of the laser diode is sensitive to temperature, which changes the band gap in the junction region of the laser diode and the length of the internal cavity of the diode, hence, causing it to resonate at a different frequency. The current passing through the laser diode changes the refractive index of the lasing medium and causes heating, which also changes the band gap energy. In addition, the output power of the laser also depends upon the amount of current. Hence ECDL frequency and output power can be varied by varying the current and the temperature of the diode along with the angle of the grating. This flexibility of the ECDL lasers makes them a primary choice for the laser systems used in ion trap and laser cooling experiments.

There are two main arrangements of the ECDL, known as Littrow and Littman-Metcalf configurations. In the most common Littrow configuration, the first order diffraction beam from the grating is sent back to the laser diode and directly reflected light forms the output beam, hence, providing a high percentage of laser light for the experiment. Unfortunately, the output beam direction is wavelength dependent resulting in slight alignment problems if the laser is tuned with the grating. The Littman-Metcalf configuration uses a grating at grazing incidence, with the first-order diffracted beam reflected back to the grating and diode laser by an additional mirror. In this case, the laser is tuned by the angle of the mirror, so that the grating and the zeroth-order reflected output beam remain fixed with the wavelength. However, compared to the Littrow configuration, this arrangement is more complex and requires an additional mirror and typically has lower output efficiency. Therefore, the Littrow configuration is preferred in the lab to build our laser systems. In order to protect the laser diode from unwanted back reflections which can permanently damage the diode, an optical isolator is used after the ECDL output.

4.2.1 Photo-ionisation laser (399-nm)

To provide the first stage of the photo-ionisation process for Yb atom, light at 399 nm is used to resonantly excite it from the $^1S_0 \rightarrow ^1P_1$ transition. It is generated by an ECDL setup consisting of a Sanyo laser diode (part number: DL-4146-301S), an aspheric lens (Part number: A390TM-A from Thorlabs) and a diffraction grating (Part number: GH13-24V from Thorlabs) with a first order efficiency of about 58%. The output power of this laser setup is about 4 mW.

4.2.2 Doppler cooling laser (369-nm)

For the second stage of the photo-ionisation process, photons with wavelength less than 394 nm are required. This is achieved by using the light at 369 nm in our lab which also cools the trapped ion immediately after ionisation by exciting its $^2S_{1/2} \leftrightarrow ^2P_{1/2}$ dipole transition. The 369-nm light is generated by frequency doubling of light at 739-nm using a non linear crystal Lithium Triborate (LBO). The 739-nm light is generated by built-in ECDL setup. The frequency doubling laser system (TA-SHG 63) is purchased from Toptica Photonics. In order to access the hyperfine levels $^2S_{1/2}(F = 1) \leftrightarrow ^2P_{1/2}(F = 0)$ in $^{171}Yb^+$ for Doppler cooling and state preparation, the doubling system is modified in our lab, first to generate 7.37 GHz frequency sidebands using an electro-optic modulator (EOM) (Part number: 4851 from New Focus). A HP 8684B signal generator is used to provide the 7.37 GHz signal which is then amplified by using a power amplifier (Part number: PA2503-3 from Advanced Microwave Inc.) and sent to the EOM. Applying the modulating signal of 31 dBm to the EOM produces $\approx 10\%$ first order sidebands then these sidebands are frequency doubled to produce 14.7 GHz to access the hyperfine transitions in $^{171}Yb^+$.

4.2.3 Re-pump laser (935-nm)

Light at 935 nm is used to drive the $^2D_{5/2} \leftrightarrow ^3D[3/2]_{1/2}$ transition to prevent the ion being lost from the Doppler-cooling cycle otherwise it can decay to the dark state state $^2D_{5/2}$. The light at 935 nm is generated by an ECDL setup consisting of a laser diode (Part number: RLT940-100GS from Roithner) with output power of 100 mW, an aspheric lens (part number: C330TM-B form ThorLabs) and a diffraction grating (Part number: GH13-1210 form Thorlabs) with 80% efficiency. It is possible to obtain 20 mW out of the

ECDL by operating the laser at 111 mA and 25^{o}C. An optical isolator (OFR: IO-5D-935-VLP) is used after the laser to prevent un unwanted back reflection of the laser beam. The frequency sidebands at 3.08 GHz are generated via current modulation to access the hyperfine levels $^2D_{5/2}(F = 1) \leftrightarrow ^3D[3/2]_{1/2}(F = 0)$ present in ^{171}Yb$^+$. The 3.08 GHz modulation signal is generated by a Systron Donner 1710B-S1087 signal generator and then combined with the DC driving current using a bias-T (Minicircuits: ZFBT-4R2G+). The signal is then amplified to 18 dBm using an amplifier (Part number: ZRL-3500+ from MiniCicuits). The generated sidebands are $\approx 5\%$ of the carrier signal and are sufficient to drive the hyperfine transition in ^{171}Yb$^+$.

4.2.4 Re-pump laser (638-nm)

The Yb$^+$ may be excited to $^2D_{5/2}$ state from $^2D_{3/2}$ due to back ground atom collisions and from here it finally decays into $^2F_{7/2}$ by spontaneous emission. From $^2F_{7/2}$ level the trapped ion needs to be re-pumped to the $^1D[5/2]_{5/2}$ state with light of 638 nm wavelength in order to bring the ion back in to the Doppler cooling cycle. Furthermore, the $^2F_{7/2} \leftrightarrow ^1D[5/2]_{5/2}$ transition has hyperfine doublets for the ^{171}Yb$^+$ and separated by 4.4 GHz. In order to access these hyperfine levels a simple and cheap solution is achieved in the lab by periodically switching the 638 nm laser wavelength from 638.610 nm to 638.616 nm. The switching of the laser frequency is achieved by scanning the laser frequency using the triangle waveform signal which is simultaneously sent to piezo actuator and to the laser diode current. Light at 638 nm is generated by using an ECDL laser setup consisting of a Sanyo laser diode (DL-6148-030) with 40 mW output power, an aspheric lens (Thorlabs: A390TM-B), and a diffraction grating (Part number: GH13-24v from Thorlabs) with 83% efficiency is used. By operating the laser at 67 mA and 17^{o}C, an output power of 17 mW in the zeroth order beam is produced. Isolation from the back-reflection is achieved by an optical isolator (OFR: IO-5-638-PBS).

4.3 Laser locking scheme

The frequencies of the laser diodes are strongly sensitive to temperature change, electric current and cavity length (acoustic oscillations). To avoid any drift in the cooling laser frequencies, it is necessary to lock the lasers with a known frequency reference during

the trapping and cooling experiments. Various electrical and optical methods have been developed and implemented to improve the frequency stability of laser diodes. The locking scheme in our lab is accomplished by locking the 739-nm and 935-nm lasers to a passively stable reference cavity using an rf (Pound-Drever-Hall) lock [64, 65].

Frequency references utilising the natural atomic transition lines are in common use in laser locking schemes. Atomic properties such as energy differences between atomic levels and thus atomic transition frequencies are generally considered as natural constants due to the fact that absorption or emission of electromagnetic radiation of frequency $f = \Delta E/h$ (where h is the Planck constant) depends upon the transition between two different energy states ΔE. Following these ideas, atomic frequency references have been developed based on a variety of atomic species. For accurate frequency measurements, wavemeter calibrations and to keep the reference laser locked with known standard wavelength, in our lab, well known $^2\mathrm{S}_{1/2} \leftrightarrow ^2\mathrm{P}_{3/2}$ Rb D_2 transition line with $\Gamma \sim 2\pi 6$ MHz [66] is used as a frequency reference. This is due to the fact that the Rb transition is close to one of the major Yb cooling and state detection un-doubled 369-nm laser (739-nm laser), which makes it more attractive frequency reference for our trap experiment. Furthermore, to ensure the reliability of the scheme, a computer controlled scanning cavity lock setup is established in our lab. By using this locking-scheme the frequency of 739-nm and 935-nm lasers are locked down to ~ 20 MHz.

4.3.1 Reference laser (780-nm)

In order to provide a frequency reference, a 780-nm ECD laser setup is constructed in the lab. The frequency of the 780-nm laser is locked to one of the hyperfine atomic transitions of Rb. In the 780-nm laser setup, a Littrow configuration is used to provide feedback to the laser diode, (784-nm laser, part number: GH0781JA2C from Thorlabs), emitting 80 mW via a diffraction grating (Part number: GR13-185 from Thorlabs). The required wavelength of 780.246 nm is achieved by adjusting the diode current with current and temperature controllers (Temperature controller, part number: TED200C and current controller part number: LDC201CU from Thorlabs).

To access the hyperfine transition of $^2\mathrm{S}_{1/2} \leftrightarrow ^2\mathrm{P}_{3/2}$ line in Rb, a saturation absorption spectroscopy set-up is constructed in the lab. Two counter-propagating overlapping *pump* and *probe* laser beams, with 1.3 mW and 0.1 mW power respectively are crossed through a Rb cell. The high power *pump* beam saturates most of the Doppler shifted levels in the Rb vapour, leaving little absorption for the *probe* beam at resonance wavelength. As the *probe*

beam is crossing in opposite direction to the *pump* beam, this results in sharp peaks at resonance wavelength in a Doppler broadened absorption spectrum. Figure 4.1(a) shows the saturation peaks with a Doppler background spectrum of ^{87}Rb and ^{85}Rb isotopes. The corresponding transitions are shown in figure 4.1(b). The saturation peaks are obtained by scanning the laser frequency around the resonance transition. The intensity of the peaks can be enhanced by adjusting the laser polarisation with a half-wave plate and *pump/probe* beam relative intensities.

By electronically differentiating the saturation peak signal using a Lock-In amplifier, a sharp zero crossing point at FWHM of the resonance corresponding to zero of the gradient is obtained. The feedback signal to stabilise the laser around this zero crossing is then provided to the laser controller using proportional integration (PI) controller. This locking scheme provides a stabilised frequency reference with an accuracy of < 1 MHz. This laser is then used to lock the cooling lasers by the transfer cavity lock method. The wavemeter (WS-7, from High Finesse) used in our lab is also regularly calibrated with the ^{87}Rb D_2 hyperfine transition.

4.3.2 Transfer cavity lock

There are two separate Fabry-Perot confocal cavities being used. A combined beam of stabilised 780-nm and 739-nm lasers using a polarising beam splitter is aligned into one Fabry-Perot confocal cavity and 935-nm is combined with the 780-nm in the other cavity. In order to achieve the resonant peaks, the cavity is scanned at the speed of 50 to 70 Hz by applying a ramp voltage function to the piezo at the cavity. The output beam from the cavity is then split into its constituents using a second polarising beam splitter and the intensities of two beams measured using photodiodes. The signal from the photodiodes is then read in computer controlled electronic analog to digital convertor cards (Part Number PCI-6143 S series from National Instruments).

4.3.3 Data acquisition and feedback control program

In order to provide long-term stabilisation to the lasers used in our lab, a computer-based multifunctional data acquisition system scans the laser cavities and synchronously reads the cavities' spectra of the multiple lasers, and by comparing peak positions relative to the stabilised Rb-locked 780-nm laser, the computer generates the error signal in real-time to control the long-term drift of the lasers.

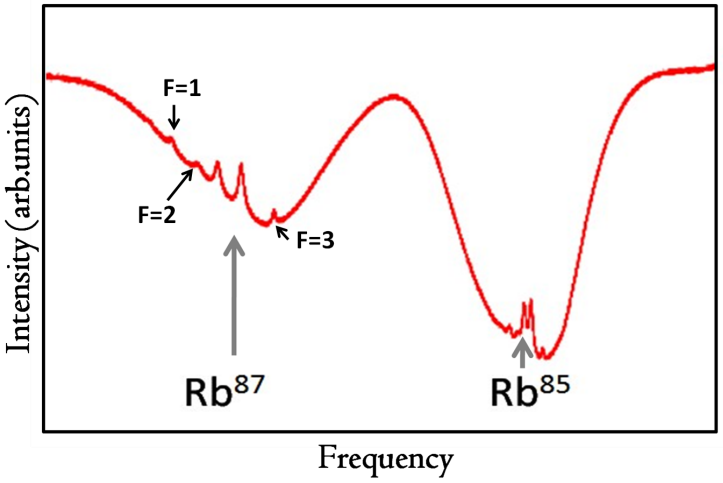

(a)

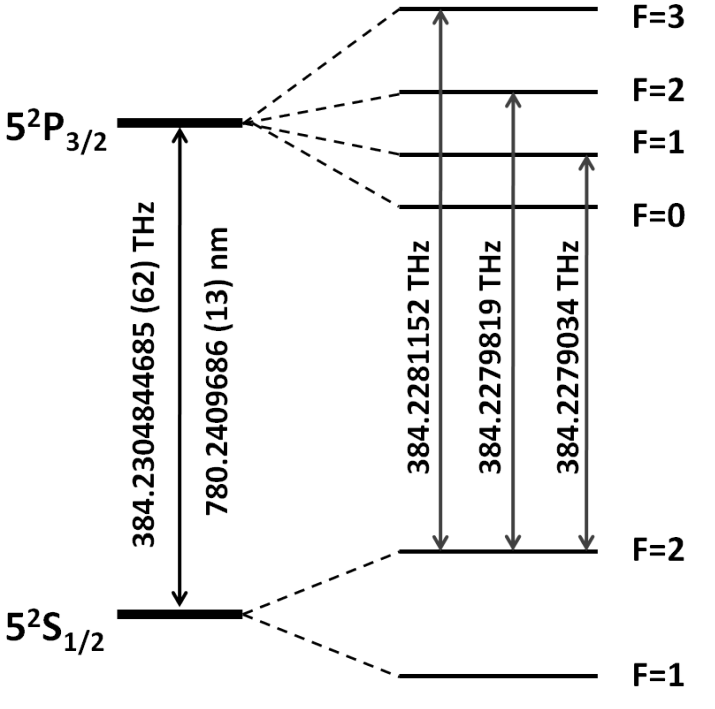

(b)

Figure 4.1: (a) The saturation absorption spectroscopy signal obtained by scanning the laser over the ^{87}Rb and ^{85}Rb. (b) Hyperfine structure of ^{87}Rb D_2 line.

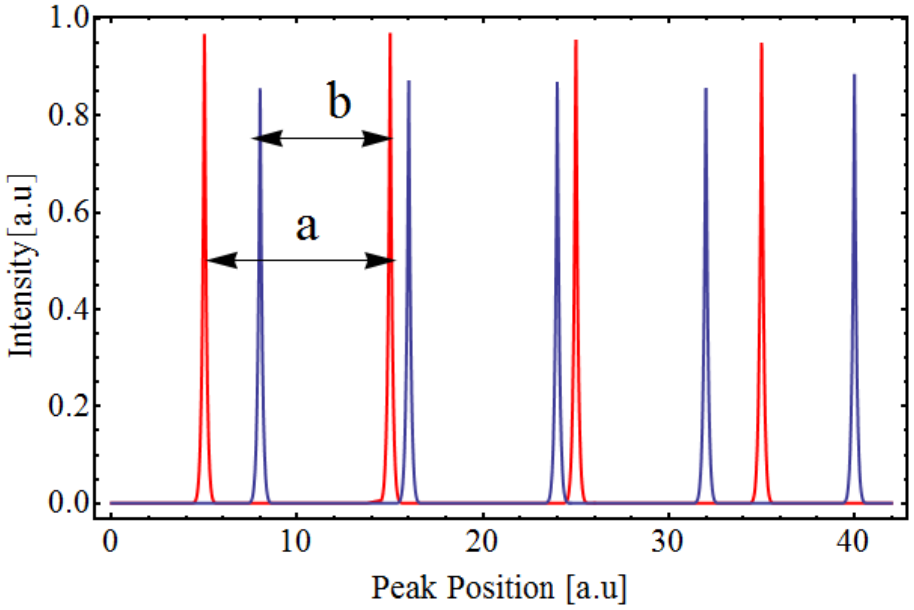

Figure 4.2: The distance between the two reference laser (780-nm) peaks is denoted as a and the separation between unstable laser (739-nm or 935-nm) peak and the reference laser peak is denoted as b. By keeping the ratio a/b constant, an error signal can be derived.

The voltage signals form the photodiodes are read through the National Instruments (NI) Data Acquisition Card (PCI-6143 S series). The computer program written in the LabVIEW Real-Time module continuously displays the spectra of the fringes for all the lasers which are sent through the cavities. The spectra fringes are obtained by scanning the lengths of the cavities with PZT. After each scan, the program calculates the fringe position of the reference laser (Rb-locked 780-nm Laser) and the other lasers and then corrects the drift in the laser frequencies by adjusting the voltages that are sent to the controller of the grating of the lasers. The error signals are generated by keeping the ratio of the positions of the spectra peaks of the lasers a/b constant. The position of the peaks are illustrated in figure 4.2. The error signal is then translated into a voltage signal and generated at the analog output card (NI PCI-6722) for feedback to the laser controllers. The laser locking program written in LabVIEW is illustrated in the block diagram shown in figure 4.3. To ensure the deterministic behaviour, the computer program is implemented on the *Real-Time Operating System* (RTOS) provided by National Instruments. The key difference between RTOS and general-computing operating systems (such as Windows, Linux, Unix etc) is the *deterministic* timing behaviour in RTOS. *Deterministic* timing means that the operating system consumes only known and expected amounts of time. The RTOS operates in a controlled environment in which computer memory and processing power are limited. The RTOS controls the execution of application software tasks and

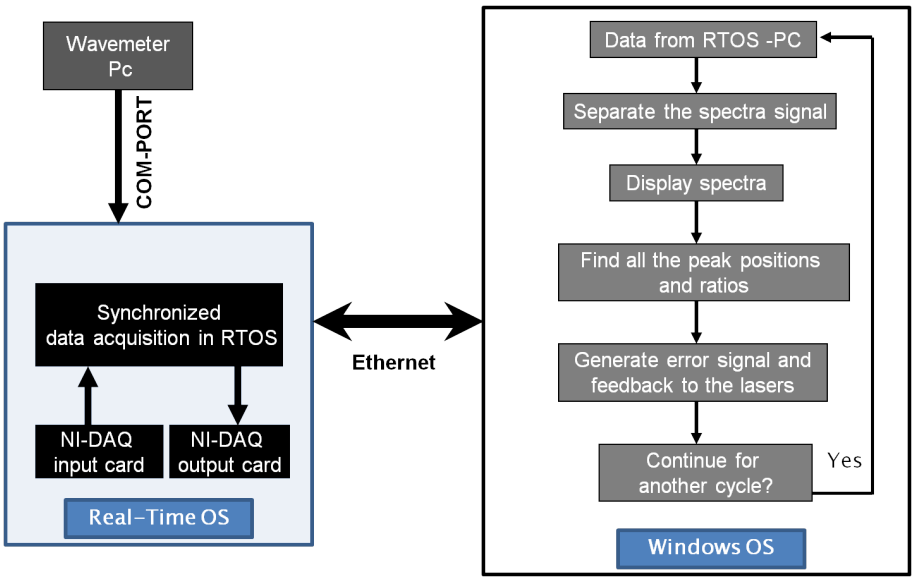

Figure 4.3: The block diagram of the real-time laser locking program, which controls the cavity scan, data acquisition and lasers

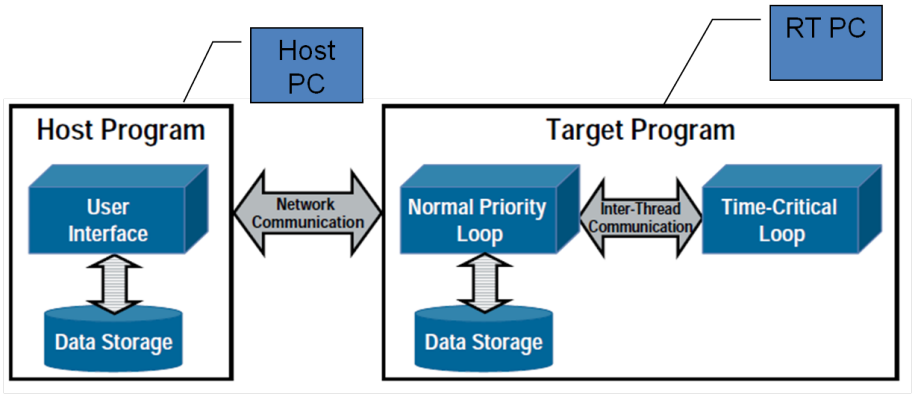

Figure 4.4: The block diagram shows working scheme of the RTOS and the communication link between the RTOS-target pc and host pc.(Taken from NI-tutorials)

provides their services within a strict time window to their users by running the tasks in a very timely and responsive way. The RTOS typically does not interface with the outside world through familiar personal computer interface devices such as a mouse, keyboard, monitor etc, but they interface through unusual interfaces such as sensors, actuators and specialised communication links. The NI-RTOS installed computer (target) used in our lab communicates with the personal computer (host) via ethernet network. The locking program runs on the target pc and its display and controls are monitored by using the host pc which runs on a Windows operation system. The communication and working of the RTOS is illustrated in the block diagram shown in figure 4.4. The details of the labVIEW program to control the locking-scheme are given in appendix C.

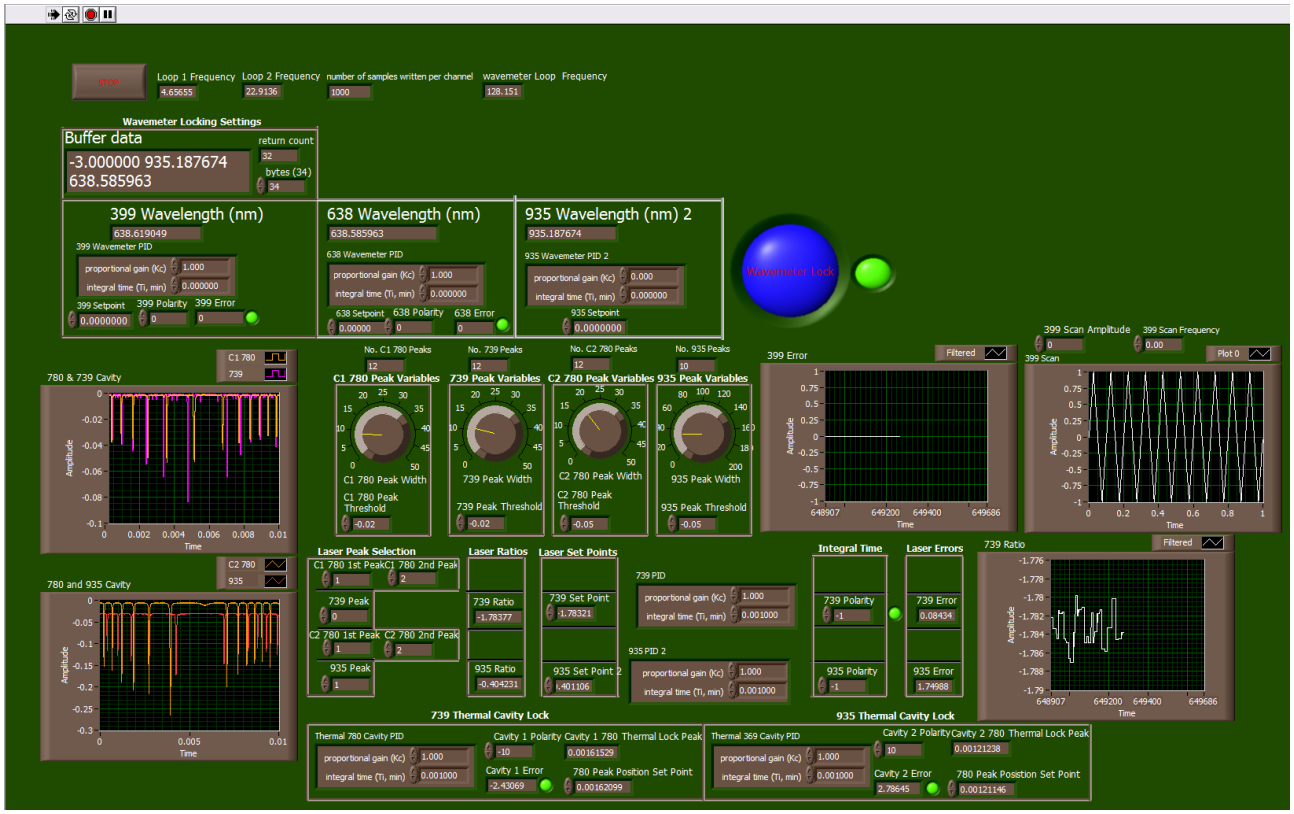

Figure 4.5: Front panel of the real-time laser locking program. User friendly controls are given to control the frequencies of the lasers.

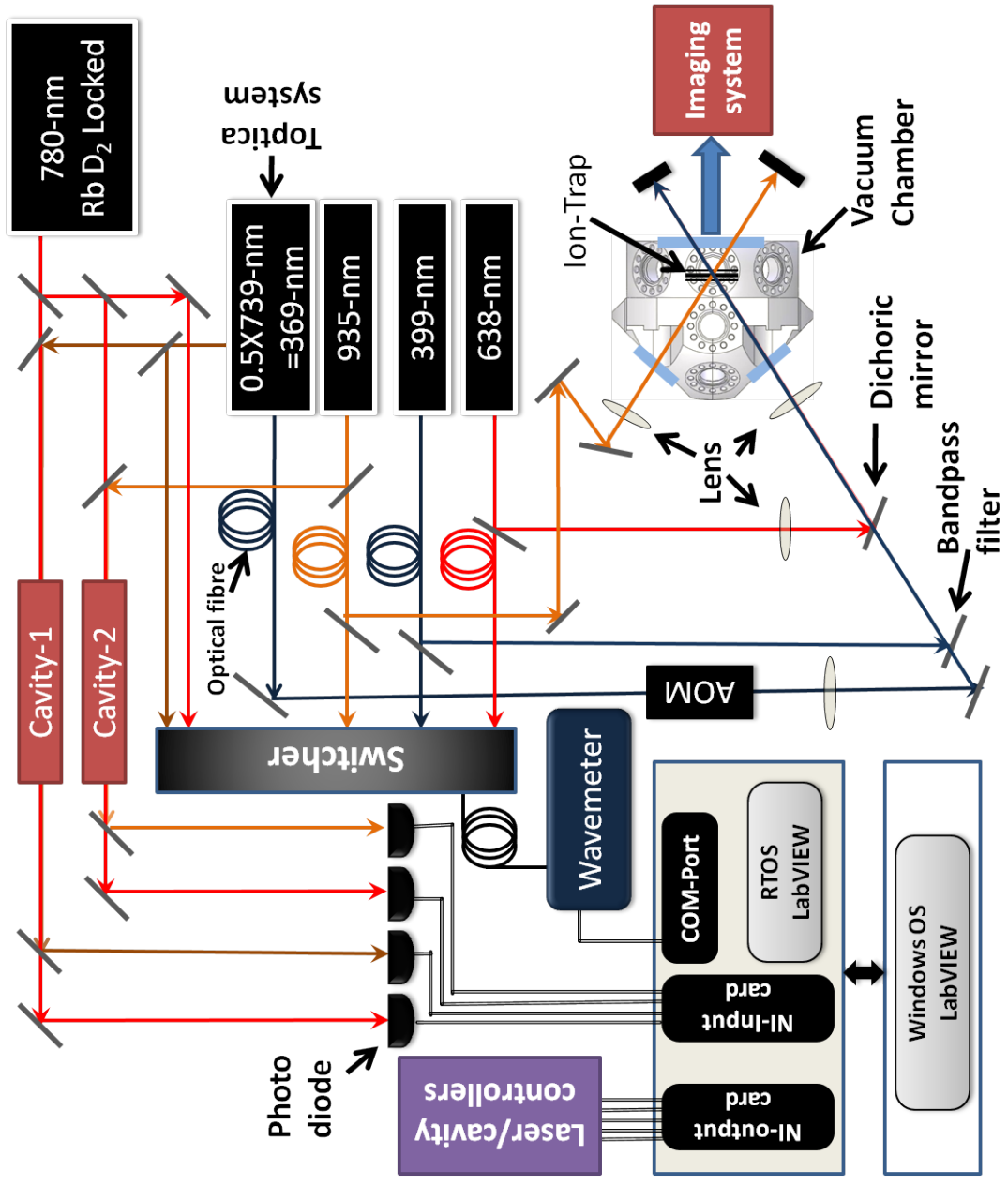

Figure 4.6: Laser locking-scheme and alignment into the trap. The computer control program, written in labVIEW real-time module, simultaneously scans the cavities and generates error signal to control the drift in the laser frequencies.

4.3.4 Wavemeter lock

The absolute error on the wavemeter used in the lab is specified as ±60 MHz and its relative uncertainty is ±10 MHz. Therefore, the wavemeter can also be used to lock those lasers where this level of accuracy is acceptable. Hence, the 399-nm ionisation laser and 638-nm re-pumping laser are locked directly to the wavemeter. To achieve this, a labVIEW program running on the wavemeter computer sends the frequency/wavelength values of the lasers which has to be locked, to the RTOS computer, via the COM-Ports of both computers. The labVIEW program's front panel shown in figure 4.5 provides control boxes where the required wavelength can be typed in and the program computes an error signal by comparing both the required and measured values. The calculated feedback is then sent to the laser controller via the output card (PCI-6722).

Laser alignment

All the frequency stabilised lasers are then carefully aligned into the trap so that they should not hit trap electrodes or any part of the chip bracket and clearly exit through the re-entrant window of the chamber. In order to increase the loading rate, the ionisation laser (399-nm) beam and the cooling laser (369-nm) beam are combined using a special bandpass filter mirror (part number: FF01-370136 from Semrock) which only transmits light at 369-nm wavelength and reflects all other wavelengths. Then the re-pump laser at 638-nm is combined with the cooling and ionisation beam using a dichoric mirror which transmits the light at 399-nm and 369-nm and reflects light at longer wavelengths. All three lasers are then aligned and focused into the trap centre and exit from the re-entrant window of the vacuum chamber. The 935-nm laser is aligned into the trap through another window of the vacuum chamber. The laser alignment and locking scheme is illustrated in figure 4.6.

4.4 Dark states destabilisation

Under certain conditions a laser driven atom can be pumped optically into a *dark state*, in which the atom cannot fluoresce because its coupling to every exited state vanishes. In this condition, the atom can not be cooled any further. To avoid this situation, dark states can be destabilised by a number of ways suggested by Berkland and Boshier [67].

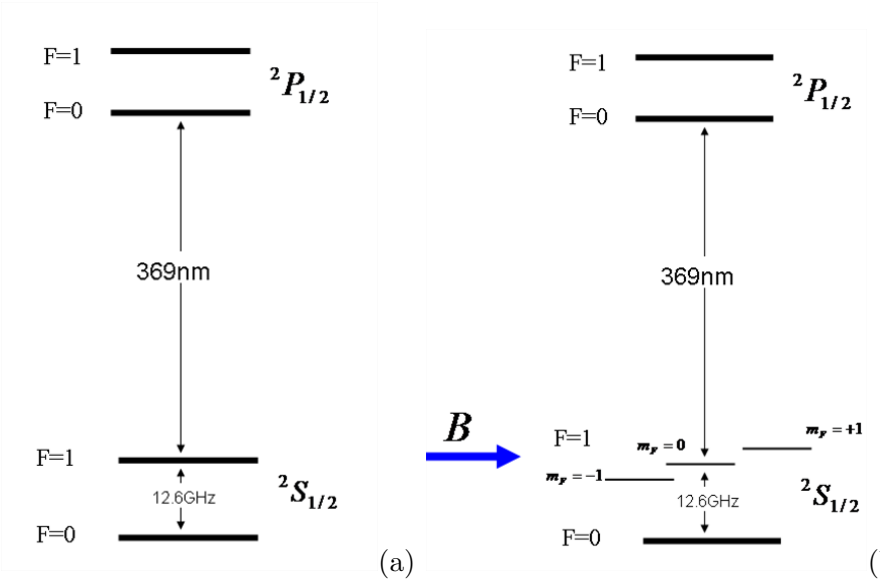

Figure 4.7: (a) Zeeman degenerate states in $^2S_{1/2} \leftrightarrow ^2 P_{1/2}$ of $^{171}Yb^+$ (b) splitting of the degenerate states after applying a magnetic field **B**.

One way is to apply an external magnetic field **B** [68] on the trapped atom as shown in figure 4.7. The required amount of **B**-field can be expressed in terms of the Zeeman shift frequency as [67]

$$\delta_B = \mu_B B/\hbar \tag{4.1}$$

where, μ_B is the Bohr Magneton, δ_B is Zeeman shift frequency.

It can be concluded from the discussion given in [67], that the magnetic field should be chosen so that $0.01\gamma < \delta_B < 0.1\gamma$ where the intensity of cooling laser is set to drive the cooling transition as hard as possible without power broadening it (which can be achieved when $\Omega \sim \gamma/3$) and the cooling laser is linearly polarised perpendicular to the magnetic field. In case of $^{171}Yb^+$ $^2S_{1/2} \leftrightarrow ^2P_{1/2}$ transition, the line width of the transition is equal to 2π 19.6 MHz then the lower limit and upper limit of the required magnetic field **B** to destabilise dark states in Yb^+ then can be estimated to be 0.014 mT and 0.14 mT respectively. The evolution rate of the dark state also depends upon the laser intensity and polarisation [69]. If the laser intensity is chosen to saturate the transition ($\Omega_{rms} >> \gamma$), then the magnetic field **B** should be adjusted so that $\delta_B = \Omega_{rms}/4$ [67], where Ω_{rms} is root mean square Rabi frequency for the particular transition.

The required magnetic field in our experimental setup is provided by using Helmholtz coils, as the amount of magnetic field can be controlled by controlling the amount of current passing through them. The coils were calibrated for magnetic field at given amount of

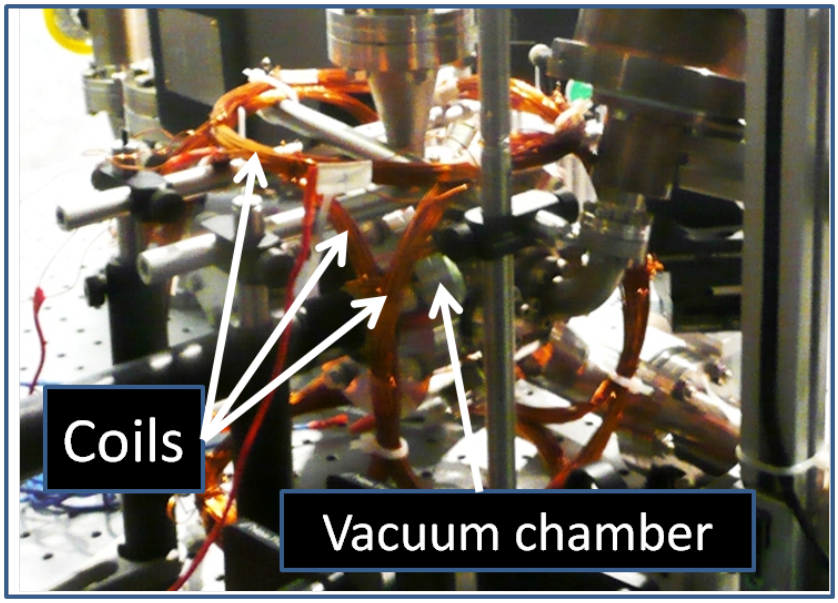

Figure 4.8: Three magnetic coils are suspended around the chamber to provide the required magnetic field at the trap centre.

current.

Helmholtz coils

Helmholtz coils are a parallel pair of two similar circular coils wound in series such that the electric current passes in the same direction in each coil. If the coils are separated one radius (of coil) apart, then the magnetic field **B** can be calculated by

$$B = 2 \times \frac{\mu_o N I R^2}{\left(R^2 + x^2\right)^{3/2}} \tag{4.2}$$

where, μ_o is the permeability of free space, I is the current, R is the radius of the coil, x is the coil separation, N is the number of turns per coil. Considering the size of our vacuum chamber, Helmholtz coils of diameter ≈17 cm with $N = 80$ are built. The distance x between the coils is set to be 12 cm, considering the trapped ion's position at the centre of the chamber. By running a stable current of 2.5 A through the coils, a magnetic field of about 0.8 mT can be generated at the trap centre. The magnetic coils are placed around the chamber as shown in figure 4.8

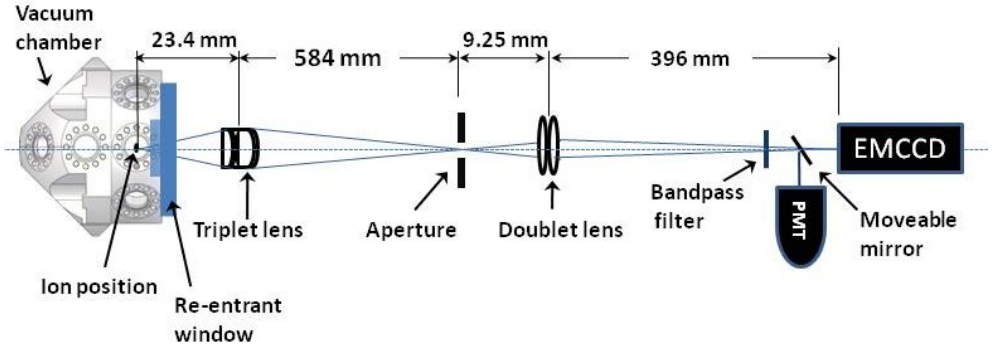

Figure 4.9: Imaging system consists of a triplet (object lens) and doublet lens. Detection system consists an EMCCD camera and PMT

4.5 Imaging system

The imaging of the ion within the trap is performed by detecting the fluorescence from the trapped ion caused by the excitation of its $^2S_{1/2}(F = 1) \leftrightarrow ^2P_{1/2}(F = 0)$ transition with a 369-nm laser. The imaging system used to detect the ion consists of an electron multiplied charge couple device (EMCCD) camera (Part Number: DU-885K-CS0-VP from Andor) and a photomultiplier tube (PMT) (part Number: H8259-01 from Hamamatsu). The EMCCD camera detects the position of the trapped ions and is able to resolve the location of more than one trapped ion, while the PMT collects the ion fluorescence. Furthermore, an optical setup is required to collect and transfer the fluorescence light with minimum loss to the EMCCD and PMT. For this purpose an optical setup consisting of triplet and doublet lenses, as shown in figure 4.9, is built in our lab. In order to have a diffraction limited image in which 85% of the emitted fluorescence is in the central spot of the diffraction pattern, OSLO (Optics Software for Layout and Optimisation) simulations for the optical setup show that for a given thickness of the viewport, the distance between the ion and the objective lens needs to be $\approx$ 23.4 mm. The objective lens is a triplet from Special Optics (part number:54-17-29-369) and anti reflection coated for 369 nm wavelength with a focal length of 30 mm. To block the scattering light from the trap electrodes, a pin hole aperture is placed at $\approx$ 58.4 cm away from the triplet lens. At $\approx$ 9.25 cm away from the pin-hole aperture, a doublet lens is then used to focus the image on the EMCCD or PMT. The distance between the doublet lens and the camera or the PMT is $\approx$ 39.6 cm. Using the OSLO simulations, it is calculated that the optical setup provides an overall magnification of $\approx$ 100 with a resolution of 1.5 μm, which is sufficient to distinguish between the two ions separated by 5 μm in a trap of 1 MHz secular frequency. A moveable

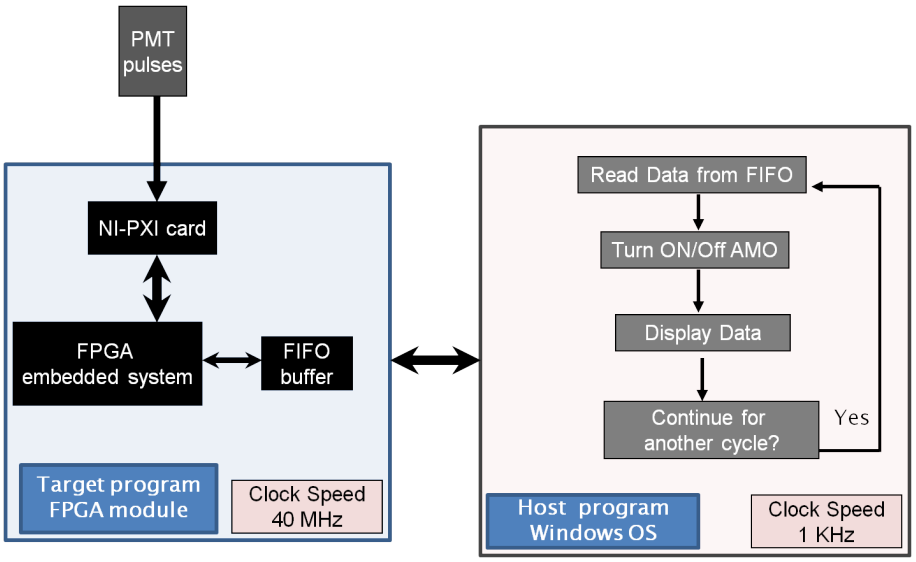

Figure 4.10: The block diagram shows the data flow from FPGA to Host PC.

mirror (part number: 8892-M from NewFocus) is used to switch between the camera and the PMT for detection. To reduce the sensitivity of the EMCCD and the PMT to the scattered light from the trap electrodes at 638 nm, 935 nm and 399 nm, a bandpass filter (part number: FF01-370136 from Semrock) is placed in front of the movable mirror to block all other wavelengths except 369-nm light where its transmission is above 94% and cut-off wavelengths are 347 nm and 393-nm where transmission drops to below 0.008%. By using this filter, the dark count rate of the PMT is about 80 s^{-1} and the background count rate when the ion is in a *dark state* and the cooling laser is incident on the ion, can be up to 3000 s^{-1}. This can be explained as a background noise caused by scattering of the 369-nm light from trap electrode. The over all detection efficiency of the imaging system is ≈ 0.1.

4.5.1 Data acquisition

Both EMCCD camera and the PMT detect ion fluorescence. It depends upon nature of the experiment, which one is better to use. In order to detect trapped ions and perform measurement experiments and gate operation on the ions, it is important to set up a fast, reliable and deterministic data acquisition system for the imaging system.

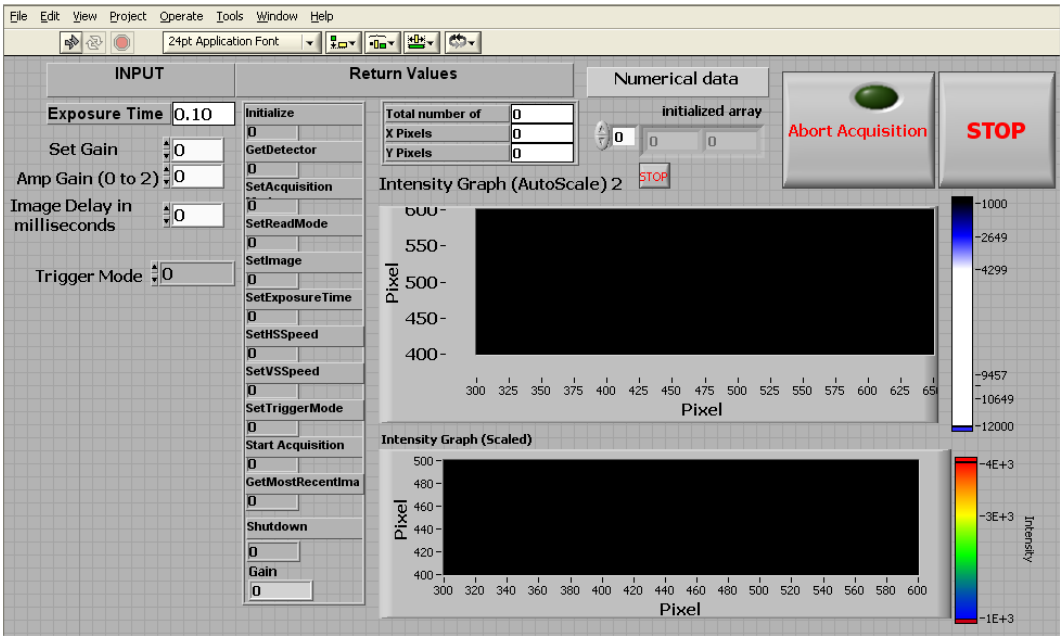

Figure 4.11: User interface for the LabVIEW program which controls the EMCCD camera and save the image data when it is required.

EMCCD camera

The EMCCD comes with its own software which runs on a windows-based computer. It works very well for overall detection purpose, but this software cannot be synchronised with rest of the experimental system. This can be done by using the software's support for LabVIEW program. By installing its LabVIEW drivers, the data can be accessed through dynamic link libraries (dll) using a LabVIEW program. In this way, the LabVIEW program provides more deterministic control over the data flow of the EMCCD and the control over EMCCD can be synchronised. The screen shot of the LabVIEW program is shown in figure 4.11. The details of the labVIEW program to control the EMCCD data are given in Appendix D.

PMT

In the PMT setup, the width of the signal pulse is about 20 ns, and hence, the photon counting signal from it at this resolution needs to be read into a special electronic card and software setup. To read the signal from the PMT, a PXI-compact system consists of National Instruments (NI) PCI express, PXI-7842R card with a 40 MHz clock speed for its digital input and output channels, installed on a chassis NI-RIO PXI-1033 (from National

Instruments) is selected. The RIO system has 2 Mega Byte on-board memory. This kind of data card needs to be programmed in a field-programmable gate array (FPGA). The PMT counting program is composed of *target* and *host* programs. The *target* program written in a LabVIEW FPGA module runs on the FPGA, the target PXI compact system, and communicates the data using an onboard memory buffer to the *host* program running on a windows based computer where the data can be displayed and stored. The block diagram shown in figure 4.10 illustrates the data flow from the FPGA to the host PC. The program also controls the acousto-optic modulator (AOM) (part number: 1212-2-949 from Isomet), which is used to turn on and off the incidence of the laser light on the trapped ion. Screen shots of the LabVIEW program are shown in figure 4.12. The details of the labVIEW program to control the PMT data are given in Appendix E.

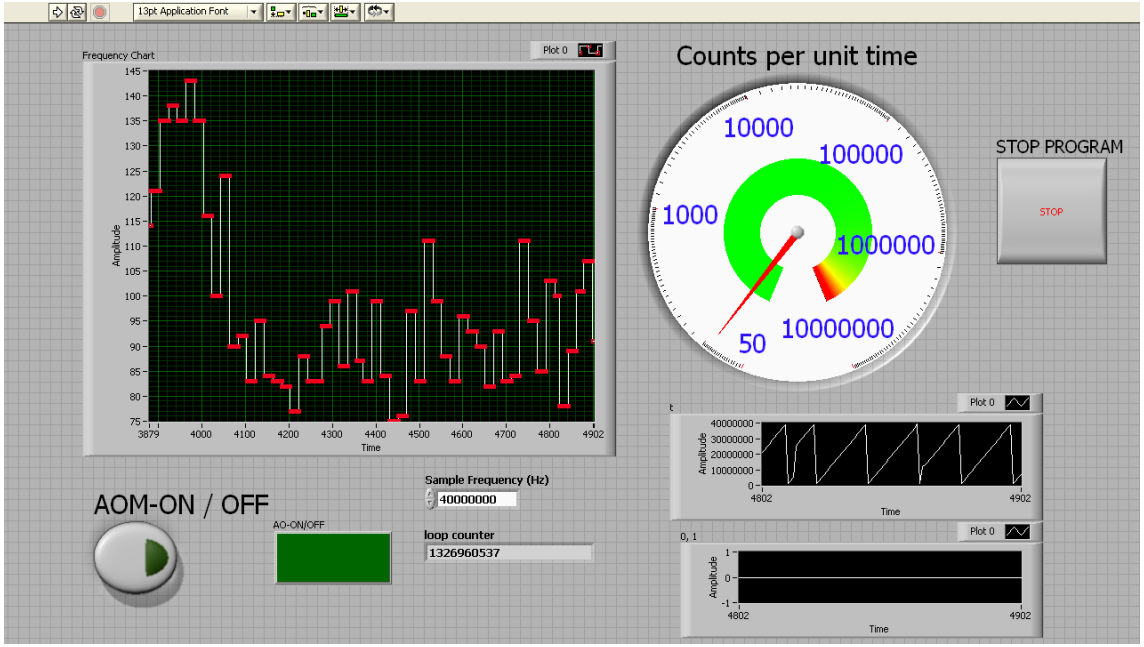

Figure 4.12: User interface for the LabVIEW program which counts the number of photons detected at the PMT. This program offers the user a convenient control on the AOM to turn the laser light on/off on the ion and set the variable time-scale at which data can be taken from the PMT.

4.6 The resonator

Paul traps usually require a large rf voltage (100 V to 1000 V). The larger the rf voltage applied to the trap, the higher the trap depth will be, for a certain secular frequency. The high frequency rf voltage cannot be supplied directly to the trap as the impedance causes severe power reflection due to the mismatching of the impedance. To avoid this situation, the rf voltage on the trap can be applied using a helical resonator. The rf resonator device is used to match the impedance between the trap and the power source and also isolates the trap from high rf voltage sources. A helical resonator can be constructed with a coil enclosed in a conductive shield. The length of the coil needs to be $\approx \lambda/4$, hence this device is called a helical quarter wave resonator. The schematics of the resonator is shown in figure 4.13.

The resonator supplies high rf voltage to the trap with very low current by transforming the applied rf power. The peak rf voltage V_p on the trap is related to the input power P in the resonator by the quality factor Q of the resonator

$$V_p = \kappa\sqrt{2PQ} \tag{4.3}$$

where, κ depends on the exact geometry of the resonator with its value ranging from ≈ 10 to 30 and Q is the quality-factor of the resonator and can be described as

$$Q = 2\pi \frac{\text{Energy stored}}{\text{Energy lost}} \text{per Cycle} \tag{4.4}$$

In order to measure the Q of the resonator, which is the ratio of resonance frequency f_o to the band width Δf, the frequency of the oscillator has to be tuned to the resonant frequency f_o and then the off-resonant amplitude of the back-reflected signal V_{max} is measured. The frequency above the resonance at which the amplitude is $V_{max}/\sqrt{2}$ is denoted as f_{H}. In the same way the frequency below the resonance when the amplitude is $V_{max}/\sqrt{2}$ is denoted as f_{L}. By measuring the f_H and f_{L}, the Q of the resonator can then be worked out by

$$Q = \frac{f_o}{\Delta f} = \frac{f_o}{f_{\mathrm{H}} - f_{\mathrm{L}}} \tag{4.5}$$

In order to avoid heating of the trap electrodes, it is necessary to raise the Q of the resonator to deliver the maximum rf voltage on the trap at a minimal input rf power.

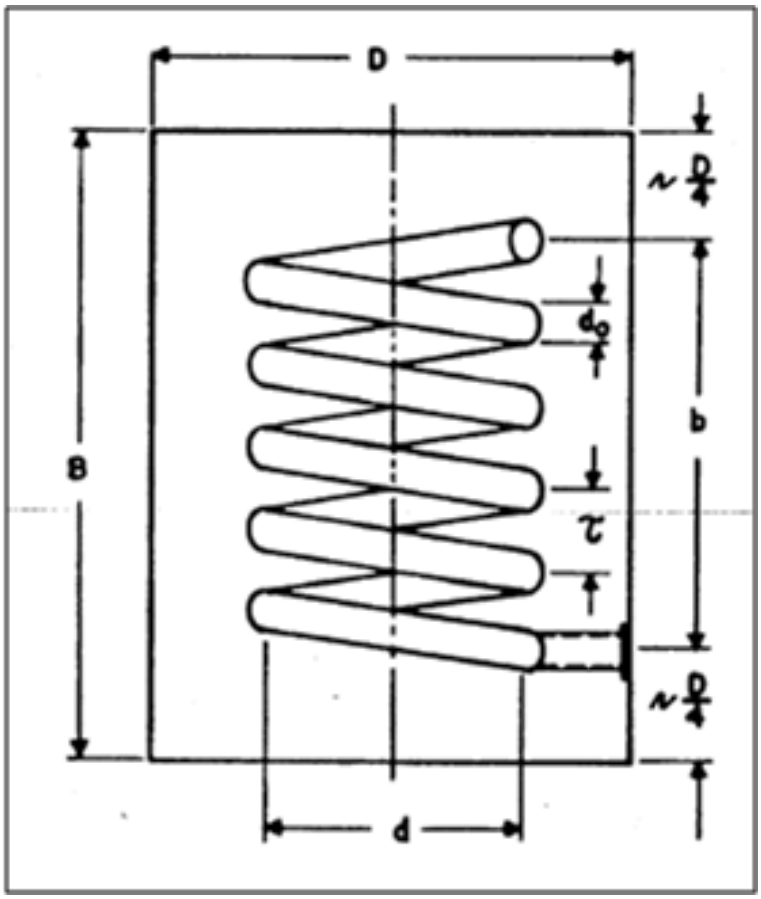

Figure 4.13: The schematic of a helical resonator. The figure is taken from [70].

The design and construction of the resonator used in the lab is discussed in [71]. The resonator is made of a copper tube of diameter D, an antenna and a coil made of a copper wire of diameter d and length b. The Q of the resonator depends upon its geometric parameters including number of turns and winding pitch of the coil. The resonator used in our lab is shown in figure 4.14. The resonator specification are following;

- Shield Diameter, $D = 76\pm1$ mm
- Shield length, $B = 103\pm1$ mm
- Coil Diameter, $d = 52\pm3$ mm
- Coil Length, $b = 63\pm5$ mm
- Coil diameter, $d_o = 3.14\pm0.03$ mm
- Winding pitch, $\tau = 6\pm2$ mm
- Number of turns, $N = 9.50\pm0.25$)
- Resonant frequency with trap load, $f_o = 21.5\pm0.1$ MHz
- Q with trap load, $Q \approx 477\pm28$

The resonator is designed to operate at frequency of ≈21.5 MHz with a capacitive load of ≈ 15 pF. Initially, the rf voltage/signal with a frequency of ≈ 20 MHz is generated using a HP 8640B function generator. This rf voltage is then amplified with a high power (30 W) rf amplifier (part number: NP-541 from MiniCircuits) and supplied to the trap using the rf resonator.

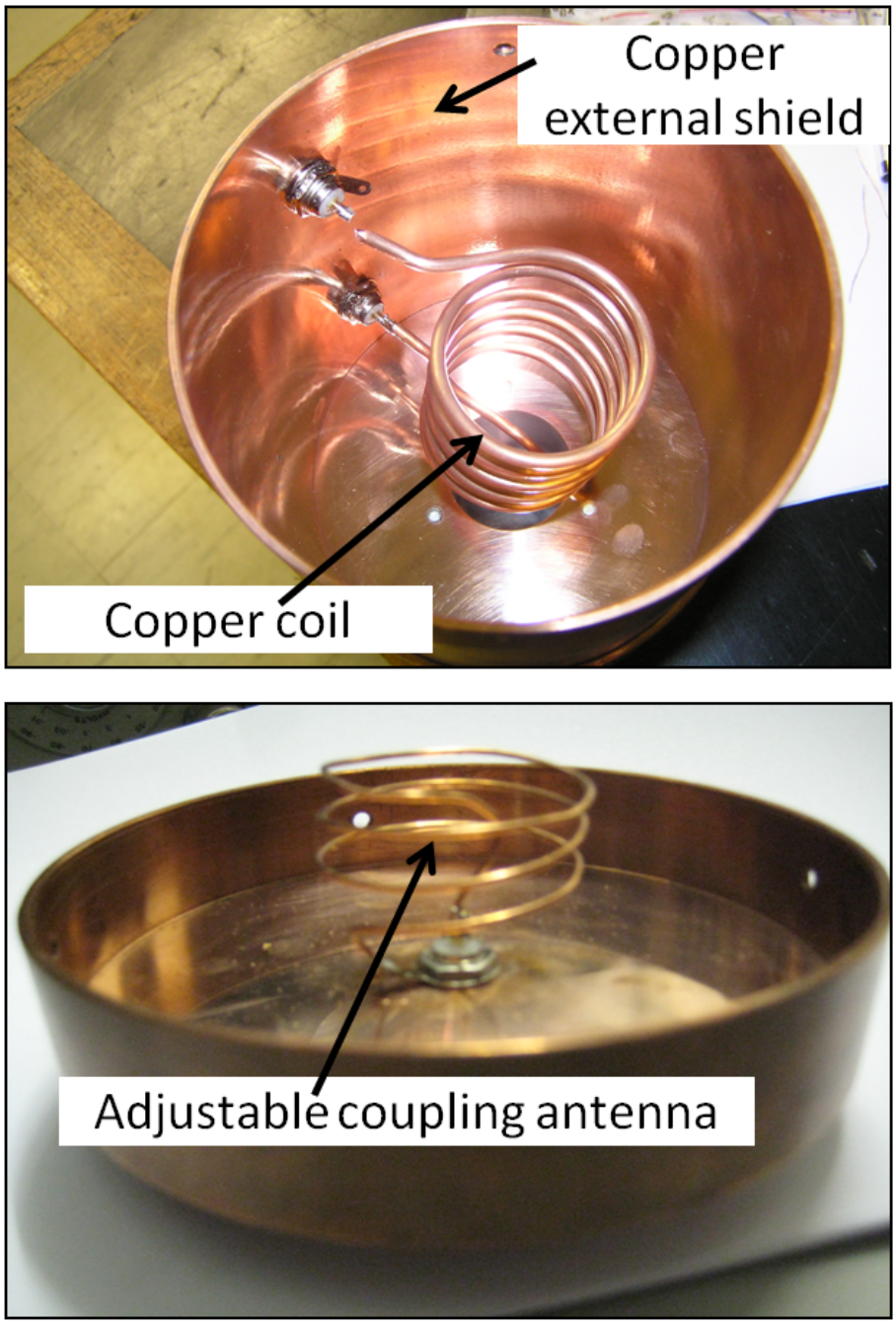

Figure 4.14: Picture shows the resonator built in our lab. (The pictures are provided by James Siverns.)

Chapter 5

Yb^+ Trap Experiment

5.1 Introduction

In order to develop scalable quantum computing chips and trap ions, it is necessary to understand the working principles and characterisation of the experiment. It is more essential when the first trap experiment is going to be performed in the lab because for the first ion trap, a large parameter space including cooling laser wavelengths, optical alignment, ion imaging and stable trap voltages are needed to be covered. Once these parameters are known, further development in the trap experiments and trap designs can be made easily. Currently, several ions are being investigated for quantum technology including Ba^+ [72], Be^+ [73], Ca^+ [74–77], Cd^+ [78], Mg^+ [10], Sr^+ [27, 79], and Yb^+ [54, 80–82]. The heavier element, ^{171}Yb, is an attractive choice for quantum information processing and for frequency standards due to its easily accessible hyperfine transition levels with off the shelf available laser diodes. [83–85].

To investigate the Yb^+-trap parameters, a simple two layer macroscopic ion trap compatible with the chip carrier mounting is designed and fabricated in our lab. The trap is modelled to provide high ion secular frequencies in all three dimensions, so that it can be used for ground-state cooling experiments [86].

In the trap experiment described in this chapter, the ion trap is characterised for its operations including ion-life, electric field noise caused by electric field fluctuations (from thermal electric Johnson-Nyquist noise) and fluctuating patch potentials on electrodes inducing motional heating of trapped ions [28, 28, 31, 34]. The motional heating rate is also measured within our ion trap using a technique where the laser cooling beam is turned off for

a certain time and ion fluorescence is monitored when the laser is turned on again [52,87]. Further, absolute frequencies for the $^2S_{1/2} \leftrightarrow {}^2P_{1/2}$ transition and the $^2D_{3/2} \leftrightarrow {}^3D[3/2]_{1/2}$ for the stable Yb isotopes ($^{170}Yb^+$, $^{171}Yb^+$, $^{172}Yb^+$, $^{174}Yb^+$ and $^{176}Yb^+$) are measured more precisely than the previously published work [88].

5.2 Blade trap

The used macroscopic trap is modelled and simulated using Charge Particle Optics (CPO) software. The electrode structure of the trap has a blade like configuration, hence, here named as blade trap. Two rf electrodes are positioned diagonally opposite spanning the entire axial length of the trap, providing confinement in the radial direction. The static voltage electrodes are segmented to provide endcap potential for confinement in the axial direction, while the central segmented electrodes can be used to rotate the principal axes. The design of the trap is shown in figure 5.1. The electrodes are separated by 343(14) μm in the x-axis and 554(14) μm in the y-axis, producing a trap aspect ratio of 1.6, and an ion-electrode separation of 310(10) μm. The length of the central control electrode is 1008(14) μm and the laser access is parallel to the x-axis. To ensure efficient laser cooling in all directions, the principal axes can be rotated by 45^o by applying a relatively small voltage of up to 1 V on the central electrodes. Upto 1 MHz of secular frequency in z-direction can be achieved by applying approximately 80 V on the four endcap electrodes. High voltages on endcap electrodes can shift the position of the ion from the *rf node*. Therefore, the ion experiences micromotion if it is not located at the *rf node*. To compensate the static potential offset, three parallel compensation electrodes (wires) 1-3 shown in figure 5.1 run through the length of the trap. These compensation electrodes are placed behind the rf electrodes. These electrodes are heavily shielded by the blade electrodes, hence require much larger static voltages.

The electrodes shown in figure 5.2 are suspended using ceramic rods held by a metal cage of a size of 33 $\times$ 33 mm and 10 mm in height and clamped into position via grub screws and insulted by PEEK spacers. The segmented electrodes are separated by approximately 50 μm. The electrodes are shaped in a way that they hide these insulation spacers from the ion. The metal cage is then mounted on top of a PEEK base shown in figure 5.3(a) providing electrical insulation from the chip bracket pin receptacles and holds the connecting wires that connect each electrode with the corresponding pin. It is observed that, the exposure of PEEK to laser radiation increases outgassing in the UHV environment and is

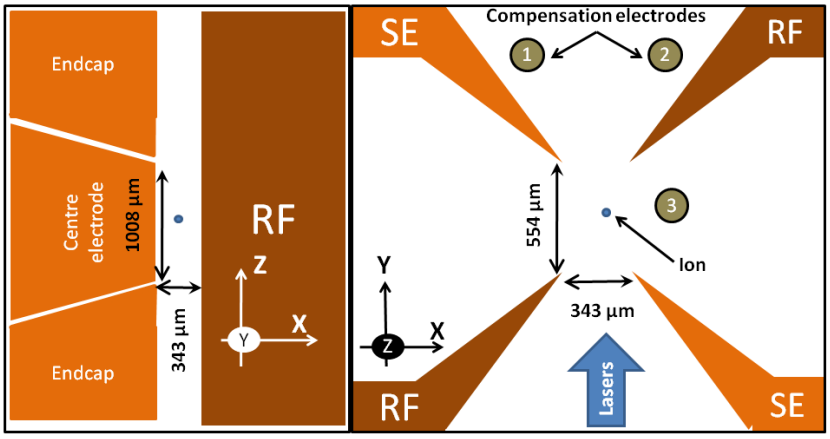

Figure 5.1: Trap electrode sizes and the numbering for voltage application.

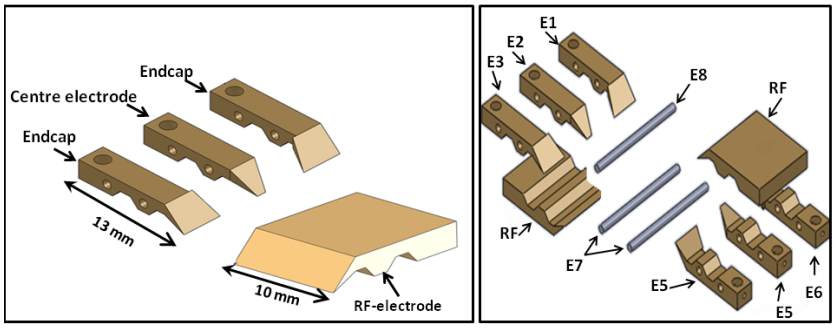

Figure 5.2: Trap electrodes.

suspected to cause its charging. Therefore, a metal-cage made of stainless steel shown in figure 5.3(b) is used to cover the PEEK base from direct or indirect exposure of lasers, and shield the ion from any exposed dielectrics. The trap electrodes shown in 5.2 are arranged in a way that the trap provides a reduced residual RF ponderomotive potential along the z axis [51] to $< 2\%$ of the radial frequency, and allows trapping of long ion chains without significant RF micromotion in the axial direction.

The electrodes are machined from stainless steel and gold plated (5μm thick) to improve surface quality and reduce rf resistance. During the assembly of the trap under a microscope, it was noticed that the machining tolerance of the electrodes was not sufficient and caused misalignment of the electrodes. Therefore, several electrodes were re-made and use of ceramic rods for alignment purposes was abandoned. The electrodes were positioned and clamped with screws manually using the micrometre translation stages. Trap assembly was performed under a microscope to ensure accurate positioning of the electrodes. The assembled trap is shown in figure 5.4.

The trap was initially designed and assembled with the electrode-electrode distance in x-direction to be $\approx 300\mu$m and $\approx 500\mu$m in y-direction. However, after 16 days of baking of the vacuum chamber at 200^oC, slight misalignment of the electrodes was observed which was suspected due to thermal expansion. To find the new positions of the electrodes inside the vacuum chamber, the trap was imaged with EMCCD camera and imaging setup, and the distance between the electrodes in x-direction and y-direction was found to be $\approx 343\mu$m and $\approx 554\mu$m respectively, which gives an ion-electrode distance of $\approx 310\mu$m. Unfortunately, one endcap and one centre electrode were shorted with the metal base of the trap. Therefore, the trap was re-simulated in CPO with new positions of the electrodes to find the *rf node* position which is now different from the geometric centre of the trap. The re-simulated pseudopotential is shown in figure 5.5.

5.3 Trap experiment

5.3.1 Ion loading

Using the experimental arrangement (discussed in chapter 4) and the trap discussed in the previous section, single ions and ion crystals of most of the stable Yb^+ isotopes including $^{171}Yb^+$ were trapped. A photoionisation technique is used to ionise the neutral Yb atoms in the trap. In the first stage, Yb atoms are excited to its $^1P_1$ state from its ground $^1S_1$ with

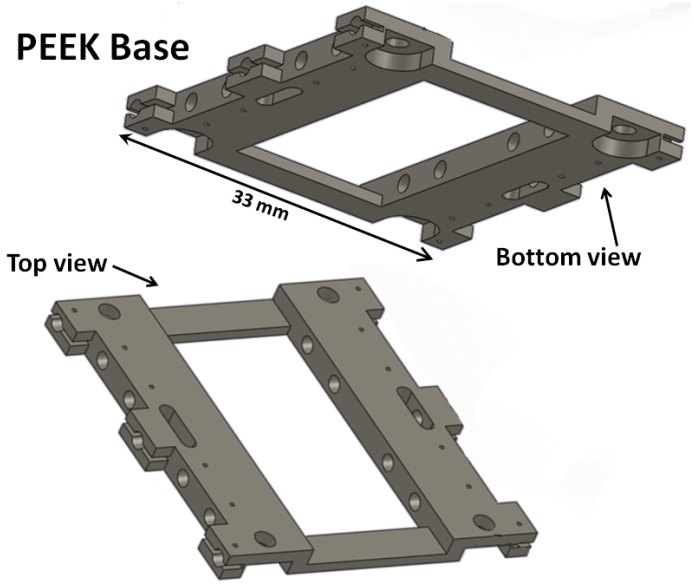

(a)

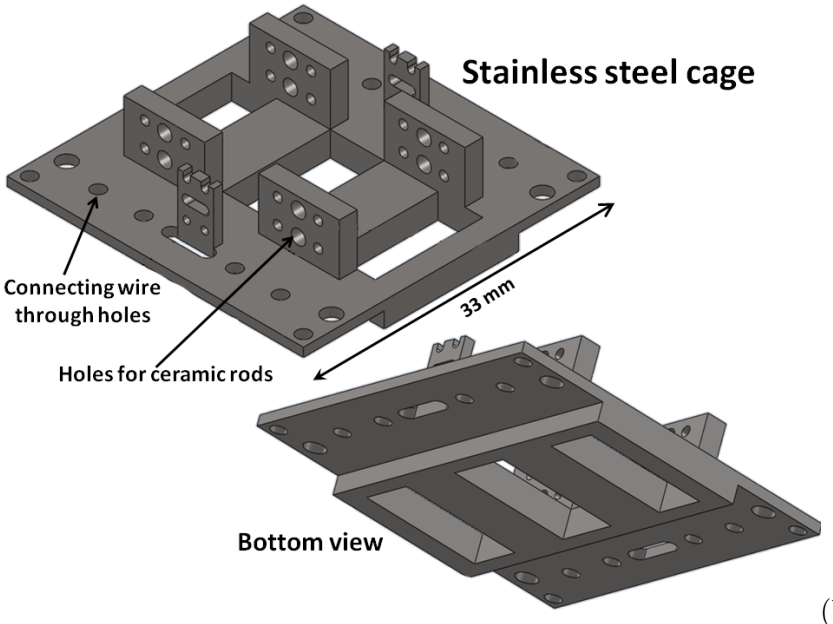

(b)

Figure 5.3: (a) Design of the PEEK base. (b) Design of the metal cage.

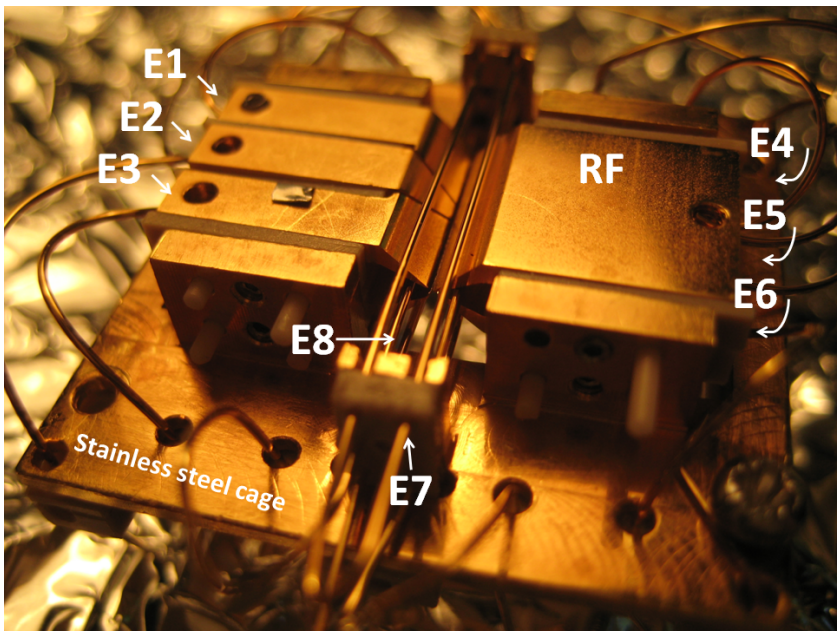

Figure 5.4: Blade trap assembly.

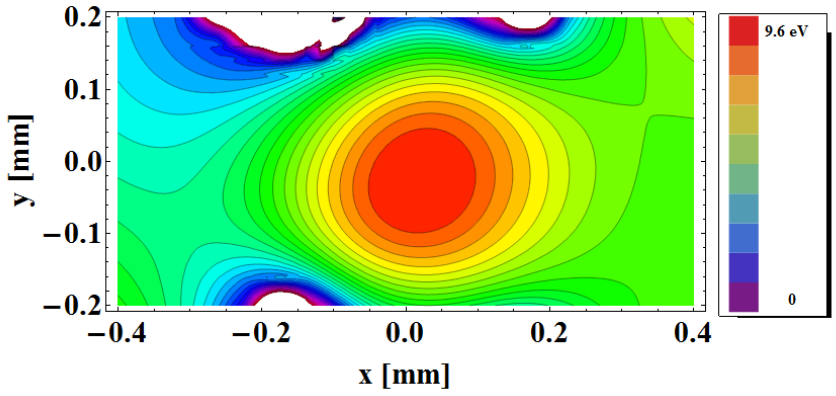

Figure 5.5: Pseudopotential created by the trap electrodes at the centre of the trap.

Yb $^1S_0 \leftrightarrow {}^1P_1$ transition wavelengths	
Isotope	wavelength [nm]
^{170}Yb	398.91051(6)
^{171}Yb	398.91070(6)
^{172}Yb	398.91083(6)
^{174}Yb	398.91114(6)
^{176}Yb	398.91144(6)

Table 5.1: The $^1S_0 \leftrightarrow {}^1P_1$ transition wavelengths apply to our setup where the neutral atomic beam and the laser beam make an angle of 63^0.

398 nm coherent light and then using the cooling laser at 369 nm, coherent light is used to reach the continuum state. The main advantage of this technique is that an ion crossing the continuum level is instantaneously cooled by the laser. The 398 nm wavelengths for the $^1S_0 \leftrightarrow {}^1P_1$ transition in Yb isotopes are found using a spot method technique discussed in chapter 6. The measured ionisation wavelengths are verified by ionising different Yb isotopes repeatedly in this experimental setup where the angle between the laser and atomic beam is approximately 63^o and were found to be consistent with the results given in chapter 6. The wavelengths used to ionise different isotopes of Yb at 63^0 are listed in table 5.1.

5.3.2 Ion trap operations

The trapped ions are then used to characterise the trap. The applied voltages on the trap electrodes are given in table 5.2, along with the corresponding trap electrode (the numbering is described in figure 5.2). The static voltages were measured at the inputs to the filter box on the vacuum system. The values are averaged out over several measurements and the errors on the voltage measurements are given by the error of the multimeter. The ion secular frequencies were measured by applying small resonant AC signal using a signal generator on one of the endcap electrodes and monitoring de-crystallisation of the ion. The error bars on the measured secular frequencies are estimated by scanning the frequency (in positive and negative directions) of the AC signal over the resonance frequencies where the ion starts to de-crystallise. The measured secular frequencies with these voltages were ω_x= 2.069±0.001 MHz, ω_y= 2.110±0.001 MHz and ω_z= 1.030±0.001 MHz. The measurements were repeated several times and averaged out. Using the measured values of the secular frequencies, the rf voltage is calculated to be 680 ± 10 (as given in table 5.2). A drive frequency of $\Omega/2\pi \approx 21.48$ MHz for the rf voltage was used in the experiment. The q-parameter for the blade trap at these values can be calculated as $q \approx 0.44$. Using the

Table 5.2: RF and static voltage on the trap electrodes. (The corresponding electrodes are shown in figure 5.2)

Electrode Voltages	
Electrode	Voltage (V)
RF	680(10)
E1	148.88(0.01)
E2	7.36(0.01)
E3	25.03(0.01)
E4	0
E5	0
E6	167.76(0.01)
E7	169.22(0.01)
E8	-2.70(0.01)

simulation, the trap depth is calculated to be $\approx 4.9 \pm 0.2$ eV.

The trapped ion crystals are shown in figure 5.6. A three ion crystal is shown in figure 5.6 (a), while in figure 5.6(c) multi-isotope crystal indicates that the trap can be used for many isotope experiments including sympathetic cooling [78]. Figure 5.6 shows a zig-zag ion crystal. The trap depth of the trap could also be measured by observing the trapped ion lifetime, which, in our trap is many hours without any laser cooling.

5.3.3 Wavelengths measurements

The exact wavelengths for the laser cooling cycle for different Yb^+ isotopes are measured by monitoring the fluorescence from a trapped ion with minimised micromotion, and measuring the wavelength on a wavemeter (High Finesse: WS7) with a specified accuracy of ± 60 MHz. By scanning the 369 nm laser's wavelength, the $^2S_{1/2} \leftrightarrow {}^2P_{1/2}$ transition resonance for Yb^+ is determined as the absolute frequency just before the fluorescence rapidly drops to background level. The drop in the ion fluorescence corresponds to the heating of the ion. In order to measure the resonant frequency of the $^2D[3/2]_{1/2} \leftrightarrow {}^2D_{3/2}$ transition, the wavelength of the laser is tuned to maximise the ion-fluorescence. To reduce the effect of power broadening, the intensity of the 369 nm and 935 nm lasers are reduced to 400 $mWcm^{-2}$ and 200 $mWcm^{-2}$ respectively. The measured wavelength for the cooling cycle of different stable isotopes of Yb^+ are given in table 5.3.

A magnetic field of 0.5 mT was applied to remove degeneracy within the hyperfine levels in $^{171}Yb^+$. Zeeman shift of 10 MHz is expected in the energy levels at this amount of magnetic field. The measured 369.5 nm cooling wavelengths for Yb^+ are in agreement

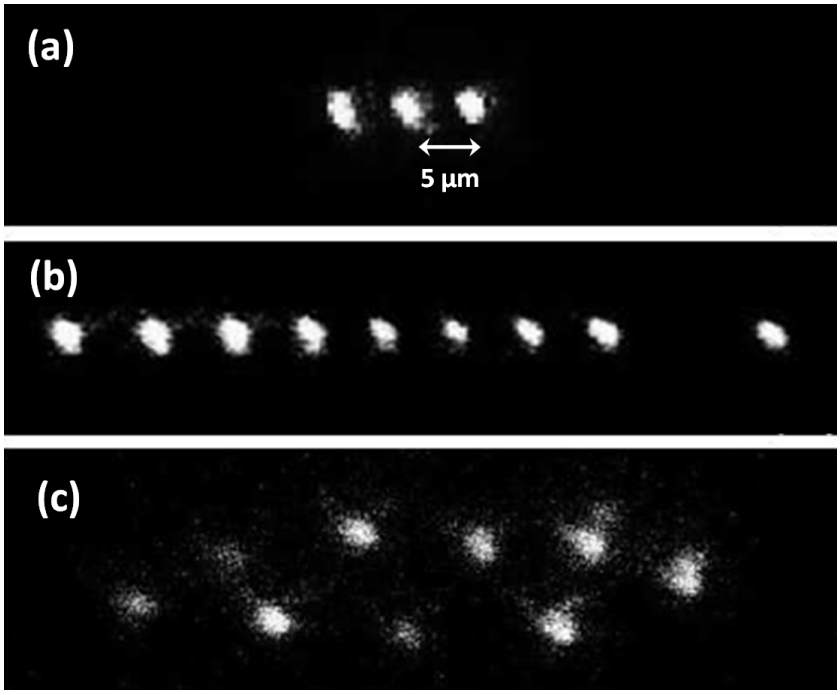

Figure 5.6: (a) Three Yb^+ ion crystal, (b) multi-isotope Yb^+ ion crystal, and (c) a zig-zag ion crystal of nine Yb^+ ions.

Yb^+ transition wavelengths		
Isotope	$^2S_{1/2} \leftrightarrow {}^2P_{1/2}$ wavelength [nm]	$^2D[3/2]_{1/2} \leftrightarrow {}^2D_{3/2}$ wavelength [nm]
$^{170}Yb^+$	369.52364(6)	935.19751(19)
$^{171}Yb^+$	369.52604(6)	935.18768(19)
$^{172}Yb^+$	369.52435(6)	935.18736(19)
$^{174}Yb^+$	369.52494(6)	935.17976(19)
$^{176}Yb^+$	369.52550(6)	935.17252(19)

Table 5.3: The cooling $^2S_{1/2} \leftrightarrow {}^2P_{1/2}$ and re-pumping $^2D[3/2]_{1/2} \leftrightarrow {}^2D_{3/2}$ transition wavelengths for different stable isotopes of Yb^+ are obtained by observing fluorescence from a trapped ion. The $^{171}Yb^+$ isotope wavelengths correspond to the $^2S_{1/2}(F=1) \leftrightarrow {}^2P_{1/2}(F=0)$ and $^2D[3/2]_{1/2}(F=1) \leftrightarrow {}^2D_{3/2}(F=1)$ transitions respectively.

however more precise than the previously published data by E. W. Streed et al. [88].

5.3.4 Error analysis

The wavelengths are measured with a commercial wavemeter (High Finesse: WS7),which is specified to have an absolute accuracy of 200 MHz below 370 nm, and 60 MHz between 370 nm to 1100 nm. The wavemeter is calibrated using a 780-nm laser which is locked to <1 MHz of the ^{87}Rb D_2 line. The calibration is confirmed using a He-Ne laser which is also calibrated to < 1 MHz. A further two point check using the frequency doubling system was performed to ensure the wavemeter specifications in the ultra violet frequency range. The 739.05 nm and 369.5 nm beams were measured simultaneously, and confirmed that the wavemeter operated within its specifications. The wavemeter was re-calibrated after the wavelength measurements and no significant drift was observed. The 369 nm wavelengths are not directly measured due to the 200 MHz error on the wavemeter for below 370 nm wavelengths, but inferred by measuring the wavelength of 739 nm beam before the doubling system. The error for 739 nm wavelength is 60 MHz. The power broadening and AC Stark shift of $^2S_{1/2} \leftrightarrow {}^2P_{1/2}$ transition caused by 369 nm laser at the applied intensity was expected to be 40 and 38 MHz respectively and the intensity of the 935 nm laser beam broadens the transition to 30 MHz and causes the AC Stark shift of 17 MHz. To avoid any Zeeman shift caused by the magnetic field, the magnetic coils were turned off during the frequency measurements of even isotopes of Yb^+ ion. The remaining magnetic field caused by Earth's magnetic field only induce a shift of ≈1 MHz. For the frequency measurements for $^{171}Yb^+$ transitions, Zeeman shifts caused by the magnetic field are considered to be negligible due to the relatively large uncertainty associated with the wavemeter. By considering all these effects, the overall uncertainty for the $^2S_{1/2} \leftrightarrow {}^2P_{1/2}$ transition wavelengths is to be ±126 MHz, while the uncertainty for $^2D_{3/2} \leftrightarrow {}^3D[3/2]_{1/2}$ transition wavelengths is to be ±70 MHz.

5.4 Heating measurements

The lifetime of a trapped ion depends upon both the heating rate and the trap depth. The ion heating rate is measured using a model proposed by J. H. Wesenberg et al. [89]. In this model, a trapped $^{174}Yb^+$ ion is allowed to heat by blocking the cooling laser 369.5 nm for periods of 1, 3, 5, and 7 seconds using an AOM (Isomet:1212-2-949, response time

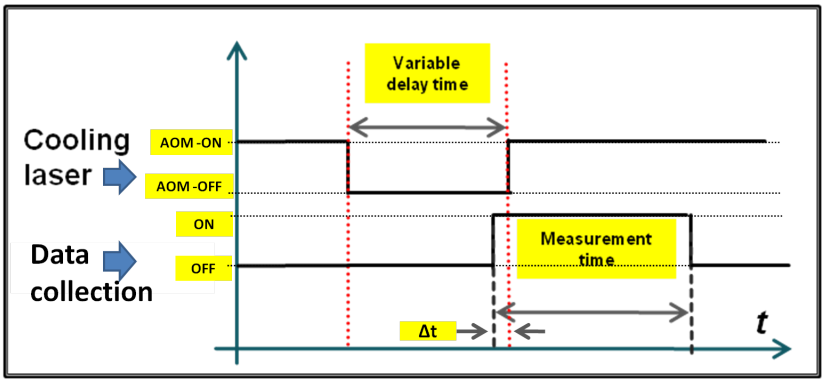

Figure 5.7: The cooling laser is turned off and on again using AOM for different time periods and simultaneously ion-fluorescence is recorded using PMT.

$\approx$ 100 ns). The cooling laser is unblocked and the fluorescence is measured in 50 μs bins for 4 ms.

The time scale of the heating measurement experiment is illustrated in figure 5.7. The experiment is computer controlled using a LabVIEW FPGA module implemented on an NI-CompactRIO and an NI-PXI-7842R card, as the experiment requires the recording of the ion fluorescence at a time scale of 25 ns, and the turning on and off of the AOM at a time scale of milli seconds. A screen shot of the FPGA LabVIEW program interface is shown in figure 5.8. The details of this program are given in the Appendix F.

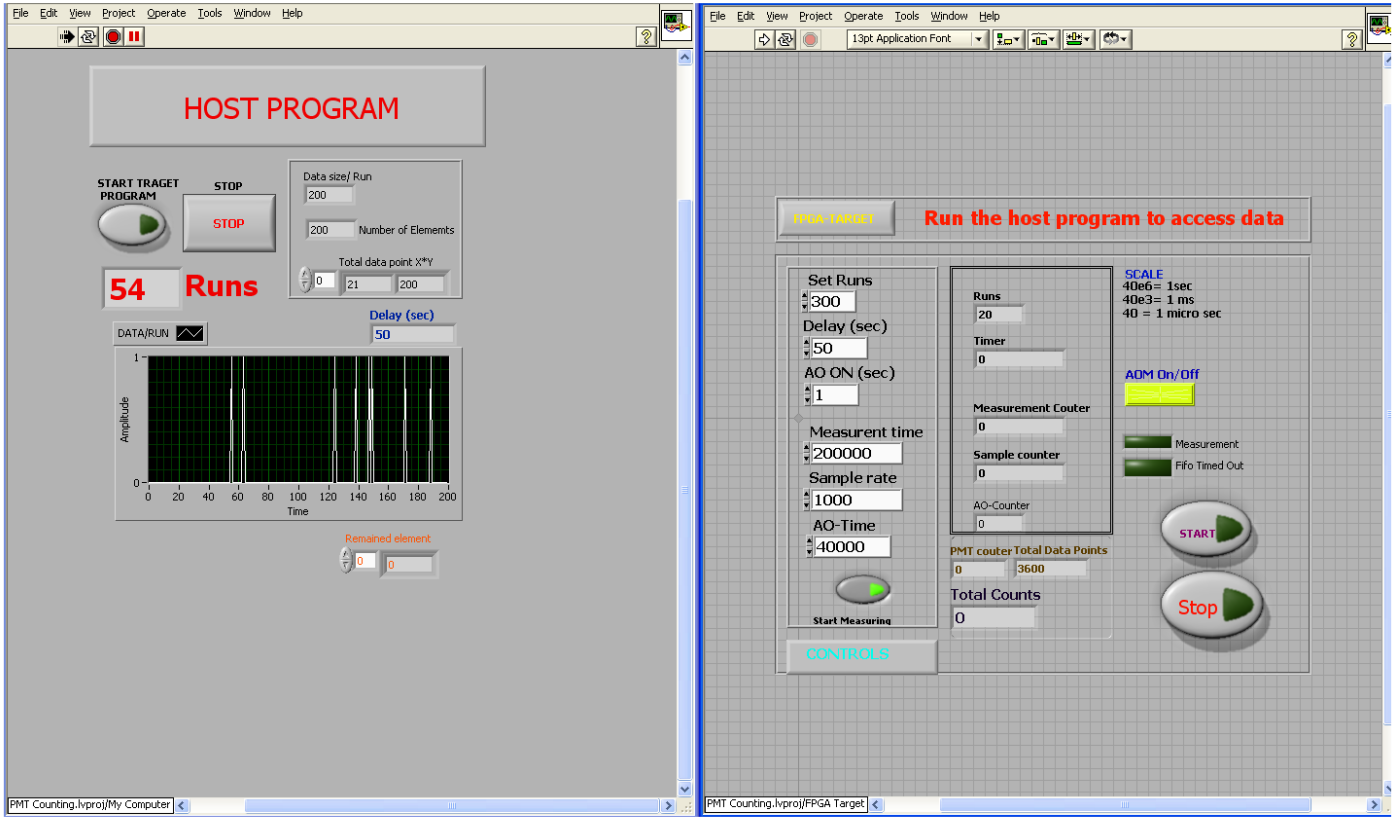

Figure 5.8: User interface for the labVIEW programs written in labVIEW FPGA module running on the FPGA target and Host PC simultaneously. The programs offer the user a convenient controls over the time required for data to be collected from the PMT and provide the control over the AOM on/off time.

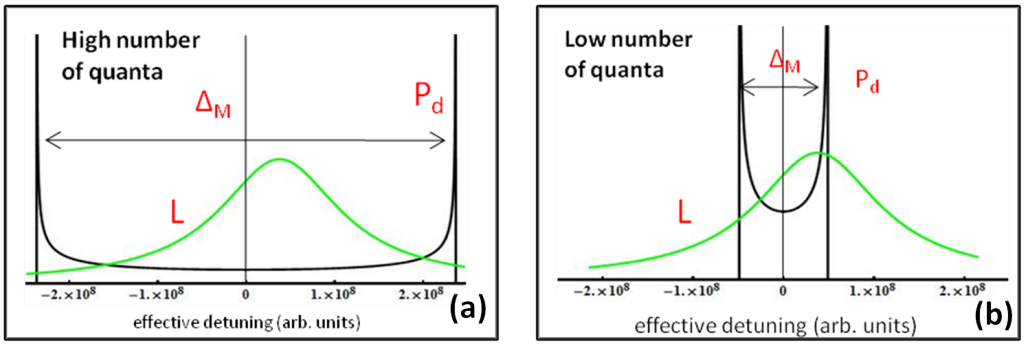

Figure 5.9: Overlap of the probability density of the Doppler shift, $P_D(\Delta_D)$ (solid line), with the transition linewidth L (green). (a) A hot ion with a maximum Doppler shift greater than the broadened transition linewidth and laser detuning, $\Delta_{max} \gg |L| + |\Delta|$. The overlap of both functions is low, leading to a low scatter rate. (b) A cold ion with less energy. The peaks of $P_D(\Delta_D)$ move closer together resulting in a stronger overlap and an increase in scatter rate

The Wesenberg model for heating measurements requires the ion energy change to be dominated by heating along one of the principal axes of the trap. The secular frequency in z-direction is decreased to allow the heating of the ion along that axis, assuming that the heating rate has a ω_z^{-2} dependence [30]. Therefore, the trap secular frequency in z-direction $\omega_z/2\pi$ is decreased to (0.178,0.287, 0.355)$\pm$0.001 MHz, resulting in dominant heating along the z-axis.

The instantaneous Doppler shift $\Delta_D = -\vec{k}\vec{v}$ (where k is the laser beam wavevector and v is the velocity of the ion) during an oscillation increases as the velocity of the ion increases due to heating.

If Δ_{max} is defined as the maximum instantaneous Doppler shift Δ_D, then the likelihood of the ion experiencing a specific instantaneous Doppler shift is described using a probability density, $P_D(\Delta_D)$ [89], and the overlap of $P_D(\Delta_D)$ with the broadened transition linewidth, L, affects the scatter rate as shown in figure 5.9. The situation for a hot ion with $\Delta_{max} \gg |L|+|\Delta|$, where L is the linewidth and Δ is the laser detuning from the resonance is shown in figure 5.9(a), where the Doppler shift probability density and transition linewidth poorly overlap, resulting in a low absorption/scatter rate. When the probability density overlaps well with the transition linewidth, it results in an increased scatter rate. Figure 5.9(b) shows the effects on a cold ion.

Due to the fact that the relative change of ion energy over one oscillation is small compared to the total energy change during the whole re-cooling process, the energy over an oscillation, and hence the scatter rate, can be averaged. The average scatter rate $\langle dN/dt \rangle$

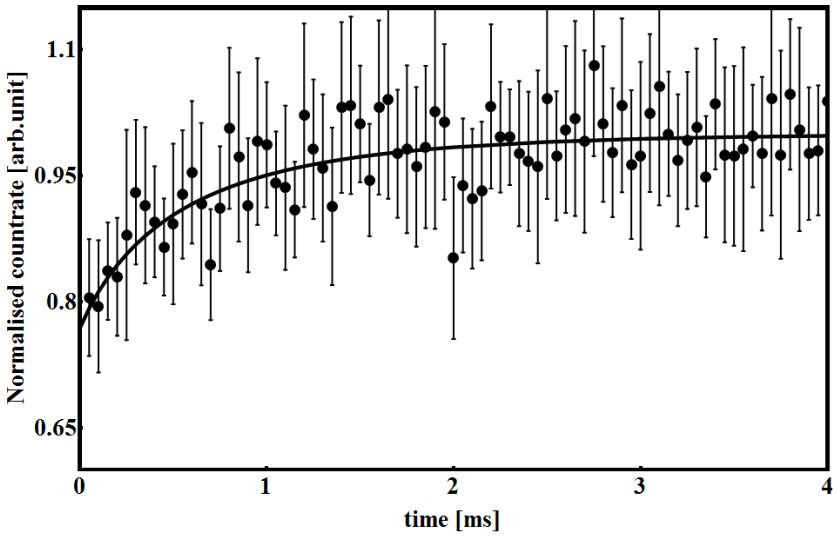

Figure 5.10: Averaged fluorescence curve obtained from 500 re-cooling cycles after blocking the cooling laser in each cycle for 3 second.

over one oscillation is [89]

$$\left\langle \frac{dN}{dt} \right\rangle = \int \frac{dN}{dt} P(\Delta_D) d\Delta_D, \tag{5.1}$$

where dN/dt is the instantaneous scatter rate. In figure 5.9(a) when the ion is hot, the probability density $P_D(\Delta_D)$ is effectively uniform over the transition linewidth. The probability density can be factored out and allows the average scatter rate over one oscillation to be expressed in terms of the ion energy as [89]

$$\left\langle \frac{dN}{dt} \right\rangle (E(E_o, t)) = \frac{1}{\sqrt{E(E_o, t)}} \frac{sL^2}{2\sqrt{\frac{2}{m}} k_z (1+s)^{3/2}}, \tag{5.2}$$

where $E(E_o, t)$ is the ion energy at time t, E_0 is the ion energy just before re-cooling, m is the ion mass, k_z is the z-component of the laser beam vector, s is the saturation intensity parameter, and L is the broadened transition linewidth. A Maxwell-Boltzmann distribution is used to describe the thermal distribution of the ion energy before re-cooling, E_o. The average scatter rate for an ion at time, t, is [89]

$$\left\langle \frac{dN}{dt} \right\rangle_{E_o} = \int_o^\infty P_{\mathrm{B}}(E_o) \left\langle \frac{dN}{dt} \right\rangle (E(E_o, t)) dE_o, \tag{5.3}$$

where $P_{\mathrm{B}}(E0)$ is the Maxwell-Boltzmann distribution.

For the heating measurement experiment, the cooling laser detuning Δ was set to 6 ± 2

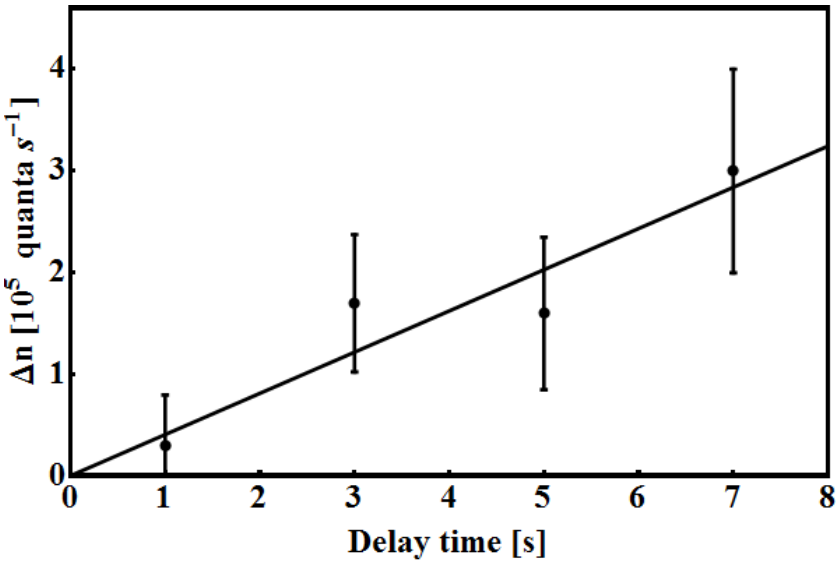

Figure 5.11: Change in ion energy in terms of motional quanta Δn after heating periods of 1, 3, 5 and 7 seconds. Each point results from 500 measurements.

MHz and saturation parameter s was set to 1.0 ± 0.2. This was done by scanning the laser frequency over the resonance frequency and simultaneously observing the fluorescence profile of the ion. Shortly after the fluorescence maximum is reached the count-rate drops sharply due to blue detuning of the laser. The ions resonance frequency now corresponds to the maximum in the observed fluorescence profile. As discussed earlier, the laser frequency was locked to better than 1 MHz. The error on the detuning was estimated by the error on the wavemeter measurement. It was observed that the transition linewidth, L was 40 ± 5 MHz, an increase in the linewidth was suspected due to power broadening and remaining micromotion. The z-component of the laser beam wave vector was $\vec{k_z} = 0.45\vec{k}$. To account for the thermal distribution of E_0, the re-cooling process was repeated 500 times and averaged. Ion energy at the start of re-cooling can be determined by fitting equation 5.3 to the average fluorescence curve. Figure 5.10 shows the averaged fluorescence curve from 500 re-cooling cycles for a 3 second delay time and the solid red line is a fit to equation 5.3.

The ion energy can be converted into motional quanta using the relation,

$$< n >= E/\hbar\omega_z, \tag{5.4}$$

and the change in motional quanta Δn after different delay periods can then be calculated. The heating rate can be calculated from the plot given in figure 5.11.

Repeating the experiment at secular frequencies of $\omega_z/2\pi = (178, 287, 355) \pm 1$ kHz pro-

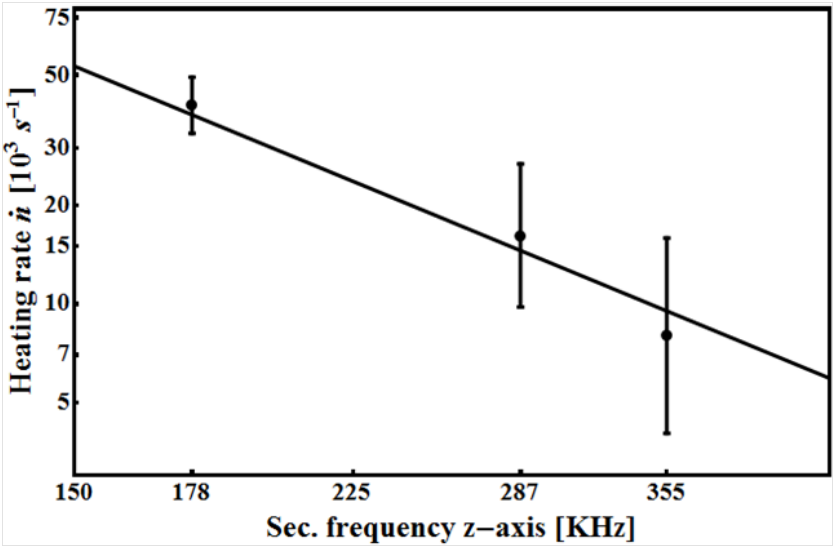

Figure 5.12: Heating rate $\dot{n}$ at three different secular frequencies $\omega_z/2\pi = (178, 287, 355)\pm1$ kHz is plotted. The solid line is a $1/\omega^2$ fit. The plot shows the data is consistent with the observed $1/\omega^2$ dependence of the trap heating rate.

duces the plot shown in figure 5.12, which is consistent with the expected $1/\omega^2$ dependence on $\dot{n}$.

The cause of ion heating is the electric field noise density, $S_{\mathrm{E}}(\omega_z)$, which is related to the heating rate, $\langle \dot{n} \rangle$ via [30, 31]

$$S_{\mathrm{E}}(\omega_z) = \frac{4m\hbar\omega_z}{q^2}\langle \dot{n} \rangle, \tag{5.5}$$

where q and m are the charge and mass of the ion. By assuming $1/\omega^2$ dependency of $\dot{n}$, $S_{\mathrm{E}}(1\ \mathrm{MHz})$ can be estimated and was found to be $3.6 \pm 0.9 \times 10^{-11}$ $\mathrm{V^2 m^{-2} Hz^{-1}}$. Considering the ion electrode spacing of 310 μm in our ion trap, the result is consistent with previously measured values of S_{E} in other ion traps at room temperature [90]. The comparison is shown in figure 5.13. This heating measurement is the first for a ytterbium ion in such a small ion-electrode distance and produces an encouraging result for the use of Yb^+ ions in quantum information processing. Figure 5.13 (adopted from [91]) puts our measured value into the context of other heating measurements.

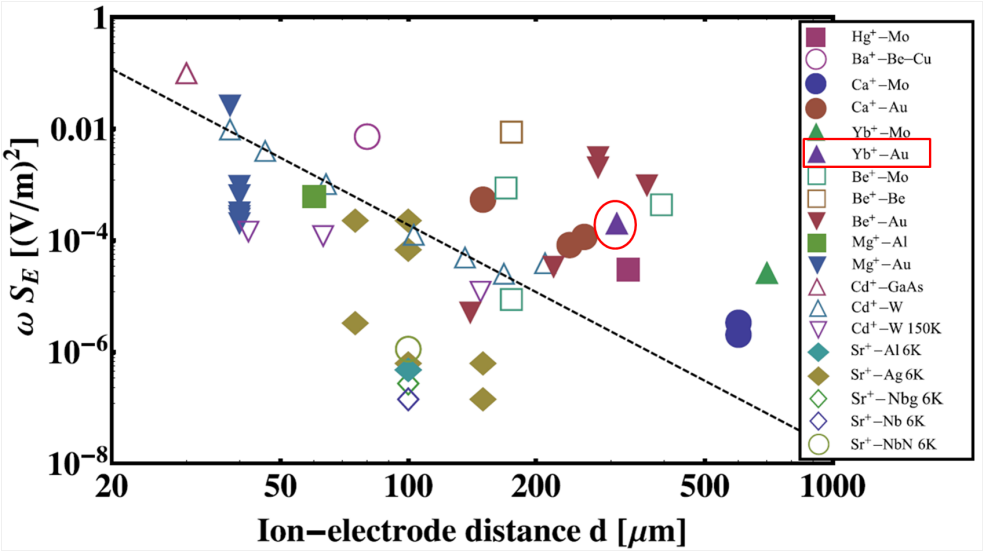

Figure 5.13: Electric field noise density, $S_E(\omega_z)$ versus ion-electrode, multiplied with the secular frequency ω_z for a number of other ion trap experiment. The labels show both the ion species and the electrode material used in the experiment. The electrode temperature is also given if the measurement is performed below room temperature. The encircled data point indicates our measurement. The figure is adopted from [91]. The data points are associated with the following references; Hg^+-Mo [92], Ba^+-Be-Cu [93], Ca^+-Mo [94], Ca^+-Au [24,95,96], Yb^+-Mo [56], Yb^+-Au [97], Be^+-Mo [56], Be^+-Be [56], Be^+-Au [30,98], Mg^+-Al [99], Mg^+-Au [12, 23, 25, 87, 99], Cd^+-GaAs [20], Cd^+-W [31], Cd^+-W 150 K [31], Sr^+-Al 6 K [100], Sr^+-Ag 6 K [28], Sr^+-Nbg 6 K, Sr^+-Nb 6 K, Sr^+-NbN 6 K [100].

Chapter 6

Yb Spectroscopy

6.1 Introduction

Ytterbium (Yb), both atomic and singly ionised, is an element widely used in experiments involving trapped atoms and ions, such as laser cooling and trapping of neutral atoms and ions [56, 83, 101–110], atomic clocks [40–43], frequency standards [36–39], quantum computing experiments [54,111], quantum optics [112] and atomic parity non-conservation experiments [113].

Ytterbium is a heavy diamagnetic rare earth element of the lanthanide series, with an atomic number of 70. It is a soft silvery malleable metal at room temperature, with a melting point of 1097 K and boiling point of 1470 K. It was first identified as an element in 1907, and is named after the Swedish village of Ytterby [38]. There are 7 naturally-occurring stable isotopes of ytterbium, five with nuclear spin 0 (even number isotopes) and 2 with nuclear spin 1/2 (odd number isotope), shown in table 6.1 with corresponding masses in a.m.u.

The odd isotope ^{171}Yb, which is significantly abundant in a natural sample (14.3%), is specially attractive for use as a qubit due to its spin 1/2 system. It has large hyperfine splitting of the ground state (12.6 GHz). It has a ground-state electron configuration of [Xe] $4f^{14}$ $6s^2$, thus having two electrons which close the valence s-shell. After ionisation Yb^+ ion behaves like a closed two level system.

Yb^+ is a suitable candidate for trapping for a few reasons. It has ground state transitions in neutral and singly ionised forms that are accessible by commercially available

Table 6.1: Relative abundance of Ytterbium isotopes

Isotope	Mass[a.m.u]	Abundance	Nuclear Spin
^{176}Yb	175.942564	12.7%	0
^{174}Yb	173.938859	31.8%	0
^{173}Yb	172.938208	16.1%	5/2
^{172}Yb	171.936378	21.9%	0
^{171}Yb	170.936323	14.3%	1/2
^{170}Yb	169.934759	3.05%	0
^{168}Yb	167.933894	0.13%	0

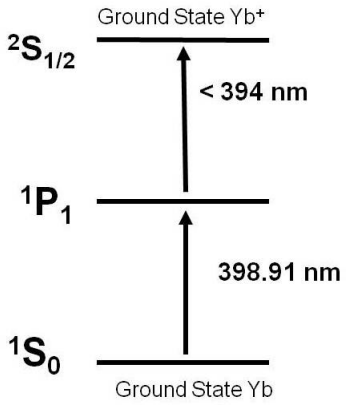

Figure 6.1: Two colour photoionisation scheme for neutral Yb. 399-nm light excites the atom from ground state (S) to excited state (P), furthermore any light with wavelength less than 394 nm excites an electron to pass the continuum.

laser diodes. It has a large hyperfine splitting (12.6 GHz) and decays spontaneously from exited state $^2P_{1/2}$ with a life time of 5.5 ns to $^2S_{1/2}$ (369.5-nm transitions line). About 0.3% of the time, the exited state decays to the $^2D_{3/2}$(2438 nm transition line) which has relatively long-lived lifetime of 52 ms [58].

In order to ionise Yb in our trap experiments discussed in chapter 5, we chose a photoionisation method, shown in figure 6.1. Traditionally, electron guns were in used to ionise neutral atoms in ion trap experiments but nowadays, photoionisation method proposed by [114] is a primary choice for ion trap experiments [39, 54, 57, 81, 115]. This technique avoids the addition of heating and stray ionisation and charging of nearby trap electrodes and chamber walls. One obvious advantage of photoionisation technique over electron gun method is that it allows isotope selective ionisation of neutral atoms based on resonance of the incident light. A neutral Yb can easily be ionised by light below 394 nm, after excitation to the P-state by 399-nm light. For the isotope selective photoionisation, accurate values of the wavelength for the $^1S_0 \leftrightarrow^1 P_1$ transition line in atomic Yb and corresponding frequency shifts for the stable isotopes are very important. This information can be equally important for the experiments involving laser cooling and trapping of neutral Yb [116].

6.2 Yb 399-nm line Spectroscopy

Various methods of spectroscopy have been used to investigate Yb $^1S_0 \leftrightarrow ^1 P_1$ transition lines, and corresponding isotope shifts. The published values for the transition wavelength and the isotope shifts can be found in [117–121]. Unfortunately, most authors only report isotope shifts while only a few report the absolute transition frequencies. Nevertheless, discrepancies between reported absolute wavelengths persist.

Ytterbium $^1S_0 \leftrightarrow ^1 P_1$ transition frequencies are measured using a novel and simple method. The measured frequencies differ from recently published results [121]. The resonant transition frequencies and corresponding isotope shifts are measured to an accuracy of 60 MHz by using a simple method described in section (6.2.2), which is based upon observing and aligning fluorescence spots of atomic Yb generated from an atomic oven in an evacuated glass bell jar. Our results are compared to the results obtained using saturation absorption spectroscopy and were further verified by ionising and trapping Yb ions.

The advantage of our technique is that it can be used to determine resonance frequencies when atom motion is not necessarily perpendicular to the propagation of the laser. This can be the case in many experiments and causes Doppler shifts in the resonance frequencies depending on the mean velocity along the atomic beam. Therefore this method is quite useful for such kind of experiments. Using our technique we were able to measure the Doppler shift of the transition frequency under a range of angles and then derive the average velocity of the atomic beam.

6.2.1 Experimental Setup

To drive the $^1S_0 \leftrightarrow ^1 P_1$ 399-nm dipole transition, an inexpensive in-house-built ultra violet external cavity diode laser (ECDL) was used. The ECDL was formed with a laser diode (wavelength selected to 399 nm, Sanyo diode: DL-4146-301S) and a diffraction grating (Newport: 53-*-240R) positioned in the Littrow configuration. A piezo electric actuator was used to adjust the angle of the grating and thus tuning of the emission wavelength. To stabilise the emission wavelength a High Finesse wavelength meter (WS-07, with specified wavelength accuracy of 60 MHz) and NI-DAQ card operating under labVIEW real time was used. The wavemeter is calibrated using a 780-nm laser which is locked to within 1 MHz of the ^{87}Rb D_2 line. It measures the wavelength of the ECDL and sends the information

to a LabVIEW program running in Real Time operating system via the COM-Port. The program determines a drift in wavelength and generates the corresponding error signal to keep the laser stable. The error signal is sent to the piezo controller of the laser via an NI-DAQ Card (NA-6143). The same program was also used to scan the frequency over the required range. To perform saturation spectroscopy on the $^1S_0 \rightarrow ^1 P_1$ 399-nm isotope transitions, the ECDL frequency was required to scan over a range of 3 GHz. However, the adjustment of the grating angle alone in the ECDL resulted in a mode hop free tuning range of only 800 MHz. To overcome this, the piezo voltage and laser diode current were adjusted simultaneously to produce a mode hop free tuning range of over 5.5 GHz. For our technique, an atomic flux propagating in a known direction was required as this enabled localised fluorescence spots that could be be spatially resolved. To generate the Yb atomic beam, a resistivly heated stainless steel oven tube (2 cm long and 1.5 mm diameter) was used. A small piece of natural Yb (Part number: GO0196 from Goodfellow Cambridge) was placed inside the oven tube and Yb atomic beam was obtained by running an electric current of 5 to 6 A over the oven. To avoid the chemical reaction of Yb atoms with surrounding air, the atomic oven was placed inside a bell jar maintained at a pressure of the order of 10^{-8} torr using turbo-molecular pump.

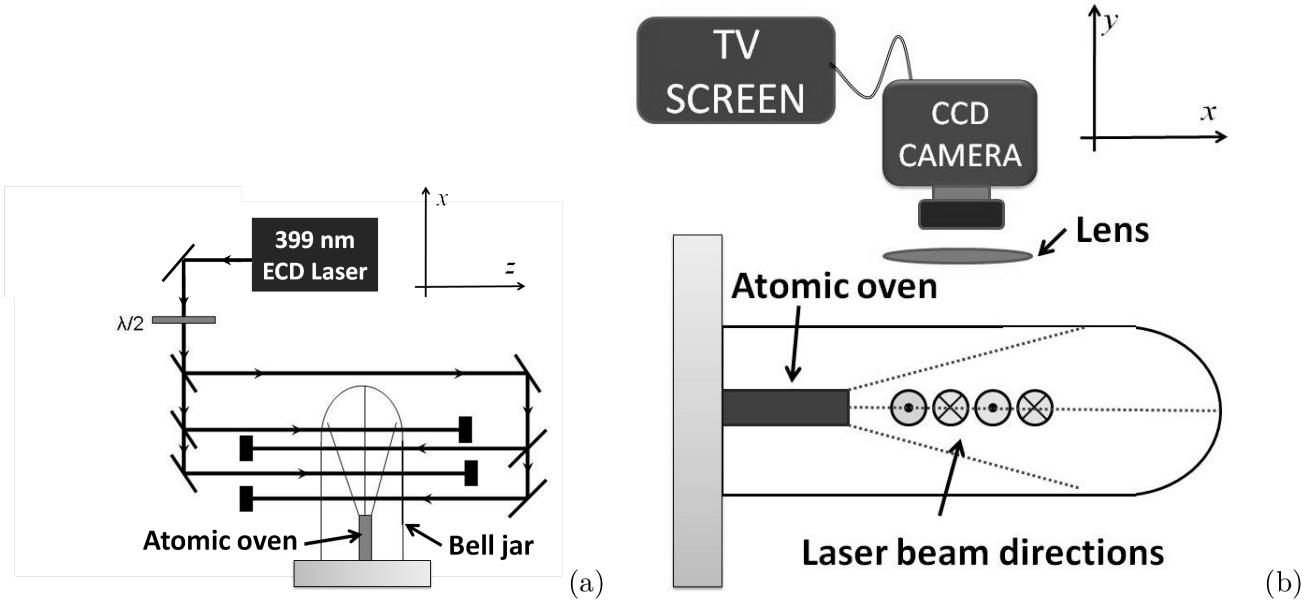

Figure 6.2: Schematic diagram (a) shows the counter propagating laser beams crossing the atomic beam and (b) shows the direction of laser beams and TV-camera setup.

6.2.2 Fluorescence spot technique

A simple method was devised that works by observing fluorescence spots using inexpensive CCD TV camera setup. Fluorescence spots are produced by laser-atom interactions at resonance wavelengths. The experimental setup for our spot method is illustrated in figure 6.2. Two pairs of non-overlapping and counter propagating laser beams are passed through the Yb atomic beam. Each beam has an intensity of approximately 4.5 mW cm^{-2}. The cylindrical axis of the oven tube is considered as the reference axis and the lasers are aligned perpendicular to this reference axis unless otherwise stated. The atoms from the oven interact with the two counter propagating pairs of laser beams and produce 4 fluorescence spots. Due to Doppler effect, absorbtion of light of a higher or lower frequency by the atom depends whether it is moving in the same direction as the laser beam or in the opposite direction. Therefore in the frame of reference of laser beam, each pair of laser beams interacts with atoms of the same velocity group. When viewed in the laboratory frame, the four spots are seen to be misaligned when the frequency is detuned from the resonance. When on resonance, the four spots are seen to be aligned perpendicular to the propagation of the laser beams, in this situation each laser is interacting with atoms of relative zero velocity. This scheme is illustrated in figure 6.3 which shows that all spots are aligned to the reference axis when the laser frequency is on resonance and misaligned when the frequency is detuned from the resonance.

The resolution of the method can be observed in figure 6.4 where 6.4(b) indicates when the laser frequency is on resonance and 6.4(a) and (c) indicate when the laser frequency is detuned -20 and +20 MHz from resonance respectively. At this resolution we were able to measure the absolute frequency within an error range of the linewidth of the transition. The resolution and accuracy of this technique can further be enhanced by making the atomic beam well collimated which reduces the size of spots. Alignment of the four spots in a straight line on resonance also occurs irrespective of the angle between the cylindrical axis of the ovens and the laser beams, which is discussed in section (6.4).

In order to obtain the $^1S_0 \leftrightarrow {}^1P_1$ transition frequencies, the frequency of the 399-nm laser diode was scanned slowly over 3 GHz. During the scan the fluorescence spots were imaged using an inexpensive CCD camera setup. After narrowing down the scanning range, the frequencies of the transitions of the different isotopes were individually measured by aligning the four spots in a straight line with the cylindrical axis of the atomic oven. This is shown in figure 6.4. The frequency of the $^{174}\mathrm{Yb}^1S_0 \leftrightarrow {}^1P_1$ transition was mea-

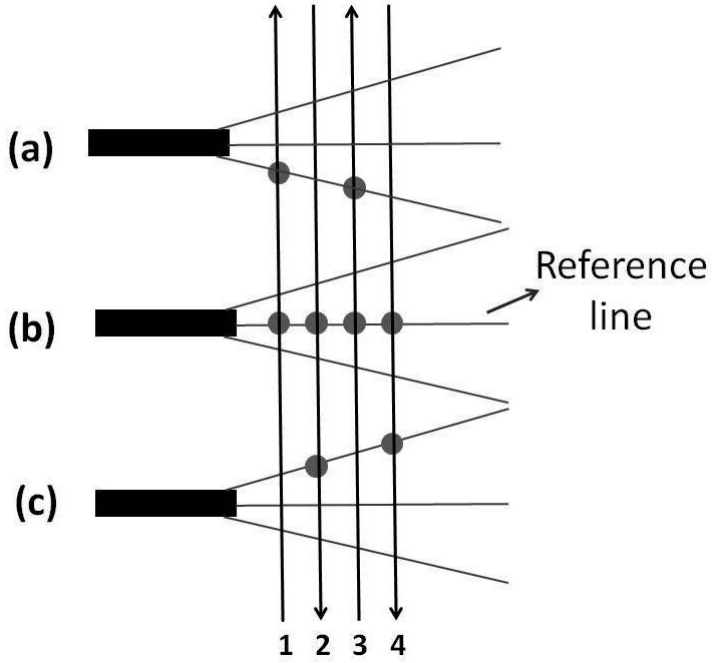

Figure 6.3: Illustration of the fluorescence spots movement according to laser detuning (a) -ve and (c) +ve. Spots are aligned with reference line in (b) when the frequency of the laser is on resonance.

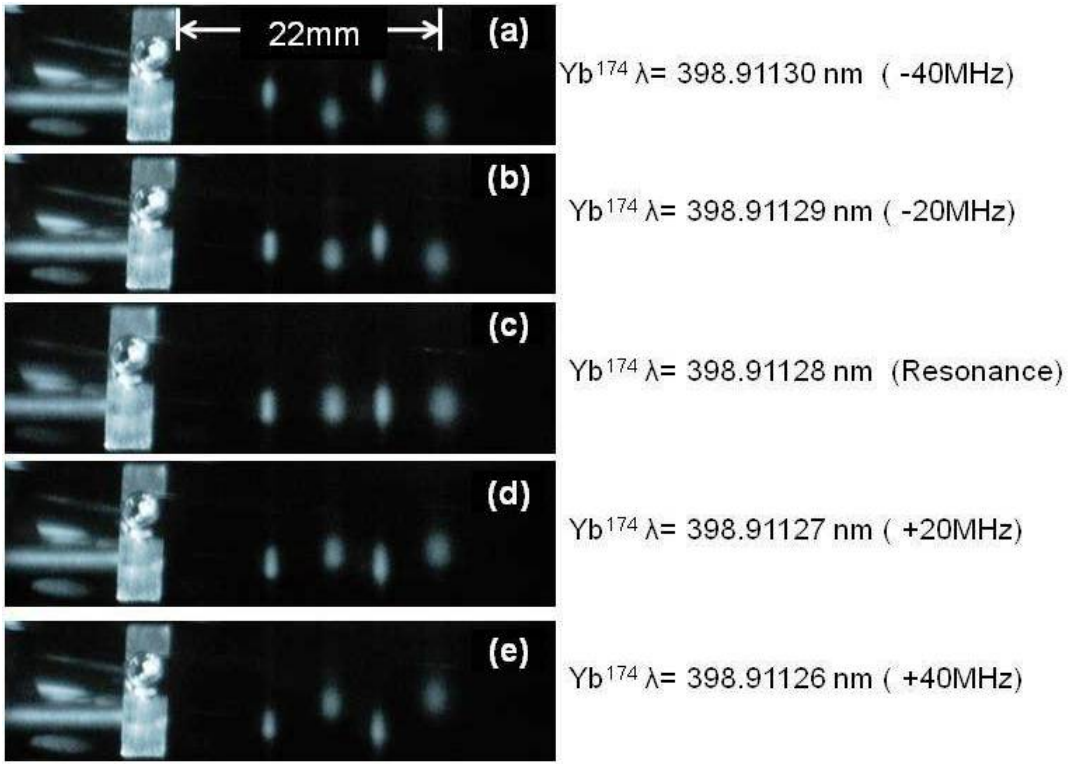

Figure 6.4: Illustration of the resolution of the spectroscopy method. Pictures show the atomic ovens and fluorescence spots where the laser beams intersect the atomic beam taken, (c) on resonance, and (a) -40 MHz, (b) -20 MHz (d) 20 MHz (e) 40 MHz detuning.

sured to be 751.526650 THz ±60 MHz which disagrees with a previously published value 751.525987761 THz ±60 kHz [121] by approximately 660 MHz. This discrepancy may be explained as, Das *et al.* [121] relied in their measurement on the stated accuracy of 20 MHz of a home built wavemeter and we speculate that the uncertainty of that wavemeter had been larger than anticipated by the authors. Our measurement differs from the NIST Atomic Spectra Database [122] by 260 MHz, which lists the energy of the Yb ^{1}P$_1$ level at 25068.222 cm^{-1} (751.52639 THz). Closer examining this discrepancy, the database lists Meggers *et al.* [117] as the most recent source of their data. However, Meggers *et al.* [117] lists the level energy at 25068.227 cm^{-1} (751.52654 THz) which is only 110 MHz away from our measurement, pointing to a possible typographical error on the NIST Atomic Spectra Database. Considering that Meggers *et al.* [117] used a natural mixture of Yb isotopes, their result is consistent with our measurement. It should also be noted that the result by Meggers *et al.* [117] shows an expected 550 MHz discrepancy with the measurement by Das *et al.* [121]. A recently published paper [123], by a group at Los Alamos National Laboratory, USA, also agrees with our measurements. After absolute resonance frequency measurements for each Yb isotope, the isotope shifts relative to the ^{174}Yb $^1S_0 \leftrightarrow^1 P_1$ transition were then calculated. The results are shown in Table: 6.2 and compared with recently published results. An overview of the isotope shifts and hyperfine splitting for Yb 399-nm line are illustrated in figure 6.5.

Not every transition line can be resolved using this method as some lines are separated by less than the linewidth, and result in overlapping of the fluorescence spots. The frequency shift between the ^{172}Yb $^1S_0(F = 0) \leftrightarrow^1 P_1(F = 1)$ and ^{173}Yb $^1S_0(F = 1/2) \leftrightarrow^1 P_1(F = 3/2)$ is 18 MHz, and between ^{172}Yb $^1S_0(F = 0) \leftrightarrow^1 P_1(F = 1)$ and ^{173}Yb $^1S_0(F = 1/2) \leftrightarrow^1 P_1(F = 7/2)$ transitions is 55 MHz, while the separation between the ^{170}Yb $^1S_0(F = 0) \leftrightarrow^1 P_1(F = 1)$ and ^{171}Yb $^1S_0(F = 1/2) \leftrightarrow^1 P_1(F = 1/2)$ transitions is only 38 MHz [121]. Thus our measurements correspond to the shift for these groups of close transitions. The isotope shifts data presented in Table: 6.2 for the $^1S_0 \leftrightarrow^1 P_1$ transition are in very good agreement with previously published work [81, 118, 119, 121].

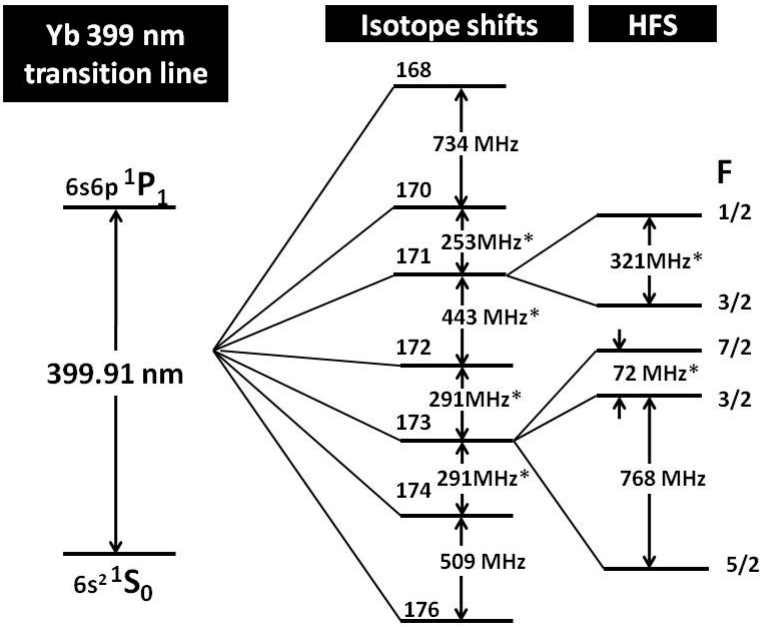

Figure 6.5: Yb isotope shifts for the 399-nm $^1S_0 \leftrightarrow ^1P_1$ transition line.
** Data taken from the Ref [121]*

Table 6.2: The frequency shifts for the various isotopes of Yb from the ^{174}Yb $^1S_0 \leftrightarrow ^1P_1$ transition line. The values are obtained from the fluorescence spot technique and compared with the previous published work.

Shift from ^{174}Yb (MHz)						
Isotope	Transition	This work	Ref. [121]	Ref. [118]	Ref. [81]	Ref. [119]
168	$^1S_0(F=0) \leftrightarrow ^1P_1(F=1)$	1883 ±30	1887.400 ±0.05			1870.2 ±5.2
170*	$^1S_0(F=0) \leftrightarrow ^1P_1(F=1)$	1149 ±60	1192.393 ±0.066	1175.7 ±8.1		1172.5 ±5.7
171*	$^1S_0(F=1/2) \leftrightarrow ^1P_1(F=1/2)$		1153.696 ±0.061	1151.4 ±5.6	1104±69	1136.2 ±5.8
171	$^1S_0(F=1/2) \leftrightarrow ^1P_1(F=3/2)$	829 ±30	832.436 ±0.05	832.5 ±5.6	822 ±51	834.4 ±4.0
172*	$^1S_0(F=0) \leftrightarrow ^1P_1(F=1)$		533.309 ±0.053	527.8 ±2.8	534±33	
173*	$^1S_0(F=1/2) \leftrightarrow ^1P_1(F=3/2)$	546 ±60	515.972 ±0.2			
173*	$^1S_0(F=1/2) \leftrightarrow ^1P_1(F=7/2)$		587.986 ±0.056	578.1 ±5.8		
173	$^1S_0(F=1/2) \leftrightarrow ^1P_1(F=5/2)$	-264 ±30	-253.418 ±0.05		-262 ±16	
176	$^1S_0(F=0) \leftrightarrow ^1P_1(F=1)$	-509 ±30	-509.310 ±0.05	-507.2 ±2.5	-554 ±35	

** can not be resolved with the spot method*

Table 6.3: The absolute frequencies for $^1S_0 \leftrightarrow ^1P_1$ transition line of Yb isotopes obtained by saturation spectroscopy and the spot technique

Peak	Yb Isotope	Transition	Frequency [MHz] (Saturation)	Frequency [MHz] (Spot Method)
1	176	$^1S_0(F=0) \leftrightarrow ^1P_1(F=1)$	751526150 ± 60	751526150 ± 60
2	172*	$^1S_0(F=0) \leftrightarrow ^1P_1(F=1)$		
	173*	$^1S_0(F=1/2) \leftrightarrow ^1P_1(F=3/2)$	751527140 ± 120	751527200 ± 120
	173*	$^1S_0(F=1/2) \leftrightarrow ^1P_1(F=7/2)$		
3	171	$^1S_0(F=1/2) \leftrightarrow ^1P_1(F=3/2)$	751527600 ± 60	751527490 ± 60
4	170*	$^1S_0(F=0) \leftrightarrow ^1P_1(F=1)$	751527790 ± 120	751527800 ± 120
	171*	$^1S_0(F=1/2) \leftrightarrow ^1P_1(F=1/2)$		

** not resolved*

The natural linewidth of the ${}^1S_0 \leftrightarrow {}^1P_1$ transition (28 MHz) causes a strong fluorescence rate [119]. Therefore, by keeping the current through the oven constant the brightness of the fluorescence spots corresponds roughly to the natural abundance of each isotope except for the odd isotopes which have hyperfine structure in the ${}^1\mathrm{P}_1$ excited state. Optical pumping into the wrong hyperfine level leads to a reduction in the fluorescence rate [67]. This phenomena can be a significant problem in magneto optical trapping (MOT) of neutral atoms and re-pumping lasers are needed to avoid the situation [124, 125]. In our case, this does not present a significant problem as we use an atomic beam in which the atoms are continuously replaced with new ones.

6.2.3 Error analysis

To determine the resonant frequencies and isotope shifts we used the WS7 wavemeter from High Finesse (specified to 60 MHz accuracy). The wavemeter is calibrated using a 780-nm laser which is locked to within 1 MHz of the ${}^{87}\mathrm{Rb}$ D_2 line. A He-Ne laser (also calibrated to 1 MHz) was then used to provide confirmation of the calibration. A further two point check was performed to ensure calibration in the ultra violet frequency range. Using our frequency doubling system, that converts 739-nm light into 369-nm, we measured the two wavelengths simultaneously and confirmed the wavemeter to operate within specifications. The wavemeter was calibrated before and after measurements and no change in calibration measurements were observed. The wavemeter is specified to have an accuracy of 60 MHz for absolute frequency measurements, but it is more accurate for relative frequency measurements of closely spaced transitions. For closely spaced transitions, the accuracy of the wavemeter corresponds to the last significant digit of a measured value. Hence, for the 399-nm transitions, the relative accuracy is about 20 MHz. Therefore the error on transition frequencies is 60 MHz and the error on isotope shifts is 30 MHz. However due to the actual line width of 20 MHz of these transitions and resulting overlap of some transition lines, isotope shift could not be resolved better than 60 MHz. Other sources of error include non-parallel alignment of the lasers where beam misalignment of 1 degree corresponds to a 15 MHz error on wavelengths. As the technique can resolve a 20 MHz detuning from resonance, it was possible to align the lasers to better than 1 degree as misalignment would result in a visible deviation of the spots. Power broadening of the transition line was insignificant as each beam was less than 4.5 ± 0.9 mW cm^{-2} whereas the saturation intensity of the transition is 60 mW cm^{-2}, which translates to a 3 MHz linewidth broadening. The potential resolution of the technique can be seen from figure

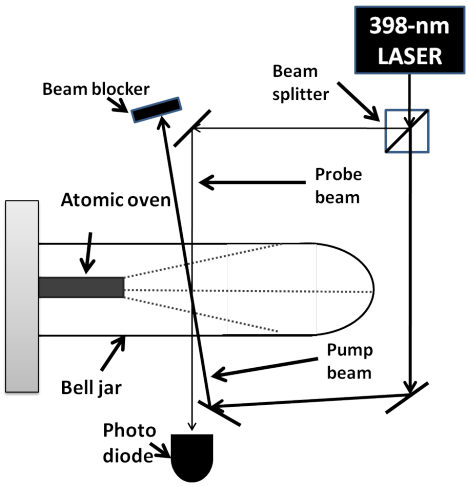

Figure 6.6: Absorption saturation spectroscopy arrangement. Two counter propagating high intensity pump beam and low intensity probe beam overlapping the atomic beam.

6.4 where the frequency of the laser has been detuned from (b) resonance by (a)-20 MHz and (c)+20 MHz. The separation from the front of the oven to the furthest spot is approximately 22 mm, and by observing spot misalignment with detuning we extrapolate that the resolution of the technique can be down to 10 MHz.

6.3 Saturation absorption spectroscopy

To provide a comparison for the transition frequencies and isotope shifts obtained by the spot method, we performed a typical absorption spectroscopy on Yb sample. Figure 6.6 shows a typical saturation absorption spectroscopy experiment set up. Two counter propagating laser beams originating from the same laser cross inside an evacuated bell jar. The two beams are termed as pump and probe. The pump beam is at least 10 times more intense than the probe beam. By scanning the laser frequency over the resonance, a spectral line can be obtained with a narrow peak centred at the transition frequency. The reason for this narrow peak is due to the fact that moving atoms absorb light of a different frequency than atoms at rest. As discussed earlier the absorbtion of light of higher or lower frequency by atoms depends upon their relative motion respect to the direction of propagation of light. Therefore if the laser is not exactly on the transition frequency each of the two counter propagating beams (pump and probe) will interact with a different velocity group. On resonance, both pump and probe beam will interact with same velocity group of atoms. The strong pump beam will saturate the transition and burn a hole in the velocity distribution of atoms [126]. The absorption of the probe beam

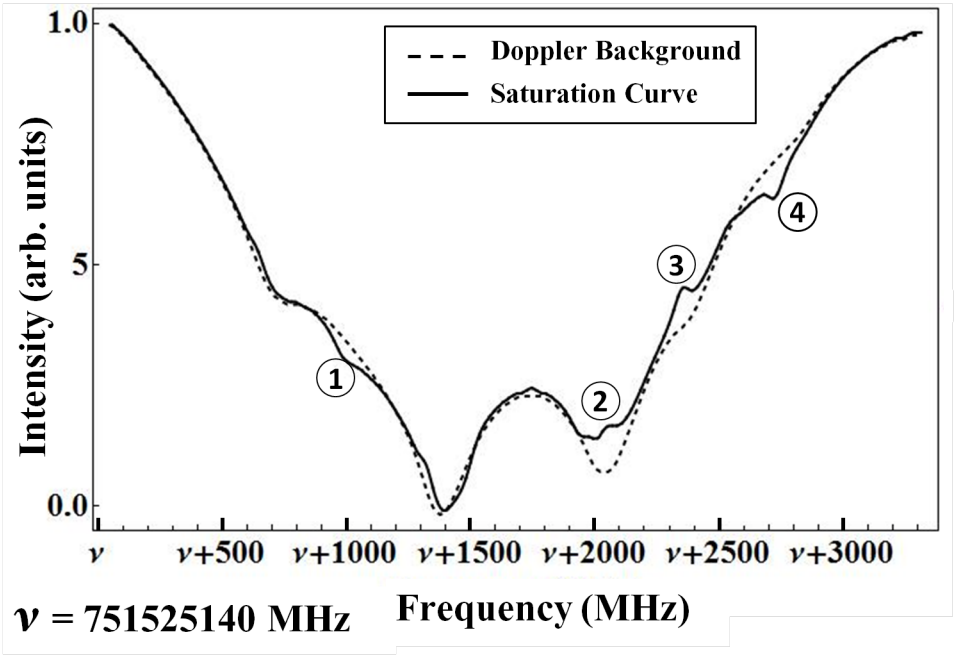

Figure 6.7: ${}^1S_0 \leftrightarrow {}^1P_1$ transition peaks for different isotopes of Yb obtained with saturation absorption spectroscopy can be observed at label 1, 2, 3 and 4. The dashed plot represents the Doppler background.

is decreased as there are less atoms are left for interaction in the ground state of the zero velocity group. This will lead to a transmission maximum of the probe beam at the exact transition frequency, which will result a peak in the absorption saturation spectrum.

The saturation spectroscopy setup in our experiment consists of counter propagating and overlapping pump and probe beam (127 mW cm^{-2} and 2 mWcm^{-2} respectively) through ytterbium atomic beam. By scanning the wavelength of the external cavity diode laser, the saturation plot shown in figure 6.7 was produced. The light dashed spectral line represents the Doppler background, which was obtained by scanning the wavelength but blocking the pump beam. With the pump beam included the dark trace was produced. Saturation peaks for different isotopes can be seen at label 1, 2, 3 and 4 on the graph and corresponding frequencies are listed in table 6.3 and compared with the results obtained with the spot method. The data in the plot is normalised to compare the saturation peaks. The original data set contains approximately 1 million samples. Therefore, on the horizontal axis, it is possible to zoom in to get a better resolution and hence, any error involving locating the peak centre is much less than the error on the wavemeter. The error on the measured frequencies presented in table 6.3 is the error attributed by the wavemeter. The error is doubled for the overlapping transition peaks.

In figure 6.7, the positive and negative going peaks in the saturation curve for odd and

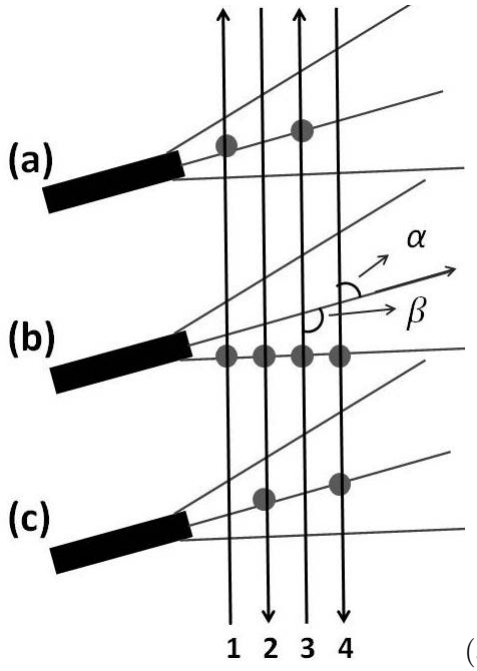

(a)

Figure 6.8: (a)Illustration of the counter propagating laser beam pairs making an angle with atomic beam. Laser beam pair (2 and 4) makes an acute angle α and pair (1 and 3) makes an obtuse angle β with the reference axis. To align the pair of spots with the reference axis, laser frequency is blue detuned in (a) and red detuned in (c). In (b) both spot pairs are aligned (but not with the reference axis) when the frequency is at resonance.

even isotopes can be explained by the fact that the polarisation of the laser light effects the relative peak intensities. In saturation spectroscopy, the orientation of the plane of polarisation of the laser beams (pump and probe) relative to the direction of magnetic field (in our case the earth magnetic field) can change the absorption (or emission) of the light [127].

In table: 6.3, it can be seen that the results obtained from the saturation spectroscopy are in good agreement with the results obtained from our fluorescence spot method. However the signal to noise ratio using this saturation spectroscopy setup is poor compared to spot method. Further, this saturation spectroscopy can only be used to determine the resonant transition frequencies but not Doppler shifted transition frequencies, which can be useful in ion trap experiments where atomic beam and laser beam are not perpendicular.

6.4 Doppler Shifted frequency measurements

By small modifications to the setup, the fluorescence spot method can also be used to measure the Doppler shifted transition frequencies that occur when the laser and the atomic

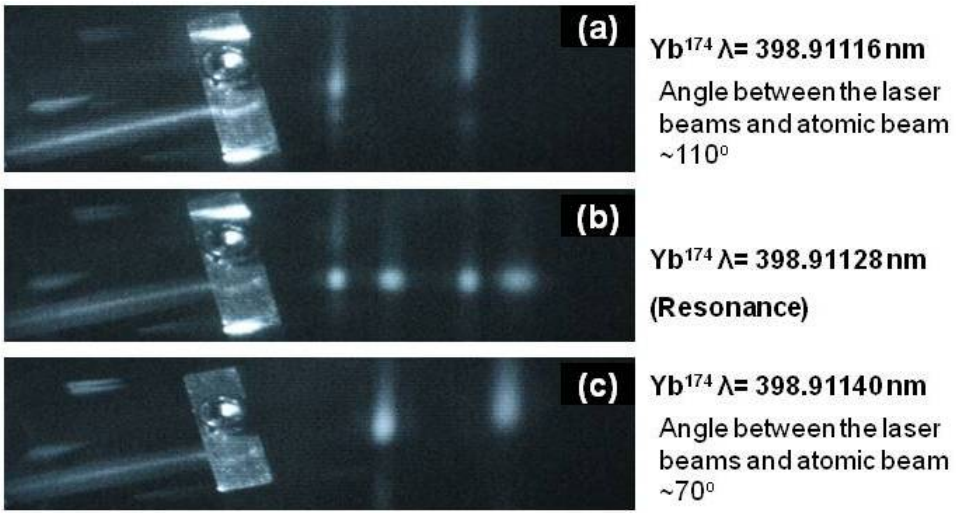

Figure 6.9: Pictures show the atomic oven and fluorescence spots where the laser beams intersect the reference axis at (a) 110^o and (c) 70^o. (b) also demonstrates the non-Doppler shifted resonance where the spots align perpendicular to the laser beams, as seen in the fluorescence spot technique

beam are not perpendicular, allowing for predictions of transition frequencies in realistic ion trap setups. In the previous section(6.2.2) the atomic motion was perpendicular to the laser beam propagation, which provided resonant transition frequencies. However, in many experiments the atomic motion is not necessarily perpendicular to the laser beams. In this situation a component of the velocity of the atoms is parallel (or anti-parallel) to the laser beam and the frequency of the resonance line becomes Doppler shifted and this Doppler shift depends on the temperature of the atomic oven. Using the spot method, these Doppler shifted transition frequencies can be measured and the average velocity of the atoms in the direction of the reference axis and the oven temperature can be determined.

As described earlier, when the frequency is detuned from the Doppler-free resonance, the two pairs of spots move in opposite directions related to the pairs of counter-propagating laser beams. To measure the Doppler shifted wavelengths, the earlier setup was adjusted by rotating the oven to form an angle with the lasers. This provided maximum atomic flux for the desired angle, while the cylindrical axis of the atomic oven offered a reference axis to which the spots could be aligned.

This scheme is illustrated in figure: 6.8, where the direction of propagation of the laser beams must be taken into account because one pair of the laser beams (2 and 4) make an acute angle α while the other pair (beam 1 and 3) form an obtuse angle β with the reference axis. In both cases the magnitude of the angular difference from 90^o (and hence

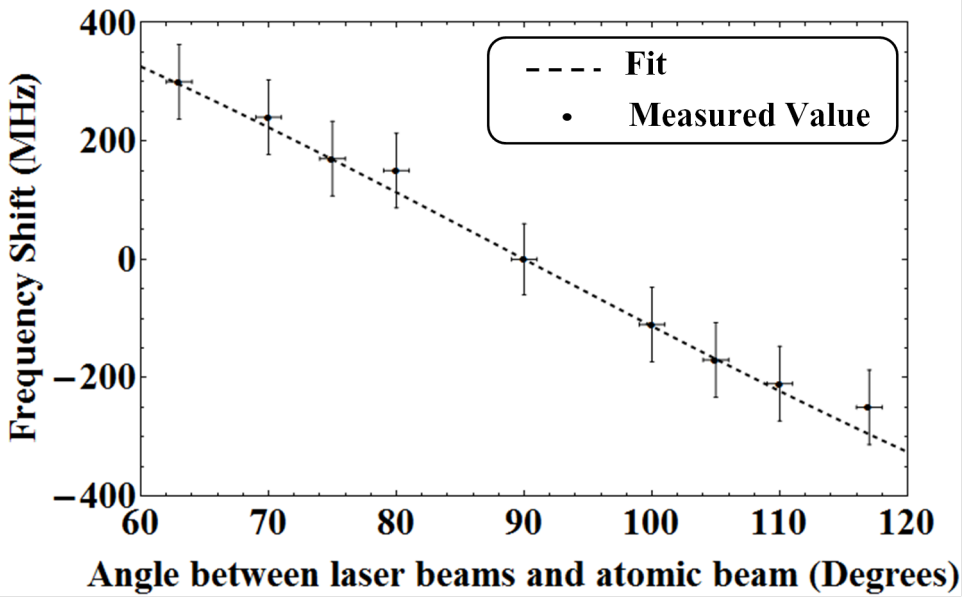

Figure 6.10: Doppler frequency shift in ${}^1S_0 \leftrightarrow {}^1P_1$ transition of Yb^{174} as a function of angle between the laser beams and atomic beam

the frequency shift) is the same, but the sign is different. To align a pair of spots to the reference axis the laser frequency was detuned from resonance by a certain amount. Blue detuning the laser frequency causes fluorescence spots (corresponding to lasers 2 and 4) to align to the reference axis, while red detuning causes fluorescence spots (from lasers 1 and 3) to align to the reference axis. Figure: 6.9 demonstrates these Doppler shifted resonance spots when the angle between laser and the atomic beam is (a) $\alpha = 70^o$ and (c) $\beta = 110^o$. A particular advantage of the spot method is that when on resonance the four spots form a line perpendicular to the laser beams, as shown in figure: 6.9(b). This allows for the resonant transition frequency to be measured independent of the angle between the laser beam and atomic beam.

The Doppler shift on the resonance frequency depends on the velocity component, of the atoms, parallel (or anti parallel) to the propagation of the lasers, which is dependant upon the cosine of the angle between the atomic motion and the propagation of laser. Therefore the frequency shift Δf is [53]

$$\Delta f = \frac{f}{c} v \cos\theta \tag{6.1}$$

where f is the Doppler free transition frequency, c is the speed of light, v is the velocity of the atoms along the direction of the atomic beam and θ is the angle between the atomic beam and laser beam. Most of the atoms in the beam are moving in the same direction and

the fluorescence is caused by those atoms which have major component of their velocities parallel to the laser beams. Therefore, the velocity ($vcos\theta$) given by equation 6.1 can be considered as the most probable velocity (the velocity possessed by the maximum fraction of the atoms in the beam in the direction of the laser beam). The mean velocity is $\approx 1.07\times$ the most probable velocity.

In this part of the experiment, the reference axis was rotated to make angles of 63, 70, 75 and 80 degrees with one pair of lasers, and hence 117, 110, 105 and 100 degrees with the other pair of lasers. We measured the Doppler shifted frequencies for ^{174}Yb, when the spots aligned with the reference axis, and our measurements of these frequencies are plotted versus angle between the laser beams and the reference axes in figure 6.10. The expression from equation 6.1 was fitted to data and enabled us to estimate the average velocity of the atoms in the direction of the reference axis. Using the Doppler-shifted frequencies, the most probable velocity of the atoms in the direction of atomic beam was determined to be $260\pm$ 20 ms^{-1}.

Using frequencies measured from spot method technique,Yb^+ isotopes were successfully photo-ionised and trapped in ion trapping experiment discussed in chapter 5. To ionise a Yb atom, a 399-nm photon is required to drive the $^1S_0 \leftrightarrow^1 P_1$ transition where a further 369-nm photon excites an electron past the continuum [54, 81]. In the ion trapping experiment [97], the atomic oven and 399-nm laser made an angle of 63 ± 2^o. In this experiment the resonance frequencies for the $^1S_0 \leftrightarrow^1 P_1$ transitions were verified by photoionisation.

Chapter 7

Surface Traps

7.1 Introduction

There are two types of trap geometries, asymmetric ion traps [12, 23–25, 27, 29], where the electrodes lie in a plane and the ions are trapped above that plane, and symmetric ion traps [7, 10, 19–22, 98], where the electrodes are symmetrically positioned around the position of the trapped ion. Usually, asymmetric traps are known as surface or planar traps and symmetric traps are known as multilayer traps.
The main benefit of the linear surface trap configuration is its ability to be extended to large arrays to build a quantum computer. However, before planar ion traps can be used for quantum computing, several challenges will have to be solved. The trap frequencies in the surface trap designs can be made comparable to those in standard multilayer traps of similar dimensions. The radial frequencies are approximately one sixth to one third of those in a standard multilayer trap of similar size for similar dimensions and voltages.

The secular frequency depends on the applied voltages on the electrodes, the geometry of the trap and it typically increases for a smaller ion-electrode distance. However, motional heating of ions increases as one moves to smaller scales [30–33]. In surface ion traps, the ion-electrode distance can be optimised to reduce the heating rate by adjusting the sizes and separation of the radio frequency (rf) electrodes, as this allows to adjust the ion height [27]. One of the main challenges in surface traps is to achieve higher trap depths at larger ion-electrode distance, since they typically offer depths of about 1% of that of multi layer symmetric traps of comparable dimensions [29].

Typically, in ion traps, loading of ions is performed by using atomic ovens. Due to the high

temperature of ovens, atoms are initially highly energetic. Therefore lower trap depths in surface traps make loading difficult. However, once the ions are loaded and laser cooled, this is not a significant problem. In surface traps, Doppler cooling and ionisation lasers pass in parallel to the traps surface and may cause diffraction effect. To avoid this situation, ions have to be trapped above the surface electrodes at larger ion-electrode distance. This is also necessary for minimising anomalous heating of the trapped ions which increases by a decreasing ion height above the surface of the planar trap. Increasing the ion height also decreases the trap depth, therefore, surface trap geometries should be optimised to achieve higher trap depths at larger ion-electrode distance.

In fact, the trap depth and secular frequencies depend on applied voltages and geometric factors of surface trap geometries. As the applied voltages are limited by the breakdown voltage of the trap electrodes, it is important to optimise the trap depth and secular frequencies by adjusting the size of electrodes. The present study addresses the issues of how to design a basic element of surface trap arrays in which ions can be trapped with a maximum trap depth at a given ion-electrode distance by applying an rf voltage on rf electrodes.

7.2 Trap potential

In a typical three-dimension linear rf Paul trap, the rf field provides trapping in the x and y dimensions (transverse axes) and a static potential provides confinement in the z direction (principal axis). For an arbitrary electric potential of the form

$$\phi(x, y, z, t) = \phi_{rf}(x, y, z)\cos(\Omega t) + \phi_{(\text{static})}(x, y, z) \tag{7.1}$$

the effective secular potential or pseudopotential is given by [128]

$$\psi_{sec}(x, y, z) = \frac{e^2}{4m\Omega^2} \mid \nabla\phi_{rf}(x, y, z) \mid^2 + e\phi_{\text{static}}(x, y, z) \tag{7.2}$$

where e, m and Ω are the charge, mass and rf drive frequency respectively and ϕ_{rf} and ϕ_{static} are the rf and static potentials.

Using the secular potential, the height h of the ion above the plane of the electrodes, the secular frequencies in the harmonic region of the potential and the trap depth can

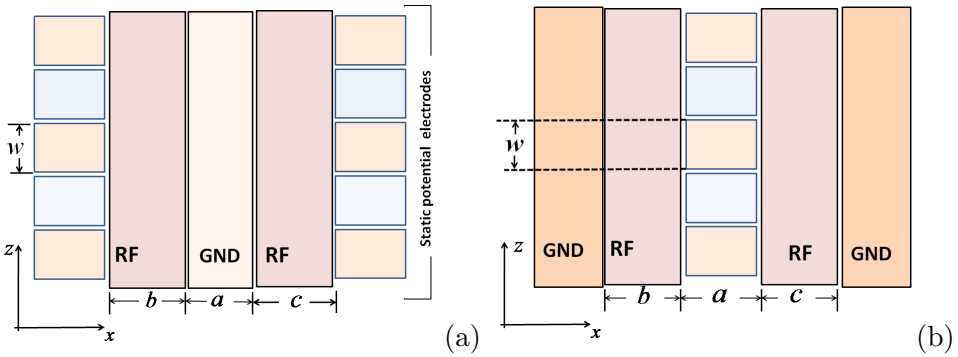

Figure 7.1: The *five-wire* planar trap designs (a) with outer and (b) centre segmented static potential electrodes of width w. The rf electrodes have widths of b and c and separated by a. Ions will be trapped between the rf electrode above the surface plane in y direction and shuttled in z direction using the static potential electrodes.

be calculated. The trap depth is defined as the minimum energy required for an ion to escape out of the trap. If the escape point is known, then the difference between the pseudopotential at the trap minimum (*rf-node*) and escape point gives the trap depth.

The surface electrode configuration is modelled in the gapless plane approximation, where the gaps between the electrodes are assumed to be infinitely small and the electrodes are extended in an infinite plane. Further, a necessary condition for the gapless plane approximation to be valid is that the ion-electrode distance h must be much greater than the size of the gaps. In microfabricated surface ion traps, these requirements are often met and usually surface traps are fabricated with small gaps, as any exposure of surface of the substrate can cause a disturbance in the operation of the trap due to the pick up of static charges [52].

In the linear Paul trap, the rf field provides trapping in the x and y directions while in the z direction the ion is confined by a static potential. For this to be achieved in surface trap geometries, the outer or centre rf ground electrode(s) are segmented as shown in figure 7.1 so that the static voltages can be applied to produce a trapping potential in the z direction. The location of the trap centre can be moved along the *rf-node* in the z direction by changing the applied voltages on the control electrodes. The electric field of the trap electrodes can be modelled by various methods using the Finite Element Method (FEM) or the Boundary Element Method (BEM). However, to work out optimum geometries, the analytical method suggested by House [129] is used as it provides faster and reliable solutions. Small gaps between the trap electrodes in realistic surface trap geometries usually have negligible effect on trap parameters [129, 130]. In order to verify this claim, two similar surface trap geometries made of rf-electrodes of 200 μm and 100

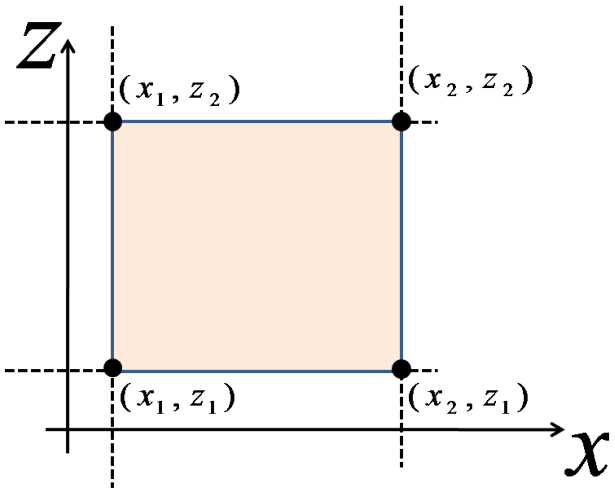

Figure 7.2: The position of an electrode defined in $x - z$ plane, where (x_1, z_1), (x_2, z_1), (x_1, z_2) and (x_2, z_2) are the positions of electrode corners.

μm widths separated by a distance of 70 μm were simulated with gapless approximation using analytical method suggested by House [129] and with BEM method including gaps of 5 μm between the separating ground electrode of width 60 μm and the rf electrodes including side trenches. The difference between the ion height and the escape point of the ion calculated from both simulation was observed $\approx 3\%$ and the difference in the trap depth was $\approx 7\%$. This shows the gapless approximation is a reasonable approximation.

The potential caused by an electric field of a rectangular surface electrode perpendicular to its surface are calculated analytically using the equation given by House [129]

$$\begin{aligned}\phi(x,y,z) =& \frac{V}{2\pi}\Bigg\{\arctan\left[\frac{(x_2-x)(z_2-z)}{y\sqrt{y^2+(x_2-x)^2+(z_2-z)^2}}\right] \\ &- \arctan\left[\frac{(x_1-x)(z_2-z)}{y\sqrt{y^2+(x_1-x)^2+(z_2-z)^2}}\right] \\ &- \arctan\left[\frac{(x_2-x)(z_1-z)}{y\sqrt{y^2+(x_2-x)^2+(z_1-z)^2}}\right] \\ &+ \arctan\left[\frac{(x_1-x)(z_1-z)}{y\sqrt{y^2+(x_1-x)^2+(z_1-z)^2}}\right]\Bigg\} \end{aligned} \tag{7.3}$$

where V is the applied voltage, and x_1, x_2, z_1 and z_2 are positions of electrode corners in the x-z plane (as shown in figure 7.2) allowing the potential to be calculated above this plane in the y-direction. In a linear Paul trap, the rf electrodes are typically very long in the direction of the principal axis (z-axis), therefore equation 7.3 can be reduced to; [129]

$$\phi(x,y) = \frac{V}{\pi}\left[\arctan\left(\frac{x_2-x}{y}\right) - \arctan\left(\frac{x_1-x}{y}\right)\right] \tag{7.4}$$

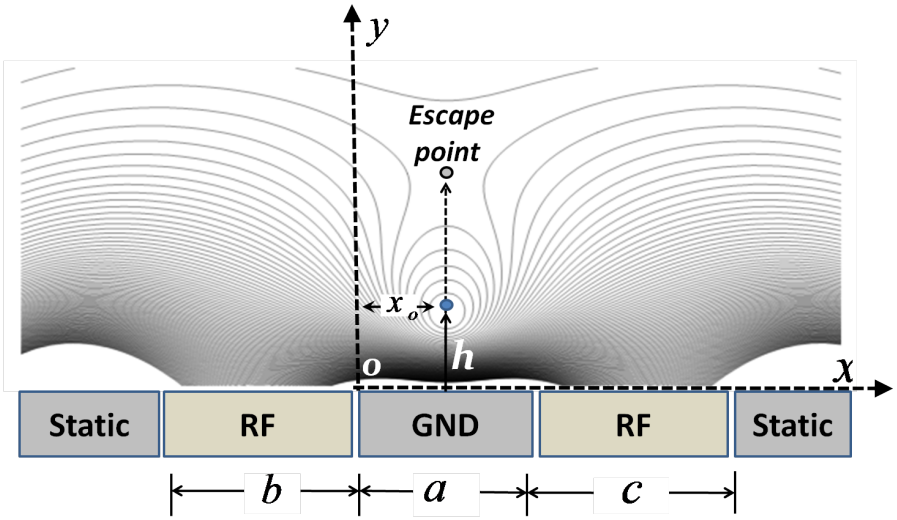

Figure 7.3: Illustration of pseudopotential field over the surface trap. x_o is the horizontal position of ion with respect to the central ground electrode, h is the height of a trapped ion above the central ground electrode, and the escape point for the ion is located beyond h. b and c are the widths of rf electrodes and a is the separation between the rf electrodes.

for the surface trap design shown in figure 7.1, the potential of the two long rf rails can be given by [129]

$$\phi(x,y) = \frac{V_{rf}}{\pi}\left[\arctan\left(\frac{a+b-x}{y}\right) - \arctan\left(\frac{a-x}{y}\right) - \arctan\left(\frac{x}{y}\right) + \arctan\left(\frac{c+x}{y}\right)\right]\cos(\Omega t) \tag{7.5}$$

where Ω is an rf drive frequency and V_{rf} is the applied peak rf voltage and b and c are the dimensions of the rf electrodes in the x direction or width of the electrodes, and a is the separation of rf electrodes or the width of the ground electrode. An ion can be trapped at the *rf-node* position where the gradient of the potential is zero i.e

$$\frac{\partial\phi(x,y)}{\partial_{(x,y)}} = 0 \tag{7.6}$$

The pseudopotential potential is obtained by applying appropriate voltages on the rf electrodes as shown in figure 7.3. All other electrodes are considered as *rf-ground*. The rf electrode dimensions are labelled as separation between rf electrodes a, while b and c are widths of rf electrodes. Figure 7.3 shows an the illustration of pseudopotential over the surface trap and the centre of an ion trap, which is located at a distance h above the ground electrode and lies between the rf electrodes. The vertical position h and the horizontal position x_o of the *node* of the ponderomotive potential can be found at [129]

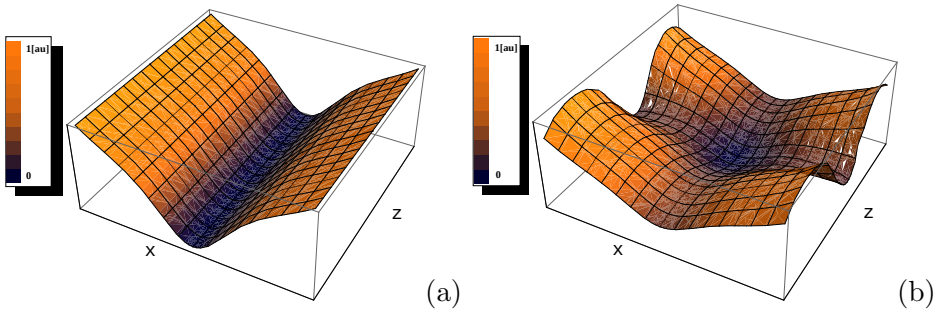

Figure 7.4: 3D plots of the pseudopotential field over the surface trap at the *rf-node* position: (a) with only rf electrodes and (b) with rf and static potential electrodes.

$$x_o = \frac{ac}{b+c}, \qquad h = \frac{\sqrt{abc(a+b+c)}}{b+c} \tag{7.7}$$

and are shown in figure 7.3. In a surface trap, the electrodes that produce the rf field are placed in a way that they create a local pseudopotential minimum above the electrode surface, in the y direction, where the ions can be trapped as shown in figure 7.3. The pseudopotential caused by rf electrodes at the *rf-node* position is illustrated in figure 7.4(a). Figure 7.4(b) shows the overall pseudopotential when the static potential generated by static electrodes is added to the rf potential.

The turning point or escape point of the pseudopotential is located above the trap centre. Beyond this point, the pseudopotential approaches zero as y approaches infinity. The turning point can be found by using numerical solutions to find a location above the trap centre where the gradient of the pseudopotential is zero, or, alternatively by using geometric parameters [129]

$$h_e = \frac{\sqrt{a(b+c)+a^2+2(a+b)\sqrt{a(b+c)+a^2)}}}{2}, \tag{7.8}$$

Equation (7.8) shows that the position of the trap centre or the ion height h above the central electrode depends on the separation a and the widths b and c of rf electrodes.

The best estimation of the depth of a trap can be approximated by calculating the difference between the potential at the trap centre (*rf-node*) and the turning point shown in figure 7.5

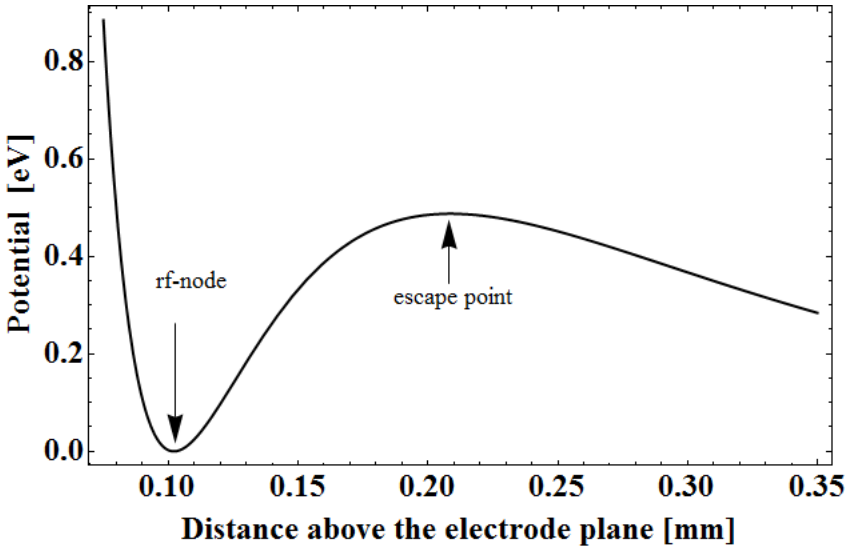

Figure 7.5: Plot of the pseudopotential field over the surface trap. *rf-node* and the escape point is located where the gradient of pseudopotential is effectively zero

7.3 Optimisation of trap depth

In a surface ion trap, the distance between the trapped ion and the electrodes must be adjusted so that proper laser access is ensured and laser scattering form the surfaces is avoided. Furthermore, a trap should be designed to achieve the maximum trap depth to keep the ion trapped for long time and heating of the ion also has to be kept at a minimum which depends upon the ion-electrode distance as earlier discussed. The trap depth is typically very low in surface trap geometries at larger ion-electrode distances [29]. Therefore trap geometries should be optimised to produce maximum trap depth at given ion-electrode distance (height h). The trap depth can be defined as the difference of the trap potential at *rf node* position (x_o and h) and the escape point (x_o and h_o). The trap potential at the escape point for the ion Ξ can be found as [129]

$$\Xi = \frac{\Gamma}{h^2}\kappa \tag{7.9}$$

where,

$$\Gamma = \frac{e^2 V_{rf}^2}{\pi^2 m \Omega^2} \tag{7.10}$$

and

$$\kappa = \left[\frac{2\sqrt{abc(a+b+c)}}{(2a+b+c)(2a+b+c+2\sqrt{a(a+b+c)}}\right]^2 \tag{7.11}$$

Equation (7.9) shows that the trap depth depends on the position of the trapped ion above

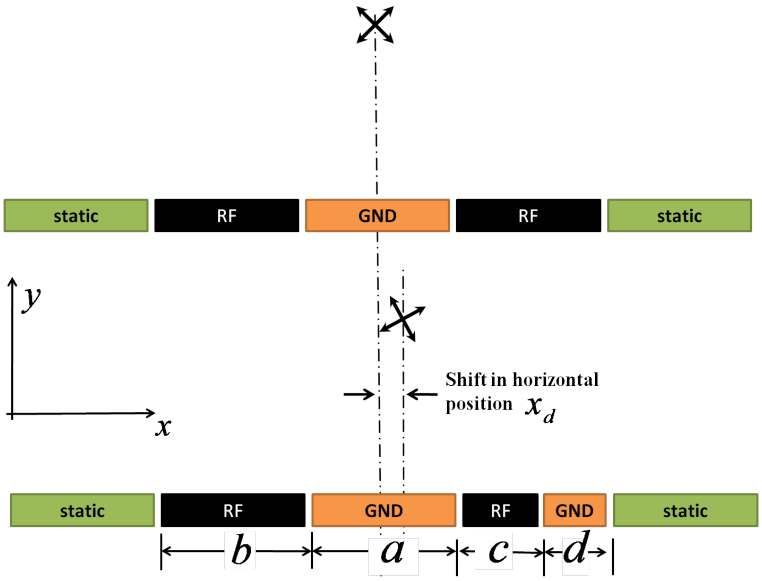

Figure 7.6: The rotation of the principal axis by breaking the symmetry of rf electrodes. Horizontal shift in ion's position caused by rf-asymmetry can be seen. To keep the static potential electrodes symmetric around the principal axes, an extra ground electrode of width d is inserted.

the electrodes h and the geometric factor κ which is defined in eq. 7.11 where a, b and c are the widths of rf electrodes (see figure 7.3). Γ is defined in equation (7.10) in terms of applied rf voltage V_{rf}, mass of the trapped ion m and rf drive frequency Ω. The trap depth geometric factor κ can be optimised by proper design and arrangement of rf electrodes. By choosing appropriate electrode widths, the trap geometries can be optimised to achieve the maximum trap depth for a given ion height. In the surface trap geometries shown in Fig. 7.1, the ion height h or *rf node* position depends on the dimensions of trap electrodes.

In surface traps, the cooling lasers pass parallel to the trap's surface without striking it. Therefore, they will leave motion along a principal axis perpendicular to the surface uncooled. The solution to this problem can often be achieved by rotating the principal axes [131]. An asymmetric rf electrode design in which one of rf electrodes is made larger in width than the other is capable of rotating the principal axis [52]. For the trap geometries shown in figure 7.1, one half of the ratio of the rf electrode width is enough to rotate the axis of these modes by 3^o [13] and hence provide efficient Doppler cooling in all directions. The rotation of the axis by breaking the symmetry of rf electrodes is illustrated in figure 7.6.

Unequal widths ($b \neq c$) of the rf electrodes cause planar asymmetry in the horizontal x-axis and set off a nonuniformity in the confinement field when equal static voltages are applied on opposite static electrodes. This issue can be addressed by introducing an

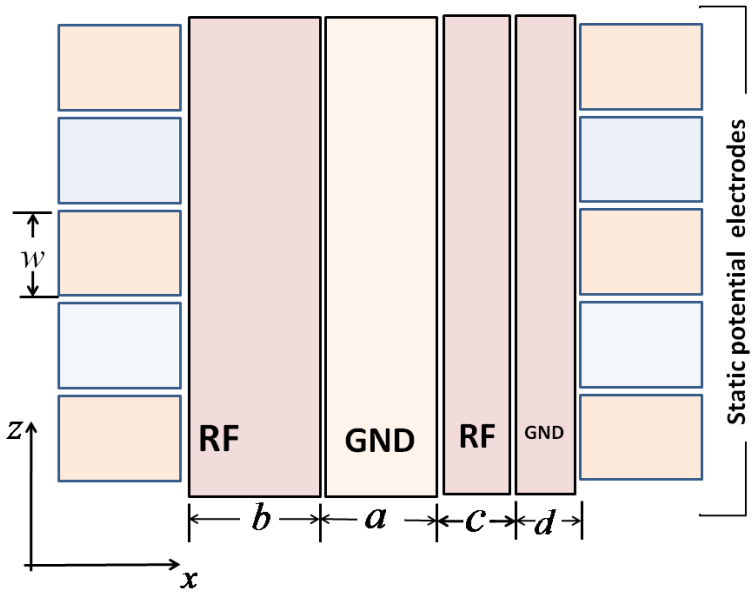

Figure 7.7: In order to keep the static potential electrodes' position symmetric around the trap axis, in case of unequal rf electrodes, an extra ground electrode of width d is introduced between the narrower rf and segmented electrodes.

extra ground electrode of width d between the narrow rf electrode and segmented static electrodes in parallel to the rf electrode as shown in figure 7.6 and figure 7.7. The width d of the ground electrode (in gapless approximation) may be chosen as the difference in the widths of the rf electrodes ($\Delta w = |b - c|$) plus the shift (x_d) in the horizontal position of *rf-node*, x_o, caused by the asymmetry,

$$\begin{aligned} d &= \Delta w + x_d \\ d &= \Delta w + \left(\frac{ac}{b+c} - \frac{a}{2}\right) \end{aligned} \tag{7.12}$$

The ratio between the rf electrode widths b and the separation between rf electrodes a in figure 7.7 is useful to characterise κ at a given ion height. Using the ratio $\zeta = b/a$, between rf electrode width b and rf electrode separation a, the geometric factor κ can be parameterised as the following

$$\kappa = \begin{cases} \dfrac{\zeta^2(1+2\zeta)}{4(1+\zeta)^2(1+\zeta+\sqrt{1+2\zeta})^2} & \text{when } c = b \\ \dfrac{4\zeta^2(2+3\zeta)}{(2+1.5\zeta)^2(4+3\zeta+4\sqrt{1+1.5\zeta})^2} & \text{when } c = b/2 \end{cases} \tag{7.13}$$

The plot of the trap depth geometric factor κ as a function of ζ is shown in figure 7.8. The

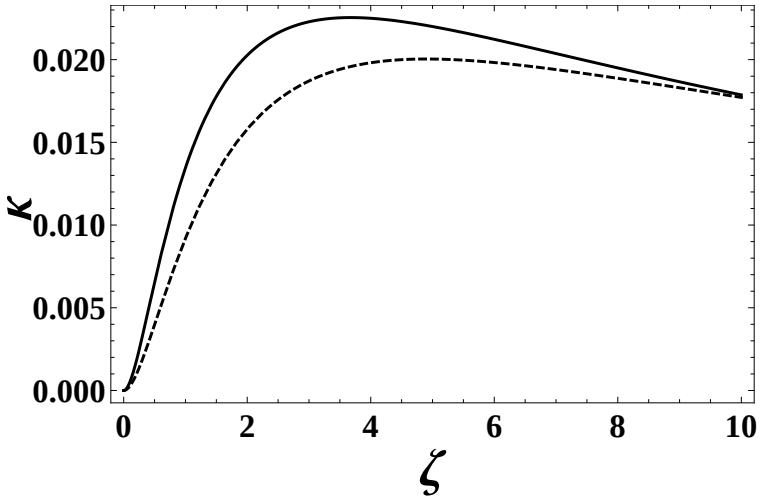

Figure 7.8: For a given ion height, trap depth geometric factor κ can be maximised for equal width rf electrodes ($c = b$) when the ratio between rf width and separation $\zeta \approx 3.68$ (solid curve). In case when rf electrodes widths are unequal and ($c = b/2$), the κ is maximum when the ratio $\zeta \approx 4.9$ (dashed curve).

solid curve in figure 7.8 shows the plot of κ at a given ion height as a function of ζ when $c = b$. The maximum κ can be found at $\zeta \approx 3.68$ for rf electrodes of equal widths and for unequal rf electrodes when $c = b/2$ at ≈ 4.9, as shown in the dashed curve in figure 7.8. For the optimised values of ζ, the ion height above the electrodes is given by $h = 0.39b$ for the equal width rf electrodes and $h = 0.26b$ when $c = b/2$. In general, the maximum trap depth decreases with increasing height of the trapped ion and scales as h^{-2}. It is important to note that anomalous heating of a trapped ion is proportional to $\sim d^{-4}$, where d is the distance between the centre of the trap and the nearest electrode [30, 31]. The trap depth increases with a decrease in ion-electrode distance, but the heating rate also increases with a decease in the distance. Therefore, the aim of an optimum trap design is to achieve the maximum trap depth at a given distance above the electrodes. This distance should be compatible with motional heating constraints of the experiment to be carried out.

7.4 Optimum voltages

Once the trap depth is optimised using the optimum trap geometry, the next step is to increase the trap depth for an ion by applying the appropriate rf voltage on the rf electrodes. This should be calculated carefully as the trap depth Ξ, a-q -parameters (trap stability) and the power dissipation P_d in the trap, are all dependent on the applied rf voltage and the drive frequency for the given ion height. The trap depth Ξ and the q-

parameter can be related using by combining the equation (7.9) and the equation (2.10) for q given in chapter 2,

$$\Xi = qV_{rf}\frac{\kappa}{2\pi^2} \tag{7.14}$$

where, $\kappa \approx 0.02$ for a surface trap in which optimum asymmetric rf electrodes are used. If there is no static voltage on the rf electrodes then the a=*0* and if q is set to ≈ 0.7 then the q-parameter is well inside the stability region shown in figure 2.2 in chapter 2.

In order to achieve the reasonable value for the trap depth at given ion height, it is necessary to work out optimum rf voltage V_{rf} for the trap. First, it is important to set an appropriate limit for the applied voltage such that it should not be close to the breakdown voltage of the materials used to fabricate the trap and the second important constraint is the dissipation of power in the trap which may cause the heating of the trap and may result in rise in the anomalous heating of the trapped ion and outgassing from the trap material. Keeping all the above constraints in mind, for a case study, a microfabricated trap made of gold electroplated electrodes on Silicon Di-Oxide (SiO_2) is considered here. The rf voltage breakdown for such electrodes depends upon the number of factors including, the gap between the trap electrodes, the insulator material used to separate the electrodes from the substrate and the level of vacuum in the chamber in which the trap has to be operated [132]. For an optimum trap geometry in which rf electrodes of widths $b = 300$ μm and $c = 150$ μm are separated by a ground electrode of width of 50 μm and electrode-electrode gap is ≈ 5 μm, an rf voltage of ≈ 500 V can safely be applied or at any time voltage difference between the electrodes (rf electrode to ground or static electrodes) should not cross above 500 V. An approximate estimation of the power dissipation P_d can be calculated using the following equation [91]

$$P_d = 0.5V_{rf}^2\Omega_{rf}^2C^2R \tag{7.15}$$

where, V_{rf} is peak to peak rf voltage, Ω_{rf} is the rf drive frequency, C and R are the capacitance between the rf electrode and the rf ground, and the resistance of the rf electrode of the trap respectively. For the above discussed trap, values of the capacitance C and resistance R are considered as ≈ 20 pF and $\approx 0.4\ \Omega$ respectively. The values are estimated by physically measuring a similar dimensioned SiO_2 trap in our lab.

After considering the basic limitation of the applied voltage, it is important to work out the rf drive frequency Ω_{rf} such that the a and q-parameters for the trap remain well inside the stability region (shown in chapter 2) for a given ion height and the power dissipation

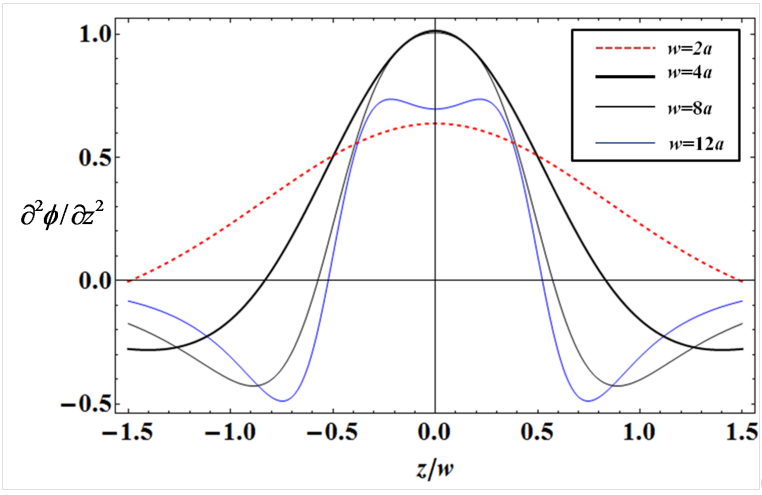

(a)

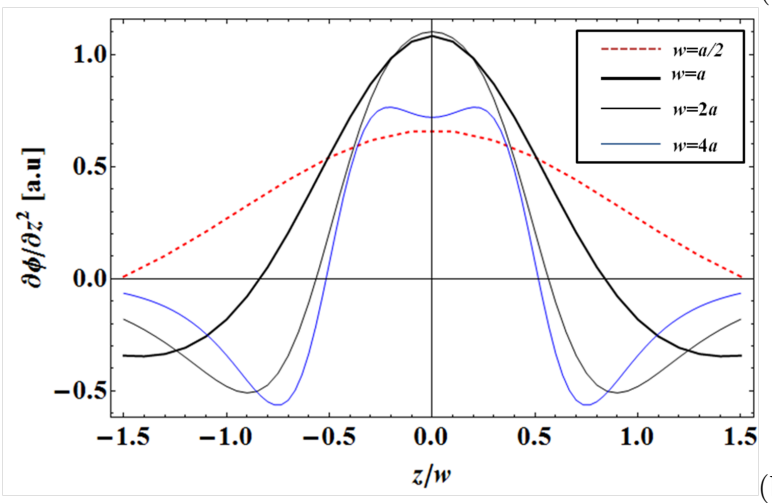

(b)

Figure 7.9: Potential curvature $\partial^2\phi/\partial z^2$ in the z direction at the trap centre as a function of z/w, where w is a width of a control electrode. For small w, the curvature is relatively small. For large w, zero in the curvature approaches to the edge of the electrode. The potential curvature has maximum at the trap centre and reaches zero near the centre of neighbouring electrode $z/w = \pm 1$ when (a) $w = 4a$ for the outer segmented electrode geometry and (b) $w = a$ for the centre segmented electrode geometry.

P_d in the trap remain at acceptable values. For a given value of $q \approx 0.7$, an rf drive frequency of $\Omega_{rf} = 2\pi$ 55 MHz can be chosen for the rf voltage of 500 V. At these given values, the power dissipation P_d is < 3 W and the trap depth of 0.35 eV can be achieved for an $^{171}Yb^+$ ion at ion height of $h = 82$ μm.

7.5 Control electrode design

As discussed earlier, the confinement of the trapped ion in the z direction is achieved by applying static voltages on the segmented electrodes and the ion can be shuttled by varying these voltages. To avoid the heating of the trapped ion during its transportation,

it is required to maintain a constant value of the curvature of the potential well in the z direction ($\partial^2\phi/\partial z^2$) along the transportation path [129]. House [129] suggested that, the width of a segmented electrode w should be chosen in a way that the field it creates has a significant curvature everywhere along the path of the ion near the electrode. Using the optimisation parameters obtained in the previous section, for symmetric distribution of the segmented electrodes in figure 7.1(a), the potential curvatures ($\partial^2\phi/\partial z^2$) for four different choices of electrode widths w are plotted in figure 7.9(a), where as the electrodes are centred at zero and corners of each electrode is at ± 0.5 on the x-axis. For a relatively small width, $w{=}a$, the influence of the electrode's potential at the trap path is small. For the relatively larger w (when $w = 8a$), the potential tends to flatten or may produce a kink at the centre (when $w = 12a$). The major concern for the larger width of electrodes is the location of the potential curvature minimum which approaches the edge of the electrode, $z = \pm w/2$, as w increases. Since the neighbouring electrodes of the same size also have a minimum near the same edge, the ion will feel less influence of the electrodes while crossing this location during the shuttling process. For the trap design shown in figure 7.1(a), outer segmented electrode widths may be chosen as $w \approx 4a$. The electrodes with this size have maximum potential curvature at the trapping path and provide sufficient overlapping of the potential curvatures at their edges as shown in figure 7.9(a). When the central rf ground electrode is segmented to provide axial confinement as shown in figure 7.1(b), the width of a segment should be chosen as $w = a$. This smaller optimum width is due to the fact that the ion has to be trapped right above these electrodes. For the central segmented electrode, the potential curvatures are plotted with different widths in figure 7.9(b).

7.6 SOI trap chip

Considering the limitations of microfabrication techniques, a surface ion trap chip is designed in our lab on the basis of the optimisation discussion in previous sections. The rf electrodes in the designed surface trap chip shown in figure 7.10 have one-half ratio of their widths, 200 μm and 100 μm, in order to rotate the principal axis. Both electrodes are seperated by 70 μm. The electrodes are arranged in a way that the *rf-node* in linear sections is at $\approx$75 μm above the trap's surface. Simulations have shown that trap depth of ≈ 0.19 eV and axial secular frequencies ($\omega_x/2\pi$ and $\omega_y/2\pi$) of 3.4 MHz and 3.5 MHz can be achieved for $^{171}Yb^{+}$ with an rf drive frequency ($\Omega/2\pi$) of 45 MHz and rf

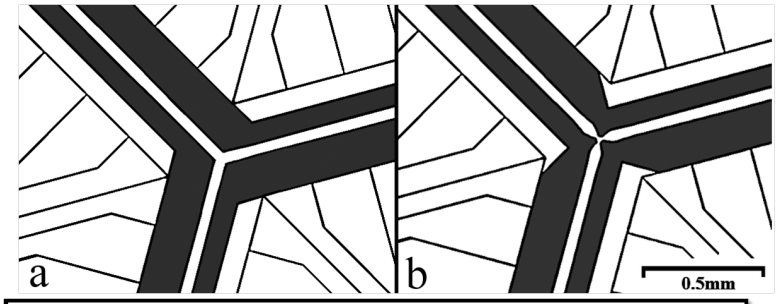

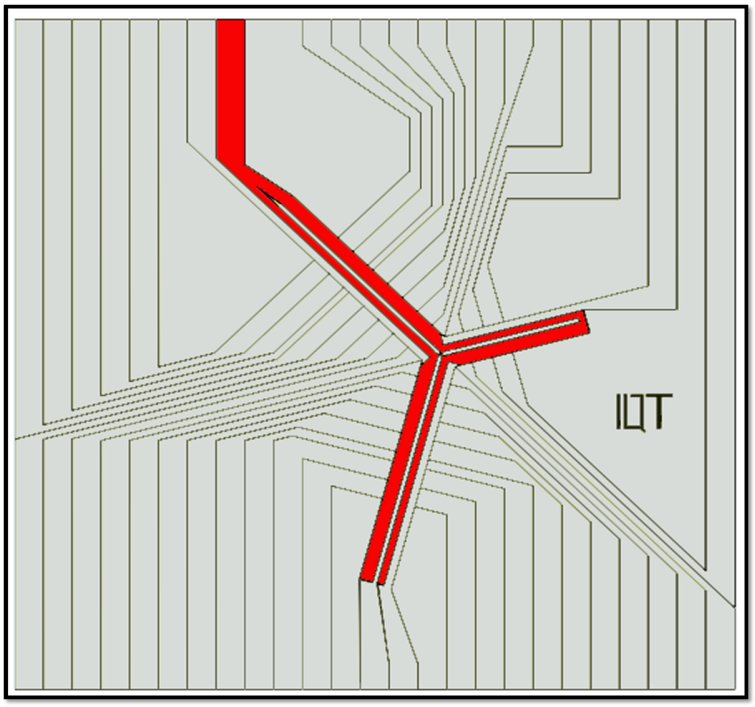

(c)

Figure 7.10: (a) Unmodified junction region and (b) Modified junction region. (c) Modified surface trap chip with 44 segmented electrodes.
(*Figures are provided by Robin Sterling*)

peak voltage of 200 V. The trap has three linear sections joining each other at an angle of 120^o and forming a Y-shaped junction. For the axial control of the trapped ions in linear and junction regions, there are 44 individually controlled static potential electrodes. The control electrodes are made by segmenting the rf ground electrode surrounding the rf electrodes. The width of each segmented electrode is chosen to be $\approx 4a$. The segmented electrodes are separated by 5 μm to avoid electrical shorting between them. In order to keep the distribution of static potential electrodes symmetric around the trap axis, an rf ground electrode is introduced on the narrower rf electrode side, parallel to the segmented electrodes.

Y-junction

In linear sections of a trap, the gradient of the potentials is zero at the rf nodal path, but where the linear regions intersect, this condition is not fulfilled due to the break down of the rf electrode symmetry. The ponderomotive field in a linear trap is predominantly quadratic in nature but where the linear traps intersect, higher order multipole terms appear and play an adverse role in trapping potentials by producing potential barriers in these regions [9]. Hence, trapped ions may feel a repulsive ponderomotive force when entering these regions which may push ions away from the junction regions [133]. Several attempts have been made on constructing trap junctions, as they are needed for large scale quantum information processing using trap networks [18, 19, 22, 25, 27, 98, 133–135].

To reduce effects of the anti-trapping nature of the trap junction and suppress the potential barriers, it is suggested by Wesenberg [9] that the linear traps should intersect at oblique angles like in X or Y junctions rather than at right angle like in T-junctions. Keeping this in mind, an ion trap array using a Y-shaped interaction path has been designed in our lab [136]. Optimisation of the junction geometry was achieved by tweaking the junction corners manually using detailed simulations, including gaps between the electrodes, side walls and trenches of a surface trap geometry in the junction region.

7.6.1 Fabrication

Stray electric charge collected on exposed dielectric surfaces of a trap geometry poses a significant problem for the trapped ion by pushing the ion out of the *rf-node* position. The main feature of our trap design is that all the exposed dielectric insulator regions

are shielded from the line of sight of the trapped ion. This will significantly reduce the electrostatic effect of stray fields generated by insulating areas of the surface.

For the fabrication of the trap, Silicon-on-insulator (SOI) wafers are used. In a commercially available SOI wafer, a thin layer of insulating material silicon dioxide (SiO_2) is sandwiched between two layers of silicon, one is called the handle layer which is of a few hundred microns thick, and a device layer which is tens of micrometers thick. These wafers can be bought with required thicknesses and resistances. The SOI wafer used in our trap fabrication has 600 μm and 30 μm handle and device layers respectively, made of heavily n-doped silicon with resistivity of 0.001-0.005 Ωcm, and a 10 μm thick layer of SiO_2. Using the etching techniques and photolithographic mask, the surface trap electrodes made of gold layer are fabricated on the device layer of the SOI wafer in a way that the insulating material (SiO_2) is shielded from the ion. This is made possible by removing the SiO_2 isotropically beneath the electrodes using hydrofloric acid (HF). The capacitance of the microfabricated trap is estimated to be 15 pF. The resistance of the trap is predicted to be 10 to 15 Ω, using the resistivity of gold and silicon.

7.7 Modelling and simulation

In order to calculate the basis functions for the trap electrodes, the analytical method suggested by House [129], gives a good approximation for the parameters of a surface trap design. As the method is based on a gapless approximation, it is also suggested to simulate a trap using actual trap geometry including the gaps and the trenches between the electrodes. Numerical methods are useful to achieve the basis function of an actual trap geometry. There are many commercial and non-commercial softwares available to simulate electrical fields of arbitrary shaped trap electrodes. The numerical method suggested by K. Singer *et al.* [137] is one of them and can be used to calculate electric potentials of the trap electrodes. The program written in **C++** is based on the Boundary Element Method (BEM). It works by dividing the trap electrodes into small surface elements of uniform surface charge density and then using Coulomb's law, calculating the potential in space caused by these elements. This BEM problem is solved using fast multipole method (FMM) algorithm. The ability of the program to read the AutoCAD files for importing geometrical structures makes it useful for generating an electric potential for an arbitrary shaped electrode. An other commercially available software package Charged Particle Optics software package (CPO) which also uses BEM method, can be also be used for

relatively smaller trap geometries. In order to compare these methods, electric potentials for the rectangular electrodes in linear regions of a trap are calculated using Singer's **C++** program, CPO and analytical model suggested by House [129] and the results were found consistent at an acceptable level of accuracy ($< 5\%$).

The accuracy of the electrical potentials calculated by Singer's program is highly dependent on the size of the mesh (three dimensional space) and the *refine* factor. The size of the mesh and refine factor depend upon trap geometries under the study. Lower refine factor and higher density of the position points defined in the mesh highly improves the reliability of the data. Using the $10 \times 10 \times 10$ mesh and $40 \times 40 \times 40$ mesh with same refine factor for the same region of the trap section, a 5% variation in the trap depth, 4% variation in the x-secular frequency and 18% in the Y-secular frequency was observed. It is observed that a denser mesh entry gives more accurate data and is consistent with the results obtained with the CPO. But a denser mesh settings in Singer's program drastically increase the compilation time and size of the data file.

By applying 1 volt to one of the trap electrodes at a time and keeping all other electrodes zero, the program calculates electrical potentials in the defined mesh region. By repeating the same process for all the trap electrodes a set of data files is generated. Then, all these potential fields are added together in Mathematica, to find the ponderomotive potential in the trapping region. The *rf-node* is calculated by using the rf pseudopotential while keeping the static potential zero. The set of all the *rf-node* points in the direction of the z-axis makes the *rf-nodal* path where the ion will be trapped and shuttled. In linear regions of the surface trap, the *nodal-path* is strictly a straight line but due to the asymmetry in the rf field caused by the shape of the rf electrodes in the Y-junction region, the *rf-nodal* path varies as it approaches the junction region. Figure 7.11 shows the horizontal and vertical shift in rf-nodal path near the junction region. To keep the ion trapped firmly, the pseudopotential in the *rf-nodal* path must be zero or close to zero. As discussed earlier, a potential barrier develops along the *rf-nodal* path in the junction region and can be seen in figure 7.12. The barrier is high in case of unmodified trap geometry. The potential barrier corresponds to an rf drive frequency of $\Omega_{rf} = 2\pi$ 45 MHz and an rf voltage of 280 V for $^{171}Yb^{+}$. An rf barrier suppression factor of ≈ 7 was achieved for an optimised trap geometry versus un optimised one. The radial secular frequencies (ω_x and ω_y) for the trapped ion also varies as the ion reaches into the junction region. The variation of the secular frequencies are plotted for the unmodified and modified junction region in the figure 7.13.

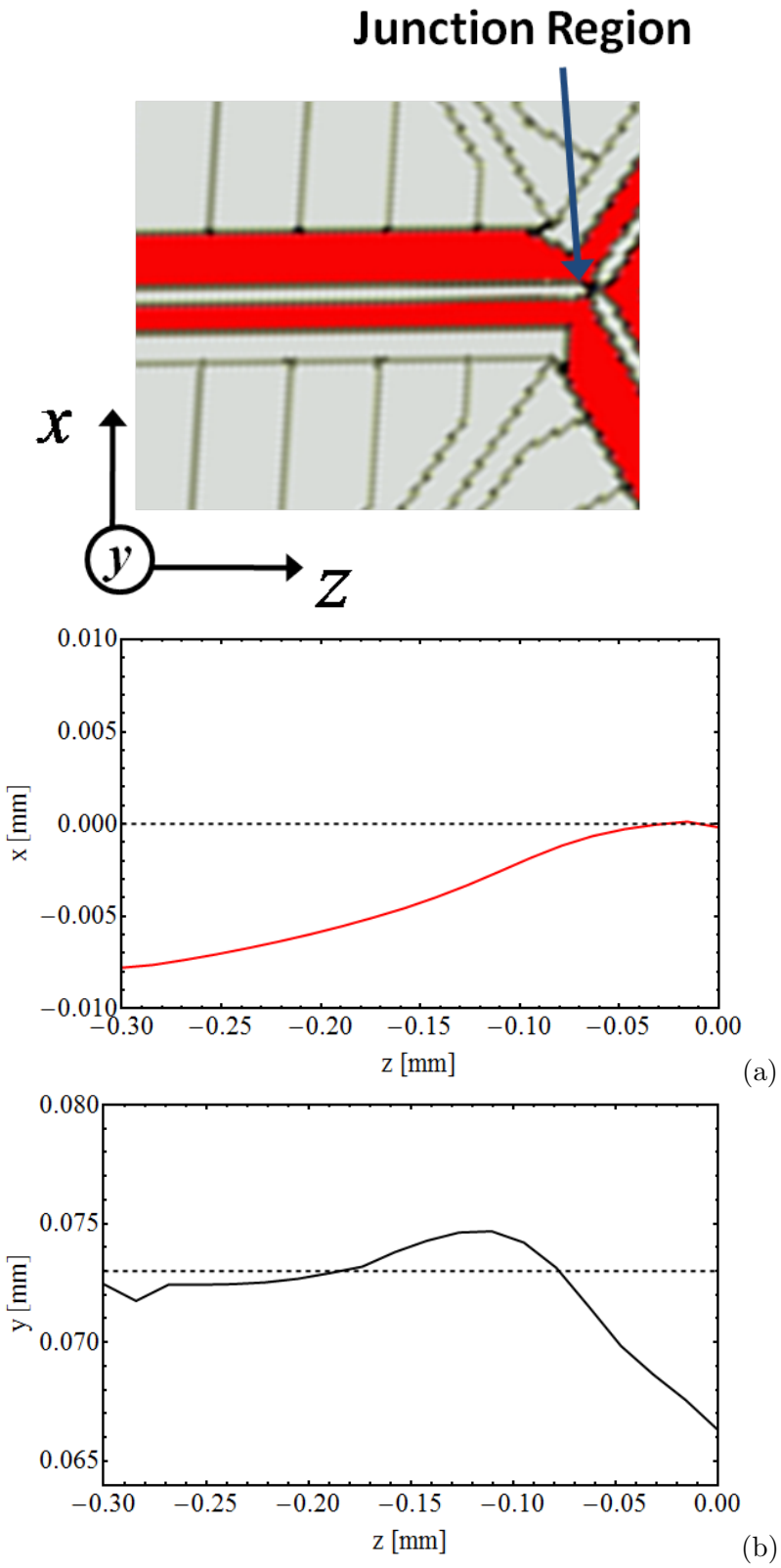

Figure 7.11: (a) Horizontal displacement of the rf-nodal path from the central line (dashed line) of the ground electrode along the z-direction towards the junction region where the zero on the horizontal axis corresponds to the centre of the junction region. (b) Variation in the ion height along the z-direction towards the junction region.

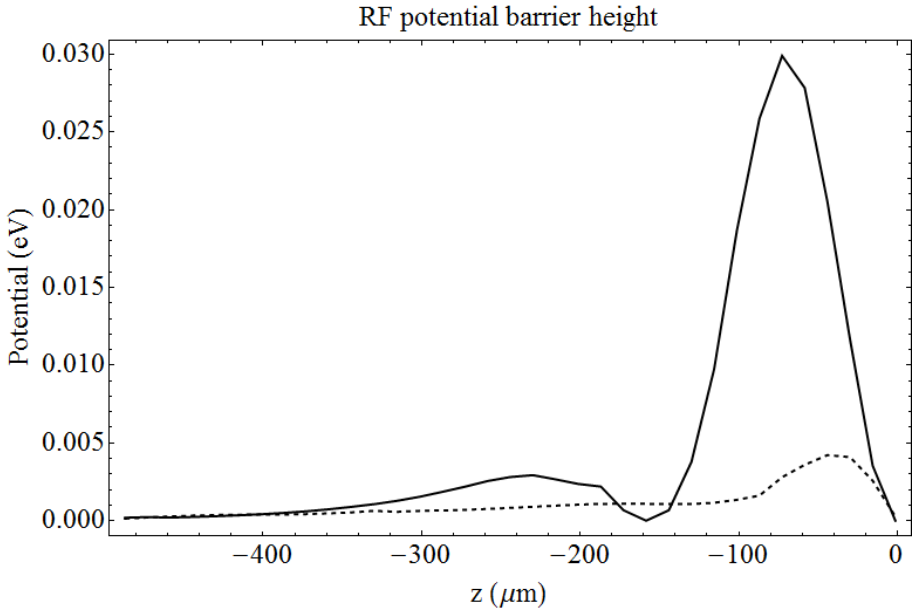

Figure 7.12: The barrier potential of the unmodified (solid line) and modified (dashed line)trap along the *rf-nodal* path near the junction region. The potential corresponds to an rf drive frequency of $\Omega_{rf} = 2\pi$ 45 MHz and an rf voltage of 280 V for $^{171}Yb^{+}$.

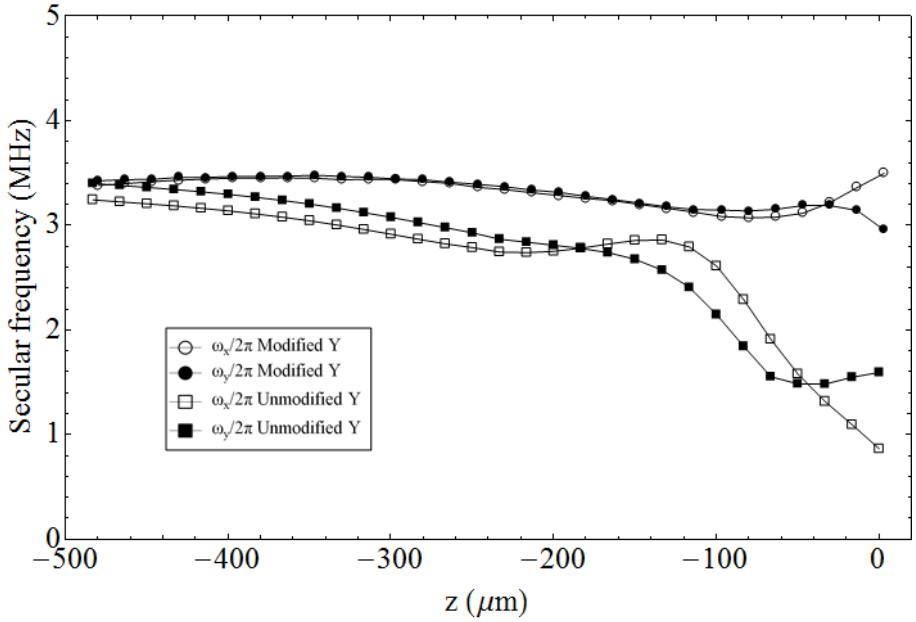

Figure 7.13: Variation of the radial secular frequencies (ω_x and ω_y) along the *rf-nodal* path near the junction region. The radial frequencies correspond to an rf drive frequency of $\Omega_{rf} = 2\pi$ 45 MHz and an rf voltage of 280 V for $^{171}Yb^{+}$.

Chapter 8

Ion Separation

8.1 Introduction

Modern microfabrication techniques are promising to build scalable ion trap arrays in which ions will be brought together and separated many times in processor zones to perform gate operations. This is best attainable when traps are designed at micrometer scale in such a way that they provide for fast ion separation and recombination. How to optimise electrode geometries for efficient ion separation and recombination has been discussed by Home et el. [138] for the general case. Optimisation for the particular case of surface ion trap arrays is discussed here. The speed of the adiabatic shuttling operation can be enhanced by maximising the secular frequency during separation and recombination inside the trap arrays [133]. The secular frequency depends on the applied voltages on the electrodes, the geometry of the traps and it typically increases for smaller ion-electrode distances. However at smaller scales, motional heating of ions increases [30–33].

In this chapter, it is discussed, how to design surface trap arrays in which ions can be trapped at a maximum trap depth at a given ion-electrode distance and can be brought together and separated rapidly by adjusting static voltages on electrodes while maintaining highest possible secular frequencies. Maximisation of the secular frequency during separation and recombination shuttling processes by adjusting the widths of the static electrodes for ion transportation in general, and fast ion separation and recombination processes in particular, is discussed in section 8.4. At the end, two designs are compared and shown that the separation process may be made faster by decreasing the ion-static-electrode distance and optimising the electrode dimensions.

8.2 Design considerations

For fast and effective ion separation, the following design guidelines should be obtained.

- The arrangement of rf and static electrodes in an ion trap should be such that it allows a path for ions to be moved into and out of the region of the close pair of trapping centres.
- To avoid odd orders of the trapping potential in the axial direction, the surface trap design should be symmetric in the trapping plane.
- In order to minimise the heating of the motional modes of the trapped ions, the surfaces of the electrodes should be kept as far as possible from the trapping regions where the ions travel. This reduces the impact of anomalous heating on the ions and allows better optical access to manipulate the ions.
- In order to maximise the speed at which ions can be moved / separated by displacing the trap centres, the trap confinement should be tight. This can be achieved by keeping the vibrational frequency of the ions as high as possible.
- To avoid electrical breakdown the electric fields at the electrode surfaces must not exceed the voltage breakdown limitations of the materials.
- The trap geometry should be capable of being fabricated accurately at the required distance scale. This may require microfabrication techniques which have their own intrinsic limitations.

8.3 Ion separation: theory

In the ion separation process, initially, ions are trapped in a single potential well with secular frequencies ω_x, ω_y and ω_z, normally $\omega_x, \omega_y >> \omega_z$, where ω_x and ω_y predominantly depend on the ponderomotive potential provided by the rf electrodes and ω_z depends on the static voltages of the control electrodes. The static potentials can be applied and used in such a way that a wedge potential can be created between the trapped ions and the single potential well can be pulled apart in two distinct potential wells or a *double well* in the z-direction of the trap geometry. The aim of an effective separation is that the ions remain trapped, acquire minimal kinetic energy during the separation process, and that the separation process is reliable. For adiabatic separation to be possible, the separation

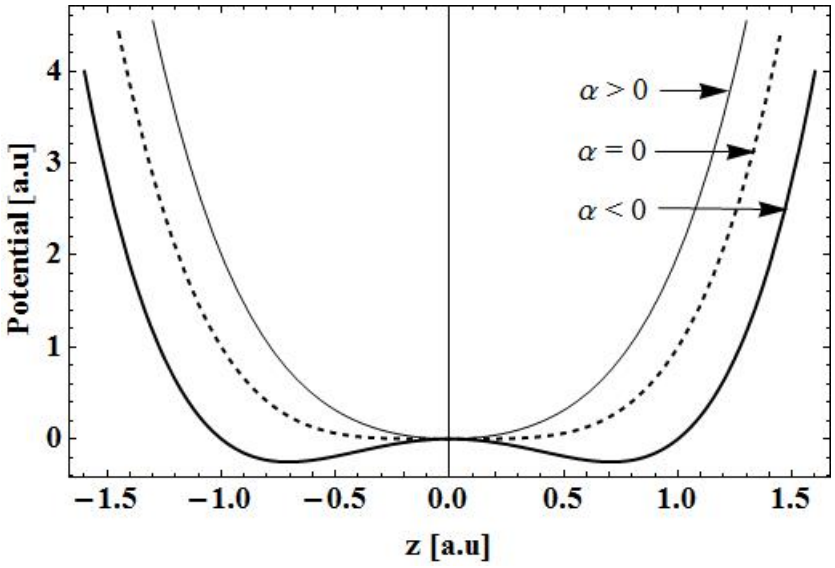

Figure 8.1: Plots of the potential when $\alpha > 0$, zero and $\alpha < 0$. The potential wedge is created when $\alpha < 0$

process must be slow compared to the minimum secular frequency during separation. In this section, the foundations of ion separation process described by Home, et al. [138] is summarised. The confinement field near the centre of a trap in the z direction can be analysed using a Taylor expansion as [138]

$$V \approx 2e\alpha z^2 + 2e\beta z^4 \tag{8.1}$$

where, V is the potential in electron Volt (eV), α and β are the coefficients of quadratic and quartic terms in units of V/m^2 and V/m^4 respectively and e is the charge of an ion. The confinement of ions in all three directions will be achieved by adding the oscillating 2D rf field to the static potential described in equation 8.1.

Figure 8.1 shows the plots of Eq.(8.1) when $\alpha > 0, \alpha = 0$ and $\alpha < 0$. A potential wedge can be seen in the middle of the trap when α becomes negative. The equilibrium position of the ions in the potential well is $z = \pm d/2$ where d can be found by using the Coulomb's force between the ions and taking the gradient of the potential defined in equation (8.1), [138]

$$\begin{aligned} F_c &= \frac{\partial V}{\partial z} \\ \frac{1}{4\pi\epsilon_o}\frac{e^2}{d^2} &= \left(\alpha d + \frac{\beta d^3}{2}\right)e \\ \text{or,} \quad \frac{e}{2\pi\epsilon_o} &= 2\alpha d^3 + \beta d^5 \end{aligned} \tag{8.2}$$

When $\alpha > 0$, ions are trapped in a well defined single potential well and d is very small, therefore $\alpha d^3 \gg \beta d^5$ in the second term on the R.H.S of equation (8.2) and d can be found as [138]

$$d \simeq \left(\frac{e}{4\pi\epsilon_o\alpha}\right)^{1/3} \tag{8.3}$$

When α approaches zero, the potential well is shallow and ions are separated at [138]

$$d \simeq \left(\frac{e}{2\pi\epsilon_o\beta}\right)^{1/5} \tag{8.4}$$

When $\alpha < 0$, a potential *double-well* is created and both ions are trapped in separate potential wells. Therefore the force between the ions is negligible and left hand side in equation (8.2) will be considered zero, hence the both trap centres are at distance [138]

$$d \simeq \sqrt{\frac{2 \mid \alpha \mid}{\beta}} \tag{8.5}$$

The secular frequency in all three regions shown in figure 8.1 can be found by taking the second derivative of the potential in equation (8.1) and dividing by the mass of the ion [138]

$$\frac{d^2V}{dz^2} = \Big(2\alpha + 12\beta z^2\Big)e \tag{8.6}$$

By defining the z in terms of d and dividing by the mass m of the ion the secular frequency ω_z can be defined as [138]

$$\omega_z \simeq \sqrt{\frac{1}{m}\frac{d^2V}{dz^2}} \simeq \sqrt{(2\alpha + 3\beta d^2)\frac{e}{m}} \tag{8.7}$$

When $\alpha > 0$ in a single well, the secular frequency can be calculated as [138]

$$\omega_z \simeq \sqrt{\frac{2\alpha e}{m}} \tag{8.8}$$

When $\alpha < 0$, by inserting the equation 8.5 for d into equation 8.7, the z-secular frequency in each *double well* can be calculated as [138]

$$\omega_z \simeq \sqrt{\frac{4e|\alpha|}{m}}. \tag{8.9}$$

During the separation process, the quadruple term α crosses zero and this is the point where the secular frequency in the z-direction ω_z, is at its *lowest*. At this point, ions are separated at a distance defined in equation (8.4) in a single well due to their Coulomb repulsions force and the secular frequency is at its minimum and given by [138]

$$\omega_{min} = \sqrt{\frac{3e}{m}}\left(\frac{e}{2\pi\epsilon_o}\right)^{1/5}\beta^{3/10} \tag{8.10}$$

The value of ω_{zm} when $\alpha = 0$ also sets an upper limit on the speed of separation. Here we aim to obtain the maximum value for ω_z at $\alpha = 0$ for the separation of ions, which ultimately provides a faster speed for the adiabatic separation process. When α is zero, ω_z is only due to the contribution of the quartic term β in equation(8.1).

8.4 Optimisation of ion separation process

From the discussion in the previous section, one can conclude that a trap design must provide negative values of α, when a voltage is applied to the *wedge* electrode, in order for ion separation to occur. Furthermore, a better trap design is one which provides higher values for the quartic term β which in turn provides higher secular frequencies during the separation process allowing for a faster speed of the adiabatic shuttling process. Both α and β terms depend on the applied voltages on the static potential electrodes and their dimensions. As the applied voltages on the static potential electrodes are limited by the breakdown voltage for these electrodes, the effective maximum value of β depends on the width of the static potential electrodes.

Two arrangements of static potential electrodes in surface traps for effective and fast ion separation process are investigated. The arrangement of rf and static potential electrodes in the two surface ion trap geometries are shown in figure 8.2. In figure 8.2(a), the outer *rf-ground* electrodes are segmented to provide confinement in the trap axis and the ion-static potential electrode distance is symmetric along the trap axis while in figure 8.2(b), the central *rf-ground* electrode is segmented. The width of the segmented electrodes are labelled as E for *endcap*, C for *control* and W for *wedge* electrodes. The gap between the electrodes is much smaller than the size of electrodes. In both designs, ions will be trapped above the central electrode(s) by adjusting the voltages on these structures [25, 29, 52].

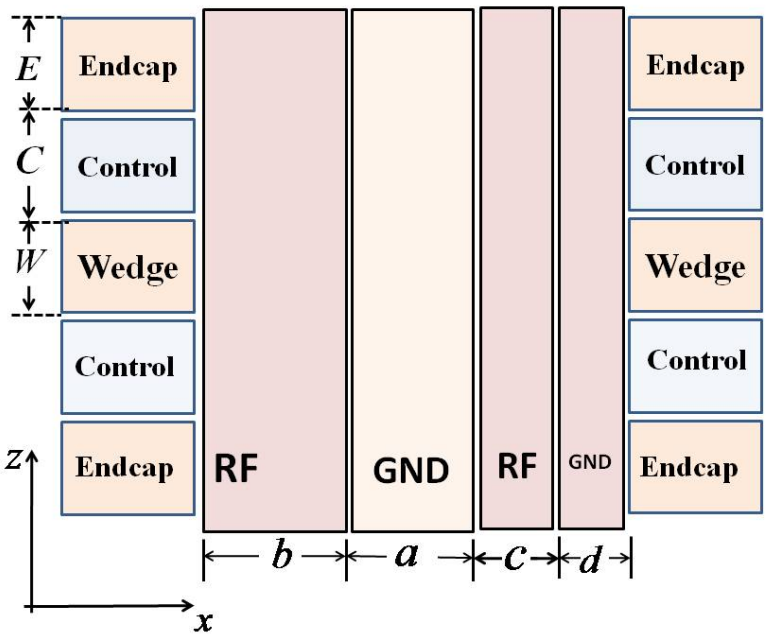

(a)

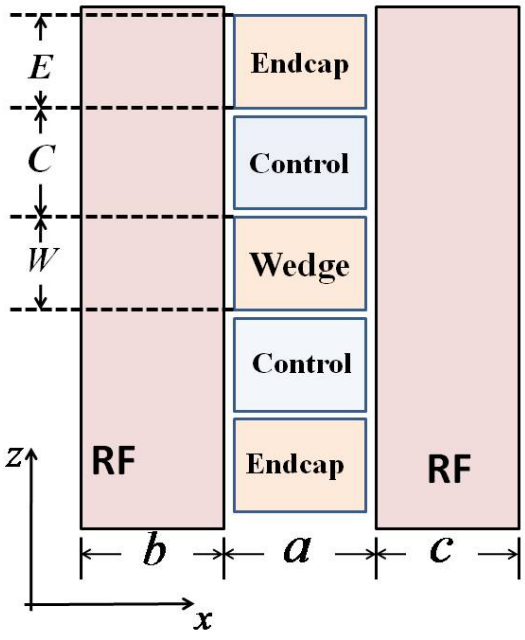

(b)

Figure 8.2: In design (a) outer electrodes are segmented in (b) the inner electrode is segmented to provide confinement in z direction.

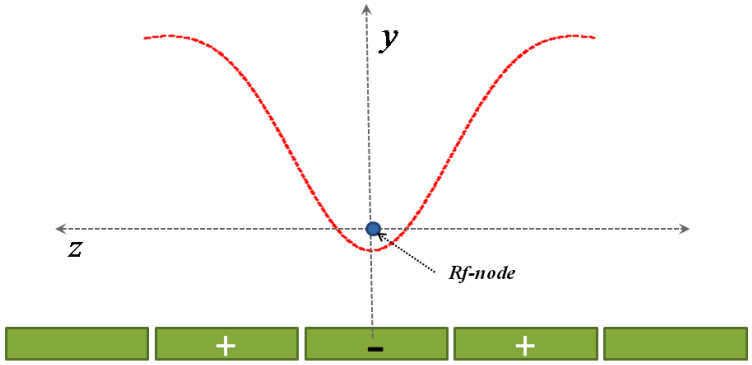

Figure 8.3: At least three control electrodes are required to provide confinement for an ion in the z direction.

A surface ion trap lacks one of the reflection symmetries, the symmetry in the direction normal to the surface [138]. Therefore, any applied voltage on the *endcap* electrodes and *wedge* electrodes to produce the separation process can easily alter the position of the trapped ions above the surface [27] and push the ions out of the *rf-node* position. The solution for this problem can be realised by applying a negative voltage on two (in case of the surface trap design shown in figure 8.2(b)) or more (in case of the surface design shown in figure 8.2(a)) *control* electrodes symmetrically around the *rf-node*. The voltage on the *control* electrodes should be maintained in such a way that the trapped ions always remain in the *rf-node* position during the separation and shuttling processes. The trap confinement in the z direction is shown in figure 8.3.

The surface trap design shown in figure 8.2(a) requires at least 6 static electrodes to trap ion(s) in a *single well* and 10 electrodes for the separation process, while design 8.2(b) requires 3 electrodes to confine ion(s) in a *single well* and 5 electrodes for the ion separation and recombination processes. Initially, when there is a single potential well, the positive voltage on the four corner *endcap* electrodes are needed to confine ions along the z-direction and the negative voltage on the two middle *wedge* electrodes is to be adjusted to keep the ion in *rf-node* position.

In order to create a potential wedge between the ions and produce a *double well*, the voltage on the *wedge* electrode is to be made positive and in order to keep the ions in the *rf node* position, a negative voltage is applied on the *control* electrodes. The required voltages on the static potential electrodes (such that the ions remain trapped during the separation process) can be found in electric field simulations. Figure 8.4 shows a typical voltage change on *wedge* and *control* electrodes in time, at a given *endcap* voltage for the

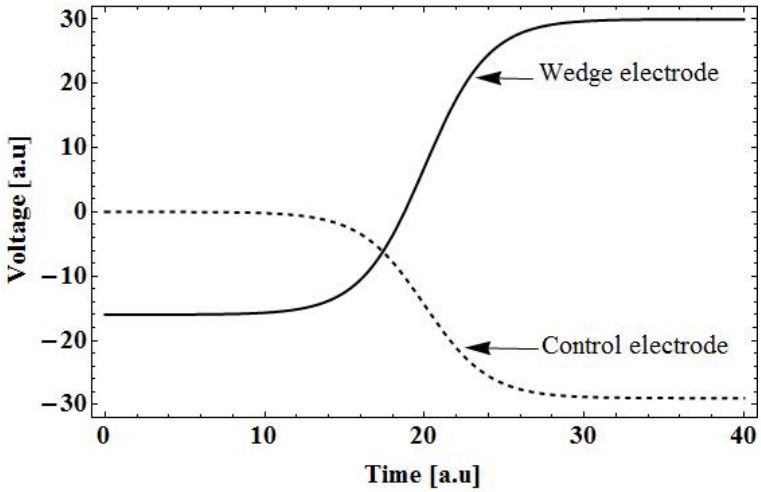

Figure 8.4: Arbitrary applied voltages on the *control* and *wedge* electrodes during the ion separation process.

designs shown in 8.2. In order to create a *double well* and separate the ions, the voltages on the static potential electrodes are varied in such a way that the ions always remain trapped at the *rf-node*. The same process can be reversed to recombine the ions. The process is illustrated in figure 8.5. To find the required static voltages using simulations, first set the static voltage to zero on the static electrodes and apply an rf voltage on the rf electrodes and find the *rf-node* position. Next, apply the fixed positive voltage on the *endcap* electrodes, which in result will push the trap centre out of the *rf-node* position. To compensate this pushing force, vary the negative voltage on the *control* electrodes until the trap centre coincides with the *rf-node* position.

As discussed in section 8.3, an efficient separation process depends on the value of β. Therefore the optimum trap geometry is one which provides maximum values for β and allows for negative values for α for certain applied voltages. The values of α and β parameters are limited by the breakdown voltage of the trap electrodes. Therefore in the simulation, the applied voltage on the electrodes is kept constant and equal to 1 V for *endcap* and *wedge* electrodes and -1 V for *control* electrodes. This approach allows to determine the dependency of the α and β terms on geometric factors of a surface trap. The first step is to determine the optimum ratio of *wedge* to *control* electrode size. For this purpose we fix the *endcap* and *control* electrode sizes and vary the width of *wedge* electrode to maximise β. To calculate the electrostatic potential for the set of electrodes shown in figure 8.2, the analytic electric field calculations for rectangular electrodes within a plane suggested by House [129] are used.

In order to determine the optimum geometry for ion separation, in the first step, the

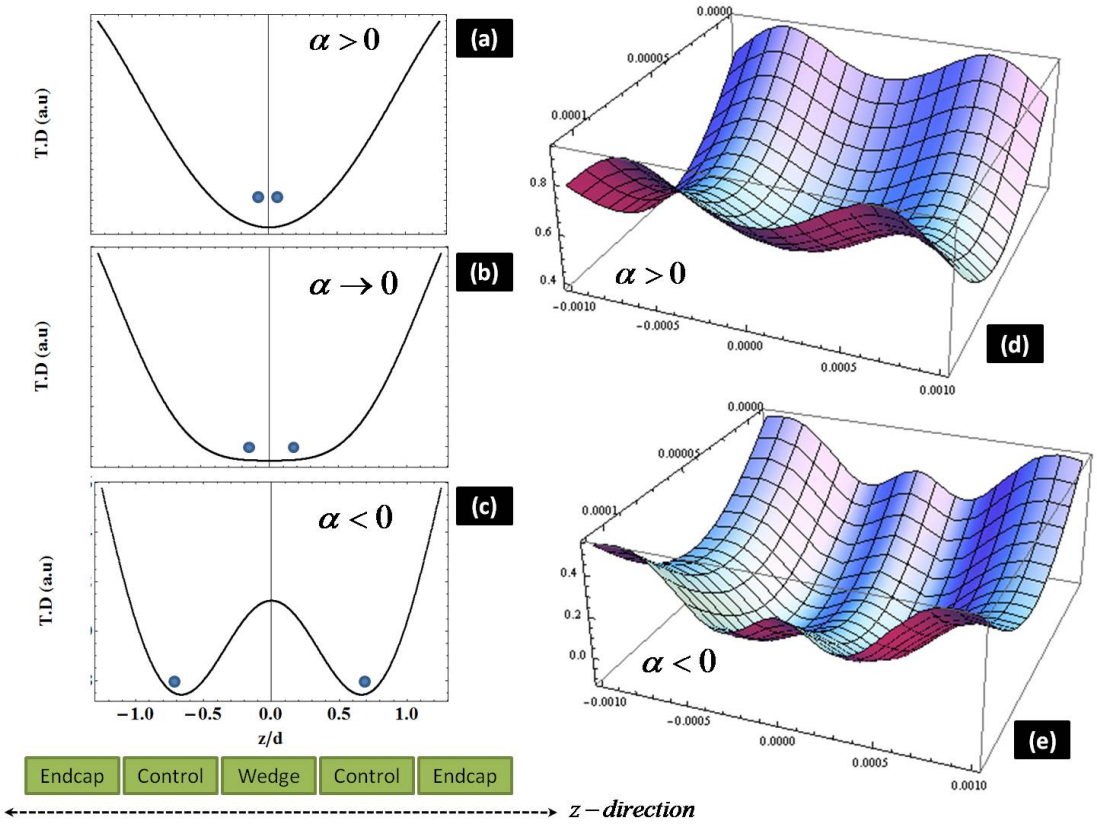

Figure 8.5: Creation of a double well is illustrated. (a) Both ions are trapped in a single potential well using the *endcap* electrodes and $\alpha > 0$, (b) a voltage is applied on the *wedge* electrode so that $\alpha \to 0$ in the single potential well, (c) the voltage on the *wedge* electrode is increased so that two distinct potential wells are appeared and the value of $\alpha < 0$. *Control* electrodes are used to keep the ion position at the *rf node* at all times. 3D plots are shown for the single potential well in (d) and the double potential well in (e).

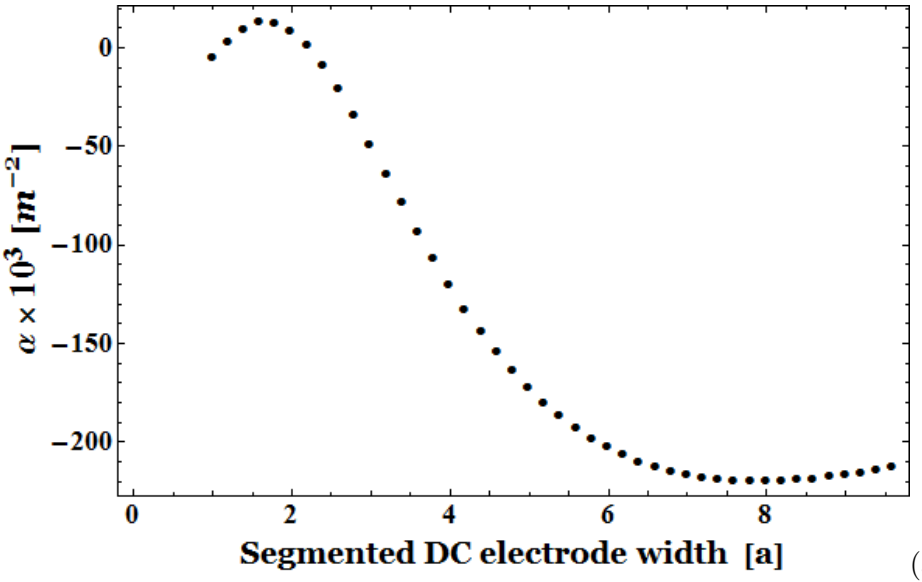

(a)

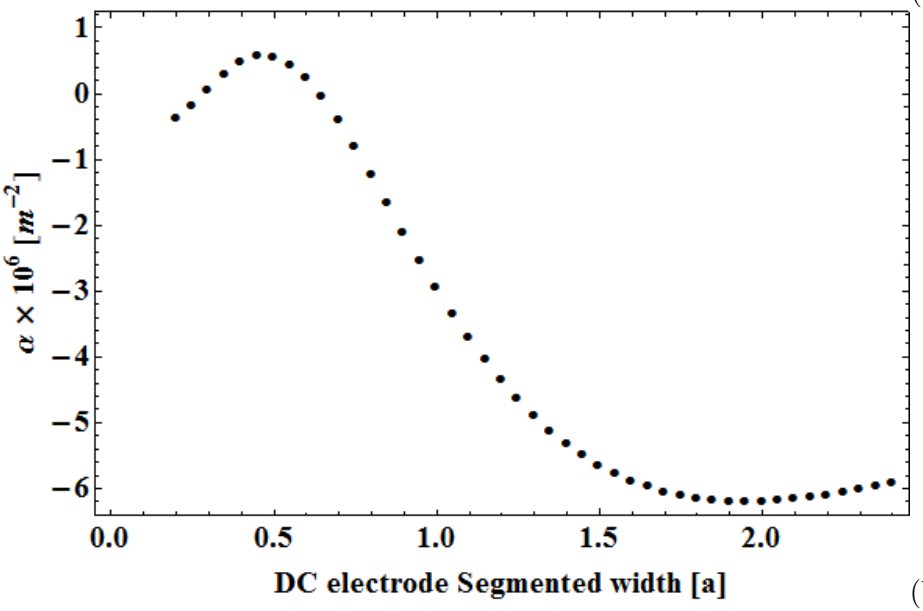

(b)

Figure 8.6: α is plotted against electrode widths (W=C=E) in the units of a (a) for the outer segmented electrode design, (b) for the central segmented electrode design.

size of the static potential electrodes which produces negative values of α and a maximum value of β has to be found. In figure 8.6, α is plotted for both surface trap designs as a function of electrode widths in units of the rf-electrode separation a. α goes negative when the electrode size in the design shown in figure 8.2(a) crosses $2a$ and reaches its maximum negative value at $8a$. For the trap design 8.2(b), α goes negative when the electrode size crosses $0.7a$ and reaches its largest negative value at $2a$. Maximum values for $|\alpha|$ are good for the secular frequencies in the single and double potential wells, but for a fast separation process, it is essential to maximise β for the given trap geometry.
In figure 8.7 β is plotted against the ratio of *wedge* W to *endcap* E electrode width for both trap designs. In these plots, it can be seen that β reaches a maximum when the width of all the static potential electrodes is approximately the same.

As already discussed in chapter 8.4, the optimum rf electrode width for maximum trap depth at given ion height is approximately $3.68a$ if $b = c$. The width of static potential electrodes should be chosen in such a way that they provide significant curvature of the potential at the centre of the trap in the z-direction and fulfil the conditions for effective ion separation by providing maximum β and negative α.

In figure 8.8, β is plotted as a function of electrode widths in units of separation of rf electrodes a for both surface trap designs for $W/E = 1$. It can be easily deduced from the plot shown in figure 8.8(a) that the maximum β can be obtained when width of the static potential electrodes is $\approx 3.75a$ for the design in figure 8.2(a). Figure 8.8(b) shows that the maximum β for the trap design shown in figure 8.2(b) is at electrode width equal to approximately a. The relationship between β and a in figure 8.8 for both designs also shows that a larger size of electrodes are required to control the ion motion when the ion electrode distance is large. For the outer-side-segmented static potential electrodes in figure 8.2(a), the ion-static potential electrode distance is $\sqrt{[(b + \frac{ac}{b+c})]^2 + [h]^2}$, and for the central segmented static potential electrodes in figure 8.2(b), this distance is $\sqrt{abc(a+b+c)}/(b+c)$. Furthermore, in figure 8.9 a comparison for both designs is given, where α and β are plotted as a function of rf electrode separation a (which corresponds to ion height above the electrodes for the optimised case). By comparing both designs it can be seen that the values for α and β are two orders of magnitude higher for the design in figure 8.2(b). A sharp rise in the values of α and β can be observed when the rf electrode separation decreases below 50 μm, but the cost for this achievement can be severe because the anomalous heating also increases rapidly with the decreasing distance

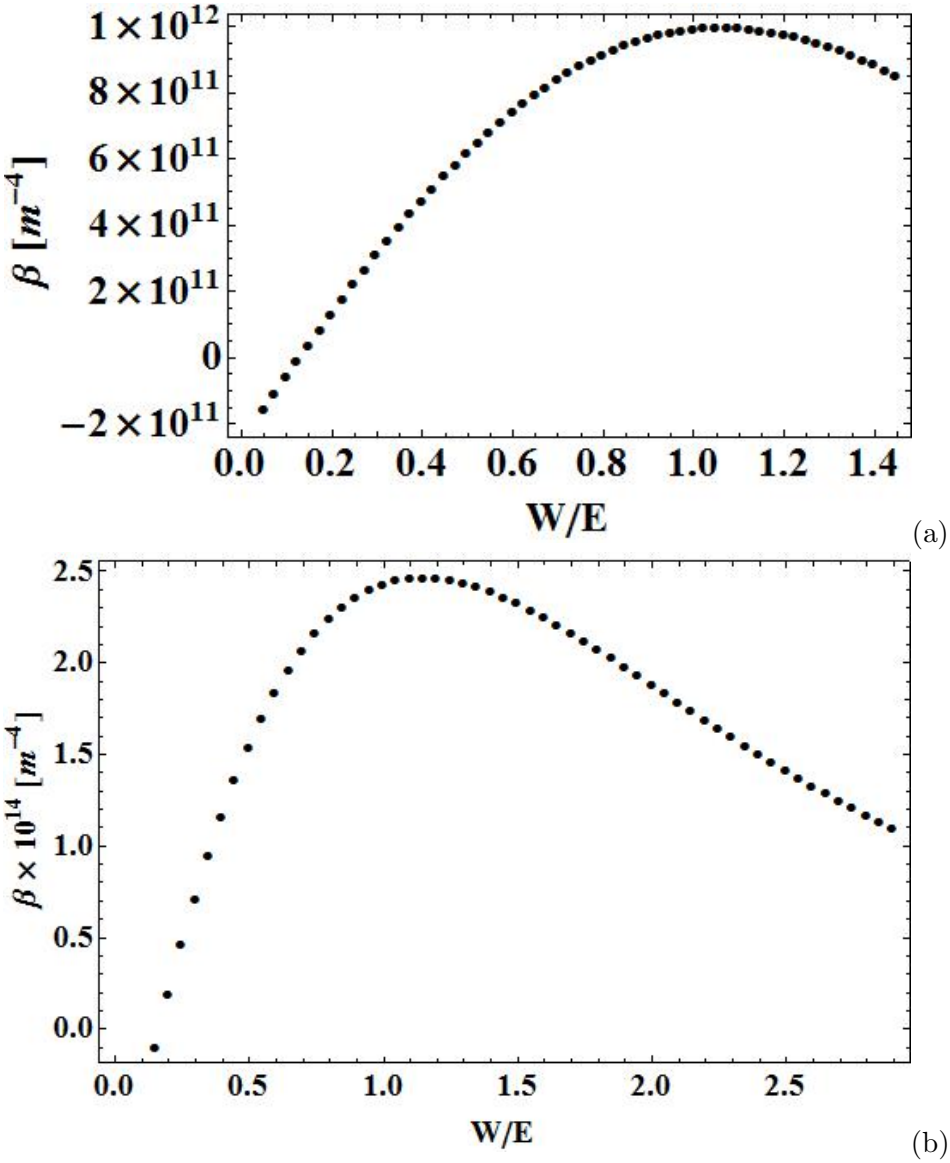

Figure 8.7: β is plotted against the ratio of wedge electrode to endcap electrode width(W/E) (a) for the outer segmented electrode design, (b) for the central segmented electrode design. In both cases an optimal value of W/E is approximately 1.1

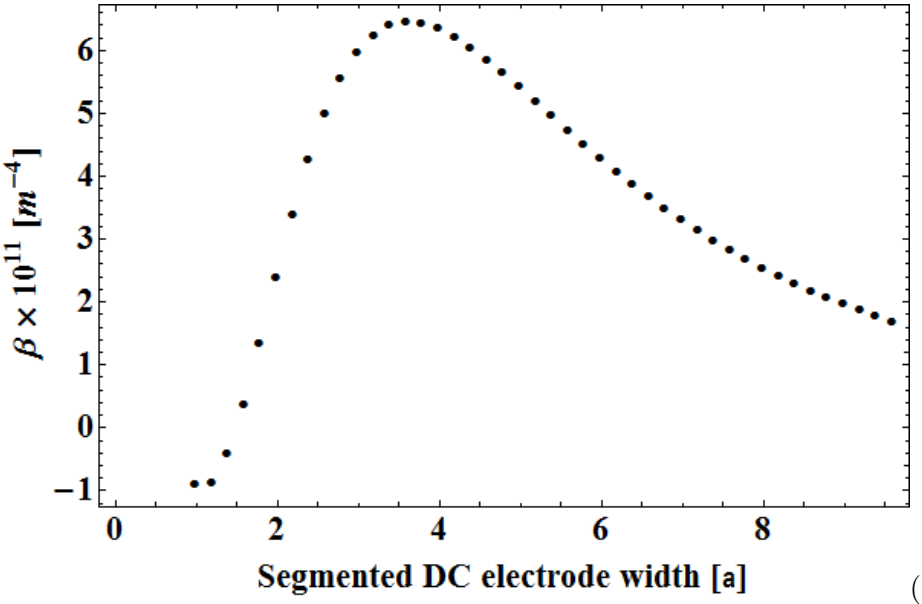

(a)

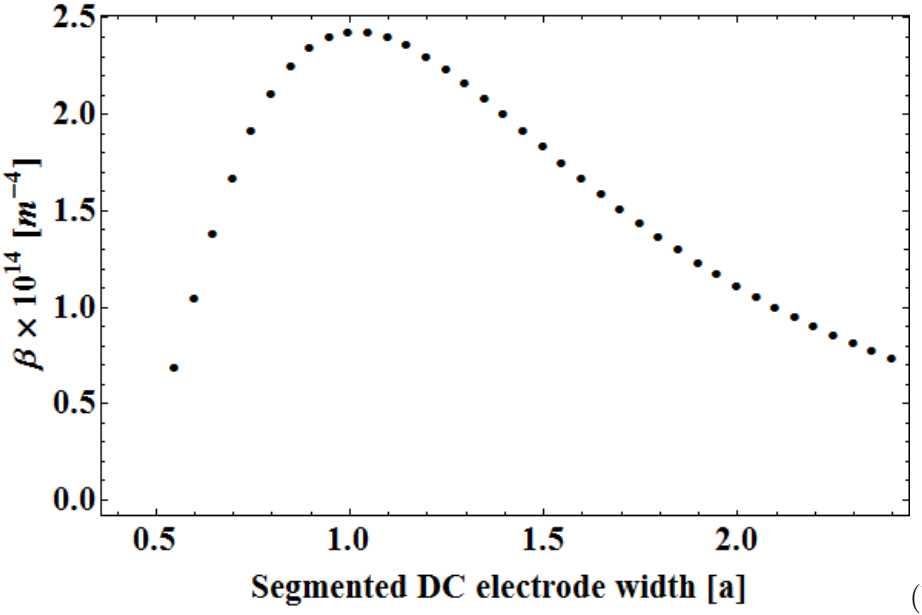

(b)

Figure 8.8: β is plotted against electrode widths (W=C=E) in the units of a (a) for the outer segmented electrode design, (b) for the central segmented electrode design.

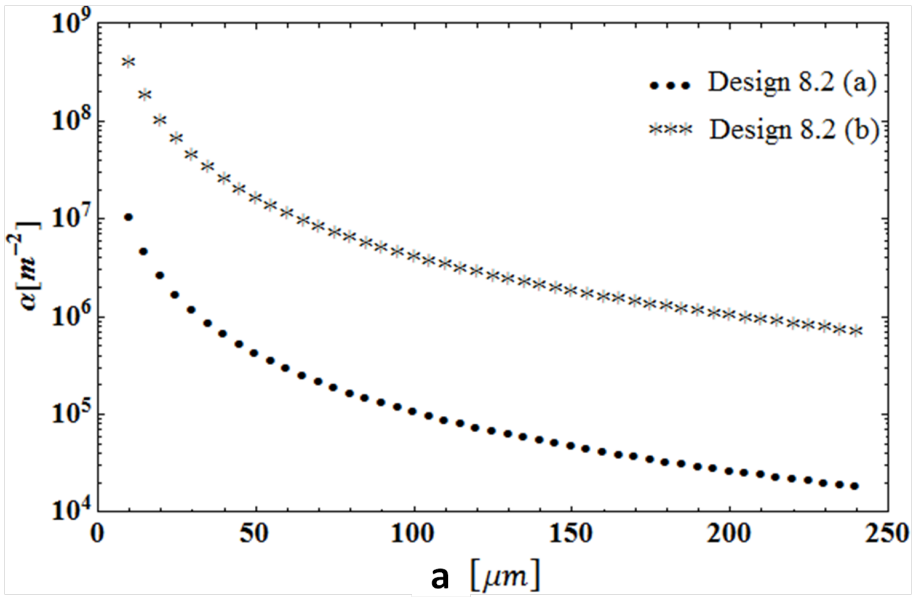

(a)

(b)

Figure 8.9: (a) α and (b) β are plotted vs rf-electrode separation a for the both trap designs shown in figure 8.2(a) and (b). Comparison shows that α and β values are higher in the surface trap geometry where ion electrode distance is small (design shown in figure 8.2(b)).

between the electrodes and ions. Cryogenic operation of ion trap chips may allow for smaller ion-electrode spacings as it is known to significantly suppress anomalous motional heating [30–32].

Chapter 9

Ion Shuttling

9.1 Introduction

Significant progress has been made in quantum information processing with trapped ions [3,7,14,44–46], including entanglement gates [8,69,111,139,140], teleportation [10,11,141] and quantum simulation [6, 55, 142–145]. It would be useful if qubits can be stored in separate trapping regions, *memory zones*, and only be brought together in a single trap, *processor zone*, when quantum operations are required [5,15–17]. Shuttling within an array of ion traps has been demonstrated successfully in linear arrays and through junctions [18, 19, 22, 25, 27, 98, 133–135]. It is important to scale these architectures to trap and shuttle hundreds of ions for any useful computation to occur. Furthermore, the shuttling of ions should be adiabatic, in which the ions are to be shuttled with negligible motional heating from one trap region to another region while preserving the internal state of the ions.

In this chapter ion shuttling processes are discussed for optimised surface trap geometries. In order to simulate the ion transportation in a trap array, accurate time dependent electric fields are required to control the ions' dynamics during the shuttling process from one trapping region to other. The basis functions for each trap electrodes are worked out using the analytical model suggested by House [129]. In order to shuttle the ions, these basis function are multiplied with the time varying voltages. The energy gain by the ions during the shuttling process can be calculated by solving the classical equation of motion using the calculated potentials created by the trap electrodes [133]. Heating of the shuttling ion by the anomalous heating sources is also considered which depends upon the

ion-electrode distance and the secular frequency of the ion during the shuttling process. The optimised surface trap geometries are analysed for linear shuttling and ion separation process and shuttling protocols are worked out which add less amount of energy to the shuttling ion.

9.2 Ion dynamics

The desired ponderomotive potential for ion transportation can be calculated by superimposing the basis function of individual control electrodes, [133]

$$\Psi(\zeta,t) \approx \frac{e^2 V_{rf}^2}{4m\Omega_T^2}|\nabla\Theta_{rf}(\zeta)|^2 + e\sum_i V_i(t)\Theta_i(\zeta) \tag{9.1}$$

where ζ is the position vector, $\Theta_i(\zeta)$ is the basis function of the ith electrode in the ζ direction, V_{rf} is the applied rf voltage at a frequency of Ω_T and $V_i(t)$ is the time varying voltage applied on the ith control electrode. The pseudopotential approximation in equation 9.1 is valid only when the a-q parameters are close to the origin of stability diagram as discussed in chapter 2. The voltage functions are explicitly time dependent. The calculation of basis functions for individual electrodes using analytical and numerical methods is discussed in section 7.7. In order to build arbitrary time dependent potentials, the calculated basis function for individual electrodes can be used. Due to the fact that the force on the charged particle corresponds to the gradient of the potential, a classical equation of motion for the ion can be found as [133]

$$\sum_j^3 m\ddot{\zeta_j} + \nabla_j\Psi(\zeta_i,t) = 0 \tag{9.2}$$

It is also possible to trace out the classical trajectories of ion motion by solving the equation (9.2) numerically. Fortunately, the ion motion caused by the variation of the voltages on the trap electrodes can be calculated classically [19, 146].

The aim of an optimum and fast shuttling protocol is to develop a system that allows ions to be transferred to arbitrary locations within the trap array, while ensuring that the stored quantum information is not destroyed after a shuttling operation. Hucul et el. [133] and Reichle et el. [134] have described a theoretical model for shuttling procedures in detail. These theoretical models identify those constraints that ensure reliable transport of

ions and construct effective shuttling protocols for different shuttling operations. Hucul et el. have highlighted the importance of the inertial forcing of shuttled ions at the beginning and end of a shuttling protocol and proposed a few shuttling protocols so that the ion does not acquire a significant amount of energy during the transporting process.

Following the discussion given by Hucul et el. [133], the rest of this section is a review of the basics of ion shuttling dynamics given by [133]. A shuttling operation can be performed by changing the voltages on the control electrodes in time, in a way that the potential minimum along the ion pathway is translated from the initial ion position to the desired final position. The potential minimum in an rf Paul trap is harmonic to a good approximation. A one-dimensional harmonic potential along the trap axis corresponds to a linearly varying electrical field $E(x)$ resulting from the potential difference between the nearest control electrodes. The electric field $E(x)$ along the shuttling path x is [133]

$$E(x) = -\kappa x \tag{9.3}$$

where $\kappa = m\omega^2/e$. The electric field at the equilibrium position $x = 0$ of a trapped ion can be superimposed by a time-dependent electric field pointing in the direction of shuttling by varying the voltages on the control electrodes, [133]

$$E(x,t) = -\kappa x + E(t) = -\kappa x + \kappa x_o(t) \tag{9.4}$$

and the resulting time dependent forcing field has a new stable equilibrium position at $x_o(t) = E(t)/\kappa$. The forcing field determines the location of the instantaneous potential minimum of the moving ion. Keeping the change in motional state of shuttling ion to minimum is of vital importance. The effects of shuttling on their motional states can be determined by solving the equation for the transitions induced in a harmonic oscillator being forced by a uniform field, [133]

$$eE(t) = m\omega^2 x_o(t) \tag{9.5}$$

Therefore, the instantaneous potential energy can be shown to be [133]

$$U(x,t) = \frac{1}{2}e\kappa\big(x - x_o(t)\big)^2 = \frac{1}{2}m\omega^2(x - x_o(t))^2. \tag{9.6}$$

In practice, the shuttling of an ion from one location to another can be performed by changing the voltage on electrodes behind and in front of the moving ion. The position of the ion $x_o(t)$ directly depends upon the time-dependent voltage difference $\Delta V(t)$ applied to the relevant control electrodes and can be obtained by [133]

$$x_o(t) = \frac{e\Delta V(t)}{m\omega^2 d} \tag{9.7}$$

where d is the centre-to-centre distance between the nearest control electrodes. The influence of variation in the frequency (ω) from that of the time-dependent electric field $E(t)$ can be separated by transforming to the rest frame of the moving potential by replacing $x - x_o(t)$ by the position term s, and introducing a pseudo-forcing term $m\ddot{x_o}s$ simultaneously in equation 9.6, [133]

$$U(s,t) = \frac{1}{2}m\omega^2 s^2 + m\ddot{x}_o(t)s \tag{9.8}$$

The forcing term on the R.H.S of the equation 9.8 is a result of the inertial force on the ion due to an acceleration in the transport of the potential.

Hucul et el. [133] have compared three type of ion trajectories; linear $x_{o\mathrm{L}}(t)$, sinusoidal $x_{o\mathrm{S}}(t)$ and hyperbolic tangential $x_{o\mathrm{T}}(t)$, and Reichle et el. [134] have discussed error function form of the ion trajectory. The trajectory functions proposed by Hucul et el. [133] are given as

$$x_{o\mathrm{L}}(t) = L\frac{t}{T}(H(t) - H(t-T)) + LH(t-T), \tag{9.9}$$

$$x_{o\mathrm{S}}(t) = \frac{L}{2}\big(1 - \cos(\frac{\pi t}{T})\big)(H(t) - H(t-T)) + LH(t-T), \tag{9.10}$$

$$x_{o\mathrm{T}}(t) = \frac{L}{2}\frac{\tanh(\frac{N(2t-T)}{T} + \tanh(N))}{\tanh(N)}(H(t) - H(t-T)) + LH(t-T). \tag{9.11}$$

In these equations L is the total shuttled distance, T is the shuttling time, H is the Heaviside step function and N in hyperbolic tangent functions is a parameter which determines

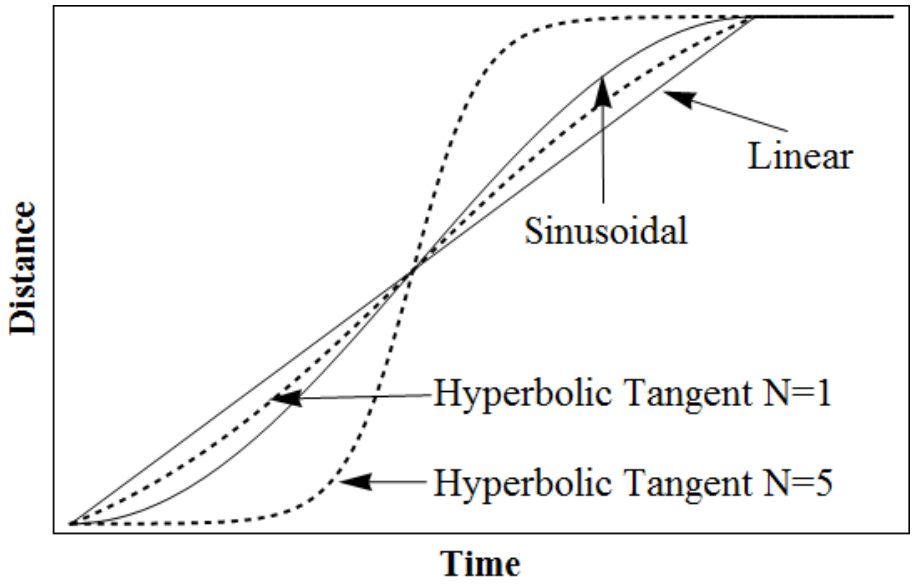

Figure 9.1: Plot of the position of the potential minimum versus time, when the time profile is linear, sinusoidal and hyperbolic tangent (N=1 and N=5)

the level of smoothness in the velocity of the potential minimum at the beginning and end of the protocol. A shuttling process starts from rest and ends at the rest position of the harmonic potential well. This includes that the ion will receive at least two kicks, one at the start of the process and one at the end of the process. The position of a particle under the influence of these time profiles are plotted in figure 9.1. From these plots, it can easily be concluded that the transition of the potential well under the influence of a hyperbolic tangent time profile is smooth or can be described as the magnitude of discontinuity in the velocity of the potential well at the beginning and end of the protocol is relatively low. The magnitude of change of the velocity of the potential well also depends on the N-parameter of the hyperbolic tangent function. Lower values (< 1) of the N-parameter for hyperbolic tangent is approximately similar to the linear function profile in which the potential well feels a sudden kick at the start and end of the shuttling protocol. Analytical solutions for an ion's motional state after shuttling a distance l under the influence of linear, sinusoidal and hyperbolic tangential are given by Hucul et el. [133].

Shuttling criteria

In an experimental arrangement, a trapped ion can smoothly be shuttled by moving the potential minimum in the axial direction by changing the voltage on distant electrodes in a way that they create a forcing field in the direction of shuttling. However, it is not possible to shuttle the ion without introducing inertial forcing on the ion. In order

to achieve adiabatic shuttling, it is necessary to design a protocol which produces little change in the motional state $\langle n \rangle$ of the ion initially prepared in the ground state [133].

Analytical calculation of $\langle n \rangle$ after implementation of linear shuttling by using linear, sinusoidal and hyperbolic tangent protocols have been shown in [133] and by using the error function protocol is given in [134].
In the following sections, $\langle n \rangle$ is obtained numerically after implementation of different shuttling processes using the simulations of ion motions in the optimised surface trap geometries.

Average motional energy

In a quantum harmonic oscillator of frequency ω_o, the average energy $\langle E \rangle$ of level $\langle n \rangle$ is given by

$$\langle E \rangle = \hbar\omega\left(\langle n \rangle + \frac{1}{2}\right) \tag{9.12}$$

and in analogy of a trapped ion to a classical harmonic oscillator, the average energy for a trapped ion can be calculated by

$$\langle E \rangle = \frac{1}{2}m\big(v - v_o(t)\big)^2 + \frac{1}{2}m\omega_t^2\big(x - x_o(t)\big)^2 \tag{9.13}$$

where m is the mass of the ion, $v_o(t)$ is the instantaneous velocity and ω_t is the instantaneous secularly frequency. By comparing equation 9.12 and 9.13 the average motional quanta gained by an ion $\langle n \rangle_s$ during the shuttling process can be calculated as [133]

$$\langle n \rangle_s = \frac{\frac{1}{2}m(v - v_o(t))^2 + \frac{1}{2}m\omega_t^2(x - x_o(t))^2}{\hbar\omega} \tag{9.14}$$

When the ion is located at the bottom of the well, the potential energy in the frame of reference of the well is considered to be zero. Hence, the total energy of the ion is only due to its kinetic energy which is maximum at the bottom of the well.

$$\langle n \rangle_s = \frac{\frac{1}{2}m(v_o(t))^2}{\hbar\omega} \tag{9.15}$$

The kinetic energy of the ion in the frame of the pseudopotential well is due to its secular motion. By plotting the kinetic energy of the ion versus the shuttling time, the maximum

kinetic energy of the ion at the start and the end of shuttling can be obtained. Hence, the change in the average motional state of the ion is then worked out as

$$\langle n \rangle_s = \frac{\text{Final } K.E_{\max} - \text{Initial } K.E_{\max}}{\hbar\omega} \tag{9.16}$$

Motional energy caused by the anomalous heating

With reasonably small ion-electrode separation ion traps, significant motional heating of an ion can be caused by anomalous heating during the shuttling process. It is observed from the experimental data that the heating rate $\langle \dot{n} \rangle_{an}$ is proportional to the ion-electrode distance scaling as $1/d^4$ and to the secular frequency scaling as $1/\omega^2$ [31]. For a typical ion trap, using the Yb^+ ion, assuming scaling laws as stated above and a recent measurement taken in our lab [91, 97], the heating rate can be written as,

$$\langle \dot{n} \rangle_{an} \approx \frac{1.97 \pm 0.15 \times 10^{26}\ \mu\text{m}^4\text{Hz}^3}{\omega^2 d^4} \tag{9.17}$$

where d is in micrometers. To reduce the motional heating gained by the ion during the shuttling process, it is necessary to shuttle the ion at the time scale of the secular frequency ω_z. The motional quanta $\langle n \rangle_{an}$ gained from the anomalous heating during the shuttling can be calculated by integrating the $\langle \dot{n} \rangle_{an}$ over the shuttling time,

$$\langle n \rangle_{an} = \int_{t_o}^{t_f} \langle \dot{n} \rangle_{an} dt \tag{9.18}$$

where, t_o and t_f are start and the end time for a shuttling process. This integral also takes account of the variation of the secular frequency ω_z during the shuttling process.

Therefore, the total number of motional quanta gained during ion transport is given by

$$\langle n \rangle = \langle n \rangle_s + \langle n \rangle_{an} \tag{9.19}$$

ODE solvers

In order to calculate the motional state of an ion, it is necessary to utilise the classical motion of a trapped ion to calculate the energy gained by the ion during a shuttling process. The classical motion of the ion can be obtained by numerically solving the equation

of motion (9.2). High accuracy solutions of equation (9.2) will provide the ion trajectories in the x, y and z direction in time t from which the kinetic energy gained by the ion can then easily be calculated. In order to obtain the ion trajectory in x, y and z directions in an ion trap array, a package "NDSolve" to solve the order differential equations (ODE) given in Mathematica-7 is used. Time taken by a computer using an *Intel i7* multi-core processor with 2.66 GHz speed with 8 GB of memory to calculate the trajectory of the shuttling ion depends on the ODE solver method and ranges from few minutes to hours depending upon the shuttling time, "AccuracyGoal" and "PrecisionGoal" settings of the "NDSolve" package of the Mathematica. The local error in each step taken by the NDSolve is dependent on the "AccuracyGoal", (ag) and the "PrecisionGoal", (pg) and given by $10^{-ag} + |x| \times 10^{-pg}$, where x is the calculated position in each step.

The "NDSolve" package provides number of methods to solve the equations numerically. In order to simulate ion shuttling accurately, the "Extrapolation" method was used. The sub-method setting for the "Extrapolation" method was "ExplicitModifiedMidpoint" method with the "AccuracyGoal" and "PrecisionGoal" settings of 10, which provides an efficient and high accuracy solution. The detailed comparison between different ODE solver methods used for ion motion simulations are discussed in [133].

In some cases, the numerical solution method can face a "stiff equations", where one of the variables in the simulations varies rapidly (as distance in case of the ion separation process). Therefore, to achieve high accuracy solutions using the "NDSolve" package provided in Mathematica-7, "StiffnessSwitching" method can be used. The sub-method settings for the "StiffnessSwitching" can be set as "ExplicitRungKutta" and "Automatic". To increase the efficiency of the ODE solver, the "StiffnessSwitching" method adoptively switch-off method from "Explicit" to "Implicit" when problem appears to be stiff. Furthermore, the "AccuracyGoal" and "PrecisionGoal" can be compromised if the problem appears highly stiff.

9.3 Shuttling in one-dimension

In a one-dimension shuttling or linear shuttling process, the trapped ion moves along a linear path from one trapping zone to another in a way that its position remains along the rf nodal path between the trapping zones. In the linear shuttling process, heating of ions occurs mostly along the shuttling path in the longitudinal direction where there is no overlapping between the transverse and longitudinal motional states of the ion [133].

In the following sections, the implementation of the earlier discussed hyperbolic tangent shuttling profiles are applied to change the voltages on the trap electrodes of the optimised surface trap geometries discussed in chapter 7.

To understand the ion dynamics in a real ion trap array, for a case study, two optimised surface designs are discussed. In one trap design, outer segmented electrodes are used to provide axial confinement and in other, centre segmented electrodes are used. In both trap designs, rf electrodes are asymmetric in size ($b \neq c$), having the width of $b = 300$ μm and $c = 150$ μm respectively, and separated by a distance of $a = 60$ μm. The size of both electrodes is optimised for a given ion height of 82 μm to achieve the highest possible trap depth. By applying the optimum set of voltages and following the voltage constraints set in section 7.4, the trap depth of ≈ 0.35 eV and the secular frequencies in x and y direction, $\omega_x \approx \omega_y \approx 4$ MHz, can easily be achieved. The width of both outer and centre segmented electrodes is also optimised for better ion confinement in axial direction. In the case of the outer segmented electrode geometry, the width of the static potential electrodes is $w \approx 3.7a$ and in centre segmented electrode geometry the width is $w = a$, where a is rf electrode separation.

As earlier discussed, the hyperbolic tangent time profile adds a comparatively low amount of motional quanta to the shuttling ion for a given shuttling time, both trap geometries are analysed for linear shuttling with different N-parameters of the timing profile. The motional quanta $\langle n \rangle_s$ and $\langle n \rangle_{an}$ gained by the shuttled ion during the transportation process are plotted against the different shuttling durations. The change in average motional quanta $\langle n \rangle_s$ for an Yb^+ ion is calculated by finding the difference in maximum kinetic energies gained by the shuttled ion shortly after the start and end of the shuttling process and then using equation (9.16) while the average motional quanta $\langle n \rangle_{an}$ is calculated by using equation (9.17) and equation (9.18).

9.3.1 Outer segmented electrode geometry

As discussed in chapter 7, a trapped ion can be confined in the z-direction by using at least 6 control electrodes, in the case of external segmented trap geometries. Hence, to create two adjacent trapping zones along the rf nodal path, it requires at least 8 control electrodes. The trapping zones 'a' and 'b' for an external segmented electrode geometry are shown in figure 9.2. The radial confinement is provided by rf electrodes (not shown in the figure). Opposite control electrodes are connected to the same voltage supply to ensure symmetry in the transverse direction. For convenience, only external segmented

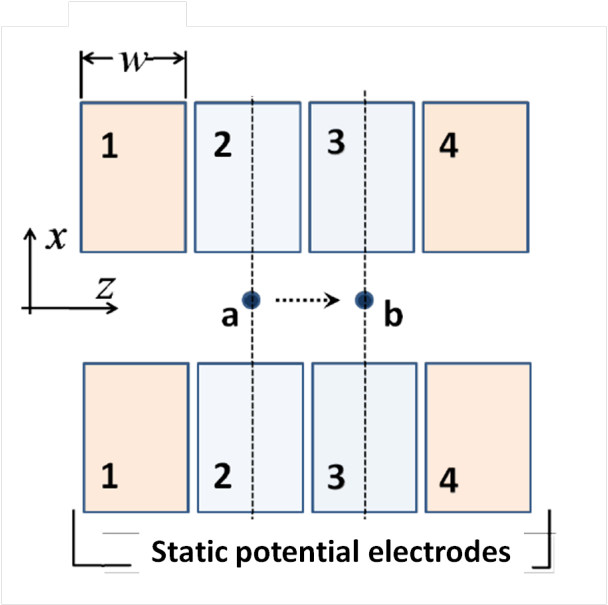

Figure 9.2: Two zone trap array implemented with outer segmented electrodes (rf electrodes are not shown).

electrodes are shown in figure 9.2.

Following the voltage constraints set in section 7.4, the rf voltage is set to $V_{rf} = 450$ V with a driving frequency of $\Omega_{rf} = 2\pi$ 52 MHz and static voltages are limited to ± 50 V. By applying the rf voltage, the secular frequencies in x and y directions are $\omega_x \approx \omega_y \approx 4$ MHz and the trap depth is ≈ 0.35 eV. In order to determine the voltage changes required for the shuttling process, in the first step, basis functions for the control electrodes are calculated analytically using the equations given by House [129]. Using these basis functions, all required parameters of the trap can then be calculated using Mathematica. In the 2nd step, voltages on the endcap electrodes (1 and 3) for trapping zone 'a' are set to some arbitrary value, and then the required voltage on electrode 2 to keep the ion at the rf node is iteratively calculated. Then, all the voltages are multiplied by a scale factor which is iteratively adjusted until a desired value of a secular frequency ($\omega_o/2\pi$) in the z-direction is obtained. The same process of voltage calculations is repeated for the trapping zone 'b'.

In order to see the effect of N-parameters of hyperbolic tangent time profile with different shuttling times for an optimum trap geometry shown in figure 9.2, the ramping profile of the voltages (shown in figure 9.3) are applied with N-parameter of $N = (2.6,\ 3.0,\ 3.4)$ values to shuttle an ion from zone 'a' to 'b'. At the start of the shuttling protocol, electrodes 1, 3 and 4 are held at +26 V and electrode 2 initially at -50 V. The secular

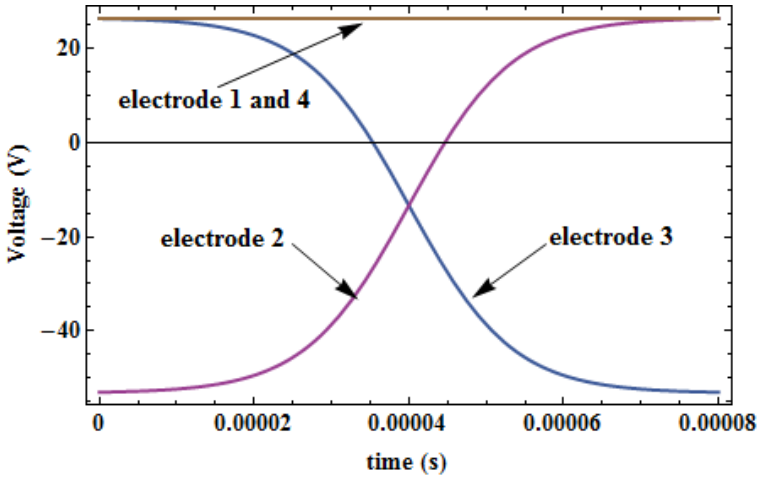

Figure 9.3: Voltage variation in time to move the ion from the trapping zone 'a' to 'b'. The hyperbolic tangent time profile is used.

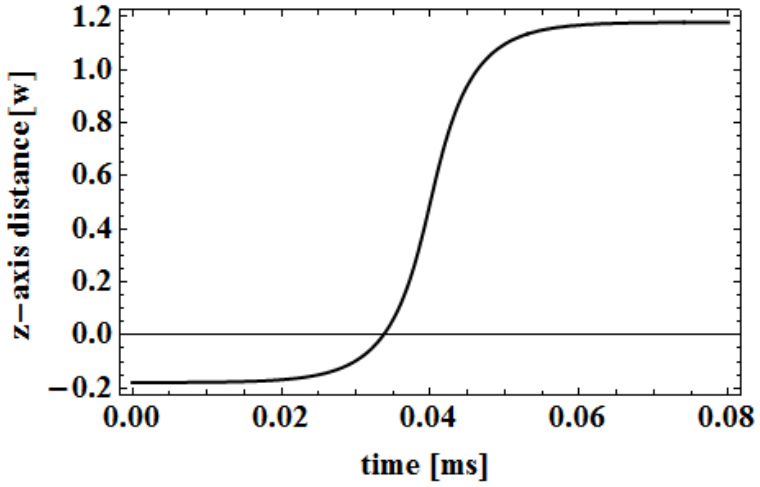

Figure 9.4: The distance shuttled by the ion when the static voltage change with a hyperbolic tangent time profile is applied. The shuttled distance in z-direction is normalised with the width of the electrode w.

frequency ω_o in the z-direction in trapping zone 'a' is calculated to be approximately $\approx$ 500 kHz. In order to move the ion from zone 'a' to zone 'b', the voltage on electrode 2 has to be brought to +26 V and the voltage on electrode 3 has to be brought to -50 V, monotonically in time t. The ion will be moved to trapping zone 'b' form initial trapping zone 'a' after the completion of the voltage ramps. The secular frequency remains the same in both trapping zones.

By following the voltage ramp profile given in figure 9.3, the ion is successfully shuttled a distance of $\approx 225\mu$m from zone 'a' to 'b'. A typical ion trajectory in the z-direction is shown in figure 9.4 when the static voltage change with the hyperbolic tangent time profile is applied.

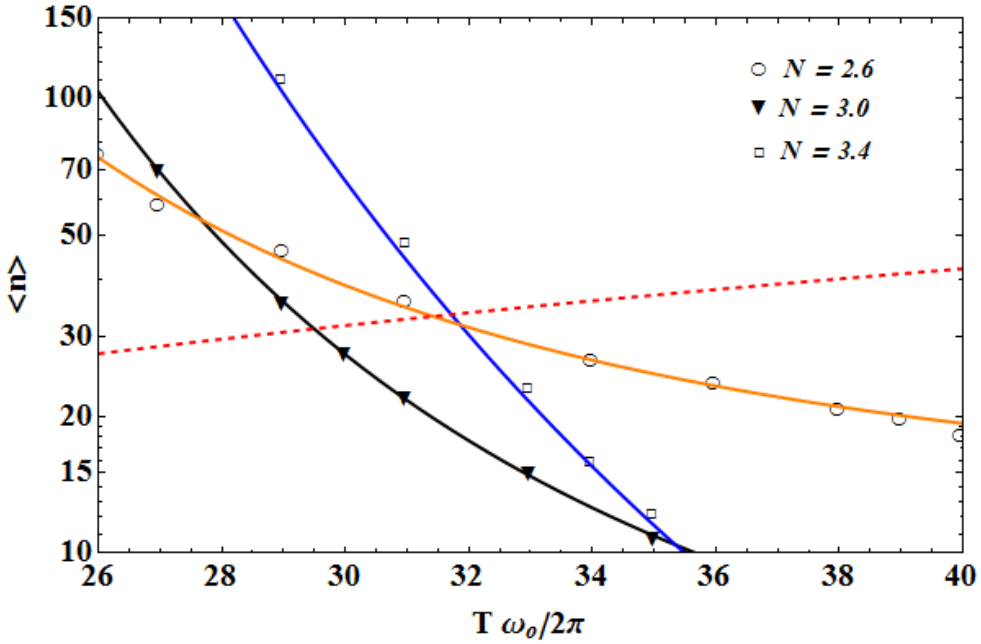

Figure 9.5: The gain in the average motional quanta $\langle n \rangle$ by the ion in a centre segmented trap geometry after the shuttling of the ion from trapping zone 'a' to 'b' following the hyperbolic tangent time profile of $N = (2.6,\ 3.0,\ 3.4)$ versus shuttling time scaled with secular frequency $\omega_o/2\pi = 500$ kHz. The solid lines represent the best fits of motional quanta $\langle n \rangle_s$ and the dashed line shows the gain of $\langle n \rangle_{an}$ from the anomalous heating of the trap. The cross over points set lower limits for the gain in $\langle n \rangle$ during the shuttling process.

The average motional quanta $\langle n \rangle$ are plotted against the shuttling periods which are scaled with the secular frequency ω_o and represented in number of cycles $(T\omega_o/2\pi)$ in the horizontal axis in figure 9.5. Here, it can be learnt from the plots that the gain of the average motional quanta $\langle n \rangle_s$ of the ion is reduced with larger shuttling time but on the other side, the longer shuttling periods add more quanta from the anomalous heating source. Hence the cross over points for $\langle n \rangle_s$ gained by following the particular hyperbolic tangent N-parameter plots (solid lines) and the $\langle n \rangle_{an}$ (dashed line) set the lower limit of the total average motional quanta $\langle n \rangle$ gained by the ion during the shuttling. Further to this, it can be seen in figure 9.5 that the hyperbolic tangent parameter $N = 3.0$ adds less quanta at the cross over point than the $N = 2.6$ or $N = 3.4$ and also provides shorter shuttling times.

9.3.2 Centre segmented electrode geometry

A trapping zone can also be created to confine an ion in the z-direction by using at least 3 control electrodes in a centre segmented electrode geometry as discussed in chapter 7.

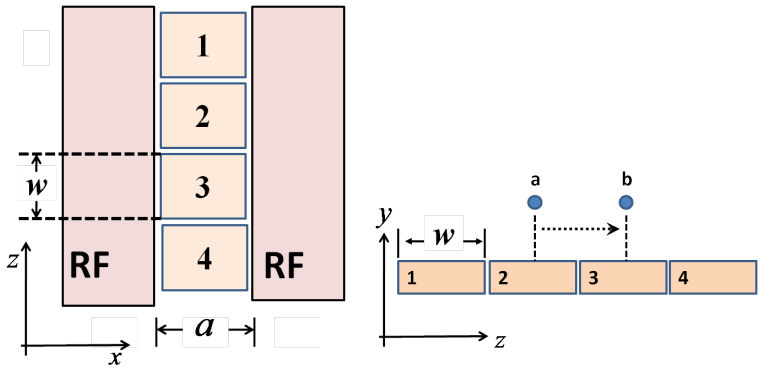

Figure 9.6: Two zone trap array implemented with centre segmented electrodes. In the cross section view, trap zone'a' and 'b' are shown above the segmented electrodes 2 and 3.

Hence, to create two neighbouring trapping zones along the rf nodal path, it requires at least 4 control electrodes as shown in figure 9.6. In the centre segmented trap geometry, as earlier discussed, the optimum width of the control electrodes is considered to be $\approx a$, where a is the separation between the rf electrodes. Here, as for an example $a \approx 60$ μm. Therefore, both trapping zones, 'a' and 'b', are separated by ≈ 60 μm. To create a trapping zone at 'a' and 'b', the radial confinement is provided by rf electrodes and axial confinement is provided by applying the specific static voltages on the control electrodes. In this type of trap design, as the ion has to be trapped right above the static potential electrodes, relatively low static voltages are required to confine the ion in the axial direction. Initially an Yb ion is trapped in zone 'a' by applying 4 V on electrode 1, 3 and 4, whilst electrode 2 is held at -2.77 V to keep the ion height in the rf nodal path. The secular frequency in z-direction ω_o is calculated to be ≈ 1 MHz. The rf voltage is set to $V_{rf} = 500$ V with a driving frequency of $\Omega_{rf} = 2\pi$ 55 MHz. By applying the rf voltage, the secular frequencies in x and y directions are $\omega_x \approx \omega_y \approx 4.3$ MHz and the trap depth is ≈ 0.37 eV. The voltages are applied to satisfy the constraints described in section 7.4. By changing the voltages on electrode 2 and 3, so that, after time t, electrodes 2 and 3 have to be 4 V and -2.77 V respectively, the ion can successfully be shuttled from zone 'a' to 'b'. The ramping profile of the voltages shown in figure 9.7 is applied on the control electrodes with a hyperbolic tangent time profile with N-parameter of $N = (2.2,\ 2.5,\ 3.0)$ to shuttle an ion from zone 'a' to 'b'.

Figure 9.8 shows the gain in the average motional quanta $\langle n \rangle$ for an Yb^+ ion for different shuttling durations represented in number of cycles completed. The same trend of motional quanta gain $\langle n \rangle$ can be seen as observed for the external segmented trap geometry. But the $\langle n \rangle$ at the cross over points is much less than the previous trap geometry. This is due

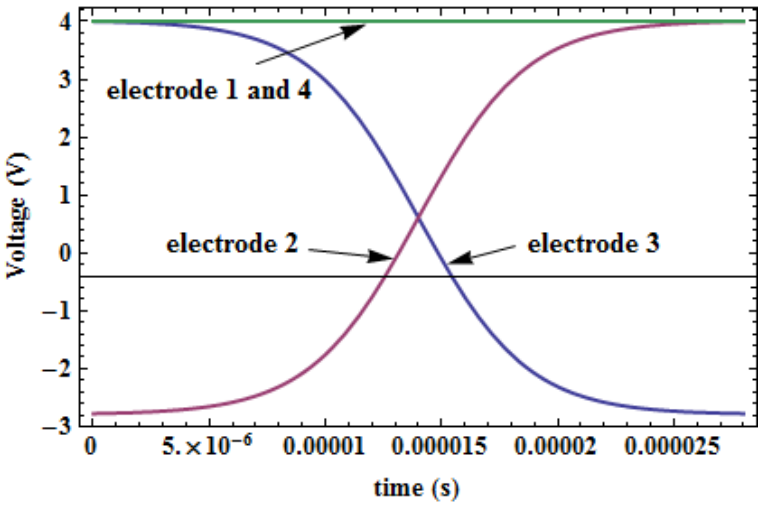

Figure 9.7: Voltage variation in time to move the ion from the trapping zone 'a' to 'b'. The hyperbolic tangent time profile is used.

to the higher axial secular frequency ω_o in this trap geometry. Furthermore, the hyperbolic tangent parameter $N = 2.5$ adds less amount of quanta at the cross over point than the $N = 2.2$ or $N = 3.0$.

9.3.3 Discussion on results

The behaviour of the gain of the motional quanta by the shuttling ion in both traps (as seen in figure 9.5 and 9.8) is consistent with the fact, that, for the same distance shuttled, the gain of motional quanta by the shuttling ion is highly dependent on the N-parameter of the hyperbolic tangent profile. Relatively smaller value of the N-parameter adds small number of quanta for shorter shuttling time as compared to the larger values of N-parameter which may add much less number of quanta for larger shuttling time but much larger number of quanta for the shorter times. This behaviour can also be observed in the analytical solutions provided by Hucul et el [133] for the motional quanta gain during the shuttling process.

As discussed earlier, the motional quanta gain $\langle n \rangle_{an}$ by the ion also depend on the heating rate of the traps, and increases by increasing the shuttling time linearly. Hence, the appropriate value of the N-parameter for the hyperbolic tangent profile to shuttle the ion should be the one which adds less number of motional quanta $\langle n \rangle_s$ at relatively shorter shuttling time. At the same time, motional quanta gain from the anomalous heating $\langle n \rangle_{an}$ during shuttling time should be minimum. The best choice of the N-parameter for the shortest shuttling period is where the total number of quanta $\langle n \rangle$ is minimum. The minimum $\langle n \rangle$ can be found after the cross-over point of both plots of $\langle n \rangle_s$ and $\langle n \rangle_{an}$.

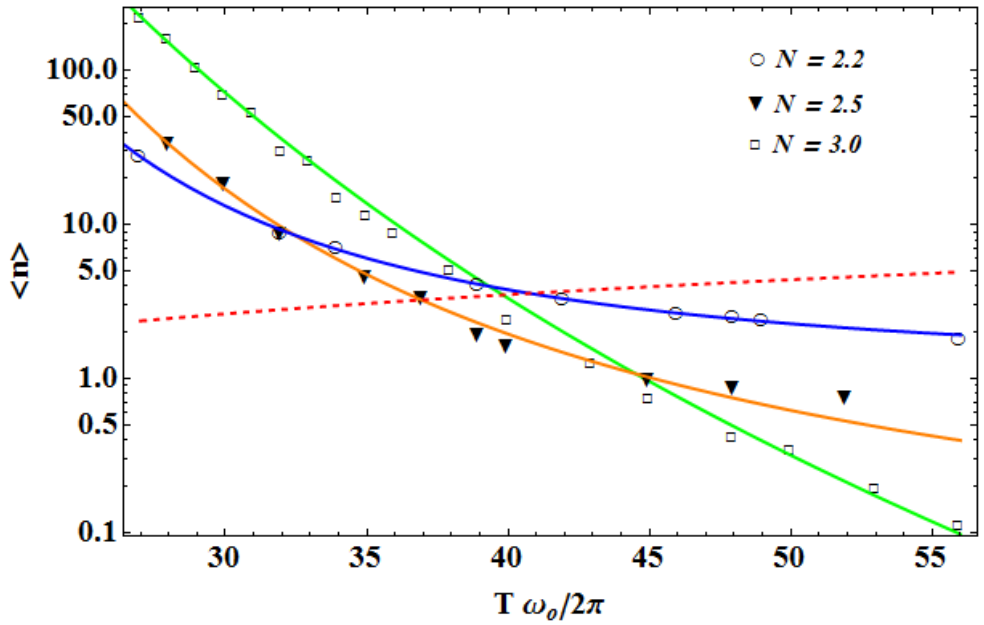

Figure 9.8: The gain in the average motional quanta $\langle n \rangle$ by the ion in a centre segmented trap geometry after the shuttling of the ion from trapping zone 'a' to 'b' following the hyperbolic tangent time profile of $N = (2.2,\ 2.5,\ 3.0)$ versus shuttling time scaled with secular frequency $\omega_o/2\pi = 1$ MHz. The solid lines represent the best fits to the motional quanta $\langle n \rangle_s$ and the dashed line shows the gain of $\langle n \rangle_{an}$ from the anomalous heating of the trap. The cross over points set lower limits for the gain in $\langle n \rangle$ during the shuttling process.

Therefore, the best choice of the N-parameter in the case of outer segmented electrode geometry is $N = 3.0$ and for the centre segmented electrode geometry it is $N = 2.5$ as seen in the plots shown in figure 9.5 and 9.8.

Another interesting result can be deduced from these plots that the choice of the N-parameter value is also dependent on the heating rate of the trap. For relatively low heating rate traps, the ion transportation under the influence of hyperbolic tangent profile with larger values of the N-parameter causes less number of quanta gain or vice versa.

9.4 Ion separation in one dimension

In chapter 8 it is shown that, in order to make the separation process faster, one has to design a trap which provides maximum values for the octupole term β in its potential field profile to maximise the secular frequency during the separation process. In this section, the ion dynamics during the separation process is discussed for both external and central segmented electrode trap geometries. To keep the consistency in the trap designs, the widths (b and c) and the separation (a) of the rf electrodes is considered to be the same as discussed in the previous sections. Whilst the width of the static potential electrodes

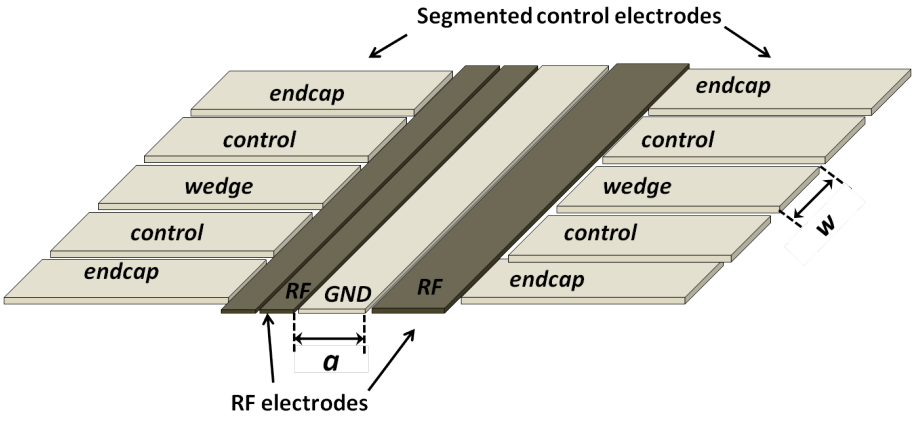

Figure 9.9: External segmented electrode surface trap geometry for separation of two ions.

are $w = 3.75\ a$ for the outer segmented electrode geometry and $w \approx\ a$ for the centre segmented electrode geometry, where a is the separation between the rf electrodes. In both traps initially two ions are trapped in a single potential well by applying an rf voltage on the rf electrodes, a positive voltage on the *endcap* electrodes and a negative voltage on the *control* and *wedge* electrodes. In order to separate the two ions, the voltage on the *wedge* electrode needs to be brought to some positive voltage from its initial negative voltage to create a potential wedge between the trapped ions in a single potential well. Meanwhile, the voltage on the *control* electrodes is also decreased further monotonically to maintain the ions position in the rf nodal path. As required voltages to produce separation between the ions on the *wedge* and *control* electrodes approaches, two distinct potential wells appear and ions are separated.

9.4.1 Ion separation in outer segmented static electrode geometry

In the simulations, a set of voltages shown in table 9.1 are applied on the static electrodes of an outer segmented electrode geometry shown in figure 9.9. The rf voltage is set to $V_{rf} = 450$ V with a driving frequency of $\Omega_{rf} = 2\pi\ 52$ MHz. The static voltages are calculated to confine the ions firmly during the separation process and satisfy the optimum

Electrode	voltage at t_o	voltage at t_f
endcap	30 V	30 V
wedge	-34 V	50
control	0	-48

Table 9.1: Applied voltages on the electrodes (shown in figure 9.9) at time t_o to produce confinement in the z-direction (single potential well) and at t_f when the double well is produced.

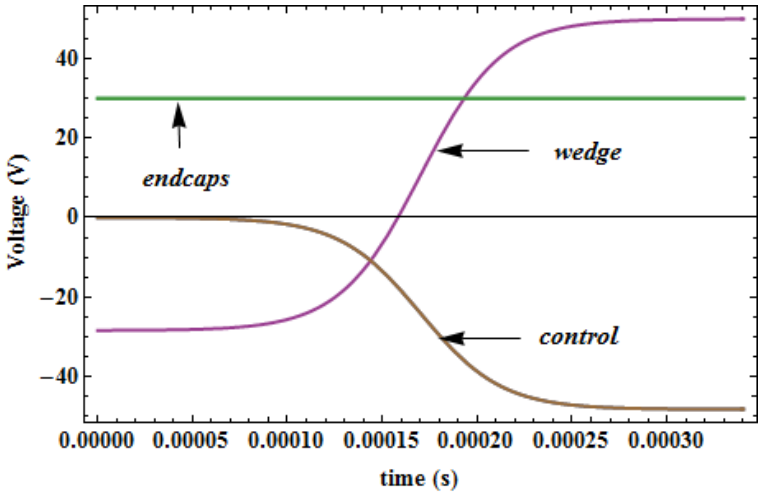

Figure 9.10: Applied voltages variation in time on the *control* and *wedge* electrodes to produce the ion separation process.

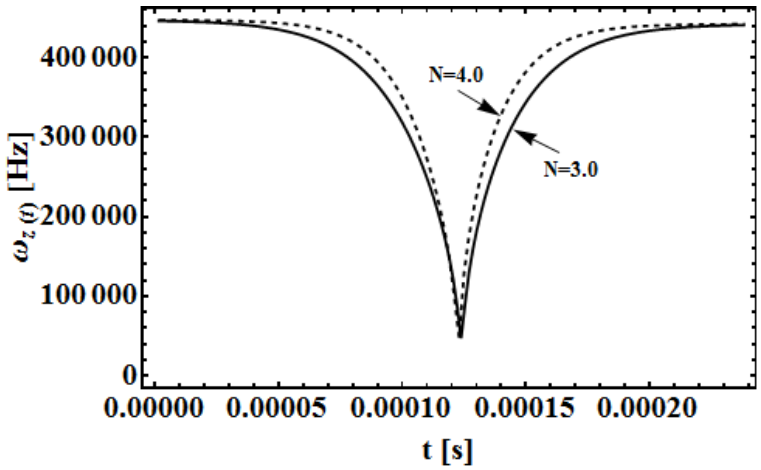

Figure 9.11: Variation of the z-secular frequency during the ion-separation process followed by hyperbolic tangent time profile of $N = 3.0$ (dashed) and $N = 4.0$ (solid). The secular frequency $\omega_z/2\pi$ is $\approx$ 500 kHz in the start and at the end of the process. The lowest frequency attained by the ions during the separation is $\omega_{min}/2\pi \approx 42$ kHz.

voltage conditions described in section 7.4. As discussed earlier that the relatively smaller values of the N-parameter of hyperbolic tangent profile are reasonable for faster shuttling process. To workout the appropriate value for the N-parameter in the separation process, $N = 4.0$ and $N = 3.0$ with different shuttling times is used to change the voltages on the static potential electrodes as shown in figure 9.10.

In order to separate two trapped ions, initially two $^{171}Yb^{+}$ ions are considered trapped in a single potential well at the centre of the *wedge* electrodes. If a which is separation of rf electrodes is set to be 60 μm, at the end of the separation process, the ions are located in two distinct potential wells $\approx 2 \times w$ distance apart.

As the applied voltages varies in time, the secular frequency in z-direction also varies

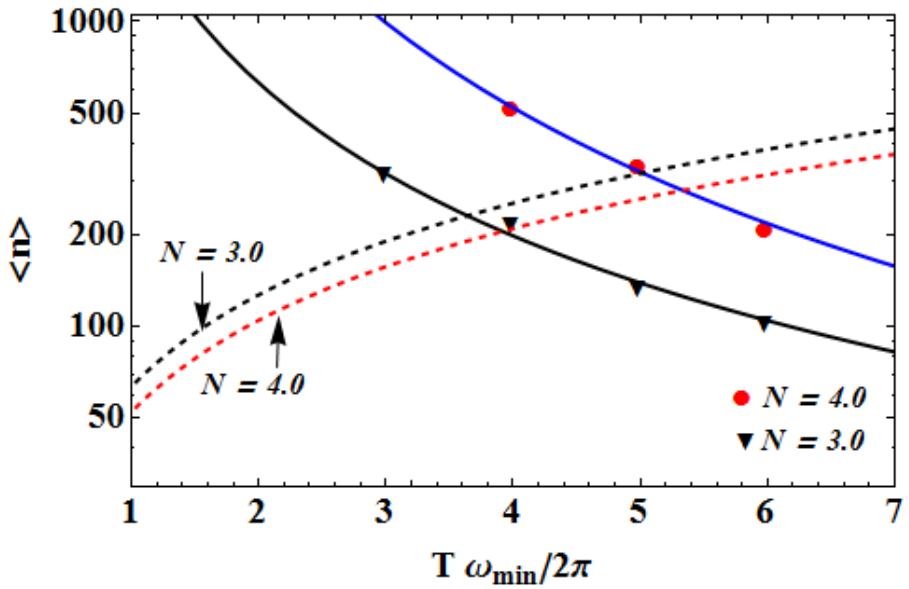

Figure 9.12: The gain in the average motional quanta $\langle n \rangle$ by the ion in an external segmented electrode geometry after the separation process. Hyperbolic tangent time profiles of $N = 4.0$ and $N = 3.0$ are used to change the voltage on the control electrodes. Total shuttling time is scaled with secular frequency $\omega_{\min}/2\pi = 42$ kHz and represented in number of cycles. The solid lines represent the best fits to the average motional quanta $\langle n \rangle_s$ and the dashed line shows the gain of $\langle n \rangle_{an}$ from the anomalous heating of the trap. The cross over points set lower limits for the gain in $\langle n \rangle$ during the shuttling process.

accordingly during the separation process as discussed in section 8.3. The variation of the secular frequency for $^{171}Yb^{+}$ ions is shown in figure 9.11, where it can be seen that the secular frequency reaches to a minimum (ω_{min}) when the double well is about to appear. The secular frequency at this moment is at its minimum and can be calculated as $\omega_{min}/2\pi = 42$ kHz using the equation (8.10) given in chapter 8.

As it is shown in figure 9.11, the secular frequency of the ions varies rapidly and at one point it is at its lowest. Therefore, it is necessary to separate the ions at the time scale of this minimum secular frequency $T\omega_{\min}/2\pi$. The gain in motional quanta $\langle n \rangle$ is plotted in figure 9.12 on various separation (shuttling) times for hyperbolic tangent with $N = 4.0$ and $N = 3.0$. The time-axis of the plots is normalised with minimum secular frequency achieved by the separated ions and represented in number of cycles $T\omega_{\min}/2\pi$, where $\omega_{\min}/2\pi \approx 42$ kHz. In the plots shown in figure 9.12, it can be seen that approximately same number of quanta are added at the cross-over points for the separation profiles with $N = 3.0$ and $N = 4.0$, but the separation duration is less in case of $N = 3.0$.

In figure 9.12, the same trend can be seen for the gain of the average motional quanta $\langle n \rangle_s$ of the ion which reduces when larger shuttling times are used but addition of motional quanta $\langle n \rangle_{an}$ (dashed line) from the anomalous heating rises with increasing shuttling

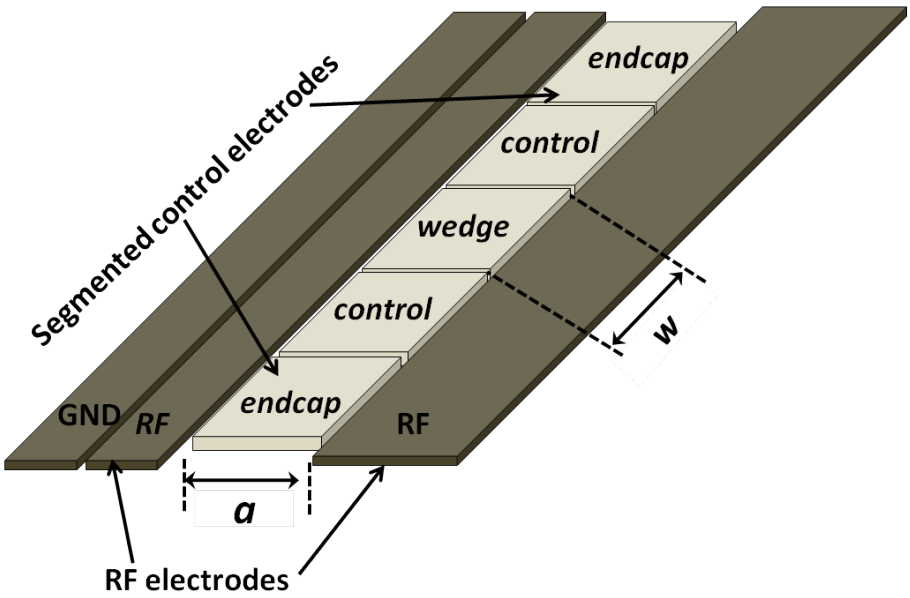

Figure 9.13: Centre segmented electrode trap geometry for separation of two ions.

Electrode	Voltage (V) at t_o	Voltage (V) at t_f
endcap	8	8
wedge	-0.04	4
control	0	-3.8

Table 9.2: Applied voltages on the trap electrodes for centre segmented trap geometry (shown in figure 9.13) at time t_o to produce confinement in the z-direction (single potential well) and at t_f when the double well is produced.

periods. The gain of the motional quanta $\langle n \rangle_{an}$ also depends on the N-parameter of the hyperbolic tangent profile and is higher for lower N. This trend can be explained by the profile of the variation of the secular frequency during the separation with $N = 3.0$ (solid curve) and $N = 4.0$ (dashed curve) shown in figure 9.11. This shows that the separating ions spend relatively larger time in lower frequency region during the separation process when the value of the N-parameters is smaller or vice versa. The cross over points of the $\langle n \rangle_s$ (solid lines) and $\langle n \rangle_{an}$ (dashed line) in figure 9.12 set the lower limit of the total average motional quanta $\langle n \rangle$ gained by the ion during the separation process.

9.4.2 Ion separation in centre segmented static electrode geometry

In an optimum central segmented electrode trap geometry shown in figure 9.13, where $w \approx a$, two ions are separated by applying the voltages shown in table 9.2 to the static potential electrodes. The voltages are varied in time using the hyperbolic tangent time profile

$N = (3.0,\ 4.0,\ 4.5)$ because the shuttling protocol with relatively smaller values of N-parameter adds less amount of quanta to the ion for shorter shuttling periods as discussed earlier. The rf voltage is set to $V_{rf} = 500$ V with a driving frequency of $\Omega_{rf} = 2\pi$ 55 MHz. The static voltages are calculated to confine the ions with maximum achievable secular frequency during the separation process and satisfy the voltage constraints set in section 7.4. Similar to the external segmented geometry, the secular frequency in z-direction varies during the separation process. The lowest secular frequency ω_{min} achieved by $^{171}Yb^{+}$ ion in this trap geometry is about 230 kHz.

Using the simulation, the average motional quanta $\langle n \rangle$ gained by the ion after separation process is plotted in figure 9.14. The time-axis of the plots is normalised with minimum secular frequency achieved by the separated ions and represented in number of cycles $T\omega_{\min}/2\pi$, where $\omega_{\min} \approx 230$ kHz. In contrast with the external segmented electrode design, the motional quanta gain from the anomalous heating $\langle n \rangle_{an}$ (dashed line) does not rise sharply and having a negligible effect of N-parameters. The cross over points of $\langle n \rangle_{s}$ (solid lines) and the $\langle n \rangle_{an}$ (dashed line) set the lower limit of the total average motional quanta $\langle n \rangle$ gained by the ion during the separation process, whereas the separation profile under the influence of the hyperbolic tangent with $N = 4.0$ adds less number of total quanta $\langle n \rangle$. Furthermore, the trend of the motional quanta gain is similar as seen in the linear shuttling protocols.

By comparing separation processes in both trap designs, it can be concluded that the gain in the total motional quanta $\langle n \rangle$ during the separation process is much lower in the centre segmented electrode geometry due to the higher value of the ω_{min}. These results confirm the importance of optimisation of surface traps geometries to achieve overall maximum secular frequency, ω_o, as well as the minimum secular frequency, ω_{min}, attained by the ion during the separation process. Addition of the motional quanta during the separation process is much less for relatively higher values of the secular frequencies and make the process faster. The hyperbolic tangent profile with relatively smaller values of N-parameter is recommended for the variation of voltages on the control electrodes, but the appropriate value depends upon the heating rate of the trap itself, if the heating rate in the trap is low than the higher value of N-parameter is preferable or vice versa.

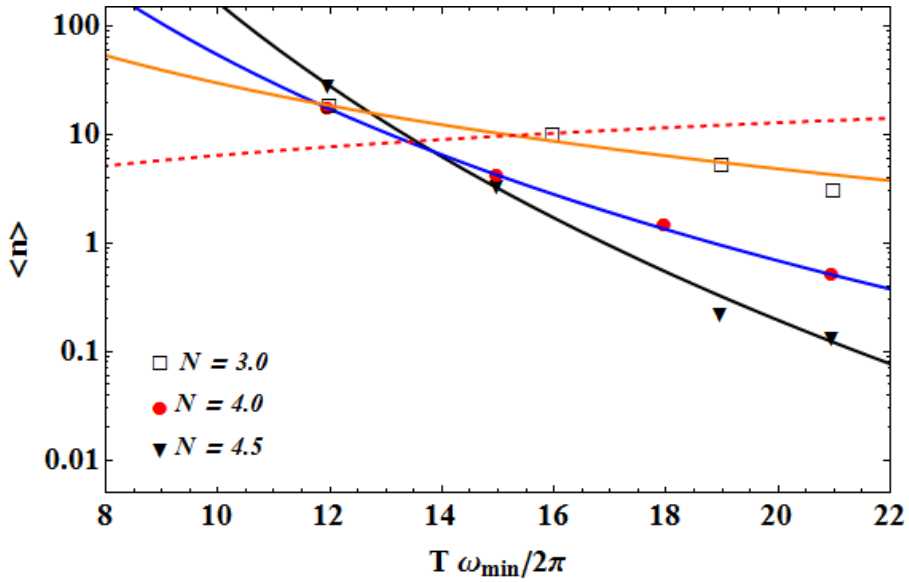

Figure 9.14: The gain in the average motional quanta $\langle n \rangle$ by the ion in an external segmented electrode geometry after the separation process. Hyperbolic tangent time profiles of $N = 3.0$, $N = 4.0$ and $N = 4.5$ are used to change the voltage on the control electrodes. Total shuttling time is scaled with secular frequency $\omega_{\min}/2\pi = 230$ kHz and represented in number of cycles. The solid lines represent the best fits of motional quanta $\langle n \rangle_s$ and the dashed line shows the gain of $\langle n \rangle_{an}$ from the anomalous heating of the trap. The cross over points set lower limits for the gain in $\langle n \rangle$ during the shuttling process.

Chapter 10

Conclusion

This thesis described an experimental setup for the reliable operations and testing of ion traps. Building of the vacuum system, stabilisation of the laser frequencies and data acquisition techniques are described in detail. Using the setup, an ion trap is characterised for its performance and a heating rate measurement is described. For Yb^+, no abnormally high heating rate was observed in a relatively small ion trap. Measurements were performed of the cooling wavelengths for different isotopes of Yb^+ which are more precise than previously published values. Furthermore, a simple technique to determine the resonant transition frequencies and isotope shifts of the $^1S_0 \rightarrow {}^1P_1$ transition for different stable Yb isotopes is also described. These transition frequencies are very important for the photoionisation of the Yb atoms. Using this technique, new values for the resonant frequencies that differ from the previously published work were presented. The same technique with little modification can also be used to measure the Doppler-shifted transition frequencies that occur when the laser and the atomic beam are not perpendicular. Hence the technique allows for predictions of transition frequencies in realistic ion-trap setups where the laser and the atomic beam are not necessarily perpendicular.

These frequency measurements are particularly useful for groups setting up an ytterbium ion trap experiment, as the availability of more precise and accurate frequency measurements significantly simplifies the initial trapping process.

Large ion trap arrays, where the qubits can be trapped and stored in separate trapping regions are required to perform large scale quantum computation. This requires fast and adiabatic transportation of the ions between the trapping regions. In order to implement fast ion shuttling and separation processes, optimisation techniques for surface trap geometries are described in this thesis. Trap designs are also optimised for maximum

trap depths at given ion height. Ion shuttling and separation protocols were investigated using optimised trap geometries and it is shown that decreasing the ion-static potential electrode distance can substantially improve the ability of a trap array to provide fast adiabatic ion transportation. Using simulations, the limiting factor for adiabatic shuttling in linear regions was shown to be the heating of the trapped ions from anomalous heating. This shows the importance of fast shuttling of ions. The same behaviour was also observed for the ion separation process whose time scale predominantly depends on the lowest frequency attained by the ions during the separation process. Therefore trap arrays having relatively high secular frequencies at larger ion heights should be designed. In microfabricated ion traps, the dissipation of power is another limiting factor to achieve relatively high secular frequencies and the trap depth. Study is in progress in our lab to design fabrication methods, so that microfabricated ion traps can handle relatively high voltages with less power dissipation in the trap.

Further study is also in progress for the optimisation of the junction regions where the potential barriers appear at the junction regions and variation of the secular frequencies is also observed which significantly limit fast and adiabatic shuttling through the junctions. The studies in this thesis provide a significant contribution towards scaling ion quantum technology and many exciting innovations are to be expected in the next few years.

Appendix A

Chip bracket pin receptacles map

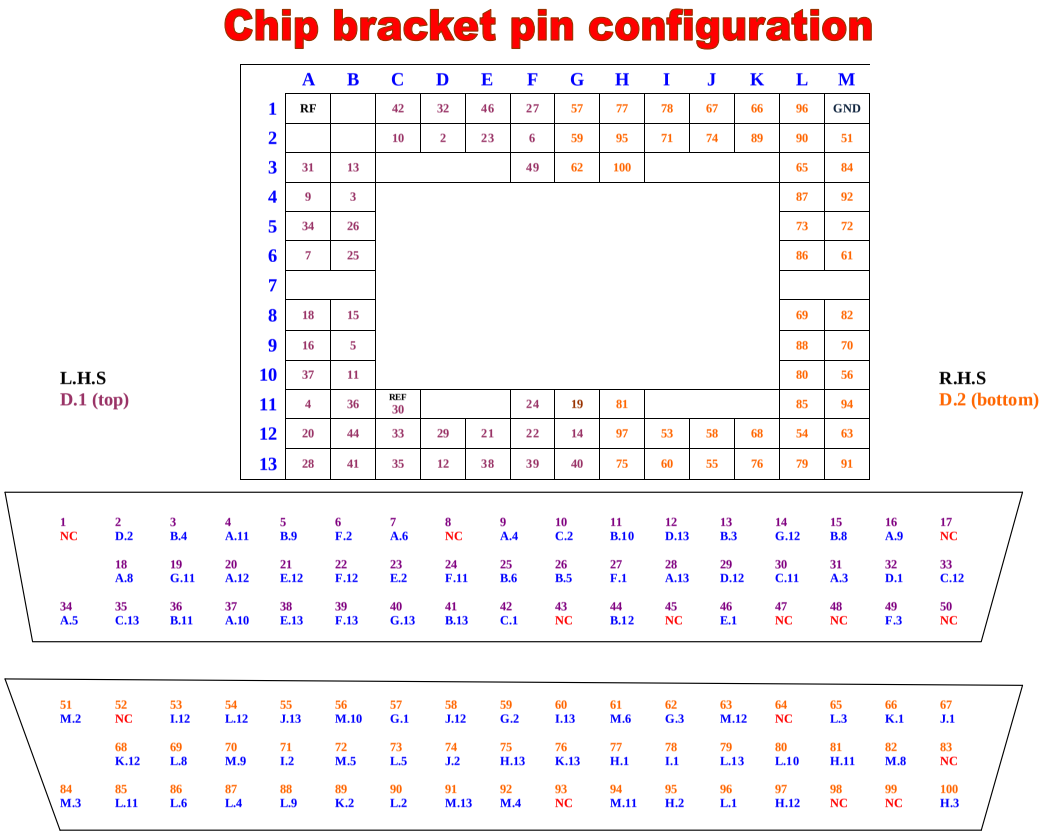

Figure A.1: Pin receptacles mapping with 50×2 D-type electrical feedthrough on the 6" CF flange. The rf and ground receptacles are connected with a separate electrical power feedthrough on 1.3" CF flange

Appendix B

Re-entrant viewport drawing

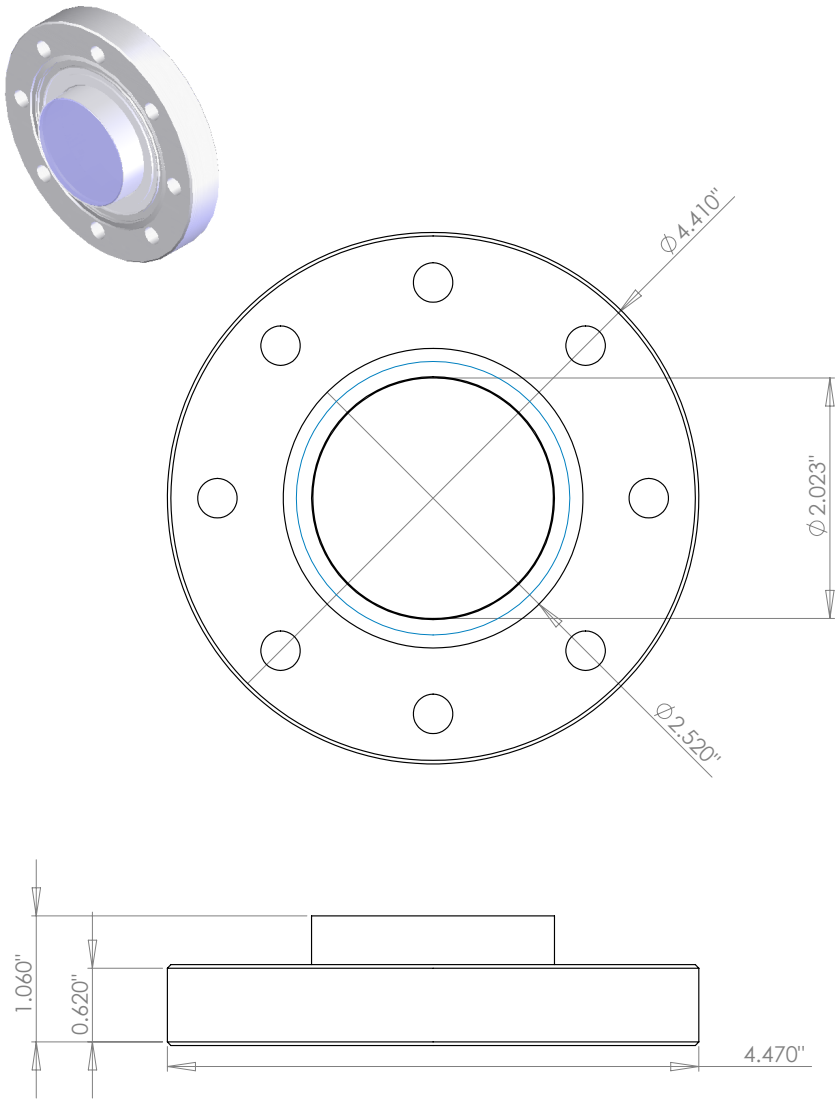

Figure B.1: SolidWork drawing of the custom view port.

Appendix C

LabVIEW program for laser locking scheme

Glossary:

LabVIEW VI: LabVIEW programs are called virtual instruments or VIs. Each VI consists of two interfaces; a block diagram and a front panel. The block diagram serves as a programmatic interface and the front panel serves as a user interface.

LabVIEW Project: The LabVIEW Project explorer helps to organise files and provide added functionality that helps in managing and developing large LabVIEW applications. The project can handle the LabVIEW files running on different operating systems (or hardware targets) simultaneously and helps to communicate between the programs.

RTOS-Module: A LabVIEW real-time module which allows the user to create an application with precise timing and absolute reliability that runs on embedded hardware targets (in our case a computer)running on real time operating systems (RTOS).

Data: Data type can be an integer (signed or unsigned number), double (fraction number), boolean, string or text type, an array, a wave form etc.

Signal: A signal can be described as a set of data representing the voltage level on an input or output analogue or digital channel of an electronic card.

Control: Controls on the front panel allow a user to input data. The control may be a button, numerical box, manu bar, scroll bar, knob etc.

Indicator: Indicators on the front panel display the data. The indicator may be a graphical or chart display, LED type display, numerical display, button display etc.

RS-232 COM-port: A communication port (COM-port) given on computers which uses RS-232 data transfer protocol. In RS-232 protocol data is sent and received as a time-series of bits.

Virtual-PID controller: A virtual proportional-integral-derivative (PID) control application given in LabVIEW. The PID controller calculates an error value by comparing the desired set point and the measured value.

The schematic diagram of the laser locking program is shown in figure C.1. To run the program on the real time installed computer, it is necessary to load the program in the real-time project. After loading the program, fill in the appropriate values in the control boxes given in the front panel of the program and then press the run button. The front panel of the laser locking program shown in figure C.2 runs on the real-time operation system (RTOS).

The program detects the voltage signals of the photodiodes on the analogue channels of the NI-PCI-6143 S card and generates output signals (error signals) on the analogue output channels of the NI-PCI-6722 card to control drift in the laser wavelengths.

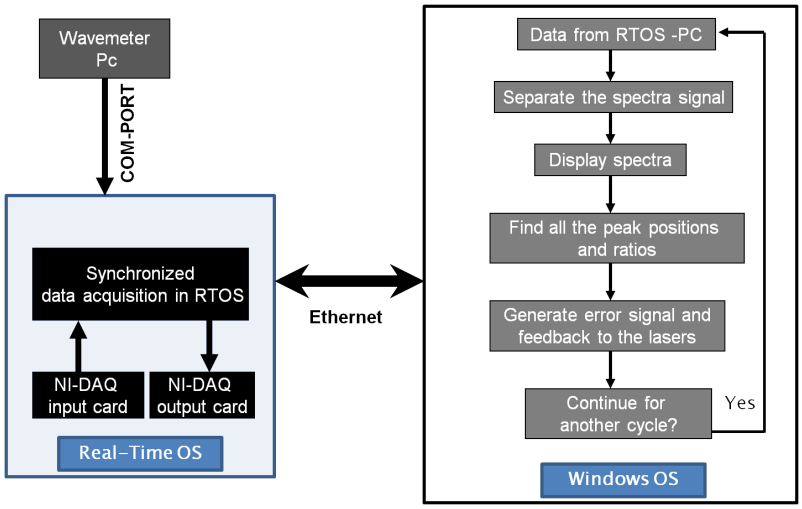

Figure C.1: Schematic diagram of laser locking project.

The program has two major parts; one uses wavemeter data and the other uses signals from scanning cavities to produce the error signals for controlling the respective laser wavelengths.

Wavemeter locking scheme

To measure the laser wavelengths, a wavemeter (Highfinesse WS7) is used in the lab. The wavemeter is specified with an absolute error of ±60 MHz over the range of frequencies which are used in the lab. The wavemeter runs on its built-in software but the data

from the wavemeter can be accessed using a LabVIEW program. In order to retrieve the data (wavelength or frequency) from the computer running the wavemeter, first run the LabVIEW program for the wavemeter on the computer. The program exports the calculated wavelength (data) in the form of "string" data type to the COM-port (RS-232) of the computer. Then the computer running the RTOS LabVIEW can access the data through its COM-port (RS-232) as shown in the figure C.1

The wavemeter section of the program is highlighted in figure C.3, where each control is numbered and their descriptions are as follows;

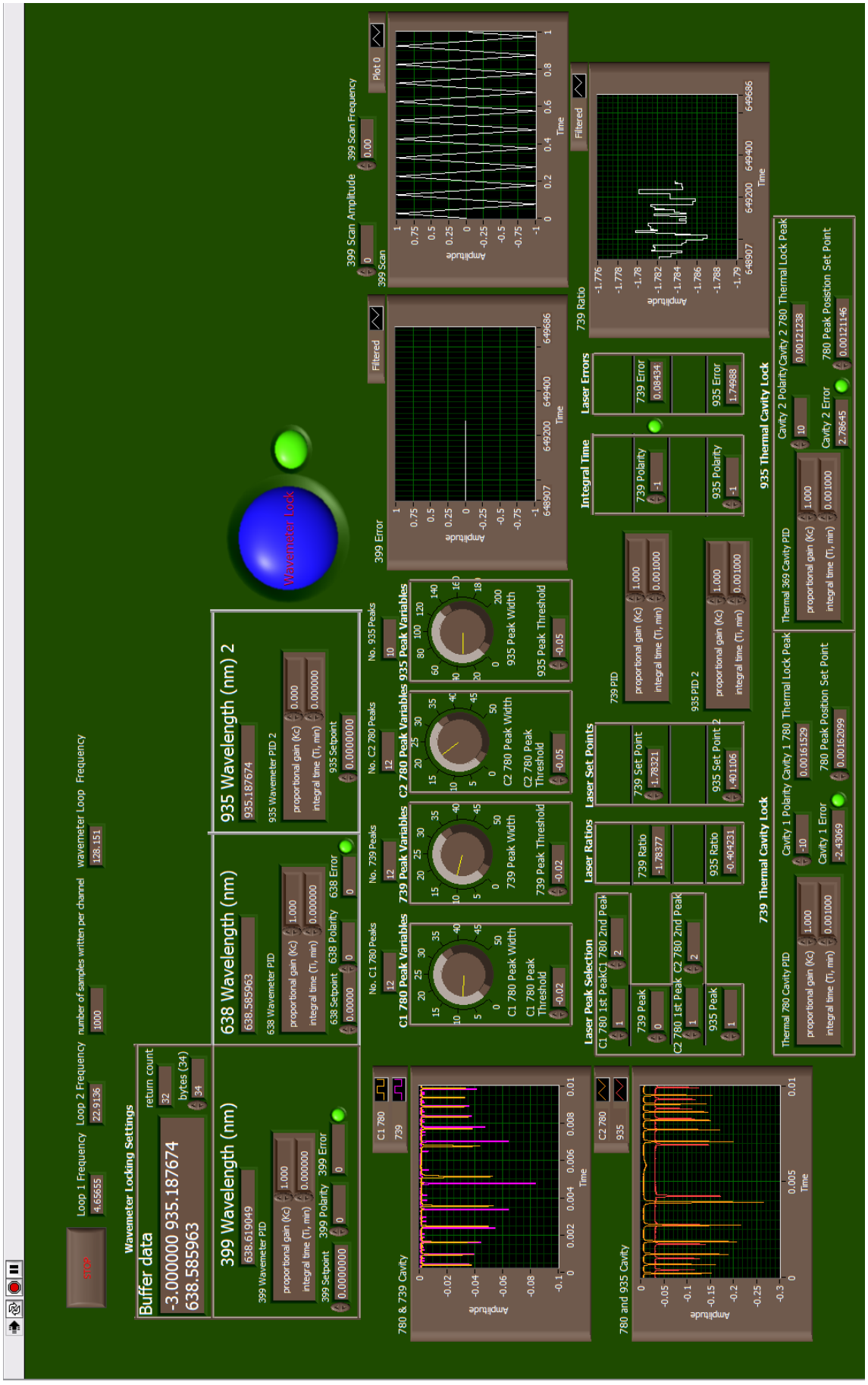

Figure C.2: Front panel of LabVIEW program for laser locking scheme.

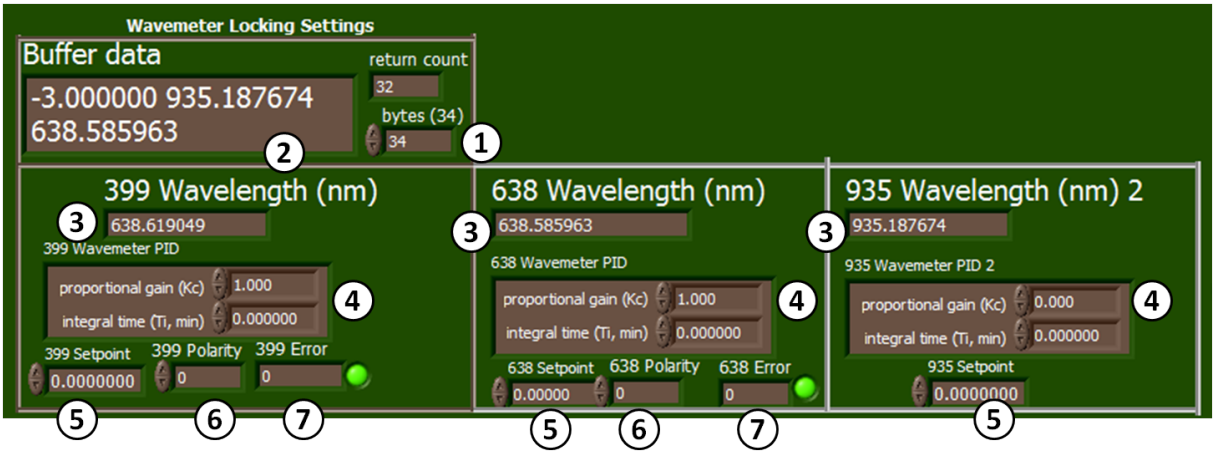

Figure C.3: Wavemeter lock section.

1. The calculated wavelength sent from the wavemeter computer is in the form of "string" data type. Each value of the wavelength (or frequency) is encoded in 10 bytes. Therefore set the number of bytes in the control box accordingly. For example 30 bytes for three wavelengths. (To ensure the reliable flow of the data set 34 bytes is recommended).

2. Indicator box of the wavelengths (in "string" data type) separated by spaces. If the display value is -3.000000 means that there is no or low intensity of the laser light on the particular channel of the wavemeter.

3. The wavelength data shown in (2) is separated and converted into *double* data type format and displayed in the separate indicator boxes.

4. Virtual-PID controller boxes. Reasonable values for these settings can be found by slowly changing the input values until the laser frequency is stabilised at the desired values. (typical range for *proportional gain*: 1 to 10 and *integral time*: 0.001 to 0.0001).

5. Setpoint control boxes allow a user to set a desired wavelength value (up to 6 decimal places) to which the laser has to be locked.

6. Control settings for the polarity of the generated voltage signal. Typical value of ± 1 depending on the required feedback, positive or negative voltage to stabilise the laser frequency.

7. Indicator for the generated voltage signal (in volts) which is fedback to the laser controller via the one of analogue output channels of the card (NI-PCI-6722).

Cavity lock

The scanning cavity section of the labVIEW program, scans the cavities and simultaneously reads the voltage signal (which appears in the form of peaks) from the photodiodes using the analog input card (NI-PCI-6143 S) and then generates an error signal (in volts) by comparing the positions of the signal peaks of the reference laser (780-nm) with the laser to be stabilised. This section of the laser locking program is shown in figure C.4. The corresponding description of the numbered *controls and indicators* are as follows;

1. Graphical indicator of the detected voltage signal from the photodiodes. Each displayed signal peak (inverted) is produced at the photodiodes while the scanning the laser cavities.

2. Control box settings to detect the position of the displayed signal peaks as seen in (1). To distinguish the peaks from each other, the *peak width* control knob (which sets the minimum peak width to be taken account) and the *threshold* control box (which sets the upper limit on the amplitude of the peak, below that, the peak would not be considered) needs to be set so that every displayed signal peak should be properly detected and its position is calculated. The settings of the controls resembles the full-width-half-maximum (FWHM) of a signal. These control settings may vary depending upon the signal from the particular laser cavity. The threshold value can be found by looking at the display (1), typically half of the amplitude of the peaks can be inserted as threshold value and then adjust the knob control until the number of peaks shown in (3) is same as the number of peaks displayed in (1).

3. Numerical indicator boxes show the number of the peaks found after adjusting the peak control settings in (2). The number of peaks should be same as the number of peaks displayed in (1). If not, adjust the settings in (2).

4. *Laser peak selection* controls offer which peaks of the lasers are to be compared. (Typically position of two adjacent peaks are to be compared).

5. Once the peak numbers are selected, the indicators display the the ratio between the position of the selected peaks.

6. *Set point* control has to be set (typically once) to the same as the value displayed in (5).

7. Virtual-PID control boxes. Reasonable values for these settings can be found by

slowly changing the input values until the laser frequency is stabilised at the desired values. (typical range for *proportional gain*: 1 to 10 and *integral time*: 0.001 to 0.0001).

8. Polarity setting controls for the generated error signal. Typical value of ±1 depending on the required feedback, positive or negative voltage to stabilise the laser frequency.

9. Virtual-PID controllers to control the thermal drift of the cavities. Typical setting for *proportional gain* and *integral time* are the same as the other PID controls (7) and the setting of *Peak Position Set Point* controls is the position of the first (or second) 780-nm laser peak which is displayed at the horizontal axis in the peak display (1) for the corresponding cavity.

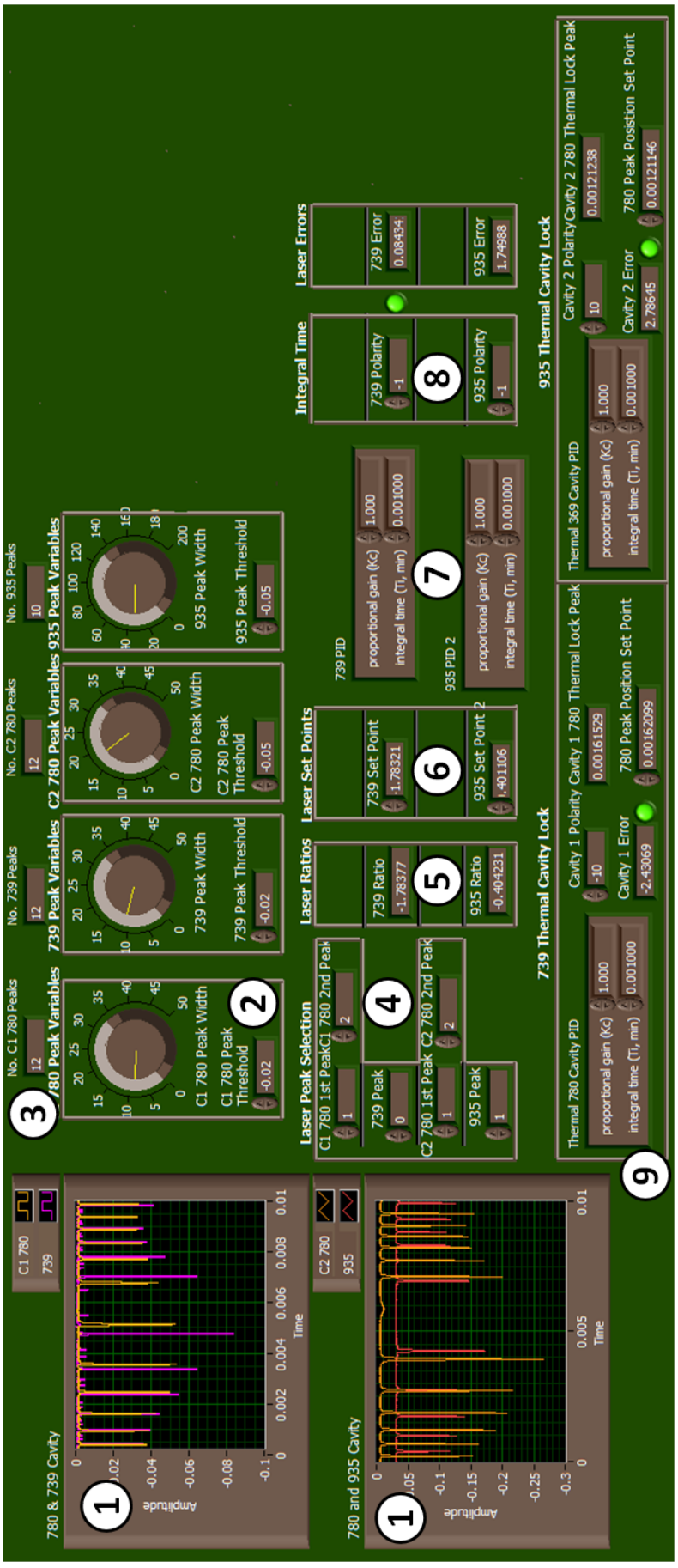

Figure C.4: Scanning cavity lock section.

Program code

The locking scheme is implemented in LabVIEW real-time module. The program code is shown in parts in figure C.5, C.6 and C.7. The portion of the locking program code which access the wavemeter data is shown in figure C.5. The code reads the data sent by the wavemeter PC using the COM-port of the real time target PC and produces an error signals for the lasers to be controlled. The portion of the code shown in figure C.6 reads the data / signal from the input DAQ-card and processes the data to produce error signals which are then to be fed back to the laser setups. The error signals produced by the program codes are then generated in form of analogue voltage signals at the output channels of the DAQ-card using the program code shown in figure C.7.

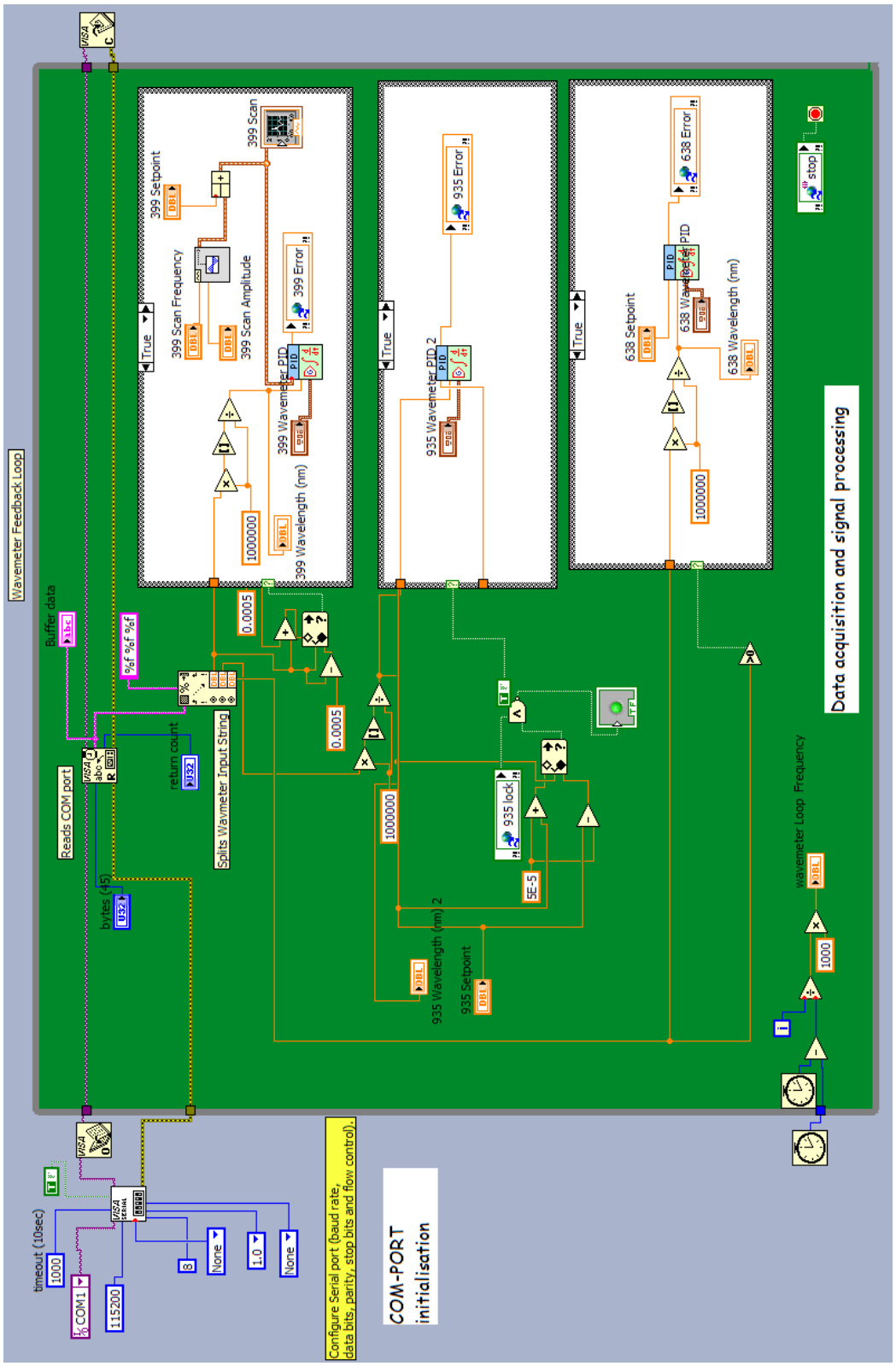

Figure C.5: Wavemeter lock code. The code access the data sent by the wavemeter software and calculates error signal.

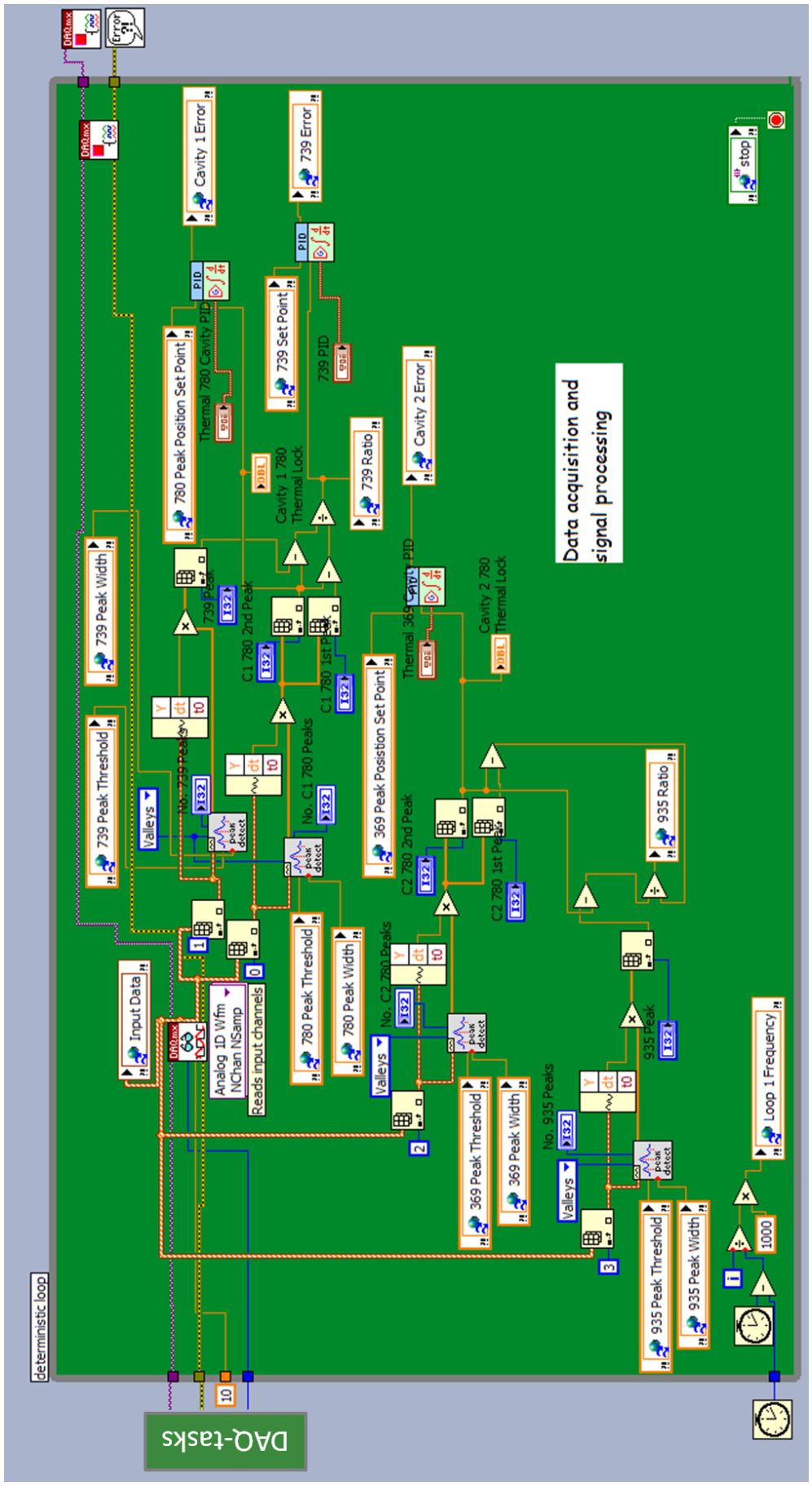

Figure C.6: Scanning cavity lock code. The code reads the data / signal from the input DAQ-card and calculates the error signal

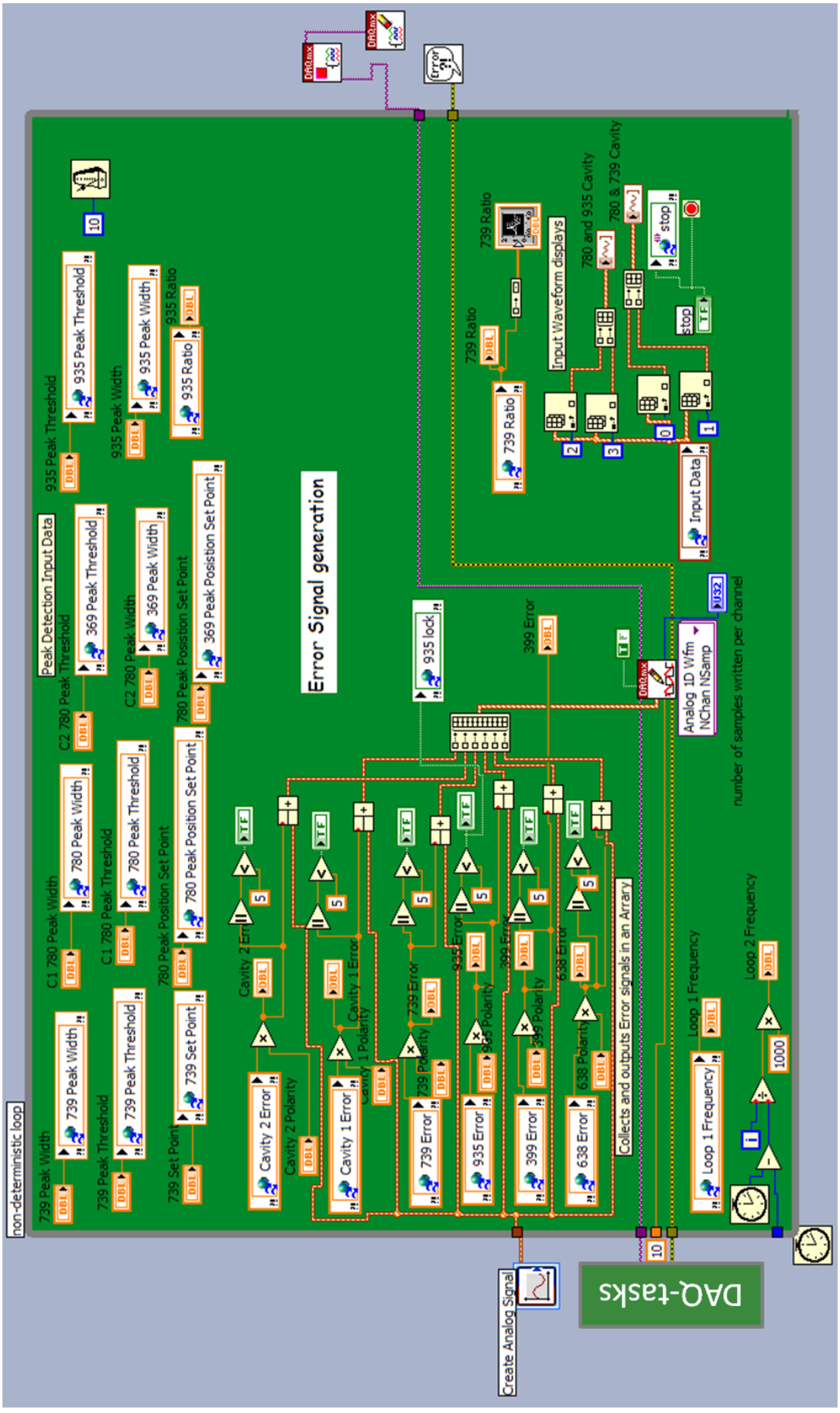

Figure C.7: Error signal output code. The code generates the output signal on the output DQA-card

Appendix D

LabVIEW program for EMCCD camera

LabVIEW VI: LabVIEW programs are called virtual instruments or VIs. Each VI consists of two interfaces; a block diagram and a front panel. The block diagram serves as a programmatic interface and the front panel serves as a user interface.

LabVIEW Project: The LabVIEW Project explorer helps to organise files and provide added functionality that helps in managing and developing large LabVIEW applications. The project can handle the LabVIEW files running on different operating systems (or hardware targets) simultaneously and helps to communicate between the programs.

Data: Data type can be an integer (signed or unsigned number), double (fraction number), boolean, string or text type, an array, a wave form etc.

Signal: A signal can be described a set of data representing the voltage level on an input or out put analogue or digital channel of an electronic card.

Control: Controls on the front panel allow an user to input data. The control may be a button, numerical box, manu bar, scroll bar, knob etc.

Indicator: Indicators on the front panel display the data. The indicator may be a graphical or chart display, LED type display, numerical display, button display etc.

The program written in LabVIEW runs on the computer where the EMCCD camera's PCI-card and drivers are installed. The program accesses the dynamic link libraries (dll) of the camera by using the LabVIEW controls provided by the company software. The

LabVIEW program controls and indicators can access all the required settings of the camera. The front panel of the LabVIEW program is shown in figure D.2. The program is written to image the trapped ions and store the data when ever needed during the ion trap experiment. The descriptions of the controls given in the program are as follows;

1. Control box to set the exposure time for the camera. Typical value is 0.1 second.

2. Control box to set the gain. This is called EMCCD gain. The input value in the control box needs to be adjusted from 0 to 255 until the image appears in the display (9).

3. Control box to set the amplifier gain. This setting is for the camera's read-out gain. Typical value is from 0 to 2. Where 0 setting means no gain. Any value above the 0 enhances the brightness of the picture.

4. Control box to set the time required to save the data taken when the program is part of a project and continuously running. If data storage is required then for a full image size ($1004 \times 1002 \approx 1$ Mega pixels) of 4 MB (given that the data type is 32 bit long integer), a typical value of 0.1 second is sufficient. LabVIEW takes some time to store the data in a data file depending on the size of the file. During this period, the program is no longer refreshing the images taken from the camera. This time delay ensures the data is properly stored.

5. Control box to set the trigger settings of the camera (0 is internal trigger and 1 is the external trigger).

6. These indicators show the error messages from the camera setting functions. The code 2002 indicates the function is working properly.

7. Array indicator returns the image size (number of pixels in X (horizontal) and Y (vertical) directions).

8. Array indicator displays the numerical data from the camera.

9. Graphical indicator displays the intensity plot of the data. To zoom in the interested region, horizontal and vertical scales can be adjusted by right clicking on the the display.

10. Coloured display of the data, horizontal and vertical scales can be adjusted similarly as in (9) to zoom in the interested region.

11. By pressing the button *Abort Acquisition*, the camera's shutter closes and the pro-

gram starts to save the data on a file. After finishing with the data saving, the program starts imaging automatically.

This program can be used in a FPGA or real-time project to synchronise with other LabVIEW programs.

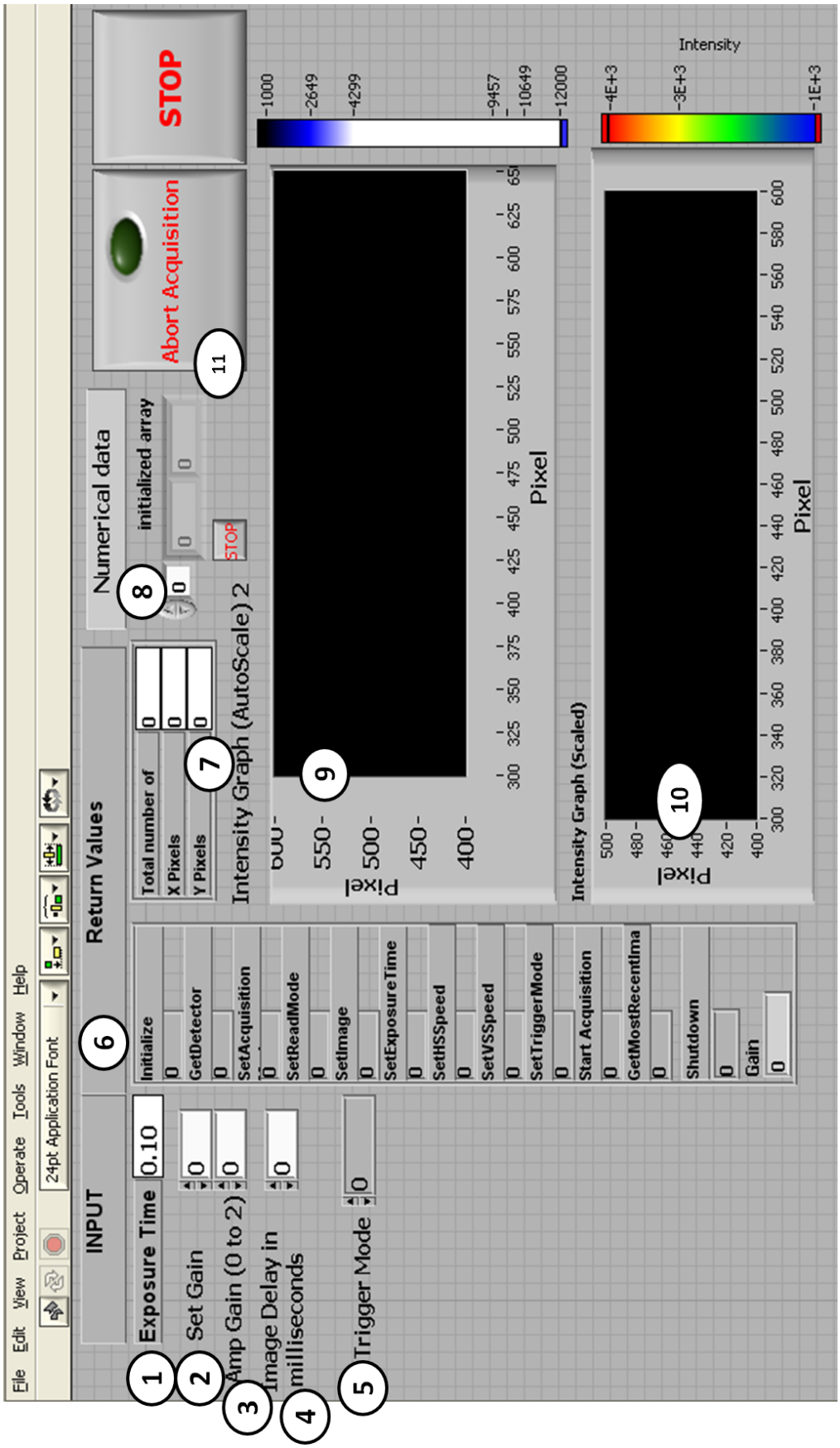

Figure D.1: Front panels of the EMCCD camera program.

Program code

The EMCCD camera software includes LabVIEW controls and program examples. These controls can be used to access the dynamic link libraries of the camera program. Using these controls a LabVIEW code is written to control the EMCCD camera functions. The code is shown in figure D.2

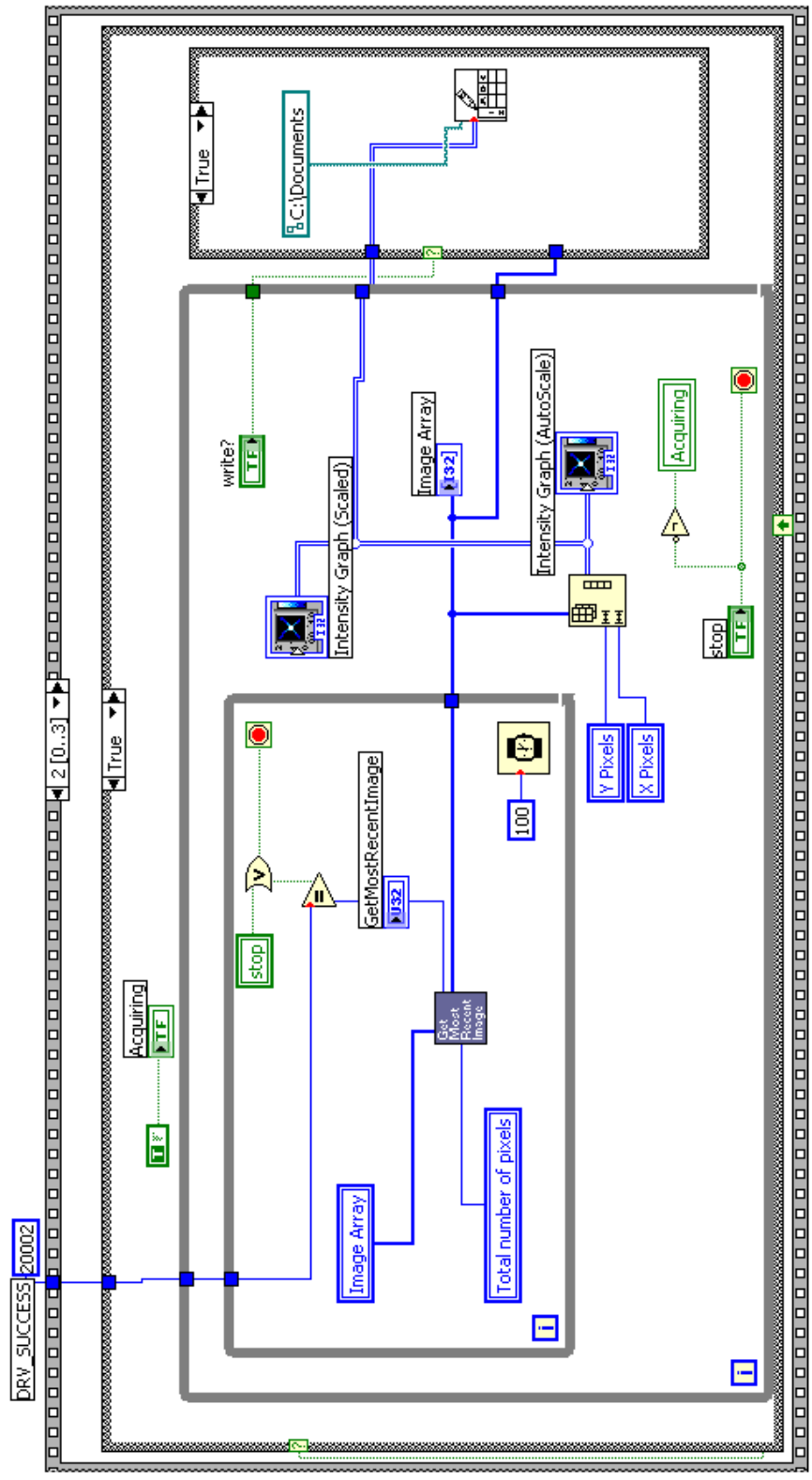

Figure D.2: The LabVIEW code which access the data using the dynamic link libraries of the camera software.

Appendix E

FPGA LabVIEW program for PMT

LabVIEW VI: The LabVIEW programs are called virtual instruments or VIs. Each VI consists of two interfaces; a block diagram and a front panel. The block diagram serves as a programmatic interface and the front panel serves as a user interface.

LabVIEW Project: The LabVIEW Project explorer helps to organise files and provide added functionality that helps in managing and developing large LabVIEW applications. The project can handle the LabVIEW files running on different operating systems (or hardware targets) simultaneously and helps to communicate between the programs.

FPGA-Module: The LabVIEW FPGA module uses LabVIEW embedded technology to program a target field-programmable gate arras (FPGAs) on specified National Instrument hardware.

Data: Data type can be an integer (signed or unsigned number), double (fraction number), boolean, string or text type, an array, a wave form etc.

Signal: A signal can be described a set of data representing the voltage level on an input or out put analogue or digital channel of an electronic card.

Control: Controls on the front panel allow an user to input data. The control may be a button, numerical box, manu bar, scroll bar, knob etc.

Indicator: Indicators on the front panel display the data. The indicator may be a graphical or chart display, LED type display, numerical display, button display etc.

The signal pulse of the PMT used in the lab has a signal pulse of 30 ns followed by a 'dead time' of 5 ns which is sufficient to detect the ion fluorescence which occurs at a rate of ≈ 20 MHz. To read the data in a real-time at this speed requires specific electronics. To read the signal (photon counting) from the PMT a PXI-Compact system, which works with a FPGA module, was used. It consists of an NI-PXI-7842R card with onboard clock of 40 MHz which provides a 40 MHz speed for its digital input and output channels. Only a program written in the FPGA LabVIEW module can operate this card. The program can only be run in a FPGA project. First, open FPGA project ① in LabVIEW as shown in figure E.1. Then under the FPGA Target (RIO0, PXI-7842R) ② run the FPGA program ③. The loaded program is shown in figure E.2. The corresponding description of the numbered controls are as follows;

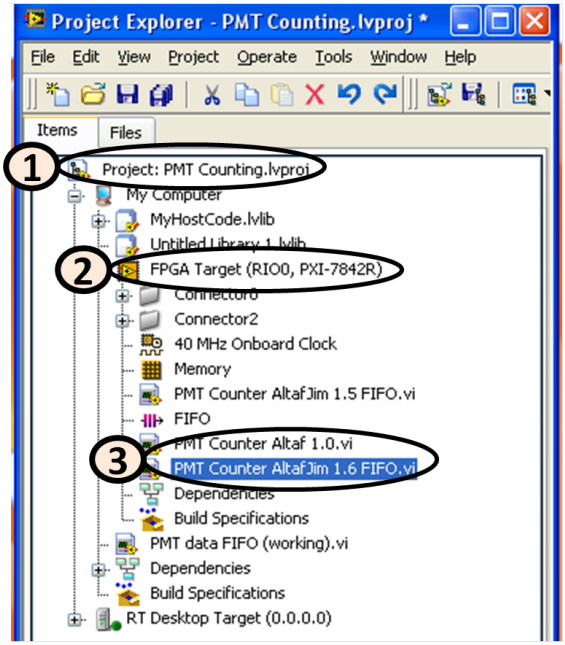

Figure E.1: FPGA project

1. This control button turns the AOM *ON* and *OFF*, which blocks (OFF) and unblocks (ON) the laser light, when pressed.

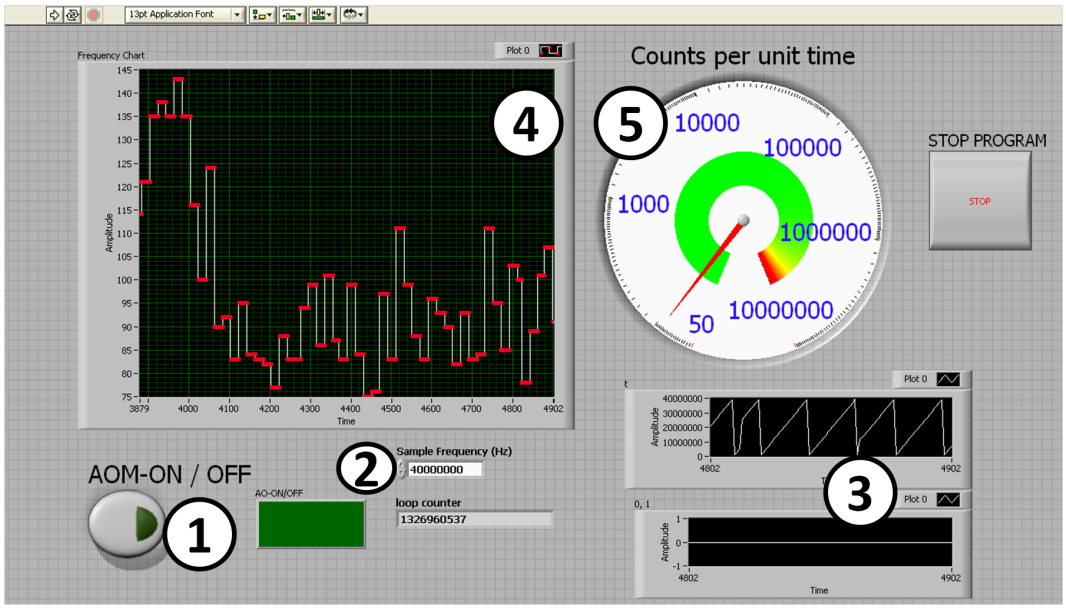

Figure E.2: Front panel of the PMT LabVIEW program.

2. In this control, set the sampling frequency of the data reading from the PMT. If set to 1, it reads the data at the maximum speed of the card. As the speed of the card is 40 MHz, entering the value of 40,000,000 in this control will result in the program counting the data (PMT counts) for a second and then display it in (4) and (5).
3. Graphical indicator illustrating the sampling frequency. Shows the number of samples counted in time.
4. Numerical indicator shows the total number of counts counted in the set time in (2).
5. Graphical indicator for the number of counts shown in a logarithmic scale.

Program code

The program code of this photon-counter program is shown in figure E.3. The code is written LabVIEW FPGA module and runs on the FPGA target.

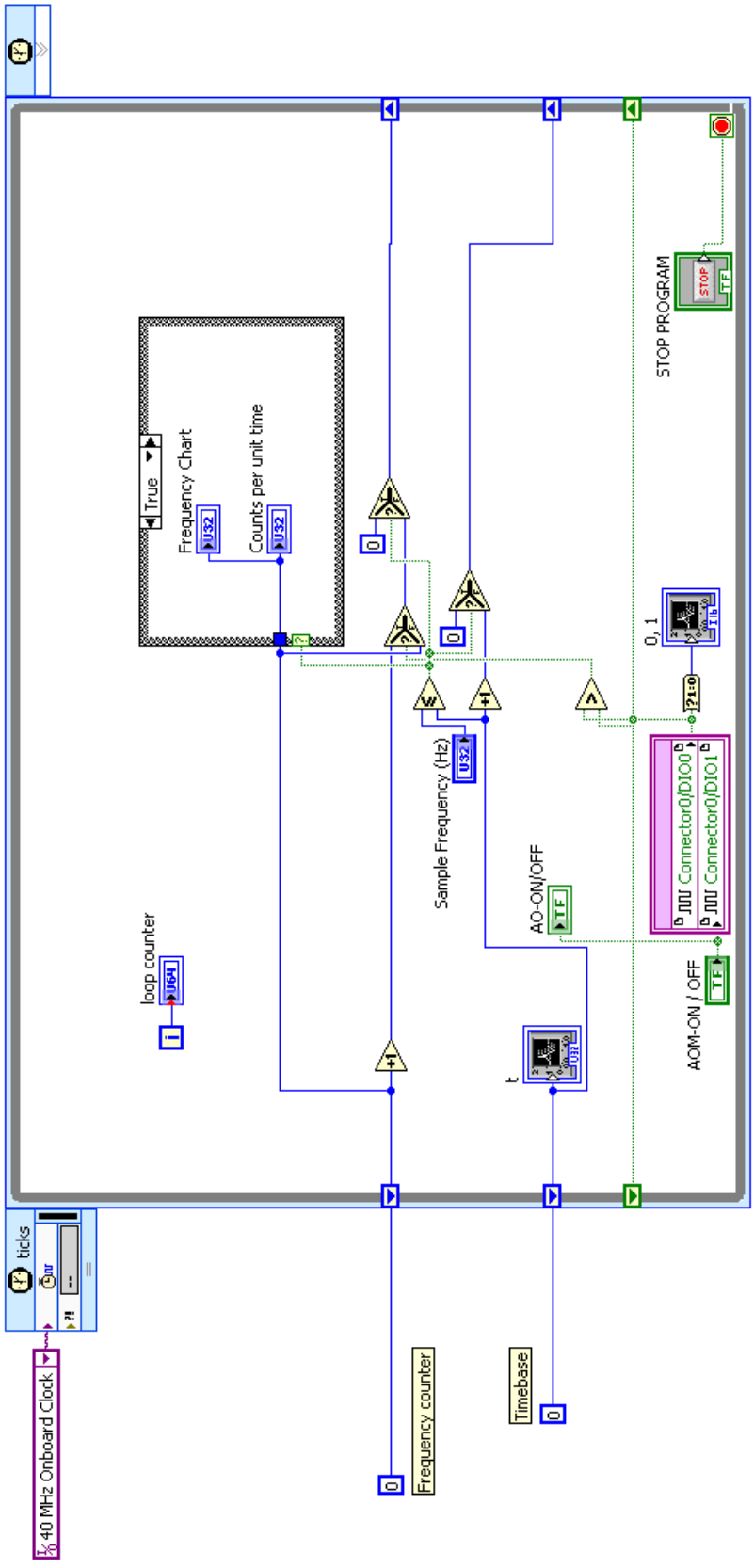

Figure E.3: Program code of the PMT LabVIEW program.

Appendix F

FPGA LabVIEW program for the heating measurement experiment

LabVIEW VI: The LabVIEW programs are called virtual instruments or VIs. Each VI consists of two interfaces; a block diagram and a front panel. The block diagram serves as a programmatic interface and the front panel serves as a user interface.

LabVIEW Project: The LabVIEW Project explorer helps to organise files and provide added functionality that helps in managing and developing large LabVIEW applications. The project can handle the LabVIEW files running on different operating systems (or hardware targets) simultaneously and helps to communicate between the programs.

FPGA-Module: The LabVIEW FPGA module uses LabVIEW embedded technology to program a target field-programmable gate arras (FPGAs) on specified National Instrument hardware.

FIFO: Readable and writable First-in-first-out memory (FIFO) on board memory. Maximum size of 1023 kB.

Data: Data type can be an integer (signed or unsigned number), double (fraction number), boolean, string or text type, an array, a wave form etc.

Signal: A signal can be described a set of data representing the voltage level on an input or out put analogue or digital channel of an electronic card.

Control: Controls on the front panel allow an user to input data. The control may be a button, numerical box, manu bar, scroll bar, knob etc.

Indicator: Indicators on the front panel display the data. The indicator may be a graphical or chart display, LED type display, numerical display, button display etc.

The heating measurement experiment requires the recording of the PMT data (photon counts) at a time scale of 25 ns (40 MHz). In the experiment, the AOM was turned ON and OFF at a time scale of milli-seconds. The timing scale of each run of the experiment is illustrated in figure F.2. After each run the data has to be recorded in a data file. The number of runs can be a few hundred. As the FPGA setup has a limited onboard memory (2 MB), this huge amount of data can not be saved on the FPGA card for long term. Therefore the data taken in a limited time (order of milli seconds) was stored on a temporary basis on a onboard memory buffer (FIFO) of the FPGA card.

The memory size (maximum 1023 kB) and data type can be set using the FIFO setting option under the FPGA target tree given in the FPGA project tree (highlighted by a dashed block in figure F.1). Before the FIFO fills up completely, the data is fetched by a program running on a windows based operating system LabVIEW program (host program) and saved on the disc of the computer and FIFO is ready to store new data for the next run.

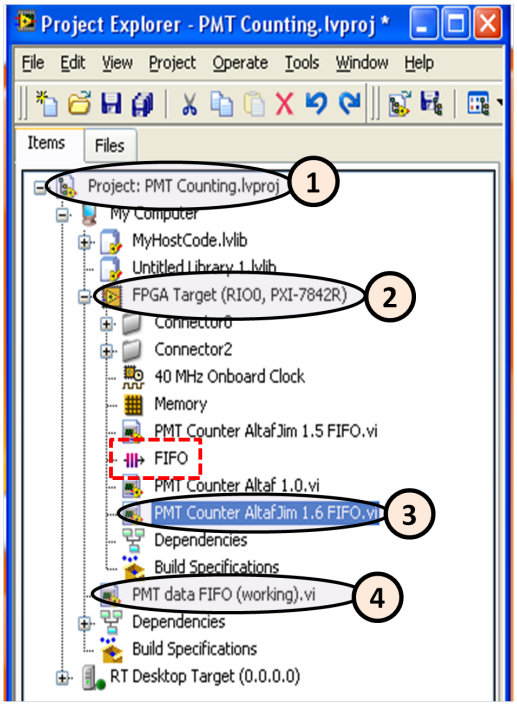

Figure F.1: FPGA project

The heating measurement *FPGA project* ① shown in figure F.1 consists of two LabVIEW programs; the *Target* ③, runs on the *FPGA target* ② which is written using the FPGA module and the *Host* ④ runs on the windows based computer, this program is added in the *My Computer* tree.

Both *Target* and *Host* programs shown in figure F.3 can be loaded by double clicking the particular program in the *project* tree. The corresponding description of the numbered controls for both programs are as follows;

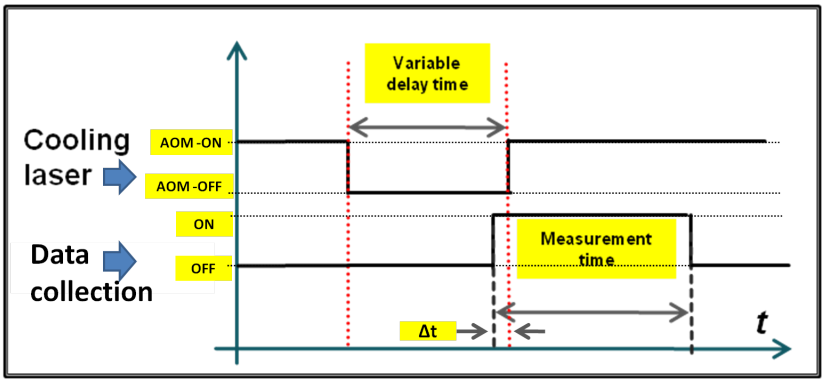

Figure F.2: The different time scales of the heating measurement experiment. The cooling laser can be blocked and un blocked using the AOM. The data (photon counts) is collected from the PMT.

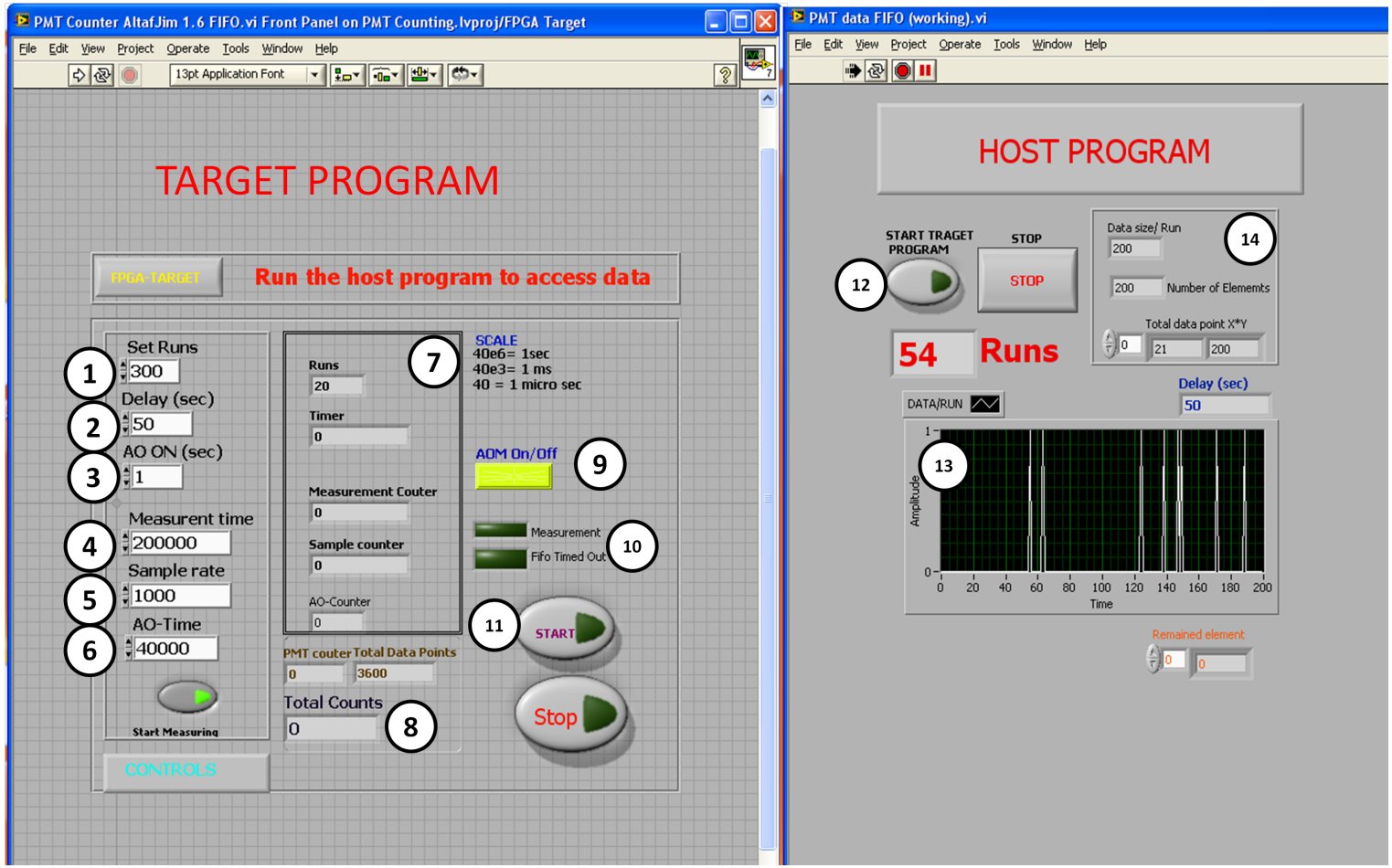

Figure F.3: Front panels of the *Target* and the *Host* programs for the heating measurement experiment.

Target Program:

1. Control box to set the number of runs (or the experiment iterations). In each run, the program will keep running with the same settings.
2. Control box to set the time in seconds during which the AOM has to be *OFF*. This delay time is illustrated in figure F.2.
3. Control box to set the time in seconds during which the AOM has to be *ON*.
4. Control box to set the measurement time (in units of sampling frequency). 40×10^6 samples are equal to 1 second.
5. In this control, set the sampling frequency of the data reading from the PMT. If set to 1, it reads the data at the maximum speed of the card. As the speed of the card is 40 MHz, entering the value of 400,000,000 in this control will results in the program counting the data (samples) for a second.
6. Set the gap time (Δt) as shown in figure F.2 in units of sampling frequency. The gap time is the time between the start of the measurement and the turning on the AOM. (The heating experiment requires that the measurement should be started before the AOM is turned on).
7. Numerical indicator boxes show the status of the program.
8. LED indicator to show the status of the AOM. (In case of green, the AOM is ON)
9. Numerical indicator shows the total number of counts per run.
10. LED indicator shows the status of the memory (FIFO). (Red indicates the FIFO is not handling the data).
11. Control button to start the measurement without involving the *Host* program if required. Otherwise the *Host* program automatically start the measurement.

Host Program:

The program is running on the windows based host computer. The program needs to be run after running the *Target* program on the FPGA-target.

12. Control button to run the target program.

13. Graphical indicator to display the data.

14. Numerical indicator shows the number of data elements in each run. The number of elements can be calculated by dividing the measurement time (4) with the sample rate (5).

After finishing the total number of "runs" set in (1), the program automatically asks to save the data file.

Program code

The program code of the target program is shown in figure F.4. The *Target* program code is written LabVIEW FPGA module and runs on the FPGA target. The data can be accessed by a *host* program written in windows based LabVIEW module. The *Host* program code is shown in figure F.5

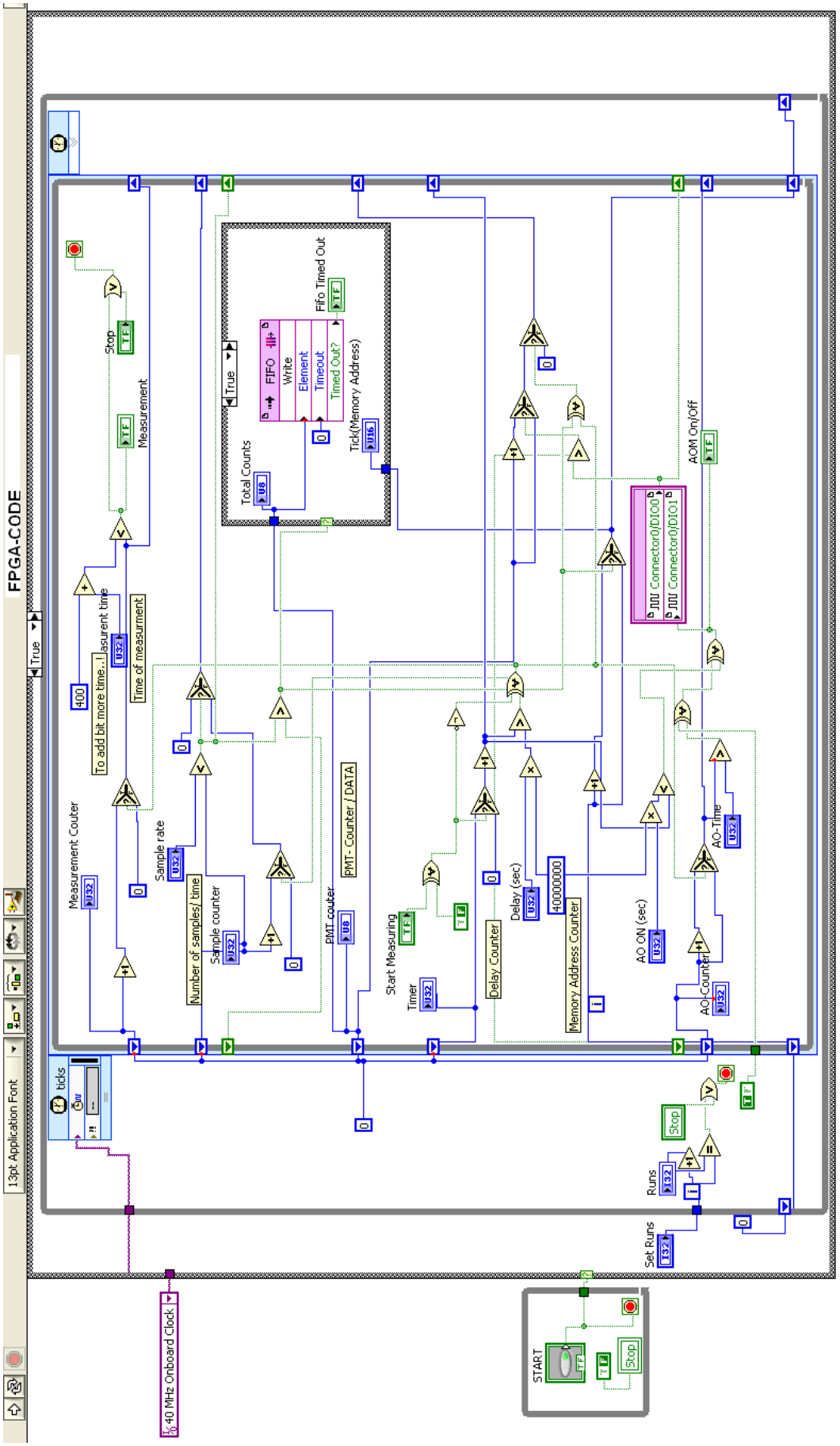

Figure F.4: The code of the *Target* program for the heating measurement experiment. The code is written in LabVIEW FPGA module.

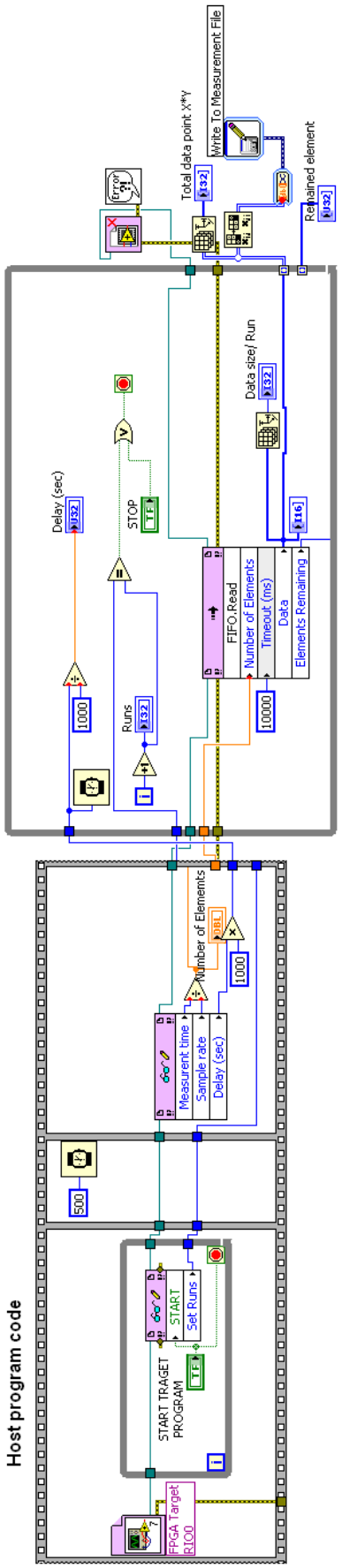

Figure F.5: The code of the *Host* program for the heating measurement experiment.

Bibliography

[1] R. P. Feynman. Simulating physics with computers. *Int. J. Th. Phys.*, 21(6/7):467–488, 1982.

[2] P.W. Shor. Algorithms for quantum computation: discrete logarithms and factoring. *Foundations of Computer Science, Annual IEEE Symposium on*, 0:124–134, 1994.

[3] J. I. Cirac and P. Zoller. Quantum computations with cold trapped ions. *Phys. Rev. Lett.*, 74(20):4091–4094, May 1995.

[4] C. Monroe, D. M. Meekhof, B. E. King, and D. J. Wineland. A Schrodinger Cat Superposition State of an Atom. *Science*, 272(5265):1131–1136, 1996.

[5] D. J. Wineland, C. Monroe, W. M. Itano, D. Leibfried1, B. E. King, and D. M. Meekhof. Experimental issues in coherent quantum-state manipulation of trapped atomic ions. *J. Res. Natl. Inst. Stand. Technol*, 103(3):259–328, Jun 1998.

[6] D. Leibfried, B. DeMarco, V. Meyer, M. Rowe, A. Ben-Kish, J. Britton, W. M. Itano, B. Jelenković, C. Langer, T. Rosenband, and D. J. Wineland. Trapped-ion quantum simulator: Experimental application to nonlinear interferometers. *Phys. Rev. Lett.*, 89(24):247901, Nov 2002.

[7] R. Blatt, H. Häffner, C. F. Roos, C. Becher, and F. Schmidt-Kaler. Ion trap quantum computing with ca^+ ions. *Quantum Information Processing*, 3(1-5):61–73, 2004.

[8] F. Schmidt-Kaler, H. Häffner, M. Riebe, S. Gulde, G. P. T. Lancaster, T. Deuschle, C. Becher, C. F. Roos, J. Eschner, and R. Blatt. Realization of the CiracZoller controlled-NOT quantum gate. *Nature*, 422:408–411, 2003.

[9] J. H. Wesenberg. Ideal intersections for radio-frequency trap networks. *Phys. Rev. A*, 79(1):013416, Jan 2009.

[10] M. D. Barrett, J. Chiaverini, T. Schaetz, J. Britton, W. M. Itano, J. D. Jost, E. Knill, C. Langer, D. Leibfried, R. Ozeri, and D. J. Wineland. Deterministic quantum teleportation of atomic qubits. *Nature*, 429:737–739, June 2004.

[11] M. Riebe, H. Häffner, C. F. Roos, W. Hansel, J. Benhelm, G. P. T. Lancaster, T. W. Korber, C. Becher, F. Schmidt-Kaler, D. F. V. James, and R. Blatt. Deterministic quantum teleportation with atoms. *Nature*, 429:734–737, June 2004.

[12] J. Britton, D. Leibfried, J. A. Beall, R. B. Blakestad, J. H. Wesenberg, and D. J. Wineland. Scalable arrays of rf paul traps in degenerate Si. *Applied Physics Letters*, 95(17):173102, October 2009.

[13] J. Chiaverini, R. B. Blakestad, J. Britton, J. D. Jost, C. Langer, D. Leibfried, R. Ozeri, and D. J. Wineland. Surface-electrode architecture for ion-trap quantum information processing. *Quantum Information and Computation*, June 2005.

[14] A. Steane. The ion trap quantum information processor. *Applied Physics B: Lasers and Optics*, 64, June 1997.

[15] D. Kielpinski, C. Monroe, , D. J. Wineland, and D. J. Wineland. Architecture for a large-scale ion-trap quantum computer. *Nature*, 417:709 to 711, Jun 2002.

[16] J. I. Cirac and P. Zoller. A scalable quantum computer with ions in an array of microtraps. *Nature*, 404, April 2000.

[17] Andrew M. Steane. How to build a 300 bit, 1 giga-operation quantum computer. *Quantum Information and Computation*, 7(3):171–183, Mar 2007.

[18] S. Schulz, U. Poschinger, K. Singer, and F. Schmidt-Kaler. Optimization of segmented linear paul traps and transport of stored particles. *Fortschr. Phys.*, 54(8-10):648665, Aug 2006.

[19] W. K. Hensinger, S. Olmschenk, D. Stick, D. Hucul, M. Yeo, M. Acton, L. Deslauriers, C. Monroe, and J. Rabchuk. T-junction ion trap array for two-dimensional ion shuttling, storage, and manipulation. *Applied Physics Letters*, 88(3):034101, 2006.

[20] D. Stick, W. K. Hensinger, S. Olmschenk, M. J. Madsen, K. Schwab, K. Schwab, and C. Monroe. Ion trap in a semiconductor chip. *Nat Phys*, 2(5265):36–39, Jan 2006.

[21] A. H. Myerson, D. J. Szwer, S. C. Webster, D. T. C. Allcock, M. J. Curtis, G. Imreh, J. A. Sherman, D. N. Stacey, A. M. Steane, and D. M. Lucas. High-fidelity readout of trapped-ion qubits. *Phys. Rev. Lett.*, 100(20):200502, May 2008.

[22] R. B. Blakestad, C. Ospelkaus, A. P. VanDevender, J. M. Amini, J. Britton, D. Leibfried, and D. J. Wineland. High-Fidelity Transport of Trapped-Ion Qubits through an X-Junction Trap Array. *Phys. Rev. Lett.*, 102(15):153002, Apr 2009.

[23] S. Seidelin, J. Chiaverini, R. Reichle, J. J. Bollinger, D. Leibfried, J. Britton, J. H. Wesenberg, R. B. Blakestad, R. J. Epstein, D. B. Hume, W. M. Itano, J. D. Jost, C. Langer, R. Ozeri, N. Shiga, and D. J. Wineland. Microfabricated surface-electrode ion trap for scalable quantum information processing. *Phys. Rev. Lett.*, 96(25):253003, Jun 2006.

[24] D. T. C. Allcock, J. A. Sherman, D. N. Stacey, A. H. Burrell, M. J. Curtis, G. Imreh, N. M. Linke, D. J. Szwer, S. C. Webster, A. M. Steane, and D. M. Lucas. Implementation of a symmetric surface-electrode ion trap with field compensation using a modulated raman effect. *New J. Phys.*, 12:053026, 2010.

[25] J. M. Amini, H. Uys, J. H. Wesenberg, S. Seidelin, J. Britton, J. J. Bollinger, D. Leibfried, C. Ospelkaus, A. P. VanDevender, and D. J. Wineland. Toward scalable ion traps for quantum information processing. *New Journal of Physics*, 12(3):033031, Mar 2010.

[26] Brown, Kenneth R. and Clark, Robert J. and Labaziewicz, Jaroslaw and Richerme, Philip and Leibrandt, David R. and Chuang, Isaac L. Loading and characterization of a printed-circuit-board atomic ion trap. *Phys. Rev. A*, 75(1):015401, Jan 2007.

[27] C. E. Pearson, D.R. Leibrandt, W.S. Bakr, W.J. Mallard, K.R. Brown, and I.L. Chuang. Experimental investigation of planar ion traps. *Physical Review A*, 73(3):032307, Mar 2006.

[28] Jaroslaw Labaziewicz, Yufei Ge, Paul Antohi, David Leibrandt, Kenneth R. Brown, and Isaac L. Chuang. Suppression of heating rates in cryogenic surface-electrode ion traps. *Phys. Rev. Lett.*, 100(1):013001, Jan 2008.

[29] J. Chiaverini, R. B. Blakestad, J. Britton, J. D. Jost, C. Langer, D. Leibfried, R. Ozeri, and D. J. Wineland. Surface-electrode architecture for ion-trap quantum information processing. *Quantum Information and Computation*, 5:419–439, Jun 2005.

[30] Q. A. Turchette, Kielpinski, B. E. King, D. Leibfried, D. M. Meekhof, C. J. Myatt, M. A. Rowe, C. A. Sackett, C. S. Wood, W. M. Itano, C. Monroe, and D. J. Wineland. Heating of trapped ions from the quantum ground state. *Phys. Rev. A*, 61(6):063418, May 2000.

[31] L. Deslauriers, S. Olmschenk, D. Stick, W. K. Hensinger, J. Sterk, and C. Monroe. Scaling and suppression of anomalous heating in ion traps. *Phys. Rev. Lett.*, 97(10):103007, Sep 2006.

[32] Jaroslaw Labaziewicz, Yufei Ge, Paul Antohi, David Leibrandt, Kenneth R. Brown, and Isaac L. Chuang. Suppression of heating rates in cryogenic surface-electrode ion traps. *Phys. Rev. Lett.*, 100(1):013001, Jan 2008.

[33] Jaroslaw Labaziewicz, Yufei Ge, David R. Leibrandt, Shannon X. Wang, Ruth Shewmon, and Isaac L. Chuang. Temperature dependence of electric field noise above gold surfaces. *Phys. Rev. Lett.*, 101(18):180602, Oct 2008.

[34] Jaroslaw Labaziewicz, Yufei Ge, David R. Leibrandt, Shannon X. Wang, Ruth Shewmon, and Isaac L. Chuang. Temperature dependence of electric field noise above gold surfaces. *Phys. Rev. Lett.*, 101(18):180602, Oct 2008.

[35] Wolfgang Paul. Electromagnetic traps for charged and neutral particles. *Rev. Mod. Phys.*, 62(3):531–540, Jul 1990.

[36] Park S.J., P.J. Manson, M.J. Wouters, R.B. Warrington, M.A. Lawn, and P.T.H. Fisk. *Proceedings of the 2007 IEEE International frequency control symposium - jointly with the 21st European frequency and time forum*, 1-4, Jun 2007.

[37] M.Roberts, P.Taylor, S.V. Gateva-Kostova, R.B.M.Clarke, W.R.C.Rowley, and P.Gill. *Physical Review A*.

[38] P. J. Blythe, S. A. Webster, H. S. Margolis, S. N. Lea, G. Huang, S.-K. Choi, W. R. C. Rowley, P. Gill, and R. S. Windeler. Subkilohertz absolute-frequency measurement of the 467-nm electric octupole transition in $^{171}Yb^{+}$. *Phys. Rev. A*, 67(2):020501, Feb 2003.

[39] Chr. Tamm, B. Lipphardt, H. Schnatz, R. Wynands, S. Weyers, T. Schneider, and E. Peik. $^{171}Yb^{+}$ single-ion optical frequency standard at 688Thz. *IEEE Transaction on instrumentation and measurements*, 56(2):601 to 604, April 2007.

[40] Z. W. Barber, J. E. Stalnaker, N. D. Lemke, N. Poli, C. W. Oates, T. M. Fortier, S. A. Diddams, L. Hollberg, C. W. Hoyt, A. V. Taichenachev, and V. I. Yudin. Optical lattice induced light shifts in an Yb atomic clock. *Physical Review Letters*, 100(10):103002–1 to 103002–4, March 2008.

[41] Sergey G. Porsev, Andrei Derevianko, and E. N. Fortson. Possibility of an optical clock using the $6^1S_0 \rightarrow 6^3P_0$ transition in ^{171,173}Yb atoms held in an optical lattice. *Phys. Rev. A*, 69(2):021403, Feb 2004.

[42] Tao Hong, Claire Cramer, Eryn Cook, Warren Nagourney, and E. N. Fortson. Observation of the $^1S_0 - ^3P_0$ transition in atomic ytterbium for optical clocks and qubit arrays. *Optics Letter*, 30(19):2644 to 2646, October 2005.

[43] Z. W. Barber, C. W. Hoyt, C. W. Oates, L. Hollberg, A. V. Taichenachev, and V. I. Yudin. Direct excitation of the forbidden clock transition in neutral ^{174}Yb atoms confined to an optical lattice. *Phys. Rev. Lett.*, 96(8):83002, Mar 2006.

[44] C. Monroe. Quantum information processing with atoms and photons. *Nature*, 416:238–246, Mar 2002.

[45] D. J. Wineland, M. Barrett, , J. Britton, J. Chiaverini, B. DeMarco, W. M. Itano, B. Jelenkovi, C. Langer, D. Leibfried, V. Meyer, T. Rosenband, and T. Schtz. Quantum information processing with trapped ions. *Phil. Trans. R. Soc. Lond. A.*, 361(1808):1349–1361, May 2003.

[46] H. Häffner, C.F. Roos, and R. Blatt. Quantum computing with trapped ions. *Physics Reports*, 469(4):155–203, 2008.

[47] B. Leibfried, R. Blatt, C. Monroe, and D. Wineland. Quantum dynamics of single trapped ions. *Review of modern physics*, 75:281, 2003.

[48] Pardip K. Ghosh. *Ion Traps.* Oxford University Press, 1995.

[49] F. G. Major, V. N. Gheorghe, and G. Werth. *Charged Particle Traps.* Springer-Verlag, 2005.

[50] E. March Ramond. Quantum dynamics of single trapped ions. *Journal of mass spectrometry*, 32:351–369, 1997.

[51] M. J. Madsen, W. K. Hensinger, D. Stick, J. A. Rabchuk, and C. Monroe. Planar ion trap geometry for microfabrication. *Applied Physics B*, 78:639–651, 2004.

[52] J. H. Wesenberg. Electrostatics of surface-electrode ion traps. *Phys. Rev. A*, 78(6):063410, Dec 2008.

[53] J. Metcalf Harold and van der Straten Peter. *Springer-Verlag New York, Inc.*

[54] Chr. Balzer, A. Braun, T. Hannemann, Chr. Paape, M. Ettler, W. Neuhauser, and Chr. Wunderlich. Electrodynamically trapped Yb^+ ions for quantum information processing. *Phys. Rev. A*, 73(4):041407, Apr 2006.

[55] Michael Johanning, Andrés F. Varón, and Christof Wunderlich. Quantum simulations with cold trapped ions. *Journal of Physics B: Atomic, Molecular and Optical Physics*, 42(15):154009, 2009.

[56] Chr. Tamm, D. Engelke, and V. Bühner. Spectroscopy of the electric-quadrupole transition ${}^2S_{1/2}(F = 0) \rightarrow {}^2D_{3/2}(F = 2)$ in trapped ${}^{171}Yb^+$. *Phys. Rev. A*, 61(5):053405, Apr 2000.

[57] U. Tanaka, H. Matsunishi, I. Morita, and S. Urabe. Isotope-selective trapping of rare calcium ions using high-power incoherent light sources for the second step of photo-ionization. *Applied Physics B. Lasers and Optics*, 81(6):795 to 799, Oct 2005.

[58] D. Engelke and Chr. Tamm. Dark times in the resonance fluorescence of trapped ${}^{171}Yb^+$ ions caused by spontaneous quantum jumps to the ${}^2D_{3/2}$ (F=2) state. *Europhysics Letters*, 33:347–352, Feb 1996.

[59] J.P. Hobson P.A. Redhead and E.V. Kornelsen. *The Physical Bases of Ultra High Vacuum*. Chapman and Hall Ltd., 1968.

[60] NASA. Outgassing data for selecting spacecraft materials, http://outgassing.nasa.gov/, February 2011.

[61] K. Odaka and S. Ueda. Dependence of outgassing rate on surface oxide layer thickness in type 304 stainless steel before and after surface oxidation in air. *Vacuum*, 47(6-8):689 – 692, 1996. Proceedings of the 13th International Vacuum Congress and the 9th International Conference on Solid Surfaces.

[62] W. Schuurman. Investigation of a low pressure Penning discharge. *Physica*, 36:136, 1967.

[63] M. Audi. Pumping speed of sputter ion pumps. *Vacuum*, 38(8-10):669 – 671, 1988.

[64] R. W. P. Drever, J. L. Hall, F. V. Kowalski, J. Hough, G. M. Ford, A. J. Munley, and H. Ward. Laser phase and frequency stabilization using an optical resonator. *Applied Physics B*, 31:97–105, 1983. 10.1007/BF00702605.

[65] E. D. Black. An introduction to pound-drever-hall laser frequency stabilization. *American Journal of Physics*, 69:79, 2001.

[66] Jun Ye, Steve Swartz, Peter Jungner, and John L. Hall. Hyperfine structure and absolute frequency of the ^{87}Rb $^{5}P_{3/2}$ state. *Opt. Lett.*, 21(16):1280–1282, 1996.

[67] D. J. Berkland and M. G. Boshier. Destabilisation of dark states and optical spectroscopy in zeeman-degenerate atomic systems. *arXive:quant-ph/0111018v1*, 2001.

[68] I. Siemers, M. Schubert, R. Blatt, W. Neuhauser, and P. E. Toschek. The "Trapped State" of a Trapped Ion-Line Shifts and Shape. *EPL (Europhysics Letters)*, 18(2):139, 1992.

[69] S. Ejtemaee, R. Thomas, and P. C. Haljan. Optimization of Yb^+ fluorescence and hyperfine-qubit detection. *Phys. Rev. A*, 82(6):063419, Dec 2010.

[70] W. W. Macalpine and R. O. Schildknecht. Coaxial resonator with helical inner conductor. *Proceedings of the IRE*, pages 2099–2105, December 1959.

[71] D. Siverns J, L. R. Simkins, S. Weibt, and W. K. Hensinger. On the applictaion of radio frequency voltages to ion traps via helical resonators. *arXive:*, 2011.

[72] M. R. Dietrich, A. Avril, R. Bowler, N. Kurz, J. S. Salacka, G. Shu, and B. B. Blinov. Barium ions for quantum computation. *arXiv:0905.2701*, 2009.

[73] D. J. Wineland, C. R. Monroe, W.M. Itano, B. E. King, D. Leibfried, D. M. Meekhof, C.J. Myatt, and C. S. Wood. Experimental primer on the trapped ion quantum computer. *Fortschritte de Physik*, 46:363 – 390, 1988.

[74] H. C. Nägerl, W. Bechter, J. Eschner, F. Schmidt-Kaler, and R. Blatt. Ion strings for quantum gates. *Applied Physics B*, 66(5):603–608, May 1998.

[75] D. M. Lucas, C. J. S. Donald, J. P. Home, M. J. McDonnell, A. Ramos, D. N. Stacey, J. P. Stacey, A. M. Steane, and S. C. Wester. Oxford ion-trap quantum computing project. *Phil. Trans. R. Soc. A*, 361(1808):1401–1408, Jul 2003.

[76] K Koo, J Sudbery, D. M. Segal, and R. C. Thompson. Doppler cooling of Ca^+ ions in a Penning trap. *Physical Review A*, 69(4), Apr 2004.

[77] U. G. Poschinger, G. Huber, F. Ziesel, M. Deiss, M. Hettrich, S. A. Schulz, K. Singer, G. Poulsen, M. Drewsen, R. J. Hendricks, and F. Schmidt-Kaler. Coherent manipulation of a $^{40}Ca^{+}$ spin qubit in a micro ion trap. *Journal Of Physica B*, 42(15), Aug 2009.

[78] B. B. Blinov, L Deslauriers, P Lee, M. J. Madsen, R Miller, and C Monroe. Sympathetic cooling of trapped Cd^{+} isotopes. *Physical Review A*, 65(4, Part A), Apr 2002.

[79] V. Letchumanan, G. Wilpers, M. Brownnutt, P. Gill, and A. G. Sinclair. Zero-point cooling and heating-rate measurements of a single $^{88}Sr^{+}$ ion. *Phys. Rev. A*, 75(6):063425, Jun 2007.

[80] A. S. Bell, P. Gill, H. A. Klein, A. P. Levick, C Tamm, and D Schnier. Laser Cooling of Trapped Ytterbium Ions Using a 4-level optical-excitation scheme. *Physical Review A*, 44(1):R20–R23, Jul 1991.

[81] A. Braun, Chr Paape, Chr Balzer, W. Neuhauser, and Chr Wunderlich. Resonance enhanced isotope-selective photoionization of Yb-I for ion trap loading. *arXiv:0712.0969v2*, Sep 2007.

[82] S. Olmschenk, K. C. Younge, D. L. Moehring, D. N. Matsukevich, P. Maunz, and C. Monroe. Manipulation and detection of a trapped Yb^{+} hyperfine qubit. *Physical Review A*, 76(5), Nov 2007.

[83] M. Roberts, P. Taylor, G. P. Barwood, P. Gill, H. A. Klein, and W. R. C. Rowley. *Phys. Rev. Lett.*, 78(10):1876–1879, Mar 1997.

[84] P. Gill, G. P. Barwood, H. A. Klein, G. Huang, S. A. Webster, P. J. Blythe, K. Hosaka, S. N. Lea, and H. S. Margolis. Trapped ion optical frequency standards. *Measurement Science and Technology*, 14(8):1174, 2003.

[85] T. Schneider, E. Peik, and Chr. Tamm. Sub-Hertz Optical Frequency Comparisons between Two Trapped $^{171}Yb^{+}$ Ions. *Phys. Rev. Lett.*, 94(23):230801, Jun 2005.

[86] J. Eschner, G. Morigi, F. Schmidt-Kaler, and R. Blatt. Laser cooling of trapped ions. *J. Opt. Soc. Am. B*, 20(5):1003–1015, 2003.

[87] R. J. Epstein, S. Seidelin, D. Leibfried, J. H. Wesenberg, J. J. Bollinger, J. M. Amini, R. B. Blakestad, J. Britton, J. P. Home, W. M. Itano, J. D. Jost, E. Knill,

C. Langer, R. Ozeri, N. Shiga, and D. J. Wineland. Simplified motional heating rate measurements of trapped ions. *Phys. Rev. A*, 76(3):033411, Sep 2007.

[88] E. W. Streed, T. J. Weinhold, and D. Kielpinski. Frequency stabilization of an ultraviolet laser to ions in a discharge. *Applied Physica Letters*, 93(7), Aug 2008.

[89] J. H. Wesenberg, R. J. Epstein, D. Leibfried, R. B. Blakestad, J. Britton, J. P. Home, W. M. Itano, J. D. Jost, E. Knill, C. Langer, R. Ozeri, S. Seidelin, and D. J. Wineland. Fluorescence during doppler cooling of a single trapped atom. *Phys. Rev. A*, 76(5):053416, Nov 2007.

[90] J. M. Amini, J. Britton, D. Leibfried, and D. J. Wineland. Microfabricated chip traps for ions. *ArXiv:0812.3907*, Dec 2008.

[91] M. D. Hughes, B. Lekitsch, J. A. Broersma, and W. K. Hensinger. Microfabricated Ion Traps. *ArXiv:1101.3207 (to appear in Contemporary Physics)*, 2011.

[92] F. Diedrich, J. C. Bergquist, Wayne M. Itano, and D. J. Wineland. Laser cooling to the zero-point energy of motion. *Phys. Rev. Lett.*, 62(4):403–406, Jan 1989.

[93] Ralph G. Diedrich and Christian Kurtsiefer. Experimental study of anomalous heating and trap instabilities in a microscopic ^{137}Ba ion trap. *Phys. Rev. A*, 65(6):063407, Jun 2002.

[94] Ch. Roos, Th. Zeiger, H. Rohde, H. C. Nägerl, J. Eschner, D. Leibfried, F. Schmidt-Kaler, and R. Blatt. Quantum state engineering on an optical transition and decoherence in a paul trap. *Phys. Rev. Lett.*, 83(23):4713–4716, Dec 1999.

[95] Stephan A. Schulz, Ulrich Poschinger, Frank Ziesel, and Ferdinand Schmidt-Kaler. Sideband cooling and coherent dynamics in a microchip multi-segmented ion trap. *New J. Phys.*, 10(045007):15, 2008.

[96] N. Daniilidis, S. Narayanan, S. A. Möller, R. Clark, T. E. Lee, P. J. Leek, A. Wallraff, St. Schulz, F. Schmidt-Kaler, and H. Häffner. Fabrication and heating rate study of microscopic surface electrode ion traps. *arXiv:1009.2834v1*, 2010.

[97] James J. McLoughlin, Altaf H. Nizamani, James D. Siverns, Robin C. Sterling, Marcus D. Hughes, Bjoern Lekitsch, Björn Stein, Seb Weidt, and Winfried K. Hensinger. Versatile ytterbium ion trap experiment for operation of scalable ion-trap chips with motional heating and transition-frequency measurements. *Phys. Rev. A*, 83(1):013406, Jan 2011.

[98] M. A. Rowe, A. Ben-Kish, B. DeMarco, D. Leibfried, V. Meyer, J. Beall, J. Britton, J. Hughes, W.M. Itano, B. Jelenkovic, C. Langer, T. Rosenband, and D.J. Wineland. Transport of qutaum states and separation of ions in a dual RF ion traps. *Quantum Inform. Comput.*, 2(4):257–271, Jun 2002.

[99] J. Britton. *Microfabrication techniques for trapped ion quantum information processing.* Ph.d. thesis, arxiv:1008.2222v1, Boulder, 2008.

[100] Shannon X. Wang, Yufei Ge, Jaroslaw Labaziewicz, Eric Dauler, Karl Berggren, and Isaac L. Chuang. Superconducting microfabricated ion traps. *Appl. Phys. Lett.*, 97:244102, 2010.

[101] H. A. Klein, A.S. Bell, G.P. Barwood, and P.Gil. Laser cooling of trapped Yb^+. *Appl. Phys. B*, 50:13 to 17, Jan 1990.

[102] H. Lehmitz, J. Hattendorf-Ledwoch, R. Blatt, and H. Harde. Population trapping in excited Yb ions. *Phys. Rev. Lett.*, 62(18):2108–2111, May 1989.

[103] V. Enders, Ph Courteille, R. Huesmann, L. S. Ma, W. Neuhauser, R. Blatt, and P. E. Toschek. Microwave-Optical Double Resonance on a Single Laser-Cooled $^{171}Yb^+$ Ion. *Europhysics Letters*, 24(5):325 to 331, Nov 1993.

[104] K. Honda, Y. Takahashi, T. Kuwamoto, M. Fujimoto, K. Toyoda, K. Ishikawa, and T. Yabuzaki. Magneto-optical trapping of Yb atoms and a limit on the branching ratio of the $^1P_1$ state. *Phys. Rev. A*, 59(2):R934 to R937, Feb 1999.

[105] U. D. Rapol, A. Krishna, A. Wasan, and V. Natarajan. Laser cooling and trapping of Yb from a thermal source. *The European Physical Journal D - Atomic, Molecular, Optical and Plasma Physics*, 29(3):409 to 414, Jun 2004.

[106] R. Huesmann, Ch. Balzer, Ph. Courteille, W. Neuhauser, and P. E. Toschek. *Phys. Rev. Lett.*, 82(8):1611–1615, Feb 1999.

[107] C. S. Edwards, P. Gill, H. A. Klein, A. P. Levick, and W. R. C. Rowley. Laser-cooling effects in few-ion clouds of ^{174}Yb. *Applied Physics B*, 59:179 to 185, May 1994.

[108] Das Dipankar and Natarajan Vasant. Laser cooling of ^{173}Yb for isotope separation and precision hyperfine spectroscopy. *Phys. Rev. A*, 76(6):062505, Dec 2007.

[109] T. Loftus, J. R. Bochinski, and T. W. Mossberg. Simultaneous multi-isotope trapping of ytterbium. *Phys. Rev. A*, 63(5):053401, Apr 2001.

[110] R. Maruyama, R. H. Wynar, M. V. Romalis, A. Andalkar, M. D. Swallows, C. E. Pearson, and E. N. Fortson. Investigation of sub-Doppler cooling in an ytterbium magneto-optical trap. *Phys. Rev. A*, 68(1):011403, Jul 2003.

[111] S. Olmschenk, K. C. Younge, D. L. Moehring, D. N. Matsukevich, P. Maunz, and C. Monroe. Manipulation and detection of a trapped Yb^+ hyperfine qubit. *Physical Review A*, 76:052314–2 to 052314–9, November 2007.

[112] A. M. Bacon, H. Z. Zhao, L. J. Wang, and J. E. Thomas. Optical Dipole Noise of Two-Level Atoms. *Phys. Rev. Lett.*, 75(7):1296–1299, Aug 1995.

[113] David DeMille. Parity Nonconservation in the $6s^2 {}^1S_0 \rightarrow 6s5d {}^3D_1$ Transition in Atomic Ytterbium. *Phys. Rev. Lett.*, 74(21):4165 to 4168, May 1995.

[114] A. Sankari, R. Sankari, S. Heinäsmäki, M. Huttula, S. Aksela, and H. Aksela. 4d photoionization and subsequent Auger decay in atomic Eu. *Phys. Rev. A*, 77(5):052703, May 2008.

[115] R.J. Hendricks, and D.M. Grant Contact Information, P.F. Herskind, A. Dantan, and M. Drewsen. An all-optical ion-loading technique for scalable microtrap architectures. *Applied Physics B*, 88:507 to 513, May 2007.

[116] Marko Cetina, Andrew Grier, Jonathan Campbell, Isaac Chuang, and Vladan Vuletić. Bright source of cold ions for surface-electrode traps. *Phys. Rev. A*, 76(4):041401, Oct 2007.

[117] W. F. Meggers and J. L. Tech. Ytterbium ion trap experiment towards scalable quantum technology. *J. L. Tech, J. Res. NBS*, 83:13, 1978.

[118] T. Loftus, R. Bochinski, and T.W.Mossberg. Optical double-resonance cooled spectroscopy. *Physical Review A*, 63:023402–1 to 023402–4, January 2001.

[119] K. Deilamian, J.D.Gillaspy, and D.E.Kelleher. Isotope shifts and hyperfine splitting of the 398.8 nm Yb-I line. *J.Opt.Soc.Am.B*, 10(5):789 to 793, May 1993.

[120] R Zinkstok, E J van Duijn, S Witte, and W Hogervorst. Hyperfine structure and isotope shift of transitions in Yb I using UV and deep-UV cw laser light and the angular distribution of fluorescence radiation. *Journal of Physics B*, 35(12):2693 to 2701, May 2002.

[121] D. Das, S. Barthwal, A. Banerjee, and Natrajan. Absolute frequency measurement in Yb with 0.08ppb uncertainity: Isotope shifts and hyperfine structure in the 399 nm $^1S_0 \rightarrow^1 P_1$ line. *Physical Review A*, 72:032506–1 to 032506–7, Sep 2005.

[122] Yu. Ralchenko, A. E. Kramida, J. Reader, and NIST ASD Team(2008). *NIST Atomic Spectra Database (Version 3.1.5)*, 83:13, 24 Aug 2010.

[123] M. M. Schauer, J. R. Danielson, D. Feldbaum, M. S. Rahaman, L. B. Wang, J. Zhang, X. Zhao, and J. R. Torgerson. Isotope-selective trapping of doubly charged Yb ions. *Phys. Rev. A*, 82(6):062518, Dec 2010.

[124] K. Honda, Y. Takahashi, T. Kuwamoto, M. Fujimoto, K. Toyoda, K. Ishikawa, and T. Yabuzaki. Magneto-optical trapping of Yb atoms and a limit on the branching ratio of the $1P1$ state. *Phys. Rev. A*, 59(2):R934 to R937, Feb 1999.

[125] M. Okano, H. Hara, M. Muramatsu, K. Doi, S. Uetake, Y. Takasu, and Y. Takahashi. Simultaneous magneto-optical trapping of lithium and ytterbium atoms towards production of ultracold polar molecules. *Applied Physics B: Lasers and Optics*, 98:691–696, 2010. 10.1007/s00340-009-3728-0.

[126] W. R. Bennett. Hole Burning Effects in a He-Ne Optical Maser. *Phys. Rev.*, 126(2):580–593, Apr 1962.

[127] W. K. Hensinger, A. G. Truscott, H. Rubinsztein-Dunlop, and N. R. Heckenberg. Variations of relative line intensity in saturation spectroscopy due to low magnetic fields. *Optical and Quantum Electronics*, 31(5/7):391–403, July 1999.

[128] H. G. Dehmelt. Radio frequency spectroscopy of stored ions. *Adv. At. Mol. Phys.*, 3:53, 1967.

[129] M. G. House. Analytic model for electrostatic fields in surface-electrode ion traps. *Phys. Rev. A*, 78(3):033402, Sep 2008.

[130] Roman Schmied. Electrostatics of gapped and finite surface electrodes. *New J. Phys.*, 102(2):023038, Feb 2010.

[131] W. M. Itano and D. J. Wineland. Laser cooling of ions stored in harmonic and penning traps. *Phys. Rev. A*, 25(1):35 to 54, January 1982.

[132] J. Mueller, and D. Pyle, and I. Chakraborty, and R. Ruiz, and W. Tang, and R. Lawton,. Feasibility Study of MEMS-Based Accelerator. Grid Systems for Micro-

Ion Engines: Electric Breakdown Characteristics. *AIAA Journal of Propulsion and Power U.S.A.*, 1999.

[133] D. Hucul, M. Yeo, W. K. Hensinger, J. Rabchuk, S. Olmschenk, and C. Monroe. On the transport of atomic ions in linear and multidimensional ion trap arrays. *Quantum Information and Computation*, 8(6&7):501, 2008.

[134] R. Reichle, D. Leibfried, R. B. Blakestad, J. Britton, J. Britton, J. D. Jost, E. Knill, C. Langer, R. Ozeri, S. Seidelin, and D. J. Wineland. Transport dynamics of single ions in segmented microstructured paul trap arrays. *Fortschr. Phys.*, 54:666–685, Aug 2006.

[135] G. Huber, T. Deuschle, W. Schnitzler, R. Reichle, K. Singer, and F. Schmidt-Kaler. Transport of ions in a segmented linear paul trap in printed-circuit-board technology. *New Journal of Physics*, 10(1):013004, Jan 2008.

[136] R. C. Sterling, annd P. Srinivasan W. K. Hensinger, H.Rattanasonti, and M. Kraft. Surface ion trap chip with shielded dielectrics.

[137] Kilian Singer, Ulrich Poschinger, Michael Murphy, Peter Ivanov, Frank Ziesel, Tommaso Calarco, and Ferdinand Schmidt-Kaler. Colloquium: Trapped ions as quantum bits; essential numerical tools. *eprint arXiv:0912.0196*, 2009.

[138] J.P. Home and A.M. Steane. Electrode configurations for fast separation of trapped ions. *Quantum Information and Computation*, 6:5, 2006.

[139] J. P. Home, M. J. McDonnell, D. M. Lucas, G. Imreh, B. C. Keitch, D. J. Szwer, N. R. Thomas, S. C. Webster, D. N. Stacey, and A. M. Steane. Deterministic entanglement and tomography of ion-spin qubits. *New Journal of Physics*, 8(9):188, Sep 2006.

[140] Shannon X. Wang, Jaroslaw Labaziewicz, Yufei Ge, Ruth Shewmon, and Isaac L. Chuang. Demonstration of a quantum logic gate in a cryogenic surface-electrode ion trap. *Phys. Rev. A*, 81(6):062332, Jun 2010.

[141] Charles H. Bennett, Gilles Brassard, Claude Crépeau, Richard Jozsa, Asher Peres, and William K. Wootters. Teleporting an unknown quantum state via dual classical and einstein-podolsky-rosen channels. *Phys. Rev. Lett.*, 70(13):1895–1899, Mar 1993.

[142] D. Porras and J. I. Cirac. Effective quantum spin systems with trapped ions. *Phys. Rev. Lett.*, 92(20):207901, May 2004.

[143] L. Lamata, J. León, T. Schätz, and E. Solano. Dirac equation and quantum relativistic effects in a single trapped ion. *Phys. Rev. Lett.*, 98(25):253005, Jun 2007.

[144] J. Chiaverini and W. E. Lybarger. Laserless trapped-ion quantum simulations without spontaneous scattering using microtrap arrays. *Phys. Rev. A*, 77(2):022324, Feb 2008.

[145] K. Kim, M.-S. Chang, S. Korenblit, R. Islam, E. E. Edwards, J. K. Freericks, G.-D. Lin, L.-M. Duan, and C. Monroe. Quantum simulation of frustrated Ising spins with trapped ions. *Nature*, 465:590593, Mar 2010.

[146] Winfried K Hensinger, Norman R Heckenberg, Gerard J Milburn, and Halina Rubinsztein-Dunlop. Experimental tests of quantum nonlinear dynamics in atom optics. *Journal of Optics B: Quantum and Semiclassical Optics*, 5(2):R83, 2003.